The Pennsylvania State University
The Graduate School

NUMERICAL SIMULATIONS OF HIGH-Z MATERIAL ABLATION IN TRANSIENT CONDITIONS

A Dissertation in

Nuclear Engineering

by

Victoria E. Hagopian

Submitted in Partial Fulfillment

of the Requirements

for the Degree of

Doctor of Philosophy

December 2022

The dissertation of Victoria E. Hagopian was reviewed and approved by the following:

Leigh Winfrey
Associate Professor of Nuclear Engineering
Dissertation Advisor
Chair of Committee

Marek Flaska
Associate Professor of Nuclear Engineering
Program Head

Venkatraman Gopalan
Professor of Materials Science and Engineering

Kenan Ünlü
Director of Radiation Science and Engineering Center, and Professor

Abstract

Operators of the Godiva IV Fast Burst Reactor discovered that, through observation and measurement, the device has lost mass, likely through an ablative process. While the loss was noted, the ablative process was never investigated, either by experimentation or simulation, until this study. It was theorized that a dusty plasma forms in the capillary like space between the Safety Block and Intermediate Inner Subassembly Plate (IISP) during normal burst operations of Godiva IV. To see if this was indeed the phenomenon that was occurring, a number of simulations and physical experiments were carried out. During the investigation, a total of 27 materials were simulated using ETCOMBFLOW, an version of the 1-D, time-dependent, electrothermal plasma code ETFLOW. The materials simulated included a suite of Tungsten-Molybdenum alloys as well as a set of Uranium-Molybdenum alloys that included the U-Mo alloy that comprises the Godiva IV device. Some of the other materials included, like TZM alloy and Pure Tungsten were included as these materials are used in tokamak applications. Based on results from these simulations, it can be concluded that the concentration of Molybdenum in the material being ablated does affect the amount of ablation seen, which higher amounts in Uranium based alloys attributing to lower amounts of ablation.

Once ETFLOW simulations were complete, a Heat Flux study was performed using the engineering software ANSYS to model mock-ups of lasers and heat impinging on a materials surface. As the physical experiments that used laser ablation spectroscopy were performed on Pure Tungsten slabs, it was decided to simulate the HELIOS ANSYS models with Pure Tungsten at 2.50 $\times$ P228 Ideal and Non-Ideal Conductivity ETFLOW data to perform a comparison between model types. For the Laser Ablation Simulations, four samples were simulated 10 times each: once for each laser power (which resulted in a different Impact Site configuration) and once for each Convective Boundary location (Top Face and Body of the Impact Site). Simulations using the HELIOS data used three configurations of depths: 10, 23, and 30 μm, the Ideal and Non-Ideal Pure Tungsten 2.50 $\times$ P228 data, and applied the same Convective Boundary locations as the Laser Ablation simulations. Simulation results from both sets were indicative of appropriate levels of material melt and ablation as would be expected in these kinds of experimental conditions, lending to the confirmation of electrothermal plasma formation.

Using the results from the ETFLOW and ANSYS simulations, a mass mitigation model has been proposed, along with other work that would benefit this area of research.

Table of Contents

List of Figures viii

List of Tables xii

List of Equations xvii

List of Symbols xviii

List of Terms xix

Acknowledgments xx

Chapter 1
Introduction and Background 1
1.1 Dusty Plasma Formation . . . 1
1.1.1 Vapor Shielding Modelling . . . 3
1.1.1.1 Vapor Shielding Opacity Model . . . 4
1.1.1.2 Vapor Shielding Energy Ratio Model . . . 4
1.2 Plasma Parameters . . . 5
1.3 HEU Systems . . . 5
1.3.1 Godiva IV . . . 5
1.3.1.1 Device Operation . . . 6
1.3.2 Mass Loss in Godiva IV . . . 6
1.4 Materials Consideration . . . 7
1.4.1 W-Mo Alloy . . . 8
1.4.2 U-Mo Alloy . . . 8
1.5 Plasma Spectroscopy . . . 8
1.5.1 Absorption Spectroscopy . . . 9
1.5.2 Emission Spectroscopy . . . 10
1.5.3 Experimental Method . . . 10

Chapter 2
Introduction and Background **11**
2.1 Dusty Plasma Formation . . . 11
2.1.1 Vapor Shielding Modelling . . . 13
2.1.1.1 Vapor Shielding Opacity Model . . . 14
2.1.1.2 Vapor Shielding Energy Ratio Model . . . 14
2.2 Plasma Parameters . . . 15
2.3 HEU Systems . . . 15
2.3.1 Godiva IV . . . 15
2.3.1.1 Device Operation . . . 16
2.3.2 Mass Loss in Godiva IV . . . 16
2.4 Materials Consideration . . . 17
2.4.1 W-Mo Alloy . . . 18
2.4.2 U-Mo Alloy . . . 18
2.5 Plasma Spectroscopy . . . 18
2.5.1 Absorption Spectroscopy . . . 19
2.5.2 Emission Spectroscopy . . . 20
2.5.3 Experimental Method . . . 20

Chapter 3
Plasma Surface Interactions In High Heat Flux Conditions **21**
3.1 HELIOS Experiment . . . 22
3.2 ETFLOW . . . 23
3.2.1 Governing Equations . . . 23
3.2.2 Plasma Conductivity . . . 24
3.2.3 Material Parameters . . . 24
3.3 Peak Plasma and Materials Parameters Results . . . 27
3.3.1 Peak Temperature . . . 27
3.3.2 Peak Electron Number Density . . . 30
3.3.3 Total Ablated Mass . . . 32
3.4 Time Varying Plasma and Materials Parameters - Simulation Results . . . 34
3.4.1 Select Material Data . . . 35
3.4.1.1 Error Associated with ETFLOW Conductivity Models . . . 36
3.4.2 Pure Material - Molybdenum . . . 37
3.4.3 Pure Material - Tantalum . . . 40
3.4.4 Pure Material - Titanium . . . 44
3.4.5 Pure Material - Tungsten . . . 47
3.4.6 Pure Material - Uranium . . . 50
3.4.7 Pure Material - Zirconium . . . 53
3.4.8 TZM Alloy . . . 56
3.5 W-Mo Alloys . . . 59
3.5.1 W-Mo(1.00%) Alloy . . . 59
3.5.2 W-Mo(1.25%) Alloy . . . 62

3.5.3 W-Mo(1.50%) Alloy . . . 65
3.5.4 W-Mo(1.75%) Alloy . . . 69
3.5.5 W-Mo(2.00%) Alloy . . . 72
3.6 Godiva IV Material Data . . . 75
3.6.1 U-Mo(1.00%) Alloy . . . 76
3.6.1.1 Ideal Simulation Comparison . . . 76
3.6.1.2 Non-Ideal Simulation Comparison . . . 77
3.6.1.3 Select Graphical Comparison . . . 79
3.6.2 U-Mo(1.25%) Alloy . . . 81
3.6.2.1 Ideal Simulation Comparison . . . 82
3.6.2.2 Non-Ideal Simulation Comparison . . . 83
3.6.2.3 Select Graphical Comparison . . . 84
3.6.3 U-Mo(1.50%) Alloy . . . 88
3.6.3.1 Ideal Simulation Comparison . . . 88
3.6.3.2 Non-Ideal Simulation Comparison . . . 89
3.6.3.3 Select Graphical Comparison . . . 90
3.6.4 U-Mo(1.75%) Alloy . . . 93
3.6.4.1 Ideal Simulation Comparison . . . 93
3.6.4.2 Non-Ideal Simulation Comparison . . . 95
3.6.4.3 Select Graphical Comparison . . . 96
3.6.5 U-Mo(2.00%) Alloy . . . 99
3.6.5.1 Ideal Simulation Comparison . . . 99
3.6.5.2 Non-Ideal Simulation Comparison . . . 100
3.6.5.3 Select Graphical Comparison . . . 101
3.7 General Conclusions . . . 103

Chapter 4
Proof of Concept: Spectroscopy Experiments and Heat Flux Study **106**
4.1 ANSYS Simulation Setup . . . 106
4.1.1 Model Creation . . . 106
4.1.2 Transient Thermal Analysis . . . 111
4.2 HELIOS Spectroscopy Simulations . . . 112
4.2.1 HELIOS ANSYS Setup . . . 112
4.2.2 HELIOS ANSYS Simulation Results . . . 113
4.3 Laser Spectroscopy – Experiments and Simulations . . . 116
4.3.1 Laser Assembly Setup . . . 116
4.3.2 Laser Ablation ANSYS Setup . . . 117
4.3.3 Laser Ablation ANSYS Simulation Results . . . 122

Chapter 5
Summary & Conclusions **125**
5.1 Summary of Work . . . 125
5.2 Mass Loss Mitigation Model . . . 126

5.2.1 Godiva IV Specific Model 127
5.2.1.1 Godiva IV Mass Loss Calculations 128
5.3 Final Conclusions 133

Chapter 6
Future Work **135**
6.1 Proposed Work 135
6.2 Impact 136

Appendix A
ETFLOW Simulation Results **137**
A.1 Tungsten-Molybdenum Alloys 137
A.1.1 W(3.00%)-Mo Results 138
A.1.2 W(5.00%)-Mo Results 140
A.1.3 W(19.5%)-Mo Results 142
A.1.4 W(90.0%)-Mo Results 144
A.1.5 W(98.5%)-Mo Results 146

Appendix B
Mass Loss Calculations **149**
B.1 Uranium Alloy Mass Loss Calculations 149
B.1.1 U-Mo(1.00%) Mass Loss Calculations 150
B.1.2 U-Mo(1.25%) Mass Loss Calculations 154
B.1.3 U-Mo(1.75%) Mass Loss Calculations 158
B.1.4 U-Mo(2.00%) Mass Loss Calculations 162

Bibliography **166**

List of Figures

1.1 Cutaway view of Godiva IV core, restraints, and proposed dusty plasma site [1]. 2
1.2 Dusty plasma formation schematic 3
1.3 Godiva IV, with the aluminum top hat [2]. 7
1.4 Example of line emission spectra that may be observed when performing plasma spectroscopy [3]. 9

2.1 Cutaway view of Godiva IV core, restraints, and proposed dusty plasma site. 12
2.2 Dusty plasma formation schematic 13
2.3 Godiva IV, with the aluminum top hat [2]. 17
2.4 Example of line emission spectra that may be observed when performing plasma spectroscopy [3]. 19

3.1 Schematic of the PIPE experimental set-up [4, 5]. 22
3.2 Peak Temperature (eV) versus the Current (kA) for the Pure Materials as generated by ETFLOW 28
3.3 Peak Temperature (eV) versus the Current (kA) for the W-Mo Alloys as generated by ETFLOW 28
3.4 Peak Temperature (eV) versus the Current (kA) for the U-Mo Alloys as generated by ETFLOW 29
3.5 Peak Electron Number Density (m^{-3}) versus the Current (kA) for the Pure Materials as generated by ETFLOW 31
3.6 Peak Electron Number Density (m^{-3}) versus the Current (kA) for the W-Mo Alloys as generated by ETFLOW 32
3.7 Peak Electron Number Density (m^{-3}) versus the Current (kA) for the U-Mo Alloys as generated by ETFLOW 33
3.8 Total Ablated Mass (mg) versus the Current (kA) for the Pure Materials as generated by ETFLOW 34
3.9 Total Ablated Mass (mg) versus the Current (kA) for the W-Mo Alloys as generated by ETFLOW 35
3.10 Total Ablated Mass (mg) versus the Current (kA) for the U-Mo Alloys as generated by ETFLOW 36
3.11 Molybdenum Temperature (eV) versus Time (μs) as generated by ETFLOW 40

3.12 Molybdenum Electron Number Density (m^{-3}) versus Time (μs) as generated by ETFLOW 41
3.13 Tantalum Temperature (eV) versus Time (μs) as generated by ETFLOW . . 42
3.14 Ta Electron Number Density (m^{-3}) versus Time (μs) as generated by ETFLOW 43
3.15 Titanium Temperature (eV) versus Time (μs) as generated by ETFLOW . . 46
3.16 Titanium Electron Number Density (m^{-3}) versus Time (μs) as generated by ETFLOW 47
3.17 Tungsten Temperature (eV) versus Time (μs) as generated by ETFLOW . . 49
3.18 Tungsten Electron Number Density (m^{-3}) versus Time (μs) as generated by ETFLOW 50
3.19 Uranium Temperature (eV) versus Time (μs) as generated by ETFLOW . . 52
3.20 Uranium Electron Number Density (m^{-3}) versus Time (μs) as generated by ETFLOW 53
3.21 Zirconium Temperature (eV) versus Time (μs) as generated by ETFLOW . 55
3.22 Zirconium Electron Number Density (m^{-3}) versus Time (μs) as generated by ETFLOW 56
3.23 TZM Alloy Temperature (eV) versus Time (μs) as generated by ETFLOW . 58
3.24 TZM Alloy Electron Number Density (m^{-3}) versus Time (μs) as generated by ETFLOW 59
3.25 W-Mo(1.00%) Temperature (eV) versus Time (μs) as generated by ETFLOW 61
3.26 W-Mo(1.00%) Electron Number Density (m^{-3}) versus Time (μs) as generated by ETFLOW 62
3.27 W-Mo(1.25%) Temperature (eV) versus Time (μs) as generated by ETFLOW 64
3.28 W-Mo(1.25%) Electron Number Density (m^{-3}) versus Time (μs) as generated by ETFLOW 65
3.29 W-Mo(1.50%) Temperature (eV) versus Time (μs) as generated by ETFLOW 68
3.30 W-Mo(1.50%) Electron Number Density (m^{-3}) versus Time (μs) as generated by ETFLOW 68
3.31 W-Mo(1.75%) Temperature (eV) versus Time (μs) as generated by ETFLOW 71
3.32 W-Mo(1.75%) Electron Number Density (m^{-3}) versus Time (μs) as generated by ETFLOW 71
3.33 W-Mo(2.00%) Temperature (eV) versus Time (μs) as generated by ETFLOW 74
3.34 W-Mo(2.00%) Electron Number Density (m^{-3}) versus Time (μs) as generated by ETFLOW 74
3.35 U-Mo(1.00%) Temperature (eV) versus Time (μs) as generated by ETFLOW using a high thermal conductivity case 79
3.36 U-Mo(1.00%) Temperature (eV) versus Time (μs) as generated by ETFLOW using a low thermal conductivity case 80
3.37 U-Mo(1.00%) Electron Number Density (m^{-3}) versus Time (μs) as generated by ETFLOW using a high thermal conductivity case 80
3.38 U-Mo(1.00%) Electron Number Density (m^{-3}) versus Time (μs) as generated by ETFLOW using a low thermal conductivity case 81

3.39 U-Mo(1.25%) Temperature (eV) versus Time (μs) as generated by ETFLOW using a high thermal conductivity case 85
3.40 U-Mo(1.25%) Temperature (eV) versus Time (μs) as generated by ETFLOW using a low thermal conductivity case 86
3.41 U-Mo(1.25%) Electron Number Density (m^{-3}) versus Time (μs) as generated by ETFLOW using a high thermal conductivity case 87
3.42 U-Mo(1.25%) Electron Number Density (m^{-3}) versus Time (μs) as generated by ETFLOW using a low thermal conductivity case 87
3.43 U-Mo(1.50%) Temperature (eV) versus Time (μs) as generated by ETFLOW using a high thermal conductivity case 91
3.44 U-Mo(1.50%) Temperature (eV) versus Time (μs) as generated by ETFLOW using a low thermal conductivity case 91
3.45 U-Mo(1.50%) Electron Number Density (m^{-3}) versus Time (μs) as generated by ETFLOW using a high thermal conductivity case 92
3.46 U-Mo(1.50%) Electron Number Density (m^{-3}) versus Time (μs) as generated by ETFLOW using a low thermal conductivity case 93
3.47 U-Mo(1.75%) Temperature (eV) versus Time (μs) as generated by ETFLOW using a high thermal conductivity case 97
3.48 U-Mo(1.75%) Temperature (eV) versus Time (μs) as generated by ETFLOW using a low thermal conductivity case 98
3.49 U-Mo(1.75%) Electron Number Density (m^{-3}) versus Time (μs) as generated by ETFLOW using a high thermal conductivity case 98
3.50 U-Mo(1.75%) Electron Number Density (m^{-3}) versus Time (μs) as generated by ETFLOW using a low thermal conductivity case 99
3.51 U-Mo(2.00%) Temperature (eV) versus Time (μs) as generated by ETFLOW using a high thermal conductivity case 102
3.52 U-Mo(2.00%) Temperature (eV) versus Time (μs) as generated by ETFLOW using a low thermal conductivity case 103
3.53 U-Mo(2.00%) Electron Number Density (m^{-3}) versus Time (μs) as generated by ETFLOW using a high thermal conductivity case 104
3.54 U-Mo(2.00%) Electron Number Density (m^{-3}) versus Time (μs) as generated by ETFLOW using a low thermal conductivity case 104

4.1 ANSYS rendering of a material block with a 11 μm diameter, 30 μm deep impact hole used for heat flux studies. 107
4.2 ANSYS rendering of a material block cross-section with updated bore hole, including the impact site crater caused by melting due to the laser. 108
4.3 Laser Impact Site Model Example 109
4.4 ANSYS rendering of a material block cross-section with the CFD mesh displayed. 110
4.5 ANSYS Total Heat Flux results based Ideal ETFLOW data with the Convective boundary set to the Top Face of the Impact Site. 114
4.6 ANSYS Total Heat Flux results based Non-Ideal ETFLOW data with the Convective boundary set to the Top Face of the Impact Site. 115

4.7 ANSYS Total Heat Flux results based Ideal ETFLOW data with the Convective boundary set to the Body of the Impact Site. 115
4.8 ANSYS Total Heat Flux results based Non-Ideal ETFLOW data with the Convective boundary set to the Body of the Impact Site. 116
4.9 Photo of Laser System in the Laboratory Setting [6]. 117
4.10 SEM Image of the laser impact site on Tungsten sample 5-1 [6]. 118
4.11 SEM Image of the laser impact site on Tungsten sample 5-2 [6]. 119
4.12 Tungsten Sample 5-4 SEM Images [6]. 119
4.13 Tungsten Sample 5-5 SEM Images [6]. 120
4.14 ANSYS Total Heat Flux results based on the laser Convective boundary being placed on the Top Face of the Impact Site. 122
4.15 ANSYS Total Heat Flux results based on the laser Convective boundary being placed on the Body of the Impact Site for Sample 5-1 ETD 094 - 0.6 W. . . 123

5.1 The Mass Loss/Normalized Surface Area (g/cm^2) plotted against the Deposited Energy (MeV) for U-Mo(1.50%) 133

A.1 W(3.00%)-Mo Temperature (eV) versus Time (μs) as generated by ETFLOW 139
A.2 W(3.00%)-Mo Electron Number Density (m^{-3}) versus Time (μs) as generated by ETFLOW 140
A.3 W(5.00%)-Mo Temperature (eV) versus Time (μs) as generated by ETFLOW 141
A.4 W(5.00%)-Mo Electron Number Density (m^{-3}) versus Time (μs) as generated by ETFLOW 142
A.5 W(19.5%)-Mo Temperature (eV) versus Time (μs) as generated by ETFLOW 143
A.6 W(19.5%)-Mo Electron Number Density (m^{-3}) versus Time (μs) as generated by ETFLOW 144
A.7 W(90.0%)-Mo Temperature (eV) versus Time (μs) as generated by ETFLOW 145
A.8 W(90.0%)-Mo Electron Number Density (m^{-3}) versus Time (μs) as generated by ETFLOW 146
A.9 W(98.5%)-Mo Temperature (eV) versus Time (μs) as generated by ETFLOW 147
A.10 W(98.5%)-Mo Electron Number Density (m^{-3}) versus Time (μs) as generated by ETFLOW 148

B.1 The Mass Loss/Normalized Surface Area (g/cm^2) plotted against the Deposited Energy (MeV) for U-Mo(1.00%) 153
B.2 The Mass Loss/Normalized Surface Area (g/cm^2) plotted against the Deposited Energy (MeV) for U-Mo(1.25%) 157
B.3 The Mass Loss/Normalized Surface Area (g/cm^2) plotted against the Deposited Energy (MeV) for U-Mo(1.75%) 161
B.4 The Mass Loss/Normalized Surface Area (g/cm^2) plotted against the Deposited Energy (MeV) for U-Mo(2.00%) 165

List of Tables

3.1 Error for the Ideal Simulation Plasma Parameters 37
3.2 Error for Non-Ideal Simulation Plasma Parameters 38
3.3 ETFLOW Simulations of Pure Molybdenum - Ideal Cases 38
3.4 ETFLOW Simulations of Pure Molybdenum - Non-Ideal Cases 39
3.5 ETFLOW Simulations of Pure Tantalum - Ideal Cases 41
3.6 ETFLOW Simulations of Pure Tantalum - Non-Ideal Cases 42
3.7 ETFLOW Simulations of Pure Titanium - Ideal Cases 44
3.8 ETFLOW Simulations of Pure Titanium - Non-Ideal Cases 45
3.9 ETFLOW Simulations of Pure Tungsten - Ideal Cases 48
3.10 ETFLOW Simulations of Pure Tungsten - Non-Ideal Cases 48
3.11 ETFLOW Simulations of Pure Uranium - Ideal Cases 51
3.12 ETFLOW Simulations of Pure Uranium - Non-Ideal Cases 51
3.13 ETFLOW Simulations of Pure Zirconium - Ideal Cases 54
3.14 ETFLOW Simulations of Pure Zirconium - Non-Ideal Cases 54
3.15 ETFLOW Simulations of TZM Alloy - Ideal Cases 57
3.16 ETFLOW Simulations of TZM Alloy - Non-Ideal Cases 57
3.17 ETFLOW Simulations of W-Mo(1.00%) Alloy - Ideal Cases 60
3.18 ETFLOW Simulations of W-Mo(1.00%) Alloy - Non-Ideal Cases 61
3.19 ETFLOW Simulations of W-Mo(1.25%) Alloy - Ideal Cases 63
3.20 ETFLOW Simulations of W-Mo(1.25%) Alloy - Non-Ideal Cases 63
3.21 ETFLOW Simulations of W-Mo(1.50%) Alloy - Ideal Cases 66
3.22 ETFLOW Simulations of W-Mo(1.50%) Alloy - Non-Ideal Cases 67
3.23 ETFLOW Simulations of W-Mo(1.75%) Alloy - Ideal Cases 69
3.24 ETFLOW Simulations of W-Mo(1.75%) Alloy - Non-Ideal Cases 70
3.25 ETFLOW Simulations of W-Mo(2.00%) Alloy - Ideal Cases 73
3.26 ETFLOW Simulations of W-Mo(2.00%) Alloy - Non-Ideal Cases 73
3.27 ETFLOW Simulations of U-Mo(1.00%) Alloy - High Thermal Conductivity - Ideal Cases 77
3.28 ETFLOW Simulations of U-Mo(1.00%) Alloy - Low Thermal Conductivity - Ideal Cases 77
3.29 ETFLOW Simulations of U-Mo(1.00%) Alloy - High Thermal Conductivity - Non-Ideal Cases 78

3.30 ETFLOW Simulations of U-Mo(1.00%) Alloy - Low Thermal Conductivity - Non-Ideal Cases . . . 78
3.31 ETFLOW Simulations of U-Mo(1.25%) Alloy - High Thermal Conductivity - Ideal Cases . . . 82
3.32 ETFLOW Simulations of U-Mo(1.25%) Alloy - Low Thermal Conductivity - Ideal Cases . . . 83
3.33 ETFLOW Simulations of U-Mo(1.25%) Alloy - High Thermal Conductivity - Non-Ideal Cases . . . 84
3.34 ETFLOW Simulations of U-Mo(1.25%) Alloy - Low Thermal Conductivity - Non-Ideal Cases . . . 84
3.35 ETFLOW Simulations of U-Mo(1.50%) Alloy - High Thermal Conductivity - Ideal Cases . . . 88
3.36 ETFLOW Simulations of U-Mo(1.50%) Alloy - Low Thermal Conductivity - Ideal Cases . . . 89
3.37 ETFLOW Simulations of U-Mo(1.50%) Alloy - High Thermal Conductivity - Non-Ideal Cases . . . 89
3.38 ETFLOW Simulations of U-Mo(1.50%) Alloy - Low Thermal Conductivity - Non-Ideal Cases . . . 90
3.39 ETFLOW Simulations of U-Mo(1.75%) Alloy - High Thermal Conductivity - Ideal Cases . . . 94
3.40 ETFLOW Simulations of U-Mo(1.75%) Alloy - Low Thermal Conductivity - Ideal Cases . . . 94
3.41 ETFLOW Simulations of U-Mo(1.75%) Alloy - High Thermal Conductivity - Non-Ideal Cases . . . 95
3.42 ETFLOW Simulations of U-Mo(1.75%) Alloy - Low Thermal Conductivity - Non-Ideal Cases . . . 96
3.43 ETFLOW Simulations of U-Mo(2.00%) Alloy - High Thermal Conductivity - Ideal Cases . . . 100
3.44 ETFLOW Simulations of U-Mo(2.00%) Alloy - Low Thermal Conductivity - Ideal Cases . . . 100
3.45 ETFLOW Simulations of U-Mo(2.00%) Alloy - High Thermal Conductivity - Non-Ideal Cases . . . 101
3.46 ETFLOW Simulations of U-Mo(2.00%) Alloy - Low Thermal Conductivity - Non-Ideal Cases . . . 101

4.1 Laser Impact Crater Dimensions . . . 107
4.2 Crater Specific Dimensions . . . 108
4.3 Material Properties for the Engineering Data entry for Tungsten in ANSYS based on the ETFLOW Materials Library. . . . 109
4.4 The number of Nodes generated for each model's CFD Mesh based on the crater and bore hole dimensions . . . 111
4.5 The number of Elements generated for each model's CFD Mesh based on the crater and bore hole dimensions . . . 111

4.6 The maximum amount of heat flux generated when the Convective boundary for the laser is set to impinge on the Top Face of the Impact Site. 114
4.7 Convection Coefficients for the Laser samples examined with SEM - Face Boundary Conditions 121
4.8 Convection Coefficients for the Laser samples examined with SEM - Body Boundary Conditions 121
4.9 The maximum amount of heat flux generated when the Convective boundary for the laser is set to impinge on the Top Face of the Impact Site. 122
4.10 The maximum amount of heat flux generated when the Convective boundary for the laser is set to impinge on the Body of the Impact Site. 123

5.1 The mass loss per surface area for U-Mo(1.50%) computed using the Godiva IV capillary zone surface area. 129
5.2 The mass loss per surface area for U-Mo(1.50%) computed using the ETFLOW capillary surface area. 129
5.3 Godiva IV mass loss per surface area for U-Mo(1.50%) normalized to the ETFLOW capillary surface area. 130
5.4 The mass loss per surface area for U-Mo(1.50%) computed using the Godiva IV capillary zone surface area for 2163 bursts. 131
5.5 The mass loss per surface area for U-Mo(1.50%) computed using the ETFLOW capillary surface area for 2163 bursts. 131
5.6 The mass loss per surface area for U-Mo(1.50%) computed using the normalized surface area for 2163 bursts. 132
5.7 The mass loss per energy deposited for U-Mo(1.50%). 132

A.1 ETFLOW Simulations of W(3.00%)-Mo - Ideal Cases 138
A.2 ETFLOW Simulations of W(3.00%)-Mo - Non-Ideal Cases 138
A.3 ETFLOW Simulations of W(5.00%)-Mo - Ideal Cases 140
A.4 ETFLOW Simulations of W(5.00%)-Mo - Non-Ideal Cases 141
A.5 ETFLOW Simulations of W(19.5%)-Mo - Ideal Cases 142
A.6 ETFLOW Simulations of W(19.5%)-Mo - Non-Ideal Cases 143
A.7 ETFLOW Simulations of W(90.0%)-Mo - Ideal Cases 144
A.8 ETFLOW Simulations of W(90.0%)-Mo - Non-Ideal Cases 145
A.9 ETFLOW Simulations of W(98.5%)-Mo - Ideal Cases 146
A.10 ETFLOW Simulations of W(98.5%)-Mo - Non-Ideal Cases 147

B.1 The mass loss per surface area for U-Mo(1.00%) computed using the Godiva IV capillary zone surface area. 150
B.2 The mass loss per surface area for U-Mo(1.00%) computed using the ETFLOW capillary surface area. 150
B.3 Godiva IV mass loss per surface area for U-Mo(1.00%) normalized to the ETFLOW capillary surface area. 151

B.4 The mass loss per surface area for U-Mo(1.00%) computed using the Godiva IV capillary zone surface area for 2163 bursts. 151
B.5 The mass loss per surface area for U-Mo(1.00%) computed using the ETFLOW capillary surface area for 2163 bursts. 152
B.6 The mass loss per surface area for U-Mo(1.00%) computed using the normalized surface area for 2163 bursts. 152
B.7 The mass loss per energy deposited for U-Mo(1.00%). 153
B.8 The mass loss per surface area for U-Mo(1.25%) computed using the Godiva IV capillary zone surface area. 154
B.9 The mass loss per surface area for U-Mo(1.25%) computed using the ETFLOW capillary surface area. 154
B.10 Godiva IV mass loss per surface area for U-Mo(1.25%) normalized to the ETFLOW capillary surface area. 155
B.11 The mass loss per surface area for U-Mo(1.25%) computed using the Godiva IV capillary zone surface area for 2163 bursts. 155
B.12 The mass loss per surface area for U-Mo(1.25%) computed using the ETFLOW capillary surface area for 2163 bursts. 156
B.13 The mass loss per surface area for U-Mo(1.25%) computed using the normalized surface area for 2163 bursts. 156
B.14 The mass loss per energy deposited for U-Mo(1.25%). 157
B.15 The mass loss per surface area for U-Mo(1.75%) computed using the Godiva IV capillary zone surface area. 158
B.16 The mass loss per surface area for U-Mo(1.75%) computed using the ETFLOW capillary surface area. 158
B.17 Godiva IV mass loss per surface area for U-Mo(1.75%) normalized to the ETFLOW capillary surface area. 159
B.18 The mass loss per surface area for U-Mo(1.75%) computed using the Godiva IV capillary zone surface area for 2163 bursts. 159
B.19 The mass loss per surface area for U-Mo(1.75%) computed using the ETFLOW capillary surface area for 2163 bursts. 160
B.20 The mass loss per surface area for U-Mo(1.75%) computed using the normalized surface area for 2163 bursts. 160
B.21 The mass loss per energy deposited for U-Mo(1.75%). 161
B.22 The mass loss per surface area for U-Mo(2.00%) computed using the Godiva IV capillary zone surface area. 162
B.23 The mass loss per surface area for U-Mo(2.00%) computed using the ETFLOW capillary surface area. 162
B.24 Godiva IV mass loss per surface area for U-Mo(2.00%) normalized to the ETFLOW capillary surface area. 163
B.25 The mass loss per surface area for U-Mo(2.00%) computed using the Godiva IV capillary zone surface area for 2163 bursts. 163

B.26 The mass loss per surface area for U-Mo(2.00%) computed using the ETFLOW capillary surface area for 2163 bursts. 164
B.27 The mass loss per surface area for U-Mo(2.00%) computed using the normalized surface area for 2163 bursts. 164
B.28 The mass loss per energy deposited for U-Mo(2.00%). 165

List of Equations

$$K_{\mathrm{UMo}} \approx 0.032T + 2.2, 298K < T < 773K \tag{1}$$

$$T_{\mathrm{m}} = 1.408 \times 10^3 - 2.912\chi_{\mathrm{Mo}} + 0.1606{\chi_{\mathrm{Mo}}}^2 \tag{2}$$

$$\rho_{\mathrm{UMo}} = X_{\mathrm{Mo}}\rho_{\mathrm{Mo}} + (1 - X_{\mathrm{Mo}})\rho_{\mathrm{U}} \tag{3}$$

$$\sigma = \sqrt{\frac{\Sigma(X - \mu)^2}{N}} \tag{4}$$

$$h = \frac{P_{\mathrm{Pulse}}}{A \cdot \Delta T}. \tag{5}$$

List of Symbols

K_{UMo}	Thermal Conductivity of U-Mo alloy [$\frac{W}{m \cdot K}$, $298K < T < 773K$], p. xvii
T	Absolute Temperature [K], p. xvii
T_{m}	Melting Temperature [K], p. xvii
χ_{Mo}	Atomic Fraction of Molybdenum in U-Mo [$0 \leq \chi_{\mathrm{Mo}} \leq 4at\%$], p. xvii
ρ_{UMo}	Material Density of U-Mo Alloys [$\frac{g}{cm^3}$], p. xvii
X_{Mo}	Molar Fraction of Molybdenum, p. xvii
ρ_{Mo}	Density of Molybdenum [$\frac{g}{cm^3}$], p. xvii
ρ_{U}	Density of Uranium [$\frac{g}{cm^3}$], p. xvii
σ	Standard Deviation associated with each ETFLOW plasma parameter
X	Actual data value
μ	Mean or average of the data
N	Number of samples in the set, $N = 27$
h	Heat Transfer Coefficient, Convection
P_{Pulse}	Laser Pulse Power
A	Area - Surface Area or Total Surface Area
ΔT	Change in Temperature between the Fluid to the Material Surface

List of Terms

ELMs	Edge Localized Mode, p. 13
ET	Electrothermal, p. 23
FBR	Fast Burst Reactor, p. 11
HEU	Highly Enriched Uranium, p. 11
LEU	Low Enriched Uranium, p. 18
VDEs	Vertical Displacement Event, p. 13
VS	Vapor Shield, p. 13

Acknowledgments

Pennsylvania State University

Dr. Leigh Winfrey - thank you for guiding me over the past 5+ years; through a Master and PhD, a move, and all of the craziness that has been my time working for you. I am eternally gratefully to you and have enjoyed being your student.

Thank you to Dazhong Ding for taking the time to perform the spectroscopy and SEM measurements and for the numerous hours of collaboration in an effort to achieve a model that made both of us proud.

A huge thank you to Dr. Merzari for taking the time to answer my numerous questions about ANSYS and helping me proceed with my research.

A huge thank you to my wonderful doctoral committee - Dr. Marek Flaska, Dr. Kenan Ünlü, and Dr. Venkatraman Gopalan, for taking the time to participate in the process of reviewing my work and providing feedback that allowed me to progress with my research.

North Carolina State University

Dr. Mohamed Bourham – thank you for taking me under your wing while I was in undergrad and giving me my first research project. You sparked not only my interest in electrothermal plasmas but grad school as well. Thank you for believing in me and giving me the guidance to reach my goals!

Lisa Marshall – you have been such a wonderful friend and guiding force in my life since my undergrad years. Thank you so much for believing in me and pushing me toward my goals!

Dr. John Mattingly - thank you for being a wonderful mentor during the latter part of my undergraduate years and for your continued support since I left NCSU.

Alamance Community College

To the wonderful instructors at ACC - you were the ones who started me off on my college journey and got me started on my way to achieving my ultimate dream. Thank you to each and every one of the amazing faculty and staff at ACC who take the time to help students like me every day.

Dedication

To my wonderful friends, family, and partner – you have stuck with me for over a decade of university, and I cannot thank you enough. We made it!

- V

Chapter 1
Introduction and Background

Previously unidentified behaviors are a common occurrence in materials, plaguing all reactor materials, regardless of material structure or composition. While the bulk of materials studies looking at uranium-based fuels have been for power reactors, not many have been conducted in which highly enriched uranium (HEU) devices were the main focus. Research into other high-Z materials, including refractory metals, for use in fusion and fast spectrum fission reactors is of significant interest for next generation systems. Knowledge gained through the work presented here will help inform both the fast burst reactor (FBR) and fusion communities, as well as the larger materials community.

1.1 Dusty Plasma Formation

It is theorized that a dusty plasma forms at the surface of an HEU device when it is pulsed in a super-critical, fast-burst manor. The dusty plasma acts as a vapor layer, which provides a self-shielding mechanism at the plasma-material interface [7]. These plasma clouds are dense and often only partially-ionized, containing neutral particles that are between μm and nm in size [8, 9]. This category of plasma is of interest to the community as they are complex systems that occur in several contexts - from space to materials processing. For large fusion devices like ITER, dust contamination from plasma facing components becomes more of a problem and it may eventually lead to operational and safety issues [9, 10].

The existence of this type of plasma formation in a system like Godiva IV is likely due to several factors that exist during the burst operations. While the energy deposited into the surface material is quite high (90 GJ), it is not enough to completely ionize all of the

material around the deposition point, increasing the likelihood of recombination occurring. Additionally, the temperature does not reach the necessary temperatures to achieve a sustained fusion event (such as that of a tokamak) given that the burst occurs over such a short period of time. Furthermore, the conditions under which the plasma is formed is not considered to be a "clean," meaning that probability of other ion species being present in the plasma due to contamination is also high.

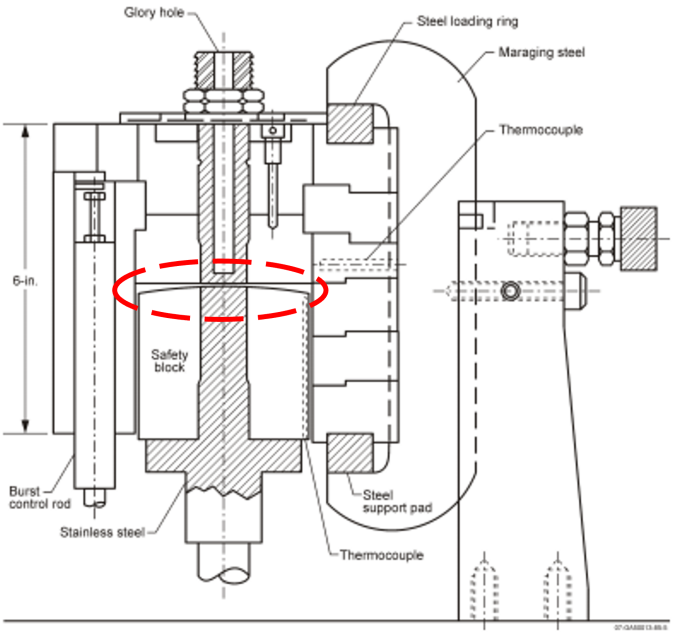

Figure 1.1: Cutaway view of Godiva IV core, restraints, and proposed dusty plasma site [1].

The proposed location of dusty plasma formation is circled in the dashed lines in Figure 2.1. This location was deemed the most likely site of ablation based on a few observations made by staff operating the Godiva IV device. Wear marks on top of the Safety Block have mad the once gentle curve of the component have a slant on one side. Additionally, mass loss has been recorded for this component and the Intermediate Inner Subassembly Plate (IISP), which the Safety Block is in very close proximity to when it is fully seated. Finally, when the Safety Block is fully seated, it forms a capillary like space with the IISP as there is a 0.25400 *cm* gap between the two components - an ideal location for a dusty plasma to form as well as to simulate using the electrothermal plasma code, ETFLOW [1].

Figure 2.2 demonstrates the scheme of such a plasma forming through energy deposition from the environment, the high energy pulse from burst operations, into the surface material. This high intensity heat flux that is impinged onto the surface causes the surface material atoms

to ablate through sudden evaporation or sublimation. Continuous evaporation/sublimation of the surface results in a vapor cloud forming near the surface and the continued interaction between the evaporated/sublimated atoms and the surface material results in further ablation of the surface, contributing to the cloud of vapor.

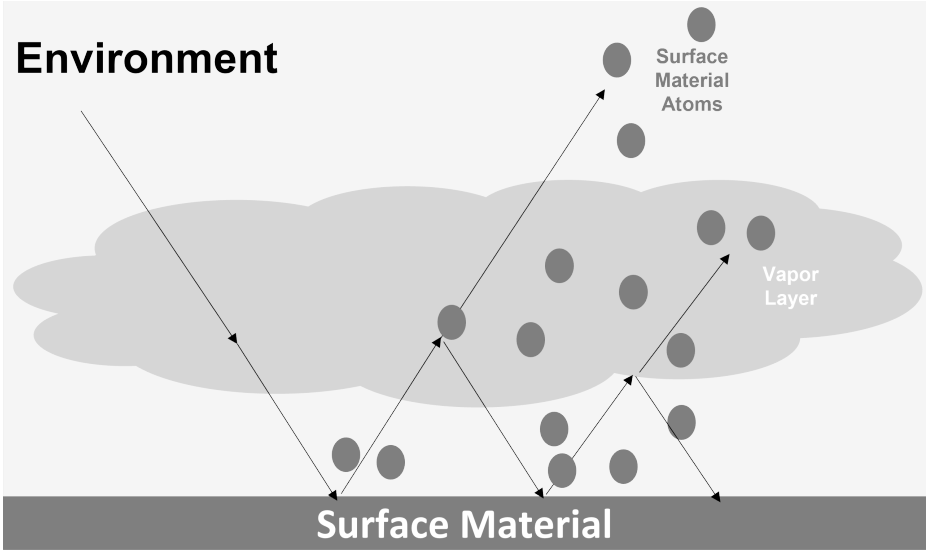

Figure 1.2: Dusty plasma formation schematic

1.1.1 Vapor Shielding Modelling

As the possible formation of the vapor layer is critical to the proposed mass loss mechanism in burst reactor operations of an HEU, it is important to provide an evaluation of the current vapor shielding modelling efforts that have been made prior to the start of work. At present, the primary focus of such vapor shielding (VS) models have been on the affects that these vapor layers have on the first wall materials of tokamak fusion reactors. As such, this work did not include the evaluation of heavy metals such as HEU or in the case of Godiva IV, a specialized U-Mo alloy [11, 12].

The main study of interest in this area was a 2016 study that was interested in the affect that vapor shielding layers had during off-normal tokamak operation event. Off-normal events occur due to perturbations that occur in or to the plasma, leading to instabilities, such as edge-localized modes (ELMs), extinguishing events, and vertical displacement events (VDEs). When such an event occurs in a tokamak, the plasma-facing components are exposed to extremely high heat fluxes of up to 100 MJ/m^2 over a short time scale, 0.1 – 1 ms, resulting

in severe damage [7, 13].

To model the VS, the researchers used a code called ETFLOW, which will be discussed more in Section 3.2, as the base of their research efforts. This code is a 1-D, time-dependent electrothermal plasma code that was developed to simulate the internal plasma parameters (described in Section 2.2) of a capillary discharge along the capillary axis. While the ETFLOW code is robust, versatile, and well-documented, it uses an approximation for the energy deposited into the vapor shield, the researchers developed a new version called ETFLOWVS which modelled the VS behavior using two methods – Vapor Shield Opacity and Vapor Shield Energy Ratio [7].

1.1.1.1 Vapor Shielding Opacity Model

Referred to as "Model 1" by researchers, the focus of this model was to simulate the radiant heat transport and transmission factor for the vapor shield as radiant heat transport in a plasma is affected by variations in the plasma opacity and emissivity. Plasma opacity, or how optically transparent (thick) the plasma is to various types of radiation, was calculated using Rosseland's averaging approximation to find the mean plasma opacity. Researchers made an additional assumption by considering the plasma as gray-body instead of using the ideal black-body approximation. This was due to the black-body approximation not being suitable for modelling kinetic plasma temperatures above 1000 K (0.08617 eV). The result of this assumption is that the gray-body heat flux emitted from the plasma is only a fraction of what would be emitted through black-body radiation for the same plasma emissivity [7, 10].

1.1.1.2 Vapor Shielding Energy Ratio Model

The second model, referred to as "Model 2," focused on the calculation of the transmission factor, f. The transmission factor is the ratio of the total amount of energy that reaches the ablating wall to the total amount of energy that is emitted towards the wall by the plasma source. The ratio can also be viewed in terms of heat fluxes, specifically the ratio of heat flux that causes the material erosion to the total heat flux radiation from the plasma core [7]. Since the heat flux impinging on the wall is proportional to the transmission factor, f, any increase in f implies a corresponding increase in ablation [14]. It was found that the transmission factor is strongly dependent on the plasma pressure, plasma density, heat of sublimation/evaporation, and the internal energy, but is only weakly dependent on the plasma kinetic energy. The authors also assumed that the incident thermal radiation is high

enough to directly sublime and then dissociate and ionize the ablated material [7, 15].

1.2 Plasma Parameters

Plasma parameters define various characteristics of a plasma and, once calculated, can be used as a point of reference when conducting experiments during which measurements are taken. Parameters typically computed during a simulation include the plasma temperature and pressure, number density, and total ablated mass. These measurements can be taken, in some cases quite easily, throughout the course of an experiment yielding one of a few results - it helps validate a new plasma model, if one is being developed, and it helps verify the results of a preexisting code, like ETFLOW.

1.3 HEU Systems

As previously stated, any work that has done in the area of VS modelling has not included HEU systems as that work focused on tokamak fusion reactor materials which do not contain the heavy metals that are of interest to this research. HEU systems were chosen as the main material focus for the study as there has not been much work performed in this area regarding surface plasma formation. As a number of FBRs are comprised of HEU of various enrichments, it is important to quantify the surface interactions that may be occurring during normal burst operations [16, 17].

Fast burst reactors lose mass slowly as they operate (mg over decades). This affects criticality over time and becomes an issue in assuring accurate calculations as the device ages. It is theorized that this mass loss is the result of surface ablation of the fuel material during each pulse. Further, we also theorize that a short-lived, dusty plasma forms that contributes to the surface ablation and mass loss. If such a plasma is formed, it can be measured during pulses and understood through modelling efforts. The main focus of the work presented here is the first step towards understanding the formation and surface effects of a dusty plasma during pulses in HEU fast-burst devices, similar to Godiva IV.

1.3.1 Godiva IV

Godiva IV (Figure 2.3) is used to conduct super-prompt-critical burst experiments which include criticality alarm testing, detector calibration, and validation for other experimental

data (e.g. neutron cross section data) [1]. While they are known for prompt-critical burst operations, Godiva-like devices are also capable of conducting delayed-critical experiments prior to the prompt burst itself, yielding a wealth of data. These experiments require that the k_{eff} calculation be as accurate and precise as possible. In turn, the k_{eff} calculation is sensitive to the total mass and composition of the system. To date, the focus of work on improving criticality calculations for Godiva IV has centered around new cross section libraries and updated system geometry. To this point the fuel mass has been assumed to be constant, however, measurements tells us this is incorrect [18, 19].

1.3.1.1 Device Operation

Burst reactor systems function effectively as neutron flux traps and are capable of neutron fluxes ($10^{17} - 10^{20}\ n^o/cm^2 \cdot s$). While their configurations may be different, the basics are the same – there is the main body of the fuel (HEU of some enrichment) with a cavity for samples to be inserted and other, smaller access ports for control mechanisms and monitoring devices. To operate the device, a portion of the HEU mass is brought together in such a way to allow a delay-critical state to occur, and when the neutron population has decayed to zero, another portion of HEU mass (i.e. a burst rod) is rapidly inserted into the fuel, triggering a pulse. After a short time, (μs), the pulse self-terminates [1].

1.3.2 Mass Loss in Godiva IV

Researchers have observed materials loss in Godiva IV that is usually attributed to ablation of the fuel. Despite 50+ years of operations, little is known about the loss mechanism. Recently, scientists have speculated that this is due to plasma formation at the surface during operation. Understanding this behavior will improve the long term viability of these types of devices and will improve upon previous modelling efforts in the area of criticality calculations. Further, we would expect that these plasmas would be very short lived ($20 - 40\ \mu s$), low electron temperature ($0.1 - 2\ eV$), and high electron number density (upwards of $10^{21}\ particles/m^3$). Given the Godiva IV's configuration and the nature of the plasmas we expect, they will best be measured by high resolution (spatial and temporal) optical spectroscopy [1].

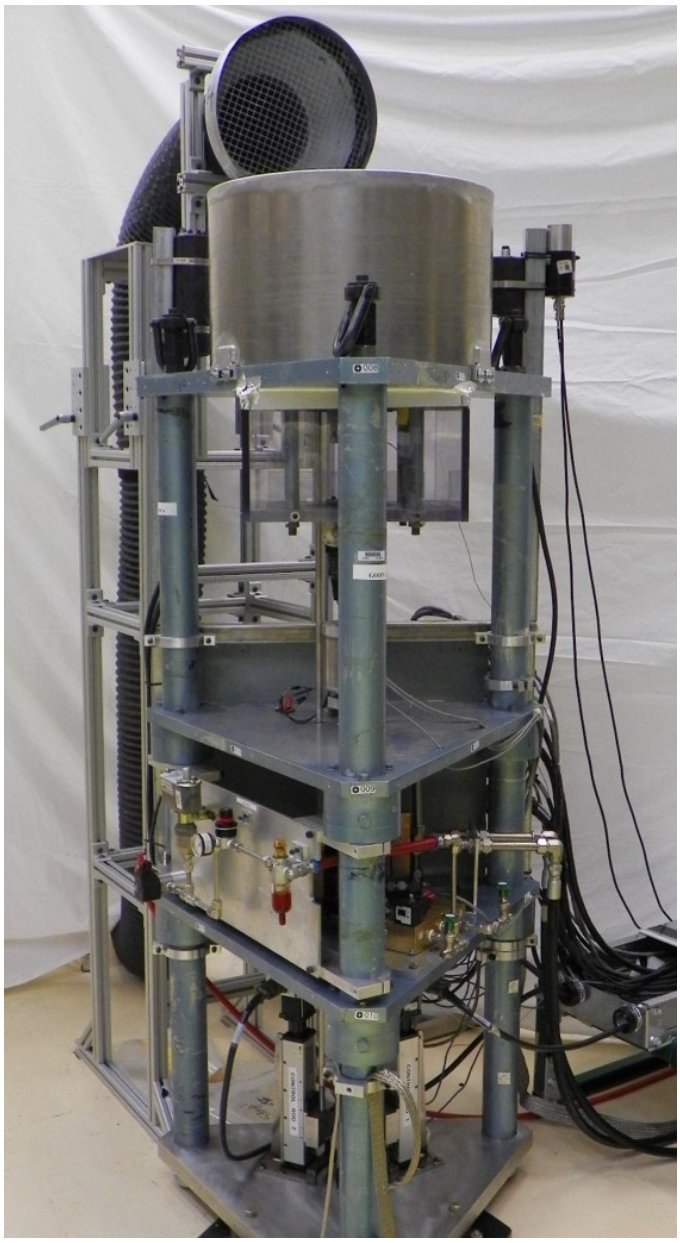

Figure 1.3: Godiva IV, with the aluminum top hat [2].

1.4 Materials Consideration

While the primary material of focus is HEU, specifically U-Mo(1.5%), other materials first had to be considered. A study was first conducted to investigate the individual materials of interest – Tungsten, Molybdenum, and Uranium. Once the individual material simulations were complete, simulations were conducted for alloys that would serve as an analogue for the

U-Mo alloy of Godiva IV as it was a material that could be readily obtained for testing – W-Mo. After satisfactory simulations were concluded for the W-Mo alloys, a U-Mo material was created for ETFLOW and then tested. ETFLOW material creation techniques will be discussed in Section 3.2.3.

1.4.1 W-Mo Alloy

At the beginning of the study, a question was posed as to whether the amount of U-235 enrichment affected the amount of ablation seen in a pulse and whether it affected the plasma parameters that were key to the study. As such, to begin answering this question, a custom analogue Tungsten-Molybdenum alloy was then made for ETFLOW in which the wt-% of Molybdenum varied, mimicking the different enrichments of Uranium-based fuels. The alloy breakdowns were as follows: W(3%, 5%, 19.5%, 90%, 98.5%)-Mo. The first two enrichment levels are those commonly see in power reactors and were chosen to evaluate enrichment effects across the enrichment spectrum. 19.5% was chosen as an upper bound of low-enriched uranium (LEU) as the cut off for what is considered to be LEU is 20.0%. The last two enrichment levels are based on the enrichment levels of previous and current Godiva devices.

1.4.2 U-Mo Alloy

As there was a concern that there was a sensitivity to the mass, the enrichment and composition of the U-Mo alloy did not vary as much as the W-Mo alloy. The target material was a 93.5% enriched U-Mo(1.5%) alloy, and was the initial material that was simulated in ETFLOW. The composition of the alloy retained the 93.5% U-235 enrichment but varied the amount of Molybdenum up and down by 0.25%, yielding the following five alloys: U-Mo(1%, 1.25%, 1.5%, 1.75%, 2%). A mass sensitivity analysis will be performed to evaluate how the Molybdenum content affected the plasma parameters that were calculated in each simulation. The results of this analysis will be found in future works.

1.5 Plasma Spectroscopy

Plasma spectroscopy is a process by which the spectra, or characteristic line radiation, of an element or plasma, is measured via one of two methods: active or passive. The active method of absorption spectroscopy and the passive method of emission spectroscopy are both used throughout the plasma physics sphere and yield valuable data on the spectra on of

plasmas of interest. Discussed briefly are both techniques, however, it was optical emissions spectroscopy that was decided upon as the for the experimental portion of the work - this will be touched upon in Section 4.3.1 [3].

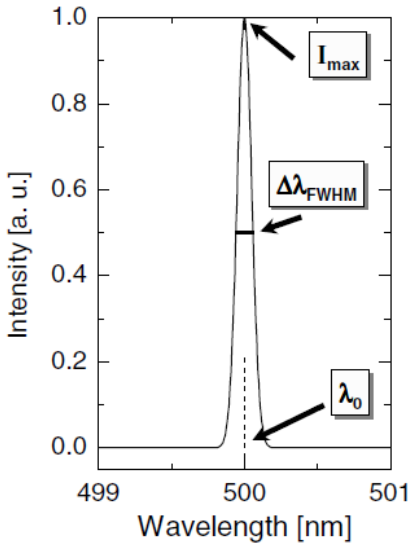

Figure 1.4: Example of line emission spectra that may be observed when performing plasma spectroscopy [3].

Figure 2.4 is a wonderful representation of the type of line emission that one might observe performing one of the various methods of spectroscopy on a plasma. The figure depicts a light impulse that is recorded of an maximum intensity, $I_{\max}$ $(a.u.)$,at a wavelength of λ_0 nm. The wave has a Full Width at Half Max (FWHM) of $\Delta\lambda_{\text{FWHM}}$. This line profile is characteristic of the element or plasma that is being examined. The intensity of the line depends on the population density of the excited level $n(p)$, which strongly depends on the plasma parameters [3].

1.5.1 Absorption Spectroscopy

An active spectroscopy method, absorption spectroscopy is a method that requires a perturbation of the plasma to produce some sort of excitation to occur before an emission can be observed and recorded. The absorption signal is a recorded signal that corresponds to the excitation from level q to level p by a radiation field, resulting in a weakening of the applied radiation field. This signal correlated with the particle density in the lower state $n(q)$, which in most cases is the ground state of the plasma. Through this correlation, the ground

state particle density is directly accessible through this spectroscopy technique, though it does require more effort to obtain such a measurement [3].

1.5.2 Emission Spectroscopy

As a passive method, emission spectroscopy measures the light (spectra) that is emitted from the plasma itself, rather than inducing the excitation to occur as part of the measurement process. The emission is due to the excitation of particles in the plasma by the impact of an electron from level q to level p and the subsequent decay to level k by spontaneous emission. This deexcitation produces a characteristic emission line which can be observed and measured, allowing researchers to quantify the plasma materials that they are working with [3, 20].

1.5.3 Experimental Method

Keeping the overall configuration of Godiva IV and the nature of the expected plasmas at the forefront of the discussion, optical emissions spectroscopy has been selected as the spectroscopy method for experimentation. The plasmas that are expected to form will be short lived (20 – 40 μs), low temperature (0.1 – 2 eV), and high density (10^{17} – 10^{20} $particles/m^3$) while remaining only partially ionized. Given these expected conditions, these plasmas will best be measured by high resolution (spatial and temporal) optical spectroscopy.

Chapter 2
Introduction and Background

Previously unidentified behaviors are a common occurrence in materials, plaguing all reactor materials, regardless of material structure or composition. While the bulk of materials studies looking at uranium-based fuels have been for power reactors, not many have been conducted in which highly enriched uranium (HEU) devices were the main focus. Research into other high-Z materials, including refractory metals, for use in fusion and fast spectrum fission reactors is of significant interest for next generation systems. Knowledge gained through the work presented here will help inform both the fast burst reactor (FBR) and fusion communities, as well as the larger materials community.

2.1 Dusty Plasma Formation

It is theorized that a dusty plasma forms at the surface of an HEU device when it is pulsed in a super-critical, fast-burst manor. The dusty plasma acts as a vapor layer, which provides a self-shielding mechanism at the plasma-material interface [7]. These plasma clouds are dense and often only partially-ionized, containing neutral particles that are between μm and nm in size [8, 9]. This category of plasma is of interest to the community as they are complex systems that occur in several contexts - from space to materials processing. For large fusion devices like ITER, dust contamination from plasma facing components becomes more of a problem and it may eventually lead to operational and safety issues [9].

The existence of this type of plasma formation in a system like Godiva IV is likely due to several factors that exist during the burst operations. While the energy deposited into the surface material is quite high (90 GJ), it is not enough to completely ionize all of the

material around the deposition point, increasing the likelihood of recombination occurring. Additionally, the temperature does not reach the necessary temperatures to achieve a sustained fusion event (such as that of a tokamak) given that the burst occurs over such a short period of time. Furthermore, the conditions under which the plasma is formed is not considered to be a "clean," meaning that probability of other ion species being present in the plasma due to contamination is also high.

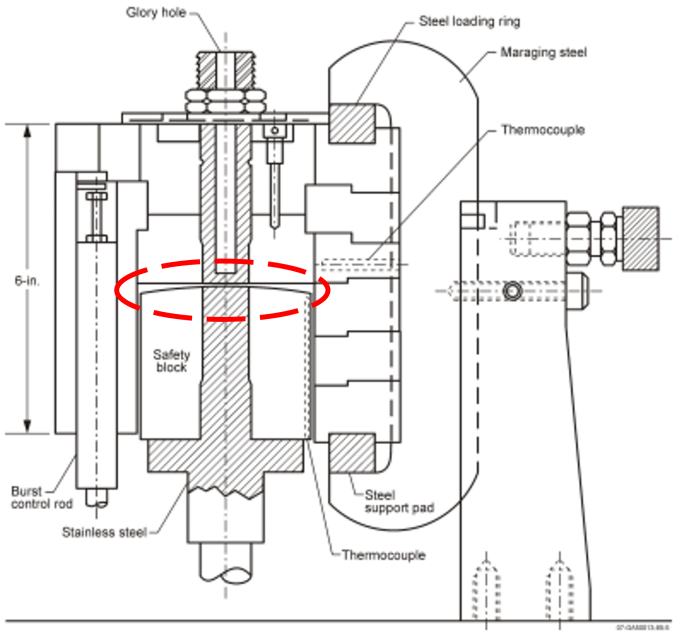

Figure 2.1: Cutaway view of Godiva IV core, restraints, and proposed dusty plasma site.

The proposed location of dusty plasma formation is circled in the dashed lines in Figure 2.1. This location was deemed the most likely site of ablation based on a few observations made by staff operating the Godiva IV device. Wear marks on top of the Safety Block have mad the once gentle curve of the component have a slant on one side. Additionally, mass loss has been recorded for this component and the Intermediate Inner Subassembly Plate (IISP), which the Safety Block is in very close proximity to when it is fully seated. Finally, when the Safety Block is fully seated, it forms a capillary like space with the IISP as there is a 0.25400 *cm* gap between the two components - an ideal location for a dusty plasma to form as well as to simulate using the electrothermal plasma code, ETFLOW [1].

Figure 2.2 demonstrates the scheme of such a plasma forming through energy deposition from the environment, the high energy pulse from burst operations, into the surface material. This high intensity heat flux that is impinged onto the surface causes the surface material atoms

to ablate through sudden evaporation or sublimation. Continuous evaporation/sublimation of the surface results in a vapor cloud forming near the surface and the continued interaction between the evaporated/sublimated atoms and the surface material results in further ablation of the surface, contributing to the cloud of vapor.

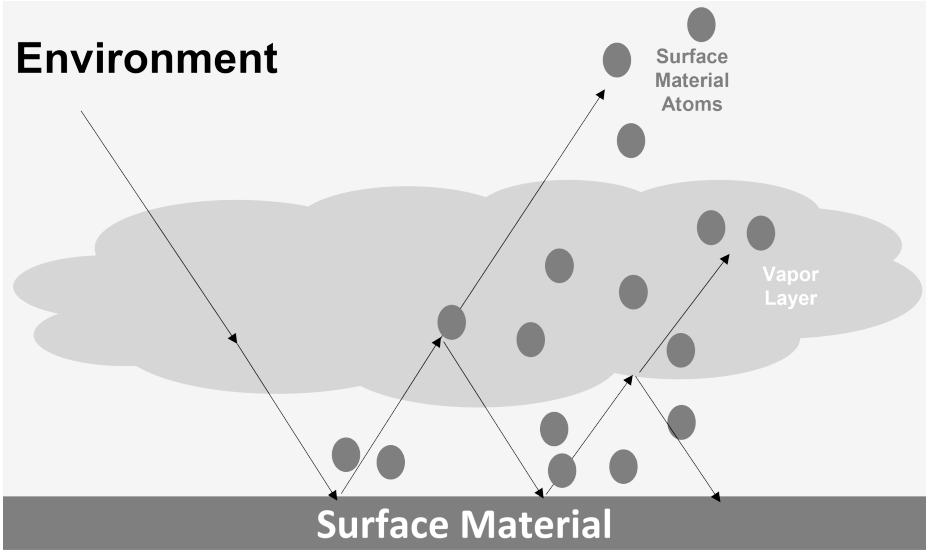

Figure 2.2: Dusty plasma formation schematic

2.1.1 Vapor Shielding Modelling

As the possible formation of the vapor layer is critical to the proposed mass loss mechanism in burst reactor operations of an HEU, it is important to provide an evaluation of the current vapor shielding modelling efforts that have been made prior to the start of work. At present, the primary focus of such vapor shielding (VS) models have been on the affects that these vapor layers have on the first wall materials of tokamak fusion reactors. As such, this work did not include the evaluation of heavy metals such as HEU or in the case of Godiva IV, a specialized U-Mo alloy.

The main study of interest in this area was a 2016 study that was interested in the affect that vapor shielding layers had during off-normal tokamak operation event. Off-normal events occur due to perturbations that occur in or to the plasma, leading to instabilities, such as edge-localized modes (ELMs), extinguishing events, and vertical displacement events (VDEs). When such an event occurs in a tokamak, the plasma-facing components are exposed to extremely high heat fluxes of up to 100 MJ/m^2 over a short time scale, 0.1 – 1 ms, resulting

in severe damage [7].

To model the VS, the researchers used a code called ETFLOW, which will be discussed more in Section 3.2, as the base of their research efforts. This code is a 1-D, time-dependent electrothermal plasma code that was developed to simulate the internal plasma parameters (described in Section 2.2) of a capillary discharge along the capillary axis. While the ETFLOW code is robust, versatile, and well-documented, it uses an approximation for the energy deposited into the vapor shield, the researchers developed a new version called ETFLOWVS which modelled the VS behavior using two methods – Vapor Shield Opacity and Vapor Shield Energy Ratio [7].

2.1.1.1 Vapor Shielding Opacity Model

Referred to as "Model 1" by researchers, the focus of this model was to simulate the radiant heat transport and transmission factor for the vapor shield as radiant heat transport in a plasma is affected by variations in the plasma opacity and emissivity. Plasma opacity, or how optically transparent (thick) the plasma is to various types of radiation, was calculated using Rosseland's averaging approximation to find the mean plasma opacity. Researchers made an additional assumption by considering the plasma as gray-body instead of using the ideal black-body approximation. This was due to the black-body approximation not being suitable for modelling kinetic plasma temperatures above 1000 K (0.08617 eV). The result of this assumption is that the gray-body heat flux emitted from the plasma is only a fraction of what would be emitted through black-body radiation for the same plasma emissivity [7].

2.1.1.2 Vapor Shielding Energy Ratio Model

The second model, referred to as "Model 2," focused on the calculation of the transmission factor, f. The transmission factor is the ratio of the total amount of energy that reaches the ablating wall to the total amount of energy that is emitted towards the wall by the plasma source. The ratio can also be viewed in terms of heat fluxes, specifically the ratio of heat flux that causes the material erosion to the total heat flux radiation from the plasma core [7]. Since the heat flux impinging on the wall is proportional to the transmission factor, f, any increase in f implies a corresponding increase in ablation [14]. It was found that the transmission factor is strongly dependent on the plasma pressure, plasma density, heat of sublimation/evaporation, and the internal energy, but is only weakly dependent on the plasma kinetic energy. The authors also assumed that the incident thermal radiation is high

enough to directly sublime and then dissociate and ionize the ablated material [7].

2.2 Plasma Parameters

Plasma parameters define various characteristics of a plasma and, once calculated, can be used as a point of reference when conducting experiments during which measurements are taken. Parameters typically computed during a simulation include the plasma temperature and pressure, number density, and total ablated mass. These measurements can be taken, in some cases quite easily, throughout the course of an experiment yielding one of a few results - it helps validate a new plasma model, if one is being developed, and it helps verify the results of a preexisting code, like ETFLOW.

2.3 HEU Systems

As previously stated, any work that has done in the area of VS modelling has not included HEU systems as that work focused on tokamak fusion reactor materials which do not contain the heavy metals that are of interest to this research. HEU systems were chosen as the main material focus for the study as there has not been much work performed in this area regarding surface plasma formation. As a number of FBRs are comprised of HEU of various enrichments, it is important to quantify the surface interactions that may be occurring during normal burst operations.

Fast burst reactors lose mass slowly as they operate (mg over decades). This affects criticality over time and becomes an issue in assuring accurate calculations as the device ages. It is theorized that this mass loss is the result of surface ablation of the fuel material during each pulse. Further, we also theorize that a short-lived, dusty plasma forms that contributes to the surface ablation and mass loss. If such a plasma is formed, it can be measured during pulses and understood through modelling efforts. The main focus of the work presented here is the first step towards understanding the formation and surface effects of a dusty plasma during pulses in HEU fast-burst devices, similar to Godiva IV.

2.3.1 Godiva IV

Godiva IV (Figure 2.3) is used to conduct super-prompt-critical burst experiments which include criticality alarm testing, detector calibration, and validation for other experimental

data (e.g. neutron cross section data) [1]. While they are known for prompt-critical burst operations, Godiva-like devices are also capable of conducting delayed-critical experiments prior to the prompt burst itself, yielding a wealth of data. These experiments require that the k_{eff} calculation be as accurate and precise as possible. In turn, the k_{eff} calculation is sensitive to the total mass and composition of the system. To date, the focus of work on improving criticality calculations for Godiva IV has centered around new cross section libraries and updated system geometry. To this point the fuel mass has been assumed to be constant, however, measurements tells us this is incorrect [18].

2.3.1.1 Device Operation

Burst reactor systems function effectively as neutron flux traps and are capable of neutron fluxes ($10^{17} - 10^{20}\ n^o/cm^2 \cdot s$). While their configurations may be different, the basics are the same – there is the main body of the fuel (HEU of some enrichment) with a cavity for samples to be inserted and other, smaller access ports for control mechanisms and monitoring devices. To operate the device, a portion of the HEU mass is brought together in such a way to allow a delay-critical state to occur, and when the neutron population has decayed to zero, another portion of HEU mass (i.e. a burst rod) is rapidly inserted into the fuel, triggering a pulse. After a short time, (μs), the pulse self-terminates [1].

2.3.2 Mass Loss in Godiva IV

Researchers have observed materials loss in Godiva IV that is usually attributed to ablation of the fuel. Despite 50+ years of operations, little is known about the loss mechanism. Recently, scientists have speculated that this is due to plasma formation at the surface during operation. Understanding this behavior will improve the long term viability of these types of devices and will improve upon previous modelling efforts in the area of criticality calculations. Further, we would expect that these plasmas would be very short lived ($20 - 40\ \mu s$), low electron temperature ($0.1 - 2\ eV$), and high electron number density (upwards of $10^{21}\ particles/m^3$). Given the Godiva IV's configuration and the nature of the plasmas we expect, they will best be measured by high resolution (spatial and temporal) optical spectroscopy [1].

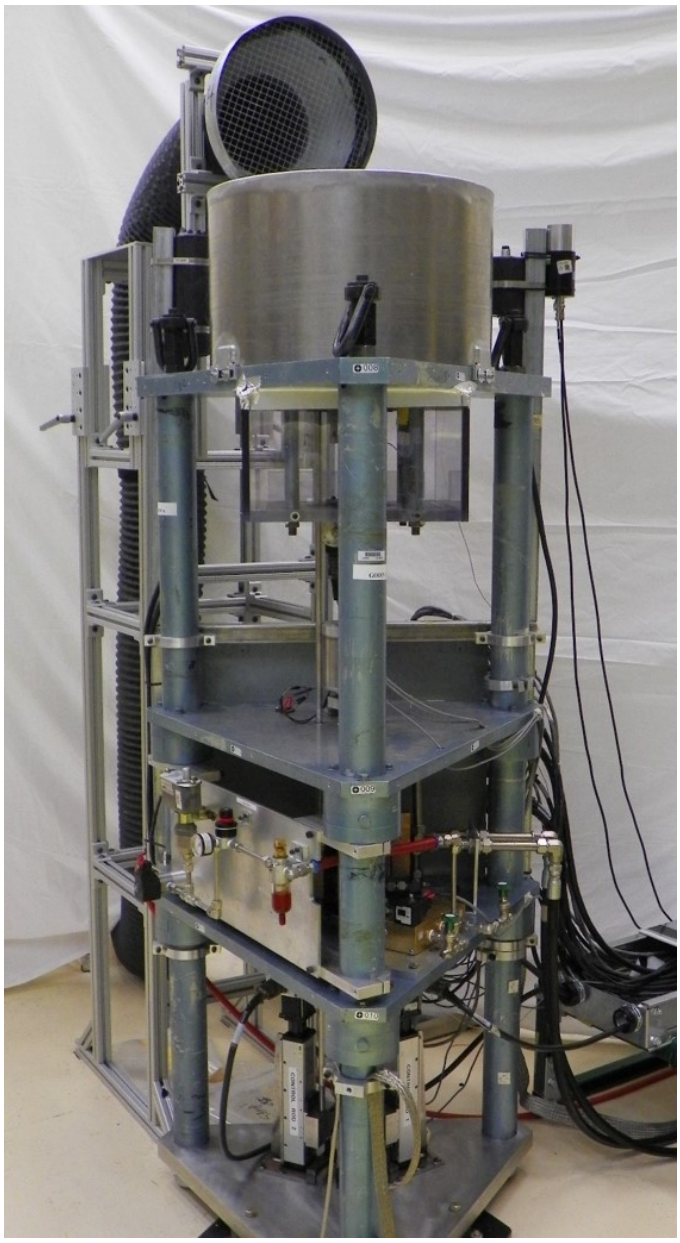

Figure 2.3: Godiva IV, with the aluminum top hat [2].

2.4 Materials Consideration

While the primary material of focus is HEU, specifically U-Mo(1.5%), other materials first had to be considered. A study was first conducted to investigate the individual materials of interest – Tungsten, Molybdenum, and Uranium. Once the individual material simulations were complete, simulations were conducted for alloys that would serve as an analogue for the

U-Mo alloy of Godiva IV as it was a material that could be readily obtained for testing – W-Mo. After satisfactory simulations were concluded for the W-Mo alloys, a U-Mo material was created for ETFLOW and then tested. ETFLOW material creation techniques will be discussed in Section 3.2.3.

2.4.1 W-Mo Alloy

At the beginning of the study, a question was posed as to whether the amount of U-235 enrichment affected the amount of ablation seen in a pulse and whether it affected the plasma parameters that were key to the study. As such, to begin answering this question, a custom analogue Tungsten-Molybdenum alloy was then made for ETFLOW in which the wt-% of Molybdenum varied, mimicking the different enrichments of Uranium-based fuels. The alloy breakdowns were as follows: W(3%, 5%, 19.5%, 90%, 98.5%)-Mo. The first two enrichment levels are those commonly see in power reactors and were chosen to evaluate enrichment effects across the enrichment spectrum. 19.5% was chosen as an upper bound of low-enriched uranium (LEU) as the cut off for what is considered to be LEU is 20.0%. The last two enrichment levels are based on the enrichment levels of previous and current Godiva devices.

2.4.2 U-Mo Alloy

As there was a concern that there was a sensitivity to the mass, the enrichment and composition of the U-Mo alloy did not vary as much as the W-Mo alloy. The target material was a 93.5% enriched U-Mo(1.5%) alloy, and was the initial material that was simulated in ETFLOW. The composition of the alloy retained the 93.5% U-235 enrichment but varied the amount of Molybdenum up and down by 0.25%, yielding the following five alloys: U-Mo(1%, 1.25%, 1.5%, 1.75%, 2%). A mass sensitivity analysis will be performed to evaluate how the Molybdenum content affected the plasma parameters that were calculated in each simulation. The results of this analysis will be found in future works.

2.5 Plasma Spectroscopy

Plasma spectroscopy is a process by which the spectra, or characteristic line radiation, of an element or plasma, is measured via one of two methods: active or passive. The active method of absorption spectroscopy and the passive method of emission spectroscopy are both used throughout the plasma physics sphere and yield valuable data on the spectra on of

plasmas of interest. Discussed briefly are both techniques, however, it was optical emissions spectroscopy that was decided upon as the for the experimental portion of the work - this will be touched upon in Section 4.3.1 [3].

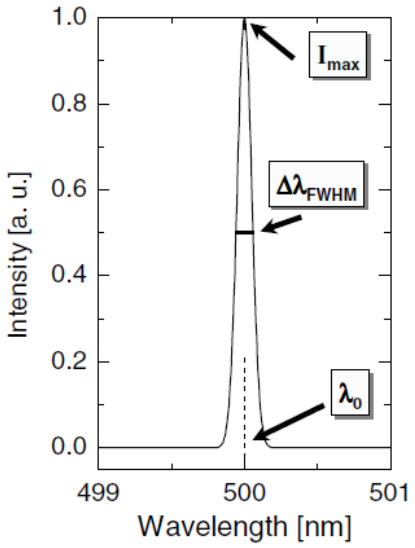

Figure 2.4: Example of line emission spectra that may be observed when performing plasma spectroscopy [3].

Figure 2.4 is a wonderful representation of the type of line emission that one might observe performing one of the various methods of spectroscopy on a plasma. The figure depicts a light impulse that is recorded of an maximum intensity, $I_{\max}$ $(a.u.)$,at a wavelength of λ_0 nm. The wave has a Full Width at Half Max (FWHM) of $\Delta\lambda_{\mathrm{FWHM}}$. This line profile is characteristic of the element or plasma that is being examined. The intensity of the line depends on the population density of the excited level $n(p)$, which strongly depends on the plasma parameters [3].

2.5.1 Absorption Spectroscopy

An active spectroscopy method, absorption spectroscopy is a method that requires a perturbation of the plasma to produce some sort of excitation to occur before an emission can be observed and recorded. The absorption signal is a recorded signal that corresponds to the excitation from level q to level p by a radiation field, resulting in a weakening of the applied radiation field. This signal correlated with the particle density in the lower state $n(q)$, which in most cases is the ground state of the plasma. Through this correlation, the ground

state particle density is directly accessible through this spectroscopy technique, though it does require more effort to obtain such a measurement [3].

2.5.2 Emission Spectroscopy

As a passive method, emission spectroscopy measures the light (spectra) that is emitted from the plasma itself, rather than inducing the excitation to occur as part of the measurement process. The emission is due to the excitation of particles in the plasma by the impact of an electron from level q to level p and the subsequent decay to level k by spontaneous emission. This deexcitation produces a characteristic emission line which can be observed and measured, allowing researchers to quantify the plasma materials that they are working with [3].

2.5.3 Experimental Method

Keeping the overall configuration of Godiva IV and the nature of the expected plasmas at the forefront of the discussion, optical emissions spectroscopy has been selected as the spectroscopy method for experimentation. The plasmas that are expected to form will be short lived (20 – 40 μs), low temperature (0.1 – 2 eV), and high density (10^{17} – 10^{20} $particles/m^3$) while remaining only partially ionized. Given these expected conditions, these plasmas will best be measured by high resolution (spatial and temporal) optical spectroscopy.

Chapter 3

Plasma Surface Interactions In High Heat Flux Conditions

Dusty plasmas are a unique and complex plasma phenomenon; couple this with the varying geometries and burst operation conditions of HEU devices like Godiva IV and the system as a whole becomes even more complex. As such, measurements on such a system are also complex in nature, lending the question of does plasma phenomena occur a more complicated solution. To begin the process of discovering and quantifying the answer, modelling of the plasma had to be completed and the plasma parameters that are key to moving forward in later physical experiments, such as the temperature and number density values, calculated. As will be discussed, as updated version of ETFLOW was used to perform this task for several materials that were of interest and scientific value.

ETFLOW simulations were performed to model the formation of a dusty plasma that forms at the surface of a metal under super-critical, fast-burst conditions. While the model in ETFLOW itself simulates an eletrothermal gun type device, the resulting plasma parameters are still accurate for this configuration as the type of plasma formation. The results have been broken into a few sections in which the Peak Performance Values have been presented and discussed. General results for all materials that were simulated can be found in Appendix A.

3.1 HELIOS Experiment

The **H**igh h**E**at f**L**ux **I**on **O**utflow **S**ource **(HELIOS)** is composed of an electrothermal plasma source that is connected to an expansion chamber [21]. An example of an electrothermal capillary discharge in PIPE can be found in Figure 3.1. The electrothermal plasma source, shown here, is comprised of a high energy density capacitor (denoted as "Power Supply"), a high-voltage, high-current spark-gap switch, a cathode (which is connected to the capacitor), a grounded anode (light blue), and a chamber that houses an ablative sleeve through which an arc discharge is passed through (orange); the resulting electrothermal plasma jet is denoted with multiple red arrows at the capillary exit [5].

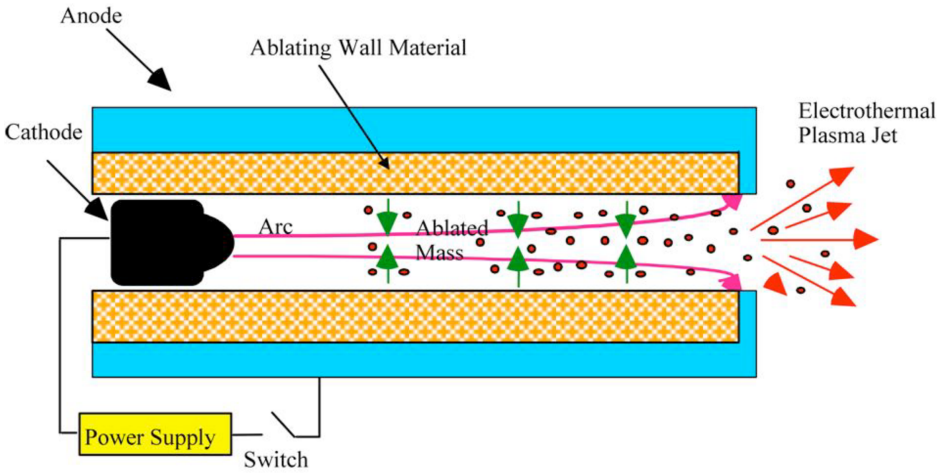

Figure 3.1: Schematic of the PIPE experimental set-up [4, 5].

A pulse is sent to the spark-gap switch, discharging the capacitor, so that an arc discharges from the cathode towards the grounded anode. The arc ablates the sleeve material, forming a dense vapor of excited atoms and molecules from the wall, forming a low-temperature (0.1-10 eV), high-density (n $\sim 10^{23}$ $/m^3$) plasma. As plasma temperature increases, plasma resistance decreases, allowing more current to pass through the sleeve, more material is then ablated, increasing the plasma density and the kinetic pressure inside the source. The cycle continues until no more joule heating occurs. This process has been modelled in an electrothermal plasma code – ETFLOW [5].

3.2 ETFLOW

ETFLOW is a program that is based off previously developed 0-D and 1-D ideal plasma codes. It is a 1-D, time-dependent electrothermal plasma code capable of simulating the internal plasma parameters of a capillary discharge. In the creation of the electrothermal (ET) plasma source model, numerous simplifying assumptions are made. For a 1-D axial model, the capillary radius R is assumed to be much smaller than the capillary length L such that the source aspect ratio, R/L is very small. The plasma parameters, mentioned in Section 2.2, can be assumed constant over the cross section of the capillary. It is assumed that the ablated wall material in the source is completely dissociated and that all heat loss due to conduction can be considered negligible. A caveat is made, however, with the inclusion of the thermal conduction in both the model and code [5].

Radial transport is assumed to be only in the radial direction and is, therefore, neglected in the axial direction. The axial direction can be safely ignored in this configuration as the radiation transport is solely responsible for the wall ablation in the radial direction. However, no radiation transport occurs during the plasma axial flow and the plasma is relatively isothermal [5].

When an ETFLOW simulation is run, the internal plasma parameters of the capillary discharge are calculated for the specified material. The program calculates the plasma parameters along the capillary axis, producing tables and plots to use in later analysis. The plasma parameters that are of most interest to researchers include temperature, pressure, velocity, heat flux, and total ablated mass that was ejected from the source.

3.2.1 Governing Equations

Simulations conducted using ETFLOW were done using an updated version of ETFLOW (Program ETCOMBFLOW version 2.00). The current profile used was from the PIPE P228 experimental shot data. This current profile was used as it is a very good, representative shot for the PIPE device as it was a "clean" shot. A clean shot is one in which the ablative sleeve, shown in orange in Figure 3.1, has not been used in previous shots and does not have soot or ash build up on the interior of the sleeve, adding contamination to the shot. The P228 shot data is frequently used in other experiments and simulations, providing numerous good reference points for new simulations.

For each material that was considered, a total of 20 simulations were performed for varying

current profiles and plasma types. The variations are based off the P228 discharge current profile in which each value is multiplied by a multiple of 0.25, thus the runs vary from 0.25 – 2.50 times the P228 discharge current, in increments of 0.25 for a total of ten (10) current variations.

3.2.2 Plasma Conductivity

As ETFLOW is capable of simulating both Ideal and Non-Ideal plasmas, a full set of ten simulations were performed for each scenario. In the cases where an Ideal plasma was modelled, the program over-estimated the plasma parameters; the reverse is true for the Non-Ideal plasma cases – this is due to charges being completely screened in the Ideal model and charges being incompletely screened in the Non-Ideal model. Incomplete screening of charges in a plasma will lead to higher number densities and changes the overall conductivity of the plasma itself, this lowers the energy that is absorbed, thus under predicting the plasma parameters as the plasma is no longer as "good as a conductor" as its Ideal counterpart. As the conductivity model for the Non-Ideal plasma is much more complex, and needs to be solved at every point, there will also be a noticeable increase in run time for Non-Ideal cases. The need for this labor intensive process is due to the fact that conductivity of the plasma is dependent on the number density, but as such, can be used for any plasma and thus, is more flexible in its uses [5, 22].

3.2.3 Material Parameters

The materials considered for the simulations included the constitute elements of the Godiva IV fuel material – Uranium (U) and Molybdenum (Mo), as well as Tungsten (W) as it was selected as an analogue material for Uranium in future spectroscopy experiments. These materials were simulated individually in ETFLOW in the fashion stated in Section 3.2.1 and their results compared in Section 3.4. A custom Tungsten-Molybdenum (W-Mo) alloy set was then made for the ETFLOW material library with the following composition: W(3%, 5%, 19.5%, 90%, 98.5%)-Mo. A custom set of Uranium-Molybdenum (U-Mo) alloys were then made for ETFLOW in which the alloys had a base enrichment of 93.5% U-235 Uranium fuel with varying amounts of Molybdenum added, yielding five alloys that were simulated: U-Mo(1%, 1.25%, 1.5%, 1.75%, 2%). A description of the reasoning behind the varying percentages used can be found in Sections 2.4.1 and 2.4.2.

When creating a new material for the ETFLOW library, there is a minimum amount of

information that is required for the material to work when called as a wall material. The material properties that are required are as follows:

- The number of atoms/molecule,
- Molar mass (g/mol),
- The heats of melting, vaporization, and sublimation (kJ/mol),
- Thermal conductivity ($W/m \cdot K$),
- Material density (g/cm^3),
- The melting and boiling temperatures (K),
- The specific heat ($J/kg \cdot K$),
- The [q0, q1, q2] (unitless),
- The radius of the molecule (pm),
- And the first and second ionization energies (unitless).

Some of the properties, such as the number of atoms/molecule and the q values are easy to discern or do not change from material to material as is the case with the q values. These values are all 1 for each material. The molar mass for each material was calculated using the following equation:

$$M_{\text{U-Mo}} = N_{\text{U}} \cdot M_{\text{U}} + N_{\text{Mo}} \cdot M_{\text{Mo}}. \tag{3.1}$$

In this equation, the number of Uranium atoms, N_{U} in a U-Mo molecule is multiplied against the calculated molar mass of Uranium, M_{U}, and added to same quantity for Molybdenum, $N_{\text{Mo}} \cdot M_{\text{Mo}}$, yielding the molar mass for the U-Mo alloy in g/mol.

In the creation of the W-Mo alloy ETFLOW material, it was decided to calculate the material properties using a ratio based on the weight percent composition of each element in the alloy. The decision was based on a study in which it was concluded that a W-Mo alloy would take on more of the properties associated with its constituent components based on weight for a particular temperature range. For example, the Heat of Melting was calculated using the following equation:

$$\Delta H_{\text{Melting}} = \gamma_{\text{W}} \cdot \Delta H_{\text{Melting, W}} + \gamma_{\text{Mo}} \cdot \Delta H_{\text{Melting, Mo}}, \tag{3.2}$$

in which the weight fraction of the Tungsten, γ_{W}, is multiplied against the Heat of Melting for Tungsten, $\Delta H_{\text{Melting, W}}$, and added to the weight fraction of the Molybdenum, γ_{Mo}, multiplied against the Heat of Melting for Molybdenum, $\Delta H_{\text{Melting, Mo}}$. As such, an alloy that had more Molybdenum by weight would have its material properties be closer that of pure Molybdenum, as with the W(3%)-Mo alloy. The alloy then takes on more of the Tungsten properties if it has more Tungsten by weight in the composition, as with the W(98.5%)-Mo alloy. This weighting ratio was applied to the three heats, thermal conductivity, material density, specific heat, melting and boiling temperatures, radius of the molecule, and the first and second ionization energies.

Additional W-Mo alloys were made to be direct comparisons to the U-Mo alloys examined later. These alloys were made using the same method as before, but with the focus being placed on the Molybdenum weight fraction varying instead. As such, the resulting W-Mo were as follows: W-Mo(1.00%, 1.25%, 1.50%, 1.75%, and 2.00%). W-Mo alloys in which the Molybdenum content was between 2 and 20 % are considered to be Solid-Solution Alloys. These alloys are less dense than their Unalloyed Tungsten counterparts, but have a more refined grain size due to the added Molybdenum. As such, W-Mo Alloys in this range may be seen in some Aerospace applications along side more well-known alloys like TZM [23].

In contrast, a simple ratio was not used when creating the U-Mo ETFLOW material as there were equations for many of the material properties needed given in a handbook published by Argonne National Laboratory (ANL) that was focused on providing a comprehensive guide to U-Mo based fuels. Of the equations listed in the handbook the equations for Thermal Conductivity, Melting Temperature, and Material Density were used. The Molar Mass was calculated for each individual component (Uranium and Molybdenum) based on the isotopics found in the ICSBEP benchmark for Godiva IV (HEU-MET-FAST-086) and then combined for the various weight fractions of Molybdenum that were to be tested: 1.00%, 1.25%, 1.50%, 1.75%, and 2.00%. The Material Density was then calculated for each of the masses based on the volume of each fuel component and then averaged together to obtain a representative density of the entire system [1, 24, 25].

3.3 Peak Plasma and Materials Parameters Results

Simulations for 27 different materials were performed, resulting in a grand total of 540 simulations across the Ideal and Non-Ideal cases once computations were complete. To distill the information and look for trends, the peak values of each run were obtained for the plasma parameters that were of interest - the temperature, electron number density, and the total ablated mass. These values were then plotted against the value that was multiplied against their current profile, such as 2.50 times the P228 current profile. The plots have been separated into the Pure Materials, which includes TZM as it is the only alloy that is not W-Mo or U-Mo, W-Mo alloys, and U-Mo alloys.

3.3.1 Peak Temperature

The general trend observed in both Figures 3.2 and 3.3 is an increase in the peak temperature with an increase in the current. Generally speaking, the Ideal cases have a higher peak temperature than their Non-Ideal counterparts - this is due to the way these values are calculated and the over estimation of the plasma parameters in the Ideal model. The pure materials - Molybdenum, Tungsten, and Uranium had higher peak temperatures than the TZM alloy - this is due to the fact that alloys have multiple elements with varying ionization energies and the alloy containing a mix of elements such as Zirconium and Carbon which may have contributed to the lower temperatures. The highest value was seen in the Ideal Tungsten 2.50 P228 run in which the peak temperature reached values of 3.38 eV. Ideal Tungsten maintained the highest peak temperatures overall for all current profiles. Non-Ideal TZM alloy had the lowest peak temperatures for all current profiles with its 2.50 P228 run value reaching only 2.28 eV.

There is an anomaly in the Uranium Non-Ideal case in which the 2.25 P228 run's peak temperature is lower than the 2.00 P228 run value. When this was observed, a second set of simulations were performed to verify the results from the initial simulations. The results were the same and after reviewing the temperature, first ionization number density, bulk velocity, and pressure, it was determined that the temperature drop was not due to a shock wave or pressure wave, but was most likely due to computational artifacting. This artifacting is likely due to the complex structure of Uranium and how it is simulated in the Non-Ideal model.

In Figure 3.3, the values are much more clumped together, though the Non-Ideal values were still lower than their Ideal counter-parts. Of the W-Mo alloys, the Ideal W-Mo(1%) alloy

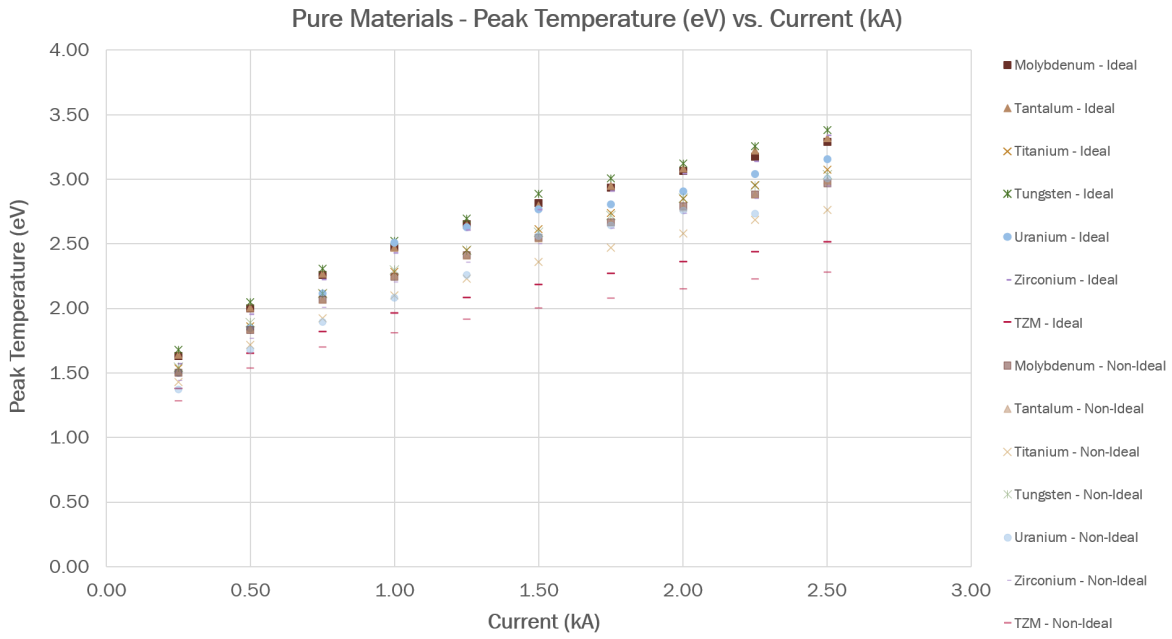

Figure 3.2: Peak Temperature (eV) versus the Current (kA) for the Pure Materials as generated by ETFLOW

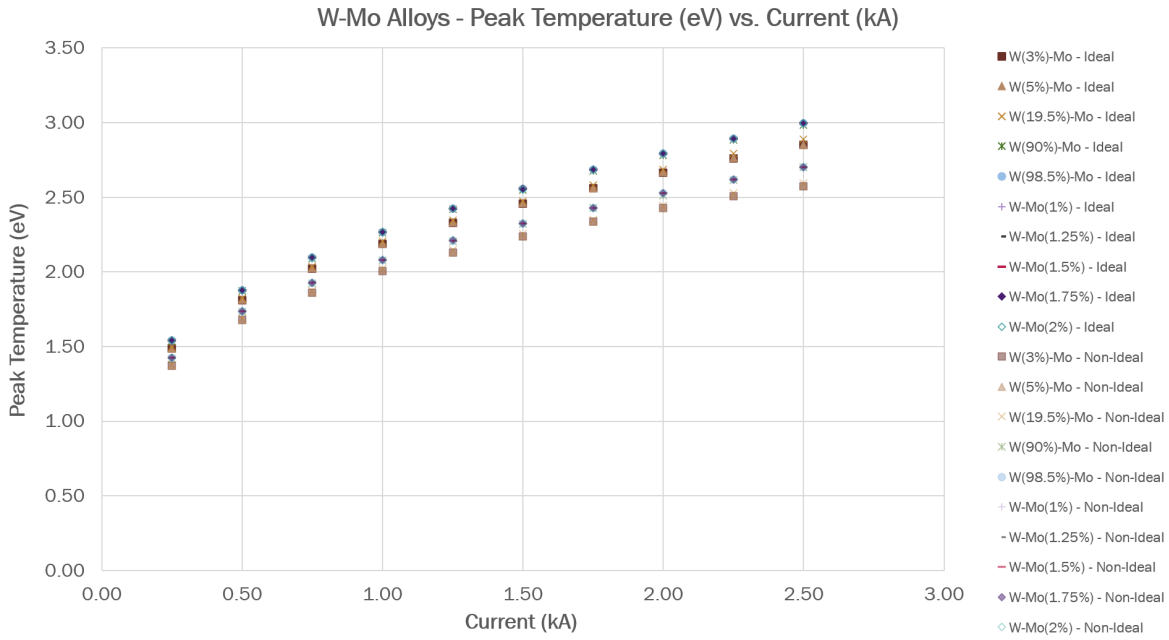

Figure 3.3: Peak Temperature (eV) versus the Current (kA) for the W-Mo Alloys as generated by ETFLOW

case had the highest peak temperature for the 2.50 P228 run with a value of 2.9965 eV. The lowest peak temperature at this current value is 2.5753 eV for the Non-Ideal W(3%)-Mo alloy case. Between the two W-Mo alloy sets, the ones in which the Tungsten content was higher resulted in higher peak temperatures than those that had more Molybdenum. This was seen in Figure 3.2 in the peak temperatures of pure Tungsten being higher than those of pure Molybdenum.

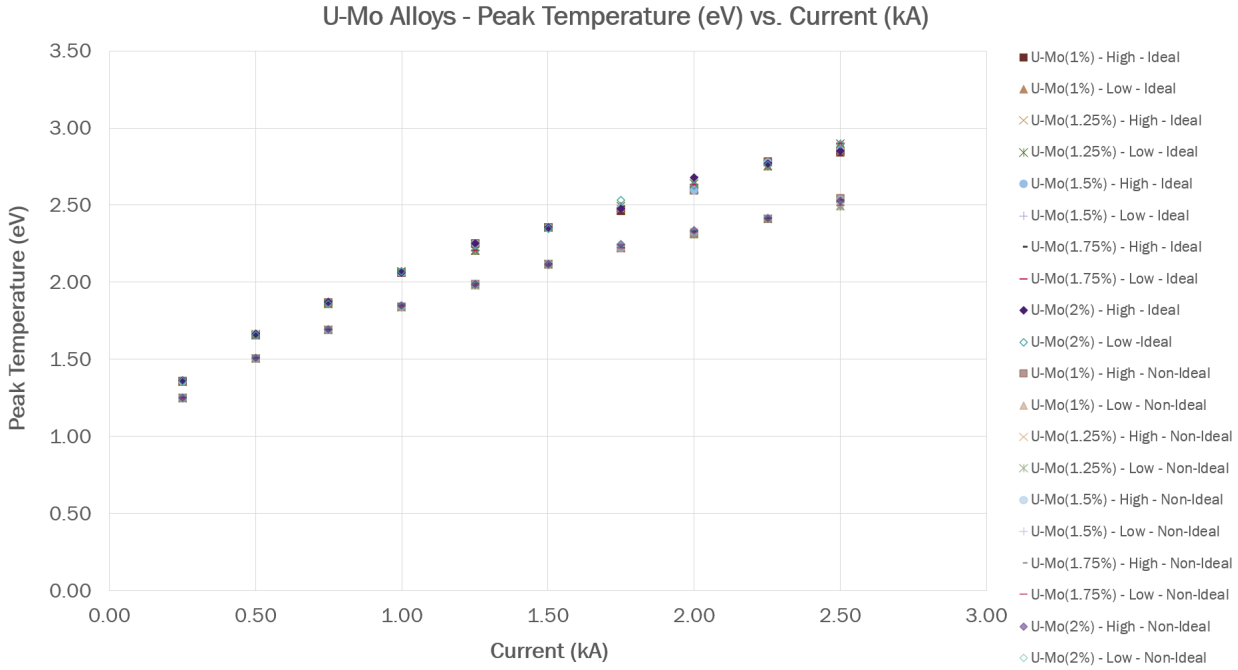

Figure 3.4: Peak Temperature (eV) versus the Current (kA) for the U-Mo Alloys as generated by ETFLOW

The trends seen in Figure 3.4 follow the patterns seen in Figures 3.2 and 3.3. As the current multiplier increases, so does the peak temperature value recorded. Additionally, there is the split between the Ideal and Non-Ideal cases, regardless of whether or not the High or Low Thermal Conductivity value was used in that particular alloy's ETFLOW material library entry. The highest peak temperature value recorded was 2.8965 eV for the Ideal case of U-Mo(2.00%) using the Low Thermal Conductivity value at the 2.50 P228 multiplier value. For the Non-Ideal cases, the highest peak temperature value was recorded at 2.50 P228 for U-Mo(2.00%) using the High Thermal Conductivity value, yielding a value of 2.5255 eV.

3.3.2 Peak Electron Number Density

The general trend observed in both Figures 3.5 and 3.6 is an increase in the peak electron number density with an increase in the current. As with the peak temperature values, the same trend can be seen in which the Ideal cases have the hear values than their Non-Ideal counterparts. The highest electron number density in Figure 3.5, by a large margin, is the value for the 2.50 P228 Ideal Uranium cases at $1.46 \times 10^{27}\ m^{-3}$. For current multiplier values of 1.50 - 2.50, Ideal Uranium had the highest values overall. For P228 multiplier values below that, Ideal TZM alloy had the highest values. The grouping of four materials below Uranium are the other four materials' Ideal cases, followed by the Non-Ideal Uranium case by itself above the grouping of the other four materials' Non-Ideal cases.

In Figure 3.6, the values are much more clumped together by Ideal and Non-Ideal, with the Ideal cases being the well above the Non-Ideal cases for the value of the electron number densities. It was found that the W-Mo alloys with a higher Molybdenum content had a higher electron number density - this was true in both the Ideal and Non-Ideal cases, though the values for the Non-Ideal cases were lower by a factor of 10 for the Non-Ideal cases. An example of this would be the values for W(3%)-Mo for its 2.50 P228 runs - its Ideal case N_E value was $1.3051 \times 10^{27}\ m^{-3}$ and its Non-Ideal case N_E value was $8.7299 \times 10^{26}\ m^{-3}$. The lowest values were found to belong to the W-Mo alloys with the highest concentration of Tungsten, W-Mo(1%) - its Ideal case N_E value was $1.2420 \times 10^{27}\ m^{-3}$ and its Non-Ideal case N_E value was $8.2623 \times 10^{26}\ m^{-3}$. It was seen in the Pure Materials that the concentration of Tungsten played a roll in lowering the peak electron number density and its values were lower than those of Pure Molybdenum across all current multiplier values.

As before, the density trends in Figure 3.7 follow the same increase in electron number density with current as the other materials. Unlike the previous two figures, however, there is much

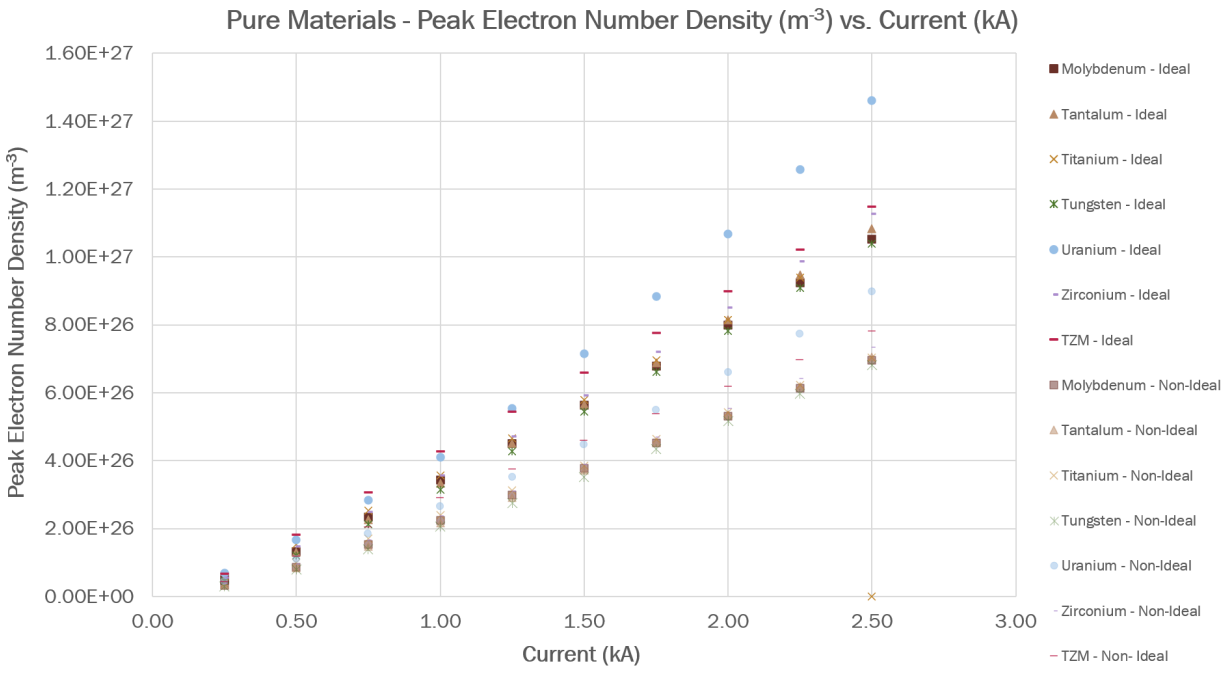

Figure 3.5: Peak Electron Number Density (m^{-3}) versus the Current (kA) for the Pure Materials as generated by ETFLOW

tighter grouping between the Ideal and Non-Ideal cases, resulting in two distinct "bands" of nearly perfectly overlapping points in each case. The top band is, as before, the Ideal case band and contains within it all five U-Mo alloys across each of the Thermal Conductivity tests. Once again, the highest peak electron number density value was at 2.50 P228, and was for U-Mo(1.00%) with the Low Thermal Conductivity, having a value of 1.5647×10^{27} m^{-3}. The Non-Ideal case band followed suit with the same case, U-Mo(1.00%) with the Low Thermal Conductivity at 2.50 P228, have the highest peak electron number density value of 9.7867×10^{26} m^{-3}. In both instances, it was the alloy with the highest concentration of Uranium, and consequently the lowest concentration of Molybdenum, that produced the highest electron number density. When comparing the two Thermal Conductivity cases, this statement still holds true, however, the density value decreases significantly when looking to the High Thermal Conductivity case - 1.5589×10^{27} m^{-3} for the Ideal case and 9.7836×10^{26} m^{-3} for the Non-Ideal case.

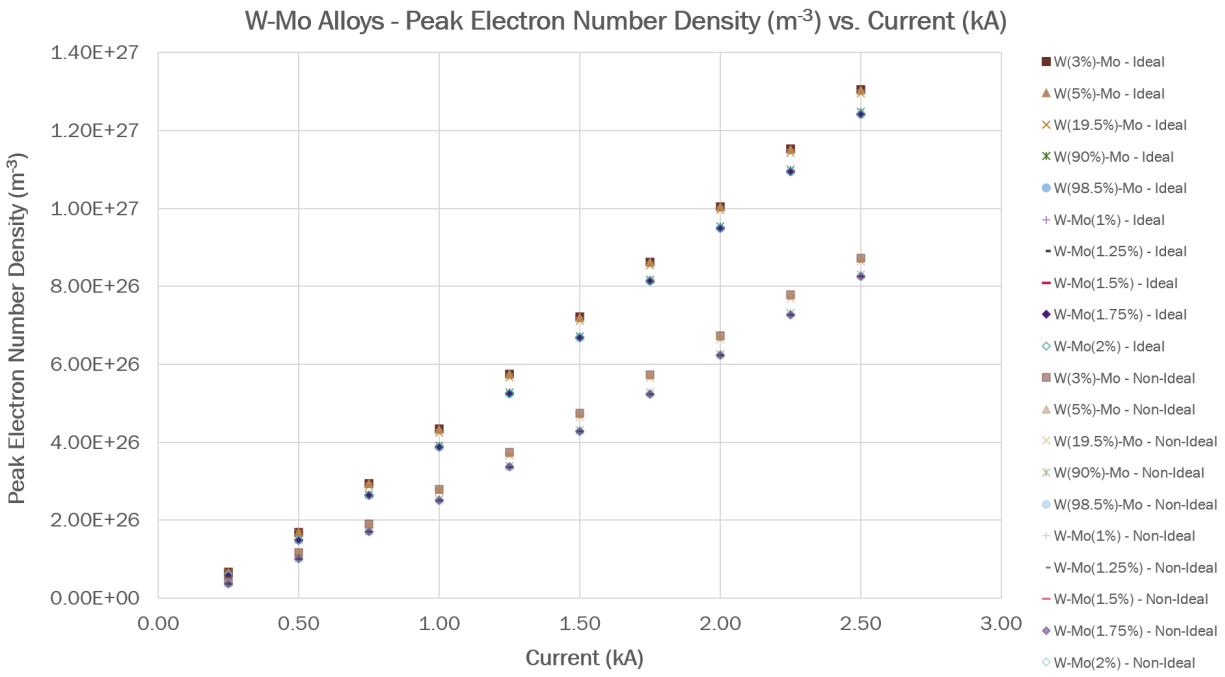

Figure 3.6: Peak Electron Number Density (m^{-3}) versus the Current (kA) for the W-Mo Alloys as generated by ETFLOW

3.3.3 Total Ablated Mass

Unlike the previous two plasma parameters, no search was performed to find this value - the total ablated mass is a value that is directly calculated by ETFLOW as part of the simulation process. However, the value that is output is in gm, so a simple calculation was performed to convert the amount into mg as this unit of measure is more realistic for the mass loss process that is being observed. As before, these values were plotted against multiple of the P228 current profile for each case.

Once again, the general trend observed in both Figures 3.8 and 3.9 is an increase in the peak temperature with an increase in the current. As before, the Ideal cases have a higher total ablated mass than their Non-Ideal counterparts. Ideal Uranium has the highest ablated mass across all ten of its current profiles, will its highest being 2.1639 mg at 2.50 P228. The lowest amount of mass ablated occurred in both instances of the TZM alloy, wish only tenths of a mg being ablated at the top end - 0.3390 mg and 0.2381 mg for the Ideal and Non-Ideal cases, respectively. The amount of mass that is ablated for the 2.00 and 2.25 P228 runs for Uranium Non-Ideal runs were not affected by the computational artifacting that affected the

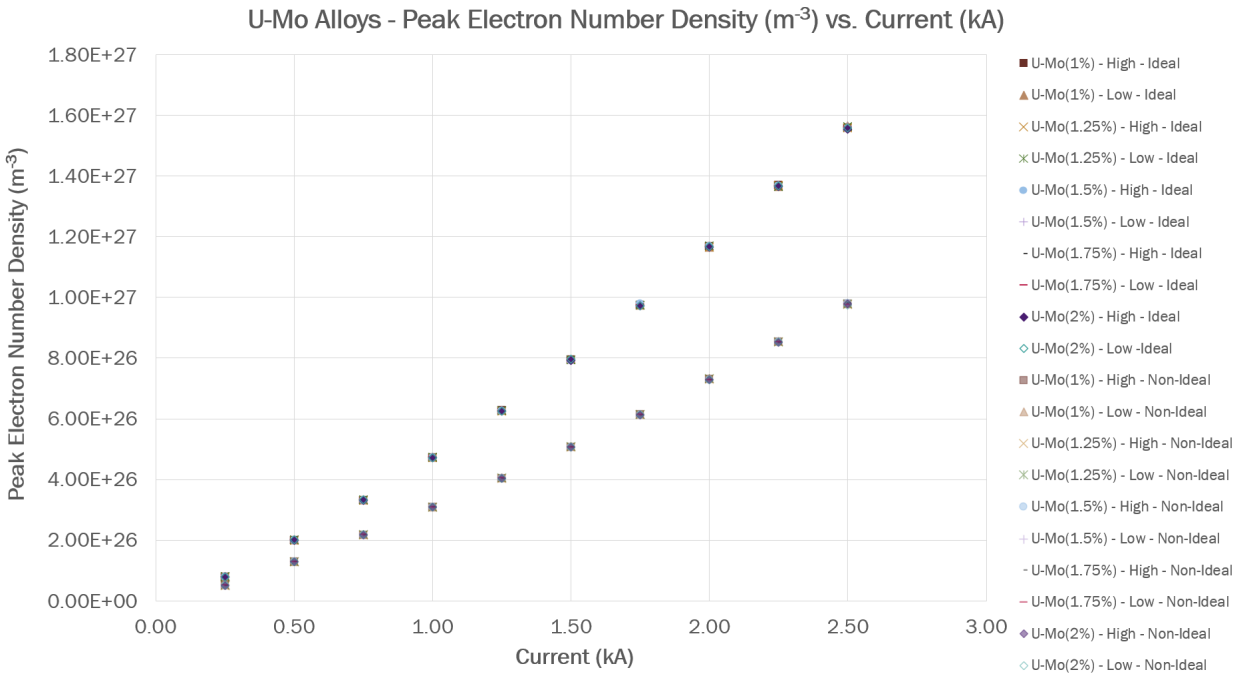

Figure 3.7: Peak Electron Number Density (m^{-3}) versus the Current (kA) for the U-Mo Alloys as generated by ETFLOW

temperature, as seen in Figure 3.2.

In Figure 3.9, the values are split into Ideal and Non-Ideal, though the Non-Ideal values were still lower than their Ideal counter-parts. The W-Mo alloys with higher concentrations of Molybdenum had higher levels of ablation, as seen in the Figure 3.8, with the highest total ablated mass occurring at 2.50 P228 current for W(3%)-Mo - Ideal, having a value of 1.6912 mg. The highest Non-Ideal ablated mass value was also at the same current multiplier value for W(3%)-Mo - 1.2120 mg. The lowest ablated mass values can be attributed to the W-Mo alloys with the highest Tungsten content - W-Mo(1%). The total ablated mass values for the Ideal and Non-Ideal cases at 2.50 P228 current were 1.6248 and 1.1574 mg.

Much like the tight bands since in Figure 3.7, there are tight bands for the Ideal and Non-Ideal cases in Figure 3.10. This implies that, the simulation type, i.e. the equations that each case used, heavily influenced the final total ablated mass results. Discussed in Section 3.2.2, ETFLOW can make use of numerous equations to consider both Ideal and Non-Ideal considers for plasma formation. As such, the end results for the Ideal case predictions are significantly higher than those of the Non-Ideal cases - this ultimately puts a realistic boundary around the actual mass that is to be lost due to ablation of this nature and that can be measured.

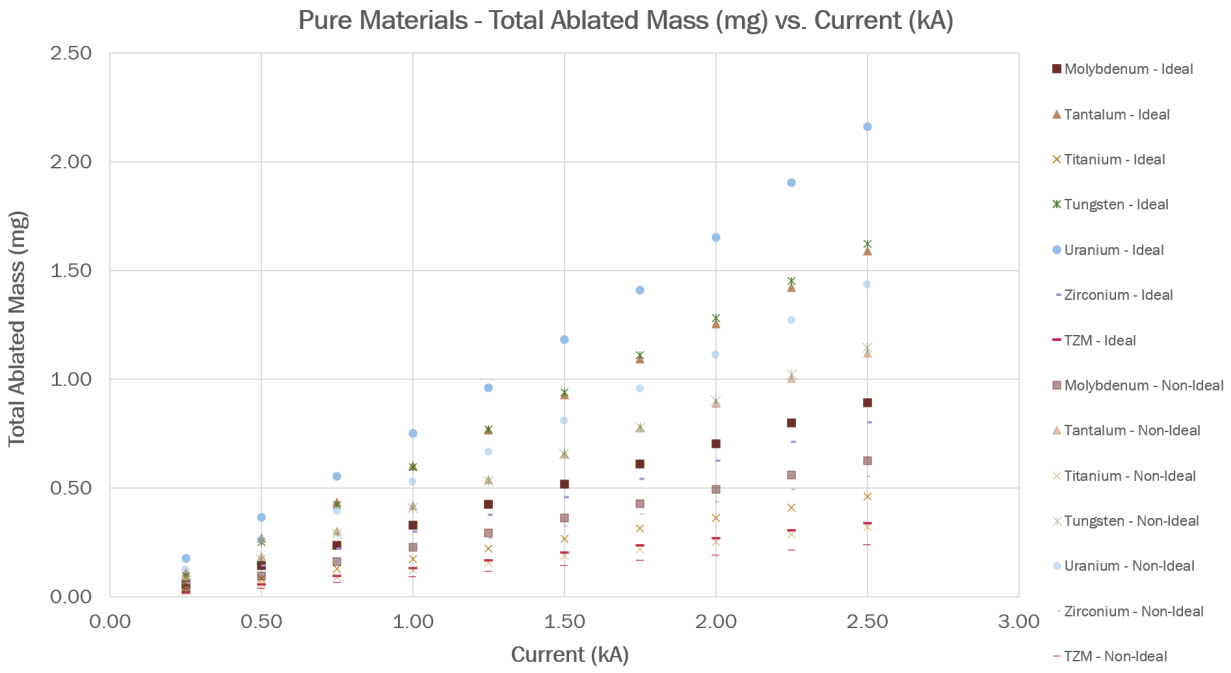

Figure 3.8: Total Ablated Mass (mg) versus the Current (kA) for the Pure Materials as generated by ETFLOW

The highest total ablated mass that was recorded for an Ideal case of U-Mo(1.00%) with the Low Thermal Conductivity at 2.50 P228 and had a value of 1.2904 mg. The highest total ablated mass recorded for a Non-Ideal case occurred for U-Mo(1.00%) with the Low Thermal Conductivity at 2.50 P228 and had a value of 0.8704 mg.

3.4 Time Varying Plasma and Materials Parameters - Simulation Results

Materials discussed within this section are those that were of interest in addition to the main alloy that makes up Godiva IV, U-Mo. A total of 540 simulations were performed to explore the formation of plasma in heavier materials, as these materials are typically not the focus of many fusion-based materials studies. However, these materials were selected based on their availability for physical testing with an SEM and their relevance to fusion applications. The format of each section is the same – tables containing the plasma parameters of interest and plots of said parameters over time. These parameters were chosen as they can be measured during the physical experiments and later compared to the computational results. Each table

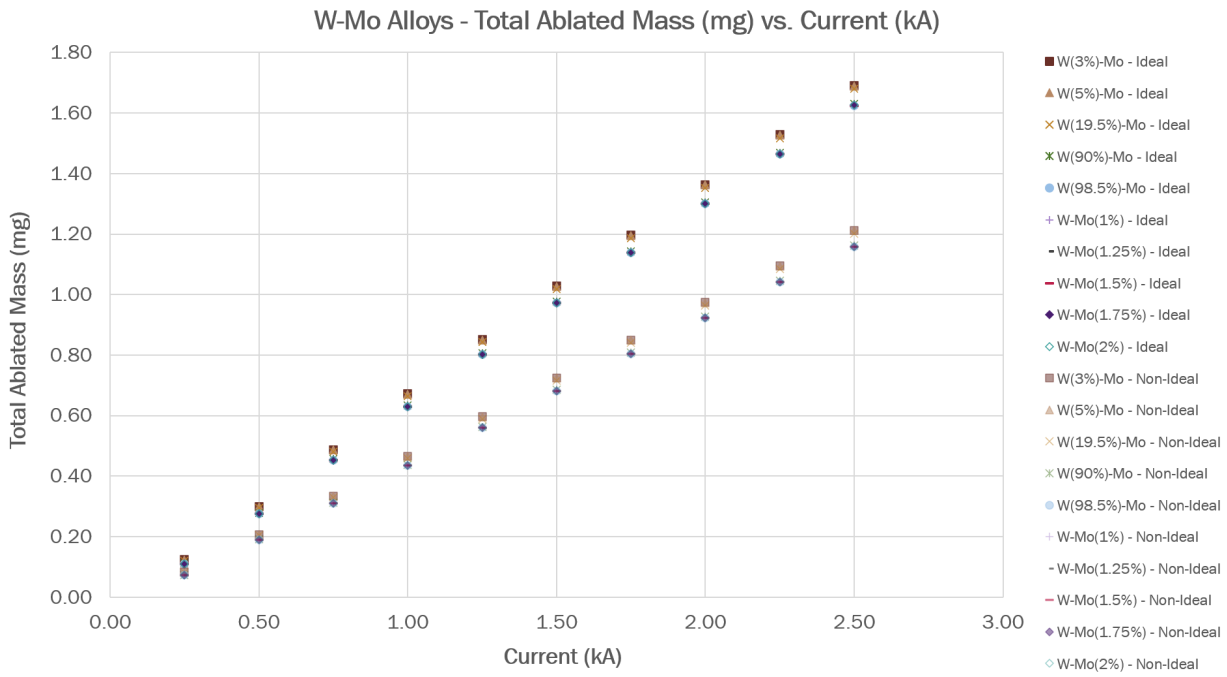

Figure 3.9: Total Ablated Mass (mg) versus the Current (kA) for the W-Mo Alloys as generated by ETFLOW

has the heat flux (GW/m^2), the peak temperature (eV), the peak electron number density (m^{-3}), and the total amount of mass lost to ablation (mg) for each current multiplier value, listed as current (kA). The results are separated into the Ideal and Non-Ideal cases, yielding two tables per material. The plots for each material display the temperature eV and electron number density (m^{-3}) as a function of time (μs).

3.4.1 Select Material Data

Materials discussed within this section are those that were of interest in addition to the main alloy that makes up Godiva IV, U-Mo. A total of 300 simulations were performed to explore the formation of plasma in heavier materials, as these materials are typically not the focus of many fusion-based materials studies. However, these materials were selected based on their availability for physical testing with an SEM and their relevance to fusion applications. The format of each section is the same – tables containing the plasma parameters of interest and plots of said parameters over time. These parameters were chosen as they can be measured during the physical experiments and later compared to the computational results. Each table has the heat flux (GW/m^2), the peak temperature (eV), the peak electron number density

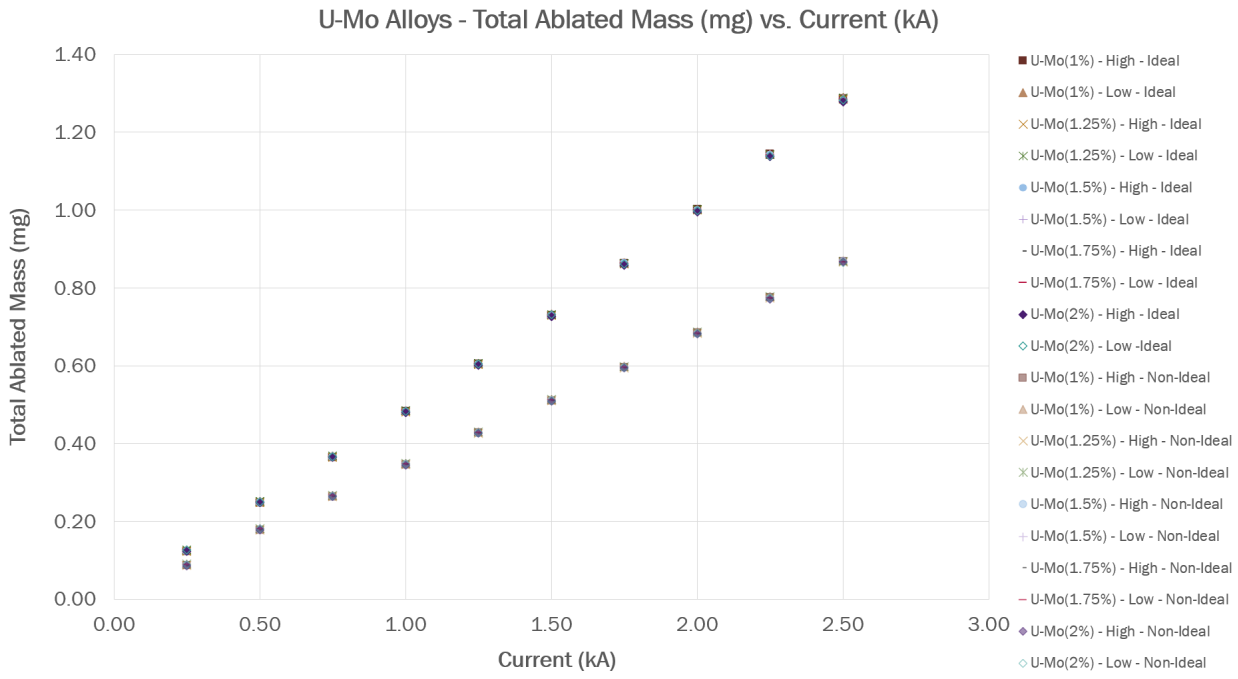

Figure 3.10: Total Ablated Mass (mg) versus the Current (kA) for the U-Mo Alloys as generated by ETFLOW

(m^{-3}), and the total amount of mass lost to ablation (mg) for each current multiplier value, listed as current (kA). The results are separated into the Ideal and Non-Ideal cases, yielding two tables per material. The plots for each material display the temperature eV and electron number density (m^{-3}) as a function of time (μs).

3.4.1.1 Error Associated with ETFLOW Conductivity Models

The error was calculated for the plasma parameters of interest for both models used in simulation, Ideal and Non-Ideal. The error was calculated using the Equation 3.3,

$$\sigma = \sqrt{\frac{\Sigma(X-\mu)^2}{N}} \tag{3.3}$$

in which the population mean, μ was calculated for each set, i.e. Ideal and Non-Ideal, for each P228 multiplier value and then this value was then subtracted from each value, X. This new value was then squared and all squared values summed together before being divided by the number of values in the population, N. This final value was this square rooted, yielding the population standard deviation for each P228 multiplier value. It should be noted that

the summations were performed across all material types at that multiplier value and that the population was $N = 25$ for both the Ideal and Non-Ideal calculations.

Table 3.1 contains the error that was calculated for all peak values that were simulated using ETFLOW's Ideal model. It was found that with decreasing current, the values of heat flux, electron number density, and total ablated mass, as a whole, deviated less than their higher current counterparts. This statement does not hold true for the temperature, however, has the deviation from the mean held fairly consistent across all current multiplier values.

Table 3.1: Error for the Ideal Simulation Plasma Parameters

Ideal Standard Deviation				
I (kA)	q" (GW/m^2)	T_{peak} (eV)	N_E (m^{-3})	M_{tot} (mg)
2.50	0.353	0.192	3.249×10^{26}	0.401
2.25	0.292	0.178	1.700×10^{26}	0.360
2.00	0.148	0.179	1.393×10^{26}	0.320
1.75	0.203	0.182	1.100×10^{26}	0.280
1.50	0.123	0.182	8.606×10^{25}	0.239
1.25	0.092	0.169	6.683×10^{25}	0.197
1.00	0.101	0.164	5.210×10^{25}	0.153
0.75	0.053	0.152	3.972×10^{25}	0.109
0.50	0.028	0.132	2.756×10^{25}	0.068
0.25	0.005	0.106	1.197×10^{25}	0.032

Like the previous table, Table 3.2 contains the error that was calculated for the peak values that were simulated using ETFLOW's Non-Ideal model. These were found to trend the same way as those for the Ideal model, however the error values for the temperature also decreased with current. The mean values of the electron number density were generally lower for the Non-Ideal simulations than for the Ideal simulations, additionally, the amount of deviation seen in these values was also lower.

These error values will be the values considered for each peak value in the proceeding tables in this section.

3.4.2 Pure Material - Molybdenum

Ideal and Non-Ideal simulations were performed in ETFLOW for Pure Molybdenum, the results of which were distilled in Tables 3.3 and 3.4. The peak values for heat flux, temperature, and electron number density, as well as the total ablated mass can be found within these two

Table 3.2: Error for Non-Ideal Simulation Plasma Parameters

Non-Ideal Standard Deviation				
I (kA)	q" (GW/m^2)	T_{peak} (eV)	N_E (m^{-3})	M_{tot} (mg)
2.50	0.545	0.195	1.054×10^{26}	0.286
2.25	0.477	0.184	8.957×10^{25}	0.257
2.00	0.212	0.186	7.402×10^{25}	0.228
1.75	0.188	0.174	6.099×10^{25}	0.198
1.50	0.232	0.172	5.150×10^{25}	0.167
1.25	0.072	0.160	4.216×10^{25}	0.136
1.00	0.082	0.155	3.432×10^{25}	0.105
0.75	0.028	0.143	2.656×10^{25}	0.075
0.50	0.047	0.131	1.639×10^{25}	0.048
0.25	0.012	0.099	7.331×10^{24}	0.023

tables. As with the Pure Tungsten cases, there were a few instances in which the Non-Ideal model did not under predict as expected for heat flux, i.e. it was higher than the value calculated for the Ideal model at that same current multiplier value. The values of heat flux that this occurred at were the 2.50, 1.75, 1.25, and 0.75 P228 current simulations.

Table 3.3: ETFLOW Simulations of Pure Molybdenum - Ideal Cases

Ideal Cases				
I (kA)	q" (GW/m^2)	T_{peak} (eV)	N_E (m^{-3})	M_{tot} (mg)
2.50	394.0	3.288	1.053×10^{27}	0.893
2.25	319.2	3.173	9.247×10^{26}	0.799
2.00	252.3	3.063	8.001×10^{26}	0.705
1.75	193.0	2.938	6.784×10^{26}	0.611
1.50	141.9	2.814	5.626×10^{26}	0.518
1.25	98.44	2.650	4.495×10^{26}	0.424
1.00	63.06	2.474	3.421×10^{26}	0.330
0.75	35.40	2.261	2.340×10^{26}	0.235
0.50	15.75	2.002	1.328×10^{26}	0.142
0.25	3.937	1.631	4.865×10^{25}	0.056

The peak temperature values follow the expected decreasing pattern seen in other materials with decreasing current, as does the electron number density. The total ablated mass decreases with current, as expected, however the values in both the Ideal and Non-Ideal cases are rather small when compared to the other materials. In some cases, more than half the amount that was ablated for the same current multiplier value as was the case for the Ideal 2.50 P228 case

when compared to the same instance for Uranium – the values are 0.893 mg and 2.164 mg respectively.

Table 3.4: ETFLOW Simulations of Pure Molybdenum - Non-Ideal Cases

Non-Ideal Cases				
I (kA)	q" (GW/m^2)	T_{peak} (eV)	N_E (m^{-3})	M_{tot} (mg)
2.50	394.1	2.972	6.953×10^{26}	0.627
2.25	319.1	2.882	6.127×10^{26}	0.560
2.00	252.1	2.791	5.316×10^{26}	0.494
1.75	193.2	2.670	4.524×10^{26}	0.428
1.50	141.7	2.548	3.766×10^{26}	0.361
1.25	98.49	2.411	2.990×10^{26}	0.294
1.00	62.97	2.245	2.246×10^{26}	0.227
0.75	35.47	2.067	1.523×10^{26}	0.161
0.50	15.74	1.832	8.627×10^{25}	0.097
0.25	3.931	1.505	3.196×10^{25}	0.038

Figure 3.11 is a plot of the temperature (eV) as a function of time (μs). The temperature profiles for each current simulation are as expected – higher temperatures with a higher peak temperature. The highest peak temperature occurs in the Ideal 2.50 P228 case at around 30 μs, yielding a value of 3.2875 eV. This value is very closely followed by the plot for the Ideal 2.25 P228 case whose peak temperature value at the same time value is 3.1725 eV. The close proximity of the two plots is two to a "bobbling" that occurs in the two plots between 20 and 40 μs - this bobble is likely due to computational artifacting that occurs during the simulation process.

Figure 3.12 details the expected electron number density (m^{-3}) per current profile as a function of time (μs). As seen in other materials, the Ideal 2.50 P228 case had the highest overall electron number density over the entire length of the shot. The number density peaked at around 70 μs with a value of 1.5027×10^{27} m^{-3}. A common trend is the Non-Ideal cases have much lower values of electron number density over the course of the shot – the lowest of which is the 0.25 P228 case, having a peak value of only 3.1921×10^{25} m^{-3}.

In general, the trends seen in both Figures 3.11 and 3.12 are as expected for the models used in the simulations. These values will be the basis for comparison in the physical experiments as they are measurable.

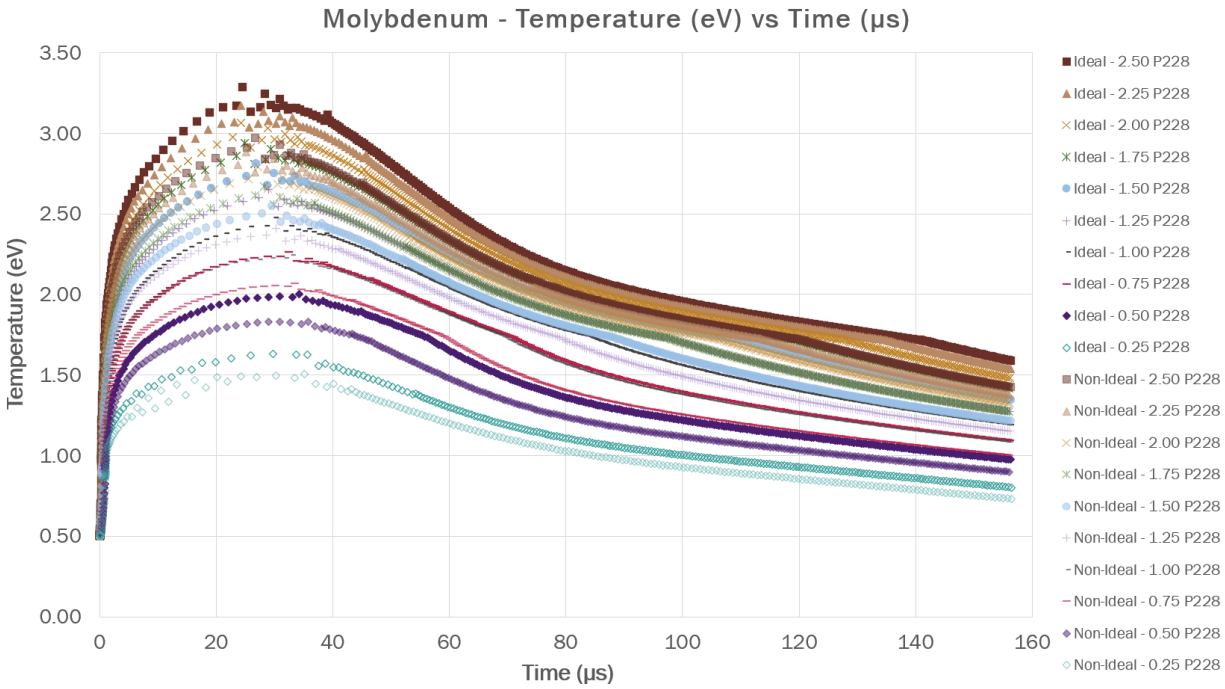

Figure 3.11: Molybdenum Temperature (eV) versus Time (μs) as generated by ETFLOW

3.4.3 Pure Material - Tantalum

Tantalum was another material that was both simulated and tested using the laser assembly and SEM. This material, while not related to Godiva IV, was of interest to the greater plasma facing material interaction research that was being conducted along side the main body of the project. This material was chosen for research as it is a prospective protective coating for plasma facing components in tokamak fusion reactors. As such, it was deemed beneficial to add more reference points to the ETFLOW simulation archive for Ideal and Non-Ideal simulations of Tantalum over a selected range of current profiles based on the P228 shot current profile data.

Table 3.5 provides a detailed look at the plasma parameters generated using the Ideal model in ETFLOW and Table 3.6 the plasma parameters generated using the Non-Ideal model in ETFLOW. As is the norm, there is a decrease in the plasma parameters with the current, and the Non-Ideal simulation values are lower than the Ideal simulation values due to how they are calculated. The exception to this "rule" is the heat flux in which several values for the Non-Ideal simulations are higher than their Ideal counterparts. These P228 values are 1.25, 1.00, 0.75, and 0.50. The values for the peak temperature eV, electron number density

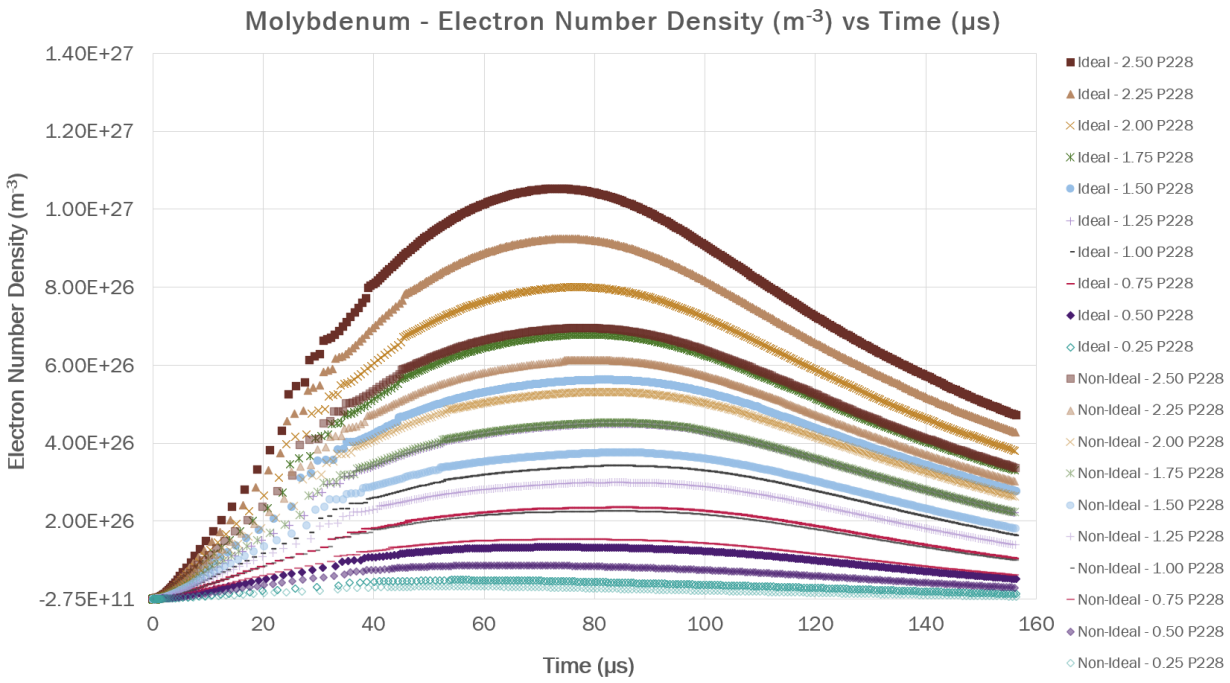

Figure 3.12: Molybdenum Electron Number Density (m^{-3}) versus Time (μs) as generated by ETFLOW

Table 3.5: ETFLOW Simulations of Pure Tantalum - Ideal Cases

Ideal Cases				
I (kA)	q" (GW/m^2)	T_{peak} (eV)	N_E (m^{-3})	M_{tot} (mg)
2.50	393.5	3.323	1.082×10^{27}	1.591
2.25	319.1	3.223	9.465×10^{26}	1.422
2.00	252.1	3.087	8.148×10^{26}	1.256
1.75	193.8	2.946	6.881×10^{26}	1.092
1.50	141.3	2.793	5.661×10^{26}	0.928
1.25	98.22	2.649	4.503×10^{26}	0.766
1.00	63.06	2.473	3.338×10^{26}	0.601
0.75	35.20	2.267	2.260×10^{26}	0.435
0.50	15.73	2.007	1.297×10^{26}	0.269
0.25	3.935	1.639	4.838×10^{25}	0.111

m^{-3}, and total ablated mass mg were on par with other material simulations that have been performed.

Figure 3.13 is a visualization of the temperature (eV) data as a function of time (μs) for all simulations performed for Tantalum, both Ideal and Non-Ideal. The simulation temperature

Table 3.6: ETFLOW Simulations of Pure Tantalum - Non-Ideal Cases

Non-Ideal Cases				
I (kA)	q" (GW/m^2)	T_{peak} (eV)	N_E (m^{-3})	M_{tot} (mg)
2.50	393.5	2.994	7.058×10^{26}	1.120
2.25	319.1	2.882	6.197×10^{26}	1.004
2.00	252.0	2.785	5.351×10^{26}	0.889
1.75	193.0	2.669	4.547×10^{26}	0.775
1.50	140.9	2.543	3.712×10^{26}	0.656
1.25	98.44	2.408	2.914×10^{26}	0.539
1.00	62.79	2.251	2.166×10^{26}	0.420
0.75	35.35	2.069	1.480×10^{26}	0.301
0.50	15.75	1.844	8.452×10^{25}	0.185
0.25	3.934	1.513	3.454×10^{25}	0.076

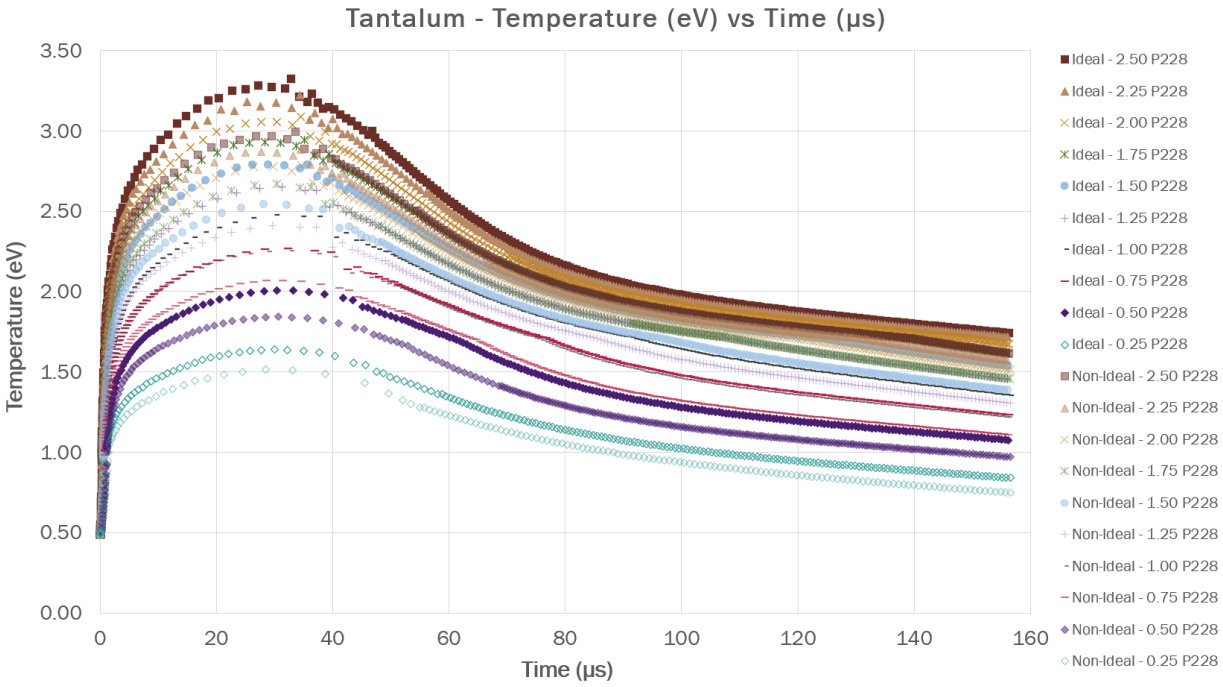

Figure 3.13: Tantalum Temperature (eV) versus Time (μs) as generated by ETFLOW

profiles all fall within the expected shape of an ETFLOW temperature computation. This material did not experience as much of the computational bobbling at the higher currents as was seen in other material simulations. There was some, however, in the Ideal 2.50 P228 temperature plot, with one of these points being the peak value, 3.3227 eV at about 35 μs. If this value was "smoothed" out, the peak value would occur around the 30 μs time mark and

would be 3.2822 eV. The Non-Ideal simulations did not experience as much computational artifacting, either, and had fairly smooth curves. The Non-Ideal curve with the highest overall temperature value was 2.9943 eV for the 2.50 P228 case and the lowest peak temperature value was 1.5133 eV for the 0.25 $\times$ P228 case.

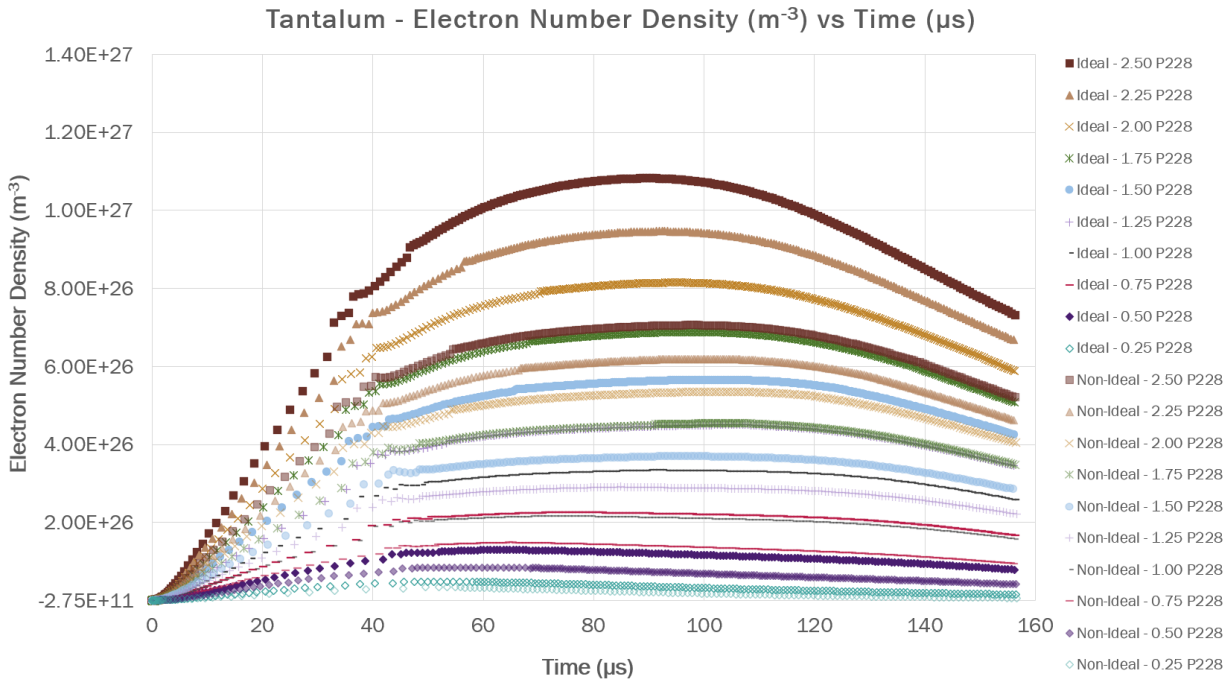

Figure 3.14: Ta Electron Number Density (m^{-3}) versus Time (μs) as generated by ETFLOW

Figure 3.14 portrays the electron number density (m^{-3}) simulation data for both the Ideal and Non-Ideal cases for Tantalum. Following suit with the other materials simulated, the Ideal cases had the highest overall values of electron number density (m^{-3}) over the length of the shot (μs). The largest peak value was that of the Ideal 2.50 P228 case, occurring around 90 μs, having a value of 1.0823×10^{27} m^{-3}. The largest peak value for the Non-Ideal cases was that of the 2.50 P228 case, also occurring around 90 μs and having a value of 7.0579×10^{26} m^{-3}. It should be noted that this is a factor of 10 difference between to the two 2.50 $\times$ P228 cases – this difference can be used to set an upper and lower bound for calculations of actual electron number densities from physical experiments and, thusly, can be further validation of the ETFLOW code and this method of study.

3.4.4 Pure Material - Titanium

From the second wave of materials simulated using ETFLOW, Titanium was selected as it is another commonly used material in the aerospace and fusion industries. Known for being a light-weight material while retaining its strength, Titanium is typically found in structural components or as an additive, like in TZM Alloys, to improve a material's mechanical or chemical properties. As with the materials in this study, two sets of 10 runs were performed using both Conductivity models available in the ETFLOW program; select results from these runs are found in Tables 3.7 and 3.8.

Table 3.7 contains the peak values for the Heat Flux, q" (GW/m^2), Temperature, T_{peak} (eV), and Electron Number Density, N_E (m^{-3}), for the 10 simulations performed using the Ideal Conductivity Model in ETFLOW. Additionally, the Total Mass Loss due to Ablation, M_{tot} (mg), which was calculated by ETFLOW, is also presented in the table. Of the Pure Materials simulated, Titanium lost the least amount of mass from ablation, with Zirconium (a material used in fuel cladding) experiencing a similarly low amount. This low amount of ablation is also reflected in the low amount of mass lost in the TZM Alloy, a material comprised of 0.5% Titanium and 0.08% Zirconium. A general statement can be made that the Peak Temperatures values for the Ideal simulations for Titanium are lower than other Pure Materials simulated in the set, while the Electron Number Density values remain some of the highest seen.

Table 3.7: ETFLOW Simulations of Pure Titanium - Ideal Cases

Ideal Cases				
I (kA)	q" (GW/m^2)	T_{peak} (eV)	N_E (m^{-3})	M_{tot} (mg)
2.50	394.1	3.073	1.061×10^{27}	0.461
2.25	319.2	2.955	9.391×10^{26}	0.411
2.00	252.3	2.851	8.143×10^{26}	0.362
1.75	193.1	2.738	6.953×10^{26}	0.314
1.50	141.8	2.613	5.780×10^{26}	0.267
1.25	98.50	2.449	4.654×10^{26}	0.220
1.00	63.04	2.285	3.567×10^{26}	0.174
0.75	35.45	2.113	2.520×10^{26}	0.128
0.50	15.76	1.866	1.529×10^{26}	0.083
0.25	3.939	1.535	5.814×10^{25}	0.037

Table 3.8 presents the Non-Ideal Conductivity Model simulation data for Pure Titanium. As expected, the values for the Non-Ideal Conductivity Model simulations were lower their

Table 3.8: ETFLOW Simulations of Pure Titanium - Non-Ideal Cases

Non-Ideal Cases				
I (kA)	q" (GW/m^2)	T_{peak} (eV)	N_E (m^{-3})	M_{tot} (mg)
2.50	394.1	2.764	7.041×10^{26}	0.319
2.25	319.1	2.646	6.225×10^{26}	0.286
2.00	252.2	2.580	5.414×10^{26}	0.252
1.75	193.1	2.474	4.636×10^{26}	0.220
1.50	141.8	2.363	3.852×10^{26}	0.187
1.25	98.51	2.229	3.117×10^{26}	0.155
1.00	63.05	2.097	2.388×10^{26}	0.123
0.75	35.48	1.921	1.700×10^{26}	0.090
0.50	15.76	1.716	1.002×10^{26}	0.058
0.25	3.938	1.430	3.825×10^{25}	0.026

Ideal Conductivity Model simulation counterparts. Like the Ideal simulations, the values for the Non-Ideal simulation Total Ablated Mass were the lowest calculated for the study. The values for the Peak Temperature and Electron Number Density were followed suit with what was seen in the Ideal simulations.

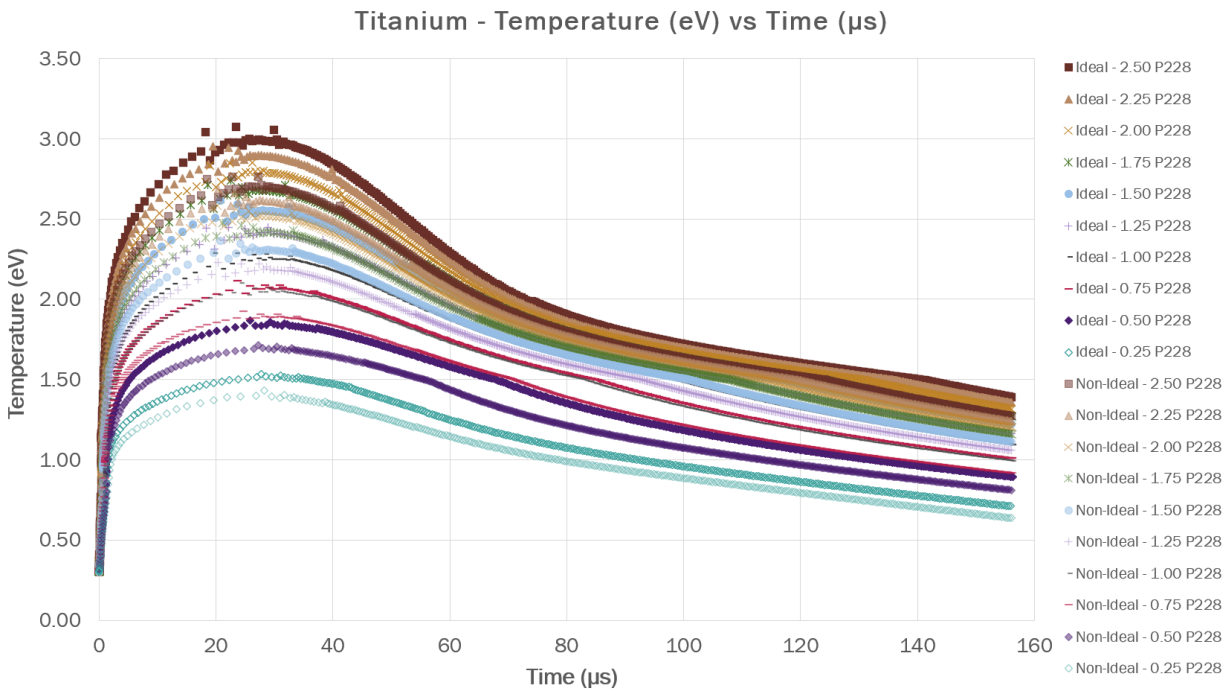

Figure 3.15: Titanium Temperature (eV) versus Time (μs) as generated by ETFLOW

Figures 3.15 and 3.16 are the Temperature and Electron Number Density plots for Titanium. Figure 3.15 depicts the ETFLOW generated Temperature, which has been converted from K to eV, as a function of Time (μs). The total shot length for each of the 20 simulations does not exceed 160 μs and each reaches its peak between 10 - 40 μs. The simulations with the highest currents, i.e. the Ideal and Non-Ideal Conductivity simulations using the 2.50 $\times$ P228 discharge current profile, had the highest overall temperatures for their simulation set, with peak values reaching 3.073 and 2.764 eV, respectively.

Figure 3.16 displays the the ETFLOW generated Electron Number Density data, (m^{-3}), as a function of Time (μs). As with the Temperature plot, the shot times do no exceed 160 μs, however, the time at which the simulations reach the peak values are shifted to the right, to between 40 and 80 μs. Like with the Temperatures, the Ideal and Non-Ideal Conductivity simulations using the 2.50 $\times$ P228 discharge current profile information saw the highest Electron Number Density values, with peak values of 1.061×10^{27} and 7.041×10^{26} m^{-3}, respectively.

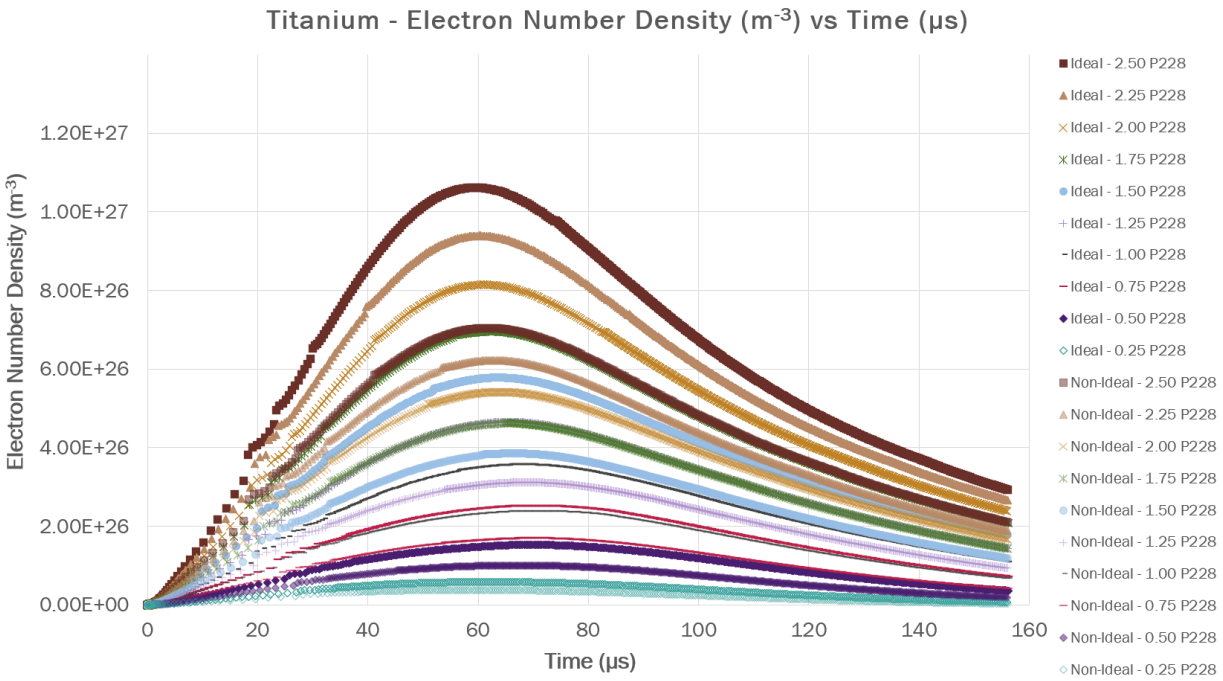

Figure 3.16: Titanium Electron Number Density (m^{-3}) versus Time (μs) as generated by ETFLOW

3.4.5 Pure Material - Tungsten

ETFLOW simulations for Pure Tungsten were performed for both the Ideal and Non-Ideal cases. The peak values for the heat flux, temperature, and electron number density, along with the total ablated mass were compiled into tables for each current profile multiplier value, see Tables 3.9 and 3.10. As previously stated, a current profile multiplier value is simply the value by which the P228 shot current value has been multiplied by to obtain the current profile for that specific run. As such, a multiplier value of 2.50 implies that the P228 shot current profile was multiplied by 2.50 across all values.

Tables 3.9 and 3.10 contain the peak values for the plasma parameters of interest, sorted by simulation type. In general, the Ideal simulation values were larger than those of the Non-Ideal simulations, i.e. over-predicting, however, there were some instances were this was not the case. The instances where this occurs are for the heat flux values at the 2.50, 1.50, 1.00, and 0.50 P228 current multiplier values; for these four values, the Non-Ideal model has a larger heat flux value. The likely reason for this over prediction from the Non-Ideal model is due to how the values that are used in the heat flux calculation are computed, i.e. along

each step of the way with a much more complex model than the Ideal case.

Table 3.9: ETFLOW Simulations of Pure Tungsten - Ideal Cases

Ideal Cases				
I (kA)	q" (GW/m^2)	T_{peak} (eV)	N_E (m^{-3})	M_{tot} (mg)
2.50	393.4	3.379	1.038×10^{27}	1.623
2.25	319.1	3.256	9.083×10^{26}	1.452
2.00	252.0	3.125	7.820×10^{26}	1.281
1.75	192.8	3.008	6.606×10^{26}	1.112
1.50	141.5	2.886	5.451×10^{26}	0.942
1.25	98.52	2.696	4.265×10^{26}	0.768
1.00	62.62	2.519	3.137×10^{26}	0.595
0.75	35.43	2.308	2.117×10^{26}	0.422
0.50	15.72	2.051	1.198×10^{26}	0.252
0.25	3.931	1.679	4.559×10^{25}	0.095

Table 3.10: ETFLOW Simulations of Pure Tungsten - Non-Ideal Cases

Non-Ideal Cases				
I (kA)	q" (GW/m^2)	T_{peak} (eV)	N_E (m^{-3})	M_{tot} (mg)
2.50	393.9	3.006	6.822×10^{26}	1.145
2.25	318.3	2.946	5.976×10^{26}	1.024
2.00	251.4	2.858	5.169×10^{26}	0.903
1.75	192.5	2.716	4.331×10^{26}	0.781
1.50	141.5	2.593	3.509×10^{26}	0.656
1.25	98.45	2.451	2.757×10^{26}	0.532
1.00	62.95	2.297	2.058×10^{26}	0.409
0.75	35.37	2.116	1.388×10^{26}	0.288
0.50	15.73	1.889	7.906×10^{25}	0.170
0.25	3.915	1.544	3.029×10^{25}	0.063

The benefit to having these data points is that they can be measured directly using RTDs and though massing the sample before and after a pulse event. As such, this data can be can critical in forming a band in which measured values can be predicted value, with Ideal values forming the upper band and Non-Ideal values forming the lower. As such, these values will be a starting point for comparison and verification of SEM techniques.

Figure 3.17 shows how the temperature (eV) of the plasma generated fluctuates as a function of time (μs) for both Ideal and Non-Ideal simulations. As expected, the Ideal simulations have the highest values overall, with the Ideal 2.50 P228 case having the highest overall

temperatures seen at all steps of the plasma generation process. It can then be said, that the Non-Ideal 0.25 P228 case having the lowest overall temperatures is also expected. The peak values of each case are 3.3789 eV and 1.5435 eV, respectively; these values can be found in Tables 3.9 and 3.10.

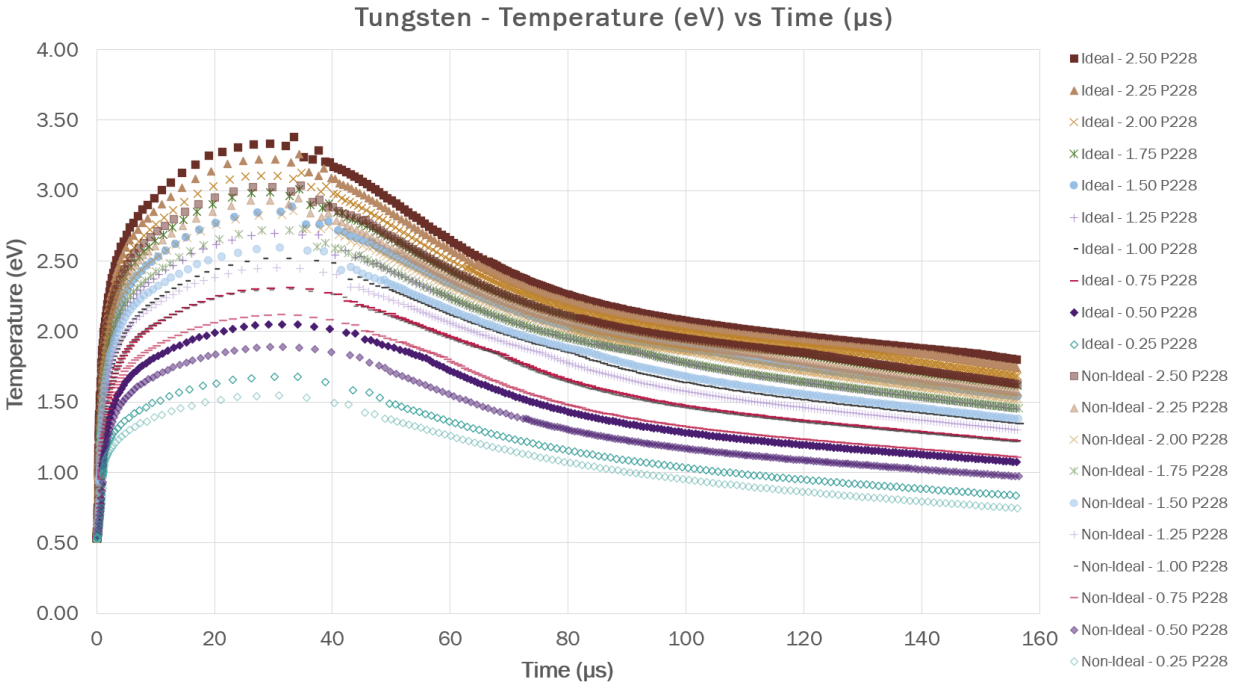

Figure 3.17: Tungsten Temperature (eV) versus Time (μs) as generated by ETFLOW

Figure 3.18 shows the expected trend of how the electron number density (m^{-3}) fluctuates with time (μs) for the Ideal and Non-Ideal simulations of ETFLOW. Like the previous plot, the Ideal 2.50 P228 case had the highest overall values for electron number density, with its peak value reaching 1.038×10^{27} m^{-3}. The lowest electron number density curve belongs to the Non-Ideal 0.25 P228 case, which only reached a peak value of 3.029×10^{25} m^{-3}. Peak values, in both cases, were reached at a time of around 90 μs.

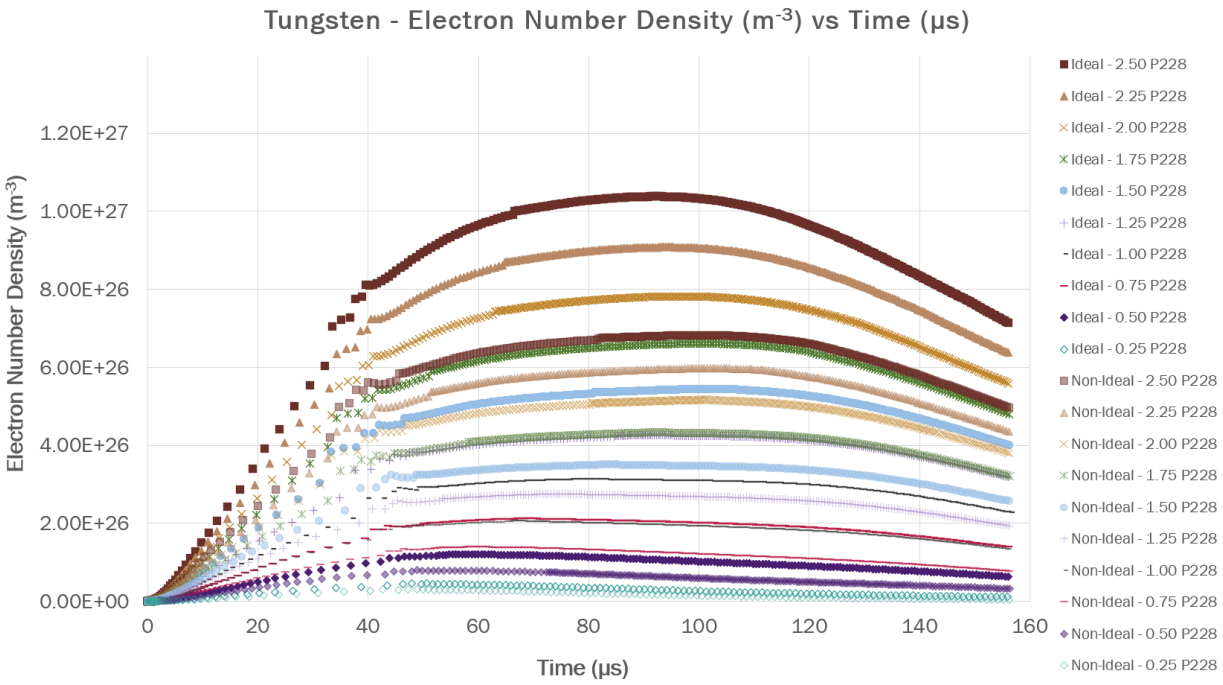

Figure 3.18: Tungsten Electron Number Density (m^{-3}) versus Time (μs) as generated by ETFLOW

3.4.6 Pure Material - Uranium

Pure Uranium, while not one of the materials that were tested in the physical experimentation phase, was important to simulate as it is one of the key components, like Molybdenum, in the alloy that makes up Godiva IV. Ideal and Non-Ideal model simulations were performed across ten current profiles, generating the tables and plots within this section. General trends seen in other material simulations were observed, though some differences were documented.

Tables 3.11 and 3.12 are the tables containing the Ideal and Non-Ideal simulation data for the Uranium ETFLOW simulations. There is the now expected decrease in values with current with the values of Non-Ideal cases being lower than their Ideal counterparts. The exception stands for certain heat flux values – in this case for the 1.75, 1.25, 0.75, and 0.25 P228 current profiles, which values being more for the Non-Ideal simulations. The total ablated mass was higher for the Ideal simulations, with the highest amount of ablation occurring in the 2.50 P228 simulation with 2.1639 mg being lost. The same case run using the Non-Ideal model only lost 1.4371 mg to ablation, showing that this model heavily under predicts the amount lost due to this process. In general, this material ablated more than the other materials at

lower currents.

Table 3.11: ETFLOW Simulations of Pure Uranium - Ideal Cases

Ideal Cases				
I (kA)	q" (GW/m^2)	T_{peak} (eV)	N_E (m^{-3})	M_{tot} (mg)
2.50	393.5	3.156	1.461×10^{27}	2.164
2.25	319.2	3.042	1.258×10^{27}	1.904
2.00	252.0	2.907	1.068×10^{27}	1.655
1.75	193.0	2.806	8.838×10^{26}	1.410
1.50	141.8	2.766	7.147×10^{26}	1.183
1.25	98.30	2.631	5.540×10^{26}	0.961
1.00	63.05	2.512	4.104×10^{26}	0.752
0.75	35.41	2.115	2.827×10^{26}	0.555
0.50	15.73	1.849	1.671×10^{26}	0.366
0.25	3.920	1.499	6.874×10^{25}	0.176

Table 3.12: ETFLOW Simulations of Pure Uranium - Non-Ideal Cases

Non-Ideal Cases				
I (kA)	q" (GW/m^2)	T_{peak} (eV)	N_E (m^{-3})	M_{tot} (mg)
2.50	393.2	3.006	8.987×10^{26}	1.437
2.25	318.8	2.736	7.742×10^{26}	1.270
2.00	251.9	2.754	6.604×10^{26}	1.111
1.75	193.1	2.641	5.491×10^{26}	0.958
1.50	141.7	2.558	4.480×10^{26}	0.810
1.25	98.52	2.259	3.524×10^{26}	0.666
1.00	62.79	2.085	2.653×10^{26}	0.528
0.75	35.43	1.897	1.841×10^{26}	0.395
0.50	15.65	1.678	1.090×10^{26}	0.262
0.25	3.938	1.370	4.498×10^{25}	0.124

An anomaly occurred, as mentioned in Section 3.3.1, in the Non-Ideal simulations when looking at the peak temperature values. Typically, it was seen across all materials that as the current decreased, the peak temperature value would decrease as well, this was not the case for the peak temperature value for the 2.00 P228 current simulation. The peak value of this simulation was 2.7543 eV, higher than the 2.25 P228 case value of 2.7363 eV. As stated before, it is believed that this is due to how the values for temperature are calculated in the Non-Ideal model and is likely due to computational artifacting and not unaccounted for physics. Looking to Figures 3.19 and 3.20 a bobbling can be seen at few places between 20

and 40 μs, corresponding to where the peak temperature value occurs. This bobbling occurs in a few of the plots, not just the 2.00 P228 simulation plot, leading to the assumption that this occurrence has more to doe with how the values are calculated and not with the presence of a shockwave or pressure wave that was not seen or accounted for. This was verified by looking at the velocity profiles for both the 2.25 and 2.00 P228 cases to ensure that there were no negative dips, which would indicate that a wave of some sort had occurred.

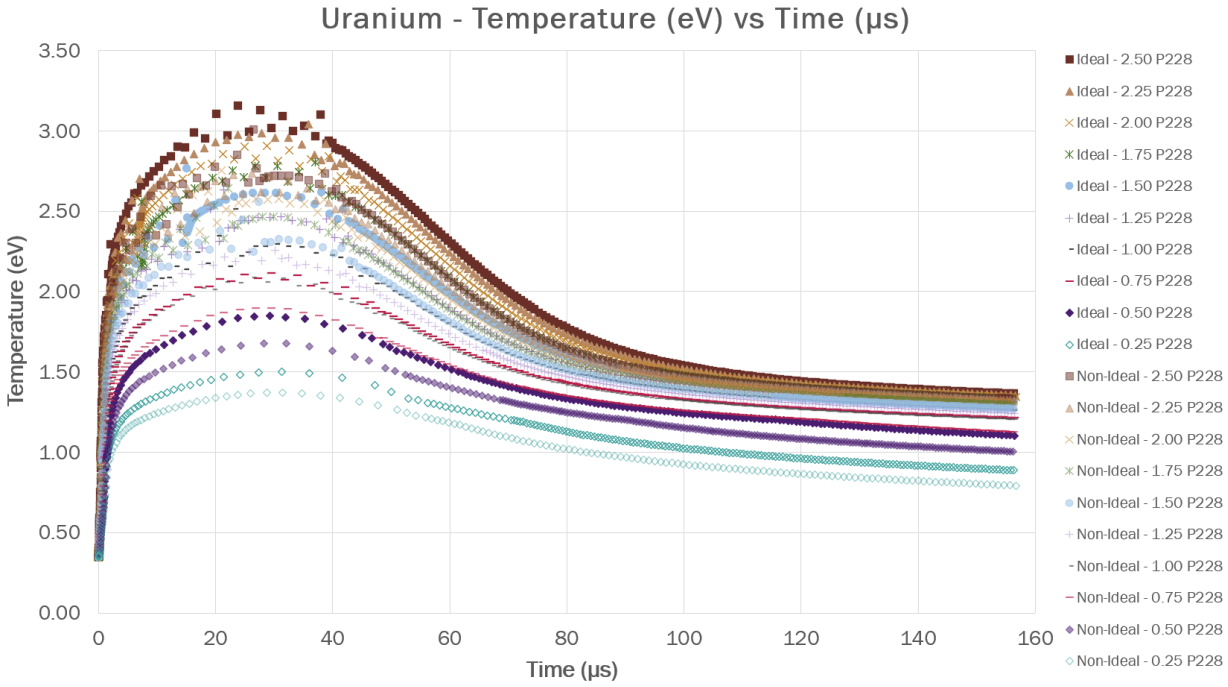

Figure 3.19: Uranium Temperature (eV) versus Time (μs) as generated by ETFLOW

Barring the artifact anomalies around the peaks, the trends seen in both Figures 3.19 and 3.20 are what is to be expected from ETFLOW for the Ideal and Non-Ideal models. In both cases, the Ideal 2.50 P228 simulation had the highest overall values, peaking at 3.1557 eV and $1.4606 \times 10^{27}\ m^{-3}$, respectively. The Non-Ideal simulations had the lower overall values, with the lowest belong to the 0.25 P228 simulation. This simulation had peak values of 1.3701 eV and $4.4977 \times 10^{25}\ m^{-3}$, respectively.

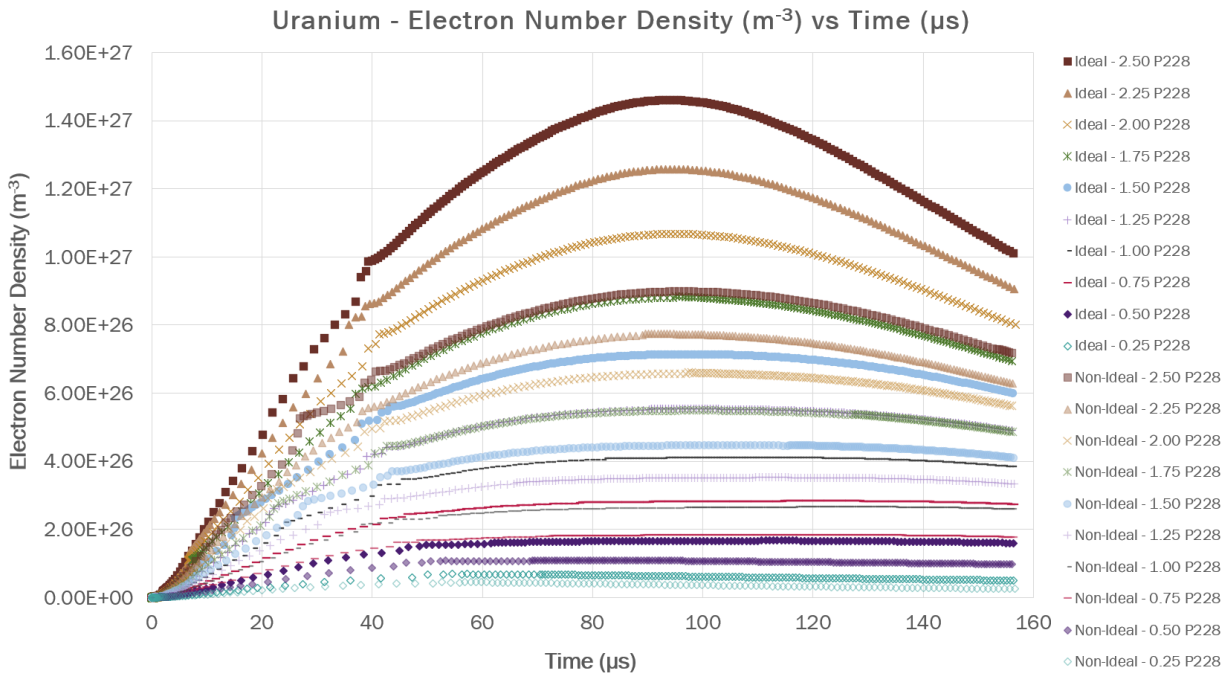

Figure 3.20: Uranium Electron Number Density (m^{-3}) versus Time (μs) as generated by ETFLOW

3.4.7 Pure Material - Zirconium

Commonly used in reactor fuel cladding, Zirconium was selected as part of this study as it was a component of the TZM Alloy that was simulated in the first round of simulations. As such, it was determined that simulations of the material were necessary as this was a material that had not been previously simulated. As before, two sets of 10 runs were performed using both Conductivity models available in the ETFLOW program; select results from these runs are found in Tables 3.13 and 3.14.

Table 3.13 features the peak data for the Heat Flux, q" (GW/m^2), Temperature, T_{peak} (eV), and Electron Number Density, N_E (m^{-3}), as well as the Total Mass Loss due to Ablation, M_{tot} (mg) for the 10 simulations performed using the Ideal Conductivity Model in ETFLOW. It should be noted that the Total Ablated Mass values were calculated by ETFLOW and were not the maximum value from the data set. The Zirconium values for the mass lost to ablation were the second lost out of all of the Pure Materials for the Ideal simulations. The simulated values for Peak Temperature were similar to those of Titanium, as well, being lower than other Pure Materials with the Electron Number Density values being, once again,

some of the highest in the study as a generalized observation.

The peak Heat Flux, Temperature, and Electron Number Density and Total Ablated Mass values in Table 3.14 were calculated using the Non-Ideal Conductivity Model in ETFLOW. As with the Ideal simulations, the Total Mass Loss values calculated with the Non-Ideal Conductivity model had the second lowest values of the Pure Materials investigated. These values were, as expected of the Non-Ideal Conductivity model, lower than their Ideal Conductivity model equivalent for the same P228 discharge current profiles.

Table 3.13: ETFLOW Simulations of Pure Zirconium - Ideal Cases

Ideal Cases				
I (kA)	q" (GW/m^2)	T_{peak} (eV)	N_E (m^{-3})	M_{tot} (mg)
2.50	394.1	3.338	1.127×10^{27}	0.802
2.25	319.0	3.133	9.878×10^{26}	0.712
2.00	252.2	3.040	8.514×10^{26}	0.626
1.75	193.0	2.906	7.203×10^{26}	0.542
1.50	141.9	2.763	5.921×10^{26}	0.459
1.25	98.53	2.603	4.706×10^{26}	0.378
1.00	63.04	2.426	3.570×10^{26}	0.299
0.75	35.40	2.218	2.497×10^{26}	0.221
0.50	15.73	1.953	1.477×10^{26}	0.142
0.25	3.936	1.565	5.568×10^{25}	0.063

Table 3.14: ETFLOW Simulations of Pure Zirconium - Non-Ideal Cases

Non-Ideal Cases				
I (kA)	q" (GW/m^2)	T_{peak} (eV)	N_E (m^{-3})	M_{tot} (mg)
2.50	394.0	2.945	7.327×10^{26}	0.552
2.25	319.3	2.852	6.408×10^{26}	0.493
2.00	252.2	2.736	5.534×10^{26}	0.436
1.75	193.1	2.620	4.694×10^{26}	0.379
1.50	141.8	2.501	3.889×10^{26}	0.323
1.25	98.37	2.355	3.101×10^{26}	0.267
1.00	63.01	2.201	2.367×10^{26}	0.212
0.75	35.46	2.005	1.649×10^{26}	0.156
0.50	15.77	1.767	9.541×10^{25}	0.099
0.25	3.940	1.441	3.683×10^{25}	0.044

Figures 3.21 and 3.22 are the Zirconium Temperature and Electron Number Density plots. Figure 3.21 depicts the ETFLOW generated Temperature data, converted from K to eV, as a function of Time (μs). Total shot time for each of the simulations does not exceed 160 μs, averaging around 156 μs in length. Peaks are reached between 10 and 40 μs and artifacting can be seen on some of the higher current simulations, such as the Ideal simulation using the 2.50 $\times$ P228 discharge current profile. Overall, it was also this same current profile that has the highest peak values for both conductivity models, reaching 3.338 and 2.945 eV for the Ideal and Non-Ideal models, respectively.

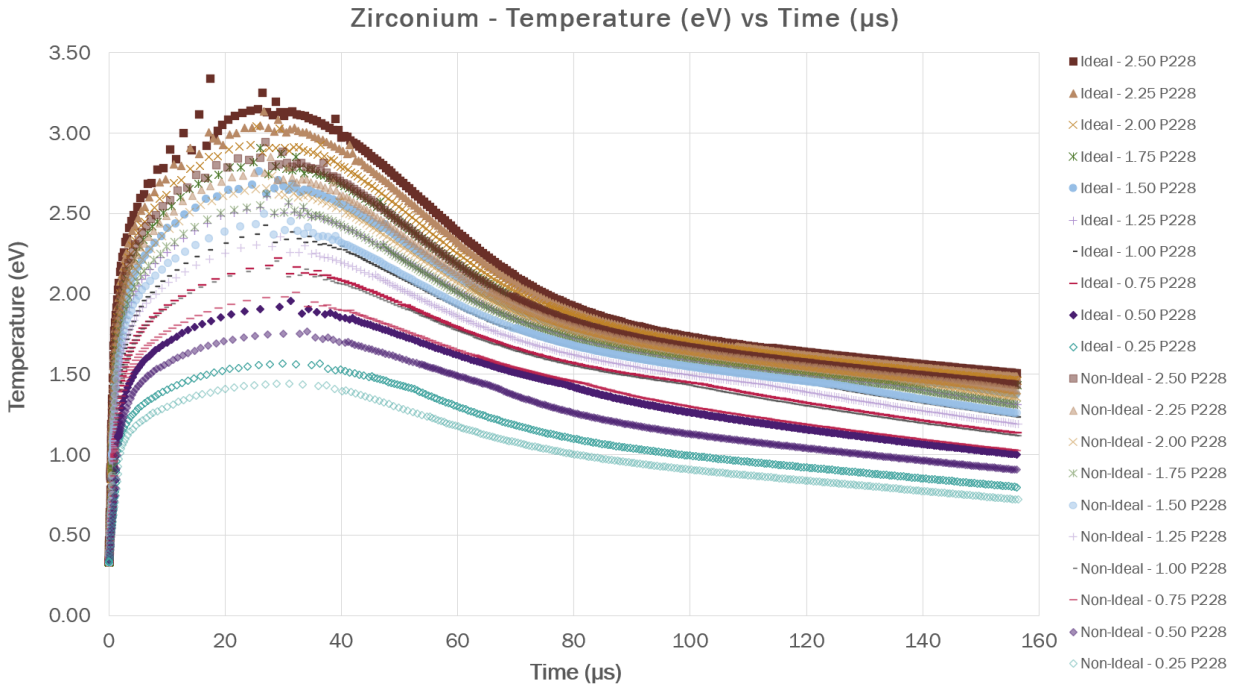

Figure 3.21: Zirconium Temperature (eV) versus Time (μs) as generated by ETFLOW

The Electron Number Density data, (m^{-3}), produced by ETFLOW is plotted as a function of Time, (μs), in Figure 3.22. As seen in the Temperature plot, shot times do not exceed 160 μs, averaging around 156 μs; the point at which the simulation peak occurs, however, is shifted right to between 40 and 80 μs. The artifacting that was seen in Figure 3.21 as a straight line to the left of the peak is reflected in this plot as a wobble in the left ascension of the peak for the 2.50 $\times$ P228 Ideal simulation. This artifacting does not affect the overall peak value as this simulation did present the highest peak Electron Number Density value of the set at 1.127×10^{27}. The same simulation using the Non-Ideal Conductivity Model generated a peak value of 7.327×10^{26}, the highest of the Non-Ideal set.

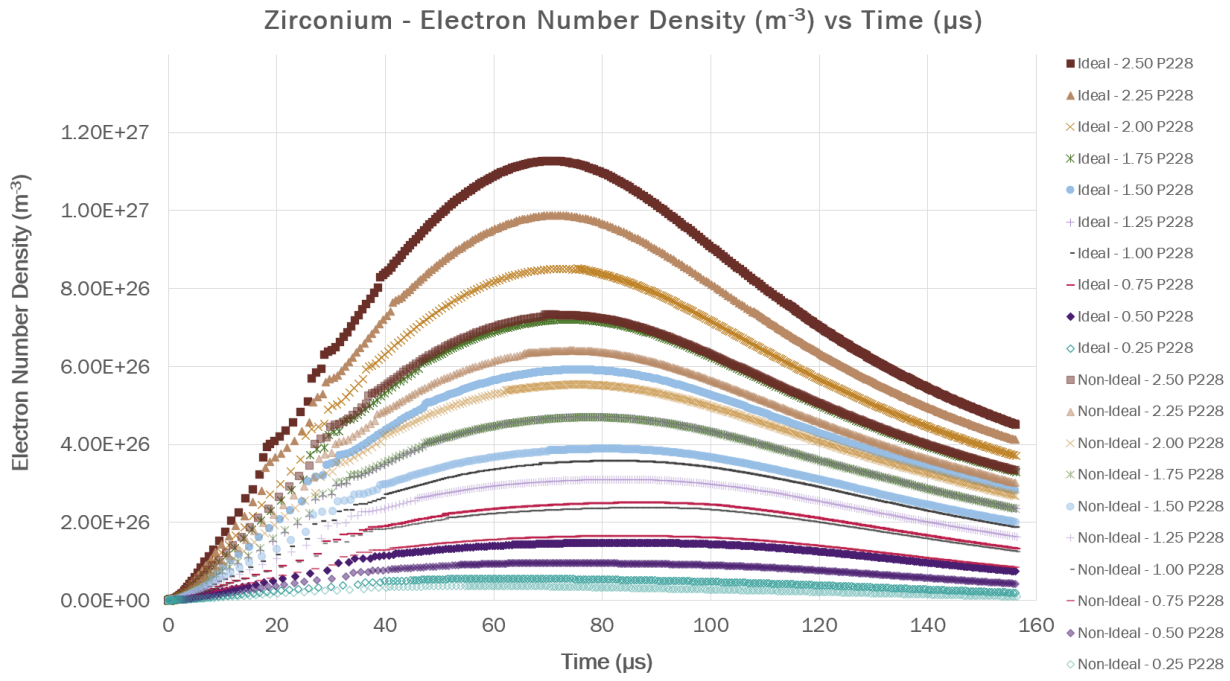

Figure 3.22: Zirconium Electron Number Density (m^{-3}) versus Time (μs) as generated by ETFLOW

3.4.8 TZM Alloy

TZM, or Titanium-Zirconium-Molybdenum, alloy is a metal alloy that had yet to be simulated in ETFLOW. Plasma formation data on TZM is valuable to not only the material science community, but also the aerospace industry as well as this is a commonly used material in the manufacturing of certain aircraft parts. Consequently, a custom material entry was made for the ETFLOW library and then simulated in Ideal and Non-Ideal conditions to obtain the reference data.

Tables 3.15 and 3.16 contain the Ideal and Non-Ideal data from the simulations that were performed in ETFLOW. In general, the values of the heat flux (GW/m^2), peak temperature (eV), peak electron number density (m^{-3}), and total ablated mass (mg) were significantly lower than other materials simulated in this body of work. Particularly of note is the lack of mass that was ablated in both the Ideal and Non-Ideal simulations – the highest amount in each case occurred in the 2.50 P228 simulation, resulting in total ablated mass losses of 0.33900 mg and 0.23811 mg, respectively. The Non-Ideal heat flux values that are higher than their Ideal counterparts are 1.50 and 1.25 P228.

Table 3.15: ETFLOW Simulations of TZM Alloy - Ideal Cases

Ideal Cases				
I (kA)	q" (GW/m^2)	T_{peak} (eV)	N_E (m^{-3})	M_{tot} (mg)
2.50	394.2	2.517	1.149×10^{27}	0.339
2.25	319.3	2.441	1.022×10^{27}	0.305
2.00	252.3	2.361	8.987×10^{26}	0.271
1.75	193.1	2.270	7.772×10^{26}	0.236
1.50	141.9	2.178	6.592×10^{26}	0.201
1.25	98.54	2.081	5.447×10^{26}	0.167
1.00	63.07	1.961	4.282×10^{26}	0.131
0.75	35.47	1.820	3.059×10^{26}	0.094
0.50	15.77	1.641	1.820×10^{26}	0.057
0.25	3.942	1.374	6.771×10^{25}	0.022

Table 3.16: ETFLOW Simulations of TZM Alloy - Non-Ideal Cases

Non-Ideal Cases				
I (kA)	q" (GW/m^2)	T_{peak} (eV)	N_E (m^{-3})	M_{tot} (mg)
2.50	394.1	2.280	7.814×10^{26}	0.238
2.25	319.3	2.226	6.968×10^{26}	0.214
2.00	252.3	2.150	6.178×10^{26}	0.190
1.75	193.1	2.078	5.378×10^{26}	0.165
1.50	141.9	2.000	4.586×10^{26}	0.140
1.25	98.54	1.913	3.751×10^{26}	0.115
1.00	63.07	1.808	2.893×10^{26}	0.090
0.75	35.47	1.699	2.032×10^{26}	0.064
0.50	15.77	1.535	1.187×10^{26}	0.038
0.25	3.940	1.282	4.358×10^{25}	0.013

Looking to Figures 3.23 and 3.24, it should be noted that these plots are much smoother than those for the other materials and this is due to the shear number of data points that were generated during each simulation. On average, each simulation generates between 250 to 450 individual data points depending on the current profile and the model that was being used for that simulation; the simulations for the TZM alloy generated between 850 and 1300 data points on average, leading to a much smoother curve. The reason for more point generation is the result of the number of ionization energies that were included for this material's library entry – this material was the only one to have five ionization energies while the others only had two, the minimum needed to successfully run in ETFLOW. This resulted in more computations being performed per current profile, and thus, more information being

generated during each run.

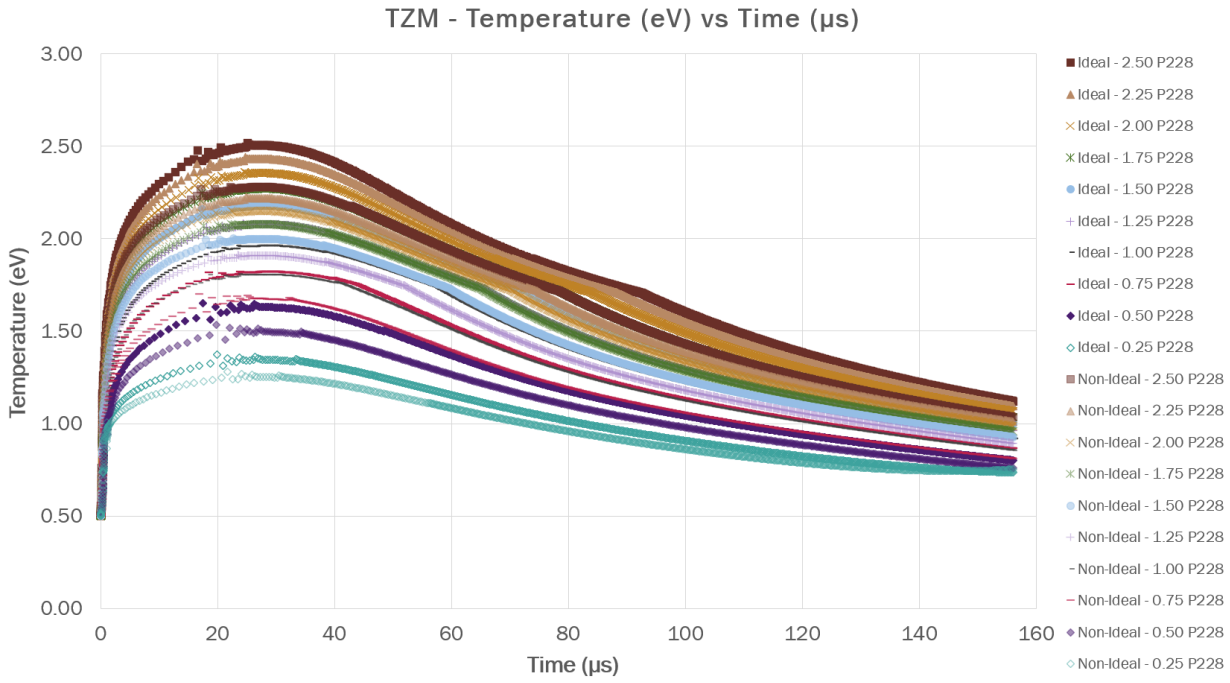

Figure 3.23: TZM Alloy Temperature (eV) versus Time (μs) as generated by ETFLOW

Figure 3.23 presents the Ideal and Non-Ideal temperature (eV) data as a function of time (μs) for the TZM alloy. There is some slight bobbling between 20 and 30 μs, just before the peak of all temperature profiles in all simulations performed and again, in some of the higher current Ideal cases at around 90 μs. The curves are much closer together than for other materials, however, the Ideal simulations still have the highest overall temperatures throughout the during of the shot. The highest temperatures were seen in the Ideal 2.50 P228 case, with a peak temperature of 2.5170 eV. The highest peak temperature seen in Non-Ideal cases was also for the 2.50 P228 case, which had a value of 2.2799 eV.

Figure 3.24 displays the electron number density (m^{-3}) data per unit time (μs) for the Ideal and Non-Ideal simulations. The computational bobbling that was seen in Figure 3.23 between 20 and 30 μs appears in this figure as well, across all simulation curves. The peaks occur just before 60 μs for all cases, with the highest peak occurring for the Ideal 2.50 P228 case, which had a value of 1.1490×10^{27} m^{-3}. The highest peak value for Non-Ideal simulations occurred during the 2.50 P228 simulation and was 7.8139×10^{26} m^{-3}, significantly lower than its Ideal simulation counterpart.

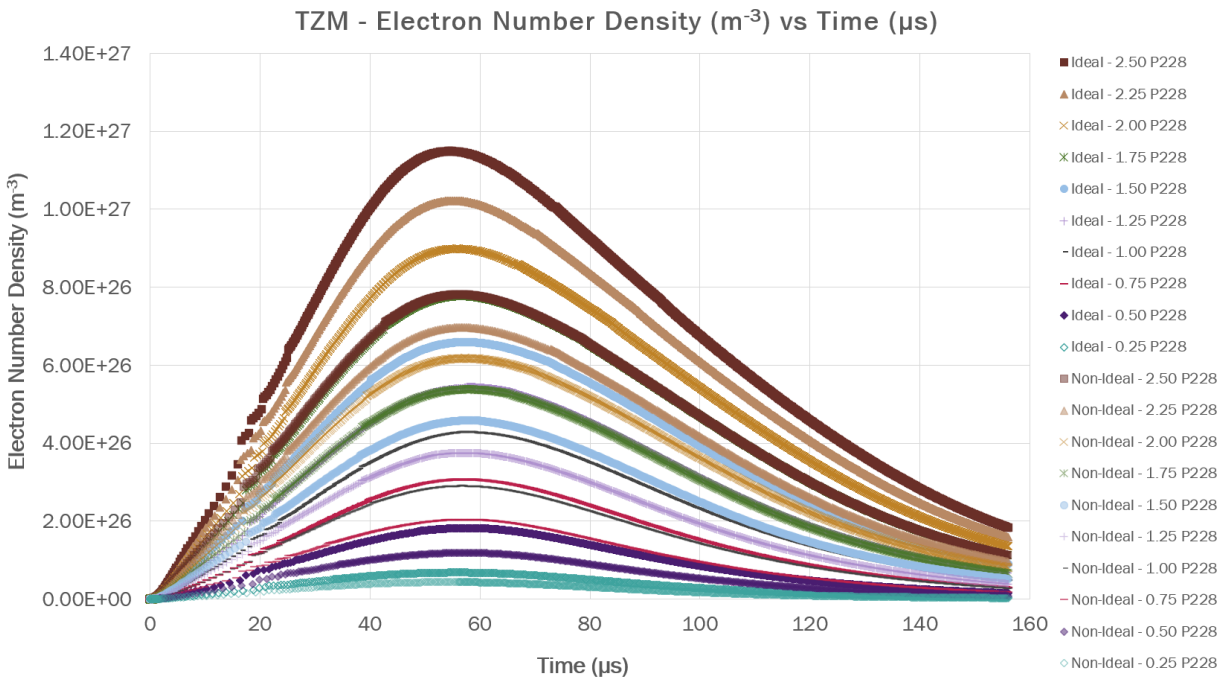

Figure 3.24: TZM Alloy Electron Number Density (m^{-3}) versus Time (μs) as generated by ETFLOW

3.5 W-Mo Alloys

The custom Tungsten-Molybdenum alloy simulations were split into two categories – one set that mimicked the concentrations of Uranium and Molybdenum in the Godiva IV section of simulations and a set that mimicked various reactor fuel enrichments. The results for the second set can be found in Appendix A.1. The main result that can be gleaned from varying that amount of Tungsten in the alloy is that having a higher Tungsten concentration results in less ablation occurring in the alloy (i.e. lower total ablated mass (mg) and electron number density (m^{-3})) and higher overall peak temperatures (eV) across all currents. This statement applies to both the Ideal and Non-Ideal models.

3.5.1 W-Mo(1.00%) Alloy

The first Tungsten-Molybdenum alloy examined was the W-Mo(1.00%) variant – this version of the alloy had the lowest concentration of Molybdenum by weight, and therefore, the highest amount of Tungsten. As such, per the earlier discussion and as can be seen in Tables 3.17 and 3.18, this material had the lowest amount of ablation out of the alloy set. That is to say,

this material, when simulated, looked the most like Pure Tungsten. This is to be expected since the method by which the material library entry was made was a weight ratio between Tungsten and Molybdenum – as such, an alloy that has higher percentage of Tungsten will have results that are closer to those of Pure Tungsten.

Table 3.17: ETFLOW Simulations of W-Mo(1.00%) Alloy - Ideal Cases

Ideal Cases				
I (kA)	q" (GW/m^2)	T_{peak} (eV)	N_E (m^{-3})	M_{tot} (mg)
2.50	393.6	2.997	1.242×10^{27}	1.625
2.25	318.6	2.894	1.095×10^{27}	1.464
2.00	252.0	2.793	9.494×10^{26}	1.301
1.75	192.6	2.686	8.129×10^{26}	1.139
1.50	141.9	2.556	6.679×10^{26}	0.972
1.25	98.44	2.426	5.244×10^{26}	0.803
1.00	63.03	2.269	3.876×10^{26}	0.629
0.75	35.42	2.096	2.632×10^{26}	0.453
0.50	15.76	1.876	1.489×10^{26}	0.277
0.25	3.932	1.541	5.772×10^{25}	0.110

Tables 3.17 and 3.18 follow the same trends seen in other material simulations in which there is a decrease in plasma parameter value with a decrease in current and, in most cases, have the Non-Ideal simulation values smaller than their Ideal equivalent. There are a few Non-Ideal heat flux (GW/m^2) values that do not follow this pattern – the heat flux values for the 2.50, 2.00, 1.75, 1.25, and 0.75 P228 current profiles.The peak temperature (eV) values across both tables falls within the average range that has been seen in other simulations; this is the same case for the total ablated mass (mg).

Figure 3.25 consists of the Ideal and Non-Ideal temperature (eV) curves per unit time (μs) for W-Mo(1.00%). The plot is consistent with other materials in the simulation set, peaking at around 25 μs. Slight computational artifacting occurs in the higher current Ideal simulations at around 40 μs - this produces the highest value of 2.8422 eV in the 2.50 P228 case. If not for this artifacting, the peak value would be closer to the actual peak of the curve, having a value of 2.9561 eV. The highest value of Non-Ideal simulations occurs in the 2.50 P228 simulation, producing a value of 2.7036 eV.

Figure 3.26 details the electron number density ($m^{-}-3$) as a function of time for the Ideal and Non-Ideal simulations. Between 30 and 45 μs, the artifacting seen in Figure 3.25 can be seen, though it is much more pronounced as there is more separation between the jumps as

Table 3.18: ETFLOW Simulations of W-Mo(1.00%) Alloy - Non-Ideal Cases

Non-Ideal Cases				
I (kA)	q" (GW/m^2)	T_{peak} (eV)	N_E (m^{-3})	M_{tot} (mg)
2.50	392.7	2.703	8.262×10^{26}	1.157
2.25	318.0	2.620	7.263×10^{26}	1.041
2.00	252.0	2.528	6.236×10^{26}	0.923
1.75	192.9	2.430	5.236×10^{26}	0.804
1.50	141.8	2.326	4.272×10^{26}	0.682
1.25	98.46	2.210	3.366×10^{26}	0.559
1.00	63.03	2.082	2.513×10^{26}	0.435
0.75	35.43	1.929	1.700×10^{26}	0.310
0.50	15.68	1.735	9.944×10^{25}	0.190
0.25	3.910	1.424	3.744×10^{25}	0.072

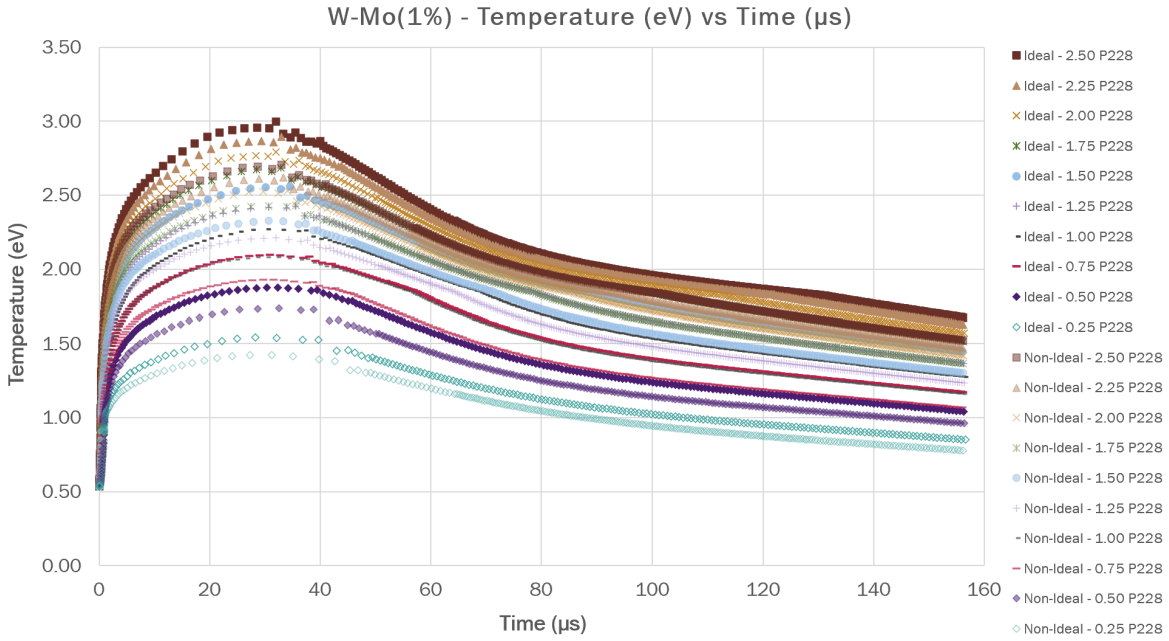

Figure 3.25: W-Mo(1.00%) Temperature (eV) versus Time (μs) as generated by ETFLOW

the values of electron number density increase. These artifacts do not, however, impact the peak values for each simulation. The highest value recorded can be, once again, attributed to the Ideal 2.50 P228 case, which had a value of $1.2421 \times 10^{27}\ m^{-3}$. The highest value recorded for Non-Ideal simulations was for the same case, 2.50 P228, and had a recorded value of $8.2623 \times 10^{26}\ m^{-3}$.

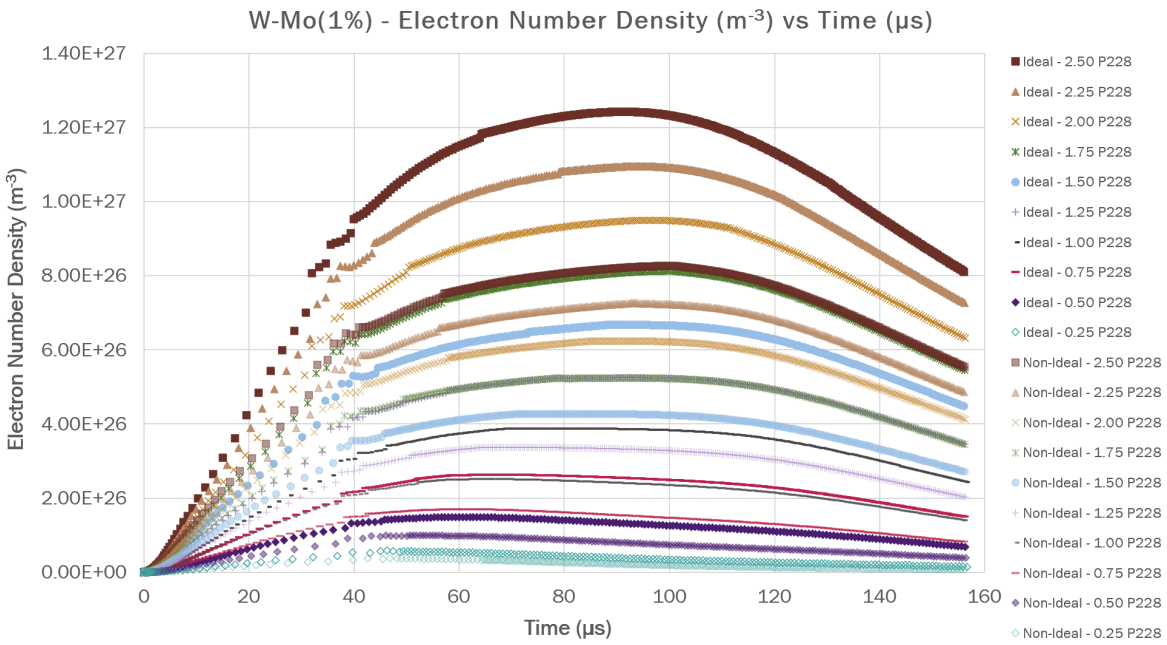

Figure 3.26: W-Mo(1.00%) Electron Number Density (m^{-3}) versus Time (μs) as generated by ETFLOW

3.5.2 W-Mo(1.25%) Alloy

The second Tungsten-Molybdenum alloy to be simulated was W-Mo(1.25%). This alloy was created by simply increasing the concentration of Molybdenum by 0.25% and re-performing the calculations for the material properties. As this was material was not that much different from the first alloy, it was expected that the plasma parameters generated in each model would not be that dissimilar from those of the preceding simulations. This assumption was proven to be correct, as can be seen in Tables 3.19 and 3.20.

Table 3.19 contains the Ideal simulation data for the W-Mo(1.25%) alloy. The results from this set of simulations were very similar to the previous simulation set for W-Mo(1.00%), with values only changing in the fourth decimal place between the two sets, though given how the values are rounded, this minor difference may not be shown. The trend of decreasing values with current still exists with the Non-Ideal simulation values being smaller than their Ideal simulation counterparts with the exception of a few heat flux (GW/m^2) values – 2.50, 2.00, 1.75, 1.25, and 0.75 P228. It should also be noted that the heat flux values for both the Ideal and Non-Ideal simulations are the same as the previous set – this is due to the change in Molybdenum concentration being so small. Table 3.20 entails the Non-Ideal simulation

data for the W-Mo(1.25%) alloy. As with the Ideal simulation results, the 1.25% Non-Ideal simulation results were quite close to those from the 1.00% simulations, with the differences in the two materials' parameters occurring in the fourth decimal place. Values in for these simulations are, while closer to the Non-Ideal Tungsten simulation values than Molybdenum, are still higher than the two sets. This was also the case for the Ideal results.

Table 3.19: ETFLOW Simulations of W-Mo(1.25%) Alloy - Ideal Cases

Ideal Cases				
I (kA)	q" (GW/m^2)	T_{peak} (eV)	N_E (m^{-3})	M_{tot} (mg)
2.50	393.3	2.996	1.242×10^{27}	1.625
2.25	318.6	2.893	1.095×10^{27}	1.464
2.00	252.0	2.793	9.495×10^{26}	1.301
1.75	192.6	2.686	8.131×10^{26}	1.139
1.50	141.9	2.556	6.680×10^{26}	0.972
1.25	98.44	2.426	5.245×10^{26}	0.803
1.00	63.03	2.269	3.877×10^{26}	0.629
0.75	35.42	2.096	2.633×10^{26}	0.453
0.50	15.76	1.876	1.490×10^{26}	0.277
0.25	3.932	1.541	5.774×10^{25}	0.111

Table 3.20: ETFLOW Simulations of W-Mo(1.25%) Alloy - Non-Ideal Cases

Non-Ideal Cases				
I (kA)	q" (GW/m^2)	T_{peak} (eV)	N_E (m^{-3})	M_{tot} (mg)
2.50	392.7	2.703	8.623×10^{26}	1.158
2.25	318.0	2.620	7.264×10^{26}	1.041
2.00	252.0	2.527	6.238×10^{26}	0.923
1.75	192.9	2.430	5.237×10^{26}	0.804
1.50	141.8	2.326	4.273×10^{26}	0.682
1.25	98.46	2.210	3.367×10^{26}	0.559
1.00	63.03	2.082	2.513×10^{26}	0.436
0.75	35.43	1.929	1.700×10^{26}	0.310
0.50	15.68	1.735	9.947×10^{25}	0.190
0.25	3.910	1.424	3.745×10^{25}	0.072

Figure 3.27 delineates the temperature (eV) data as a function of time (μs) for both the Ideal and Non-Ideal models of the ETFLOW simulations performed for the W-Mo(1.25%) alloy. The peak for all of the curves, regardless of model, occurs around 30 μs. The highest temperatures occurred during the Ideal model simulations, with the peak occurring during

the 2.50 P228 simulation being the highest value at 2.9962 eV. This value, however, is due to computational artifacting, as is common in this set of simulations and is shifted to the right at 30 μs. The true peak value would, thus, be 2.9953 eV at 30 μs. The Non-Ideal 2.50 P228 simulation has a peak value of 2.6113 eV at around 30 μs when the artifacting that is seen at 35 μs is accounted for. While some artifacting did occur, the curves for temperature profile were as expected for an ETFLOW simulation.

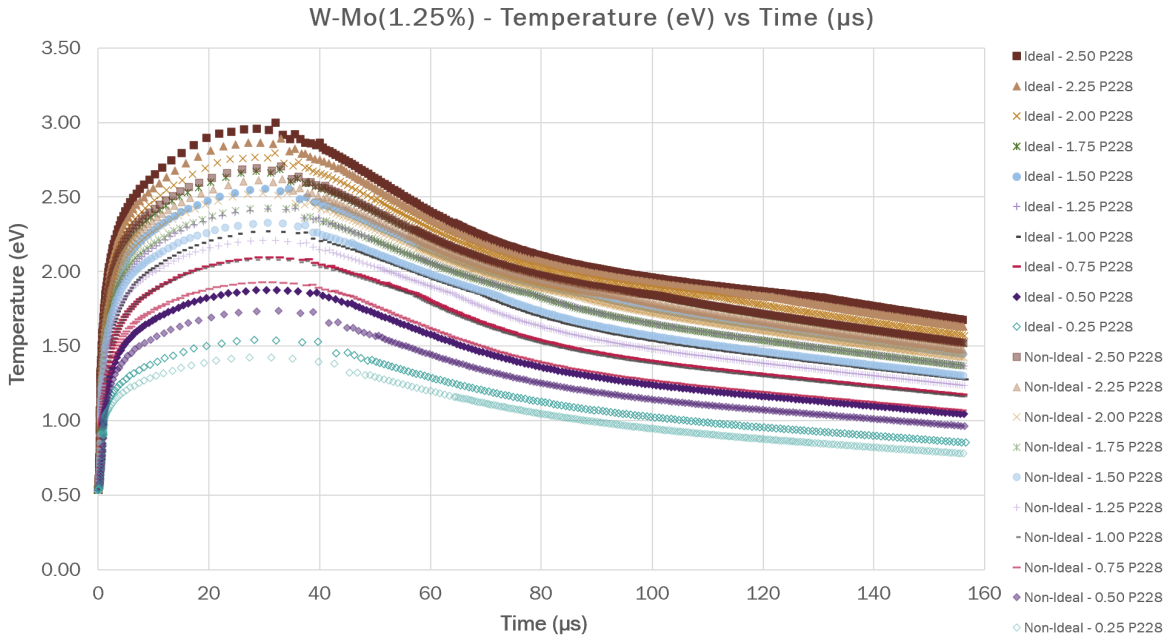

Figure 3.27: W-Mo(1.25%) Temperature (eV) versus Time (μs) as generated by ETFLOW

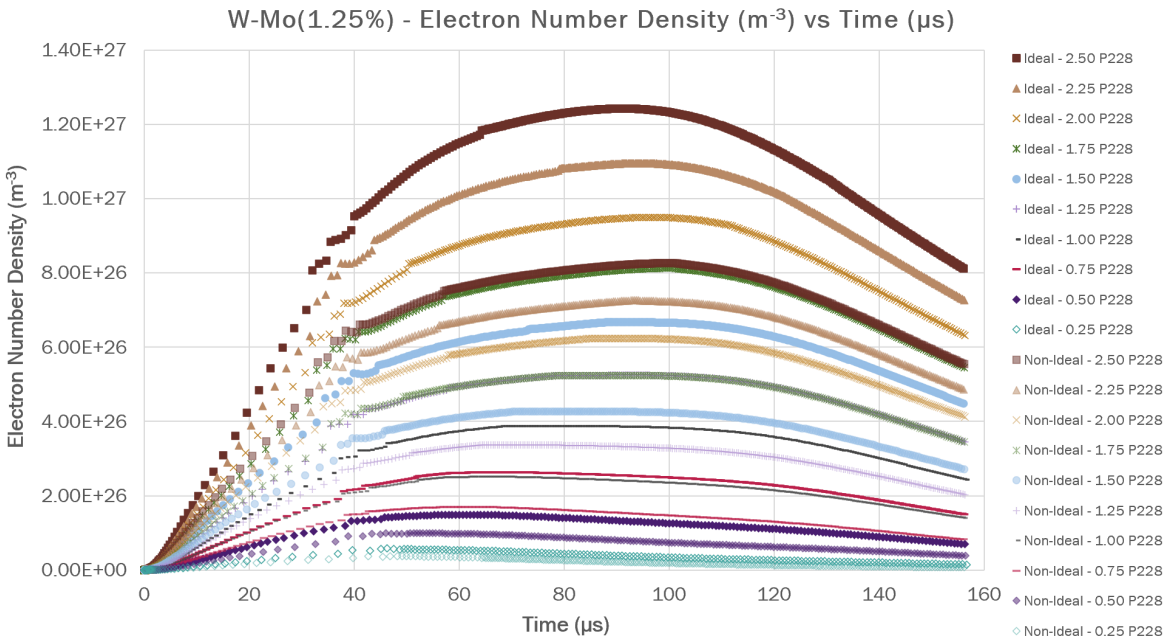

Figure 3.28: W-Mo(1.25%) Electron Number Density (m^{-3}) versus Time (μs) as generated by ETFLOW

Figure 3.28 is the plot of all electron number density (m^{-3}) data as a function of time (μs) for the Ideal and Non-Ideal model simulations of W-Mo(1.25%) performed using ETFLOW. There was some computational artifacting around 40 μs in which a "stepping" feature occurred as the curve made some quick jumps up in number density. These steps were particularly apparent in the higher current Ideal simulations. Unlike the peak temperature, which these steps can be directly linked to, this computational bobbling did not affect the overall peak of the curve as the electron number density did not peak until around 90 μs for all simulations. The highest peak value recorded was for the 2.50 P228 Ideal simulation, which had a peak electron number density of $1.2422 \times 10^{27}\ m^{-3}$. The highest peak value for Non-Ideal simulations occurred for the same current simulation, 2.50 P228, and had a value of $8.2628 \times 10^{26}\ m^{-3}$.

3.5.3 W-Mo(1.50%) Alloy

The third Tungsten-Molybdenum alloy examined in the set was the direct analogue to Godiva IV: W-Mo(1.50%). This alloy had the same weight ratio of Molybdenum to Tungsten as Godiva IV does with Molybdenum to Highly Enriched Uranium. The theory was that the two materials would simulate similarly – which ever material in the alloy had the highest

concentration would cause the plasma parameters to lean towards that one more heavily, as has been seen in the alloy results with more Tungsten thus far. Additionally, acquisition of a Tungsten-Molybdenum alloy sample with these specifications for testing and later comparison against computational results is a much easier feat than attempting acquire a sample of Uranium-Molybdenum alloy to specification. As such, simulation of this particular alloy was highly needed.

Tables 3.21 and 3.22 are the collection of peak data from the Ideal and Non-Ideal simulations of W-Mo(1.50%). As stated in Section 3.5.2, the heat flux (GW/m^2) values did not change with the increase in Molybdenum concentration. As such, the same values of Non-Ideal heat flux that were larger than their Ideal equivalents were also the same: 2.50, 2.00, 1.75, 1.25, and 0.75 P228. The trend of decreasing temperature (eV), electron number density (m^{-3}), and total ablated mass (mg) with decreasing current multiplier value is still seen in both sets of simulations.

The temperature, electron number density, and total ablated mass values in Table 3.21 are quite consistent with the other Ideal simulation values of this alloy set. In fact, when rounded to three decimal places, the peak temperature values for W-Mo(1.50%) are the same as the peak temperature values for W-Mo(1.75%) and W-Mo(2.00%) (*see Tables 3.23 and 3.25*). The electron number density and total ablated mass are on par with the other Ideal simulations as well, being towards the middle of the bounds set by the W-Mo(1.00%) and W-Mo(2.00%) simulations. There is an increase in these two values, however, it is in the fourth decimal place and therefore does not show up in the tables.

Table 3.21: ETFLOW Simulations of W-Mo(1.50%) Alloy - Ideal Cases

Ideal Cases				
I (kA)	q" (GW/m^2)	T_{peak} (eV)	N_E (m^{-3})	M_{tot} (mg)
2.50	393.6	2.996	1.242×10^{27}	1.625
2.25	318.6	2.893	1.095×10^{27}	1.464
2.00	252.0	2.793	9.497×10^{26}	1.301
1.75	192.6	2.685	8.133×10^{26}	1.139
1.50	141.9	2.555	6.681×10^{26}	0.972
1.25	98.44	2.426	5.246×10^{26}	0.803
1.00	63.03	2.268	3.878×10^{26}	0.629
0.75	35.42	2.096	2.633×10^{26}	0.453
0.50	15.76	1.876	1.490×10^{26}	0.277
0.25	3.932	1.540	5.776×10^{25}	0.111

The Non-Ideal simulation values in Table 3.22 portray a similar story to those in Table 3.21. Generated values of temperature, electron number density, and total ablated mass are in line with other Non-Ideal simulations of this alloy set. There is an increase in the total ablated mass and electron number density, however, as seen in the Ideal simulations, these increases are in fourth and fifth decimal places, therefore making the values appear virtually the same across current Molybdenum concentration increases when looking at each current profile individually. The same "micro-increases" occur in the temperature data as well.

Table 3.22: ETFLOW Simulations of W-Mo(1.50%) Alloy - Non-Ideal Cases

Non-Ideal Cases				
I (kA)	q" (GW/m^2)	T_{peak} (eV)	N_E (m^{-3})	M_{tot} (mg)
2.50	392.7	2.703	8.263×10^{26}	1.158
2.25	318.0	2.620	7.264×10^{26}	1.041
2.00	252.0	2.527	6.239×10^{26}	0.923
1.75	192.9	2.430	5.239×10^{26}	0.804
1.50	141.8	2.326	4.274×10^{26}	0.682
1.25	98.46	2.210	3.368×10^{26}	0.560
1.00	63.03	2.081	2.514×10^{26}	0.436
0.75	35.43	1.929	1.701×10^{26}	0.310
0.50	15.68	1.735	9.950×10^{25}	0.190
0.25	3.910	1.424	3.747×10^{25}	0.072

In Figure 3.29, temperature data (eV) is plotted against time (μs) for both the Ideal and Non-Ideal simulations of W-Mo(1.50%). As seen in other temperature plots in this alloy set, there is computational artifacting in the higher current simulation temperature curves with little to no artifacting occurring in the lower current simulations. The peak of all of the temperature plots occurs around 30 μs, with the artifacting occurring slightly after this peak. The highest peak temperature value recorded was for the Ideal 2.50 P228 simulation and was 2.9959 eV. The highest recorded peak temperature value for Non-Ideal simulations was 2.7031 eV for the same current profile.

Figure 3.30 presents the electron number density data (m^{-3}) as a function of time (μs) in graphical form for the Ideal and Non-Ideal simulations of W-Mo(1.50%). The artifacting seen in the temperature plot can be seen occurring between 30 and 40 μs, however, it is not allocated to just the higher current simulations as with just the temperature. Unlike the temperature, where the artifacting may or may not affect the resulting peak value, this artifacting does not, as the peak for all electron number density curves occurs much

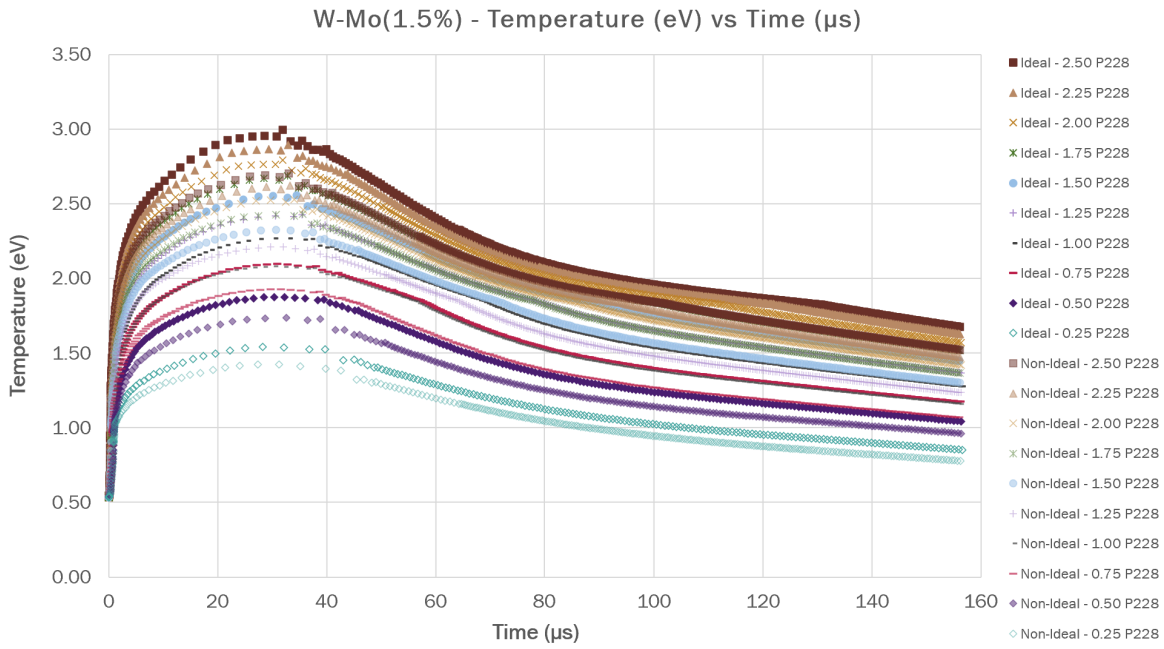

Figure 3.29: W-Mo(1.50%) Temperature (eV) versus Time (μs) as generated by ETFLOW

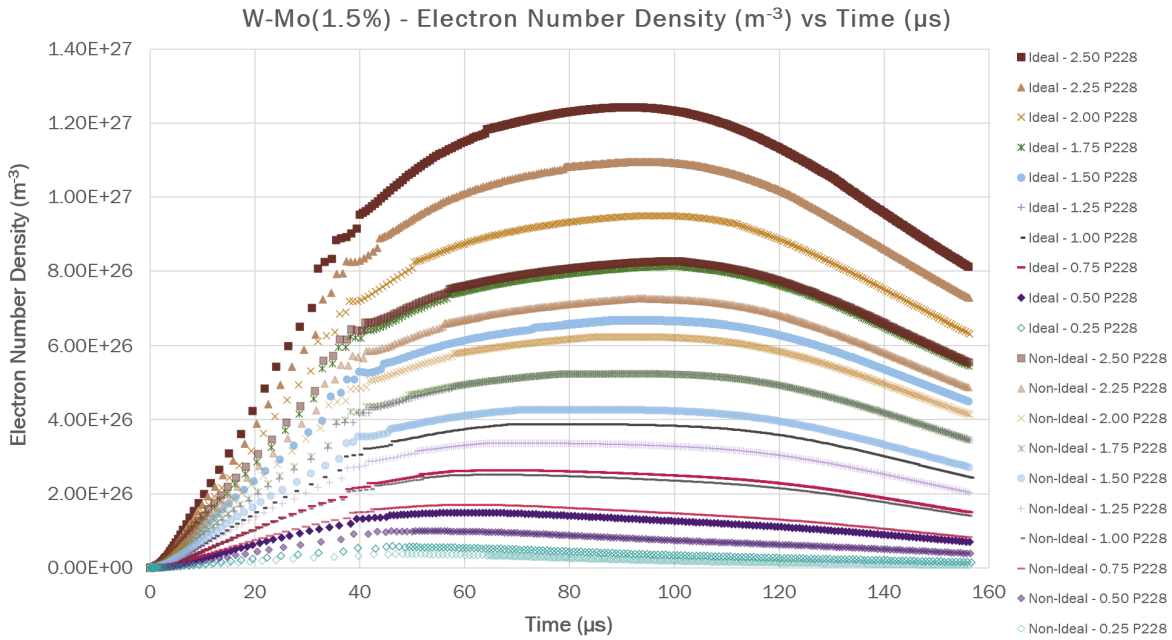

Figure 3.30: W-Mo(1.50%) Electron Number Density (m^{-3}) versus Time (μs) as generated by ETFLOW

later, at around 90 μs. Once again, the highest electron number density occurs in the Ideal simulation with the highest current, 2.50 P228, and peaked at $1.2424 \times 10^{27}\ m^{-3}$. The highest Non-Ideal electron number density also occurred during the 2.50 P228 simulation and peaked at $8.2629 \times 10^{26}\ m^{-3}$.

3.5.4 W-Mo(1.75%) Alloy

The fourth Tungsten-Molybdenum alloy computationally examined was W-Mo(1.75%). This alloy had 0.25% more Molybdenum by weight in it than the Godiva IV analogue, making it one of the two "top end" W-Mo alloys investigated. Top end in this case simply refers to alloys that have concentrations of Molybdenum above the 1.50% that is present in the Godiva IV "control."

Table 3.23 contains the select peak data for the plasma parameters generated using the Ideal model in ETFLOW. The general trend was such that a decrease in current resulted in a decrease in the values of heat flux (GW/m^2), temperature (eV), electron number density (m^{-3}), and total ablated mass (mg). As with the three previous alloys in the set, the heat flux values did not change with the increase in Molybdenum concentration. The same set of heat flux values were not larger than their Non-Ideal counterparts, as the Non-Ideal heat flux did not change as well. Once again, these values were for the 2.50, 2.00, 1.75, 1.25, and 0.75 P228 current profiles.

Table 3.23: ETFLOW Simulations of W-Mo(1.75%) Alloy - Ideal Cases

Ideal Cases				
I (kA)	q" (GW/m^2)	T_{peak} (eV)	N_E (m^{-3})	M_{tot} (mg)
2.50	393.6	2.996	1.243×10^{27}	1.625
2.25	318.6	2.893	1.095×10^{27}	1.464
2.00	252.0	2.792	9.498×10^{26}	1.301
1.75	192.9	2.685	8.135×10^{26}	1.139
1.50	141.9	2.555	6.683×10^{26}	0.972
1.25	98.44	2.425	5.247×10^{26}	0.803
1.00	63.03	2.268	3.879×10^{26}	0.629
0.75	35.42	2.096	2.634×10^{26}	0.454
0.50	15.74	1.876	1.491×10^{26}	0.277
0.25	3.932	1.540	5.778×10^{25}	0.111

Table 3.24 is comprised of the select peak data for plasma parameters generated using the Non-Ideal model in ETFLOW. The heat flux (GW/m^2), temperature (eV), electron number

density (m^{-3}), and total ablated mass (mg) values generated using the Non-Ideal model follow the trend of decreasing with decreasing current (kA). As previously stated, the heat flux values did not change and are the same as other alloys in this set when looking at their Non-Ideal simulations. The values of temperature are steadily decreasing in the fourth decimal place, which may not be reflected in the table. The values for the electron number density and total ablation are increasing, suggesting that more ionization is occurring in the material and, thus, ablation of the material.

Table 3.24: ETFLOW Simulations of W-Mo(1.75%) Alloy - Non-Ideal Cases

Non-Ideal Cases				
I (kA)	q" (GW/m^2)	T_{peak} (eV)	N_E (m^{-3})	M_{tot} (mg)
2.50	392.7	2.703	8.264×10^{26}	1.158
2.25	318.0	2.619	7.265×10^{26}	1.042
2.00	252.0	2.527	6.240×10^{26}	0.924
1.75	192.9	2.430	5.240×10^{26}	0.804
1.50	141.8	2.326	4.275×10^{26}	0.682
1.25	98.29	2.211	3.370×10^{26}	0.560
1.00	62.03	2.081	2.514×10^{26}	0.436
0.75	35.43	1.929	1.701×10^{26}	0.310
0.50	15.74	1.737	1.021×10^{26}	0.190
0.25	3.910	1.424	3.748×10^{25}	0.072

Represented in Figure 3.31 is the plot of temperature (eV) data as a function of time (μs) for the Ideal and Non-Ideal ETFLOW simulations performed for W-Mo(1.75%). The temperature curves all have their peaks around the expected 30 μs, with the Ideal simulations having the highest overall temperature curves. There is also the expected artifacting at around 35 μs that occurs in the higher current simulations. The highest peak temperature recorded was for the Ideal 2.50 P228 simulation, which had a peak temperature of 2.9956 eV. The highest peak temperature recorded for the Non-Ideal simulations was also for their 2.50 P228 simulation and was noted to be 2.7028 eV.

The diagram in Figure 3.32 presents the electron number density (m^{-3}) data of both the Ideal and Non-Ideal simulations as a function of time (μs). Between 20 and 40 μs is the expected computational bobbling that occurs in all simulation profiles. The electron number densities later peak at around 90 μs and are, as usual, unaffected by this artifacting. The Ideal simulations have more ablation occurring, and therefore have a higher overall electron number density per unit time across numerous simulations, which the highest occurring

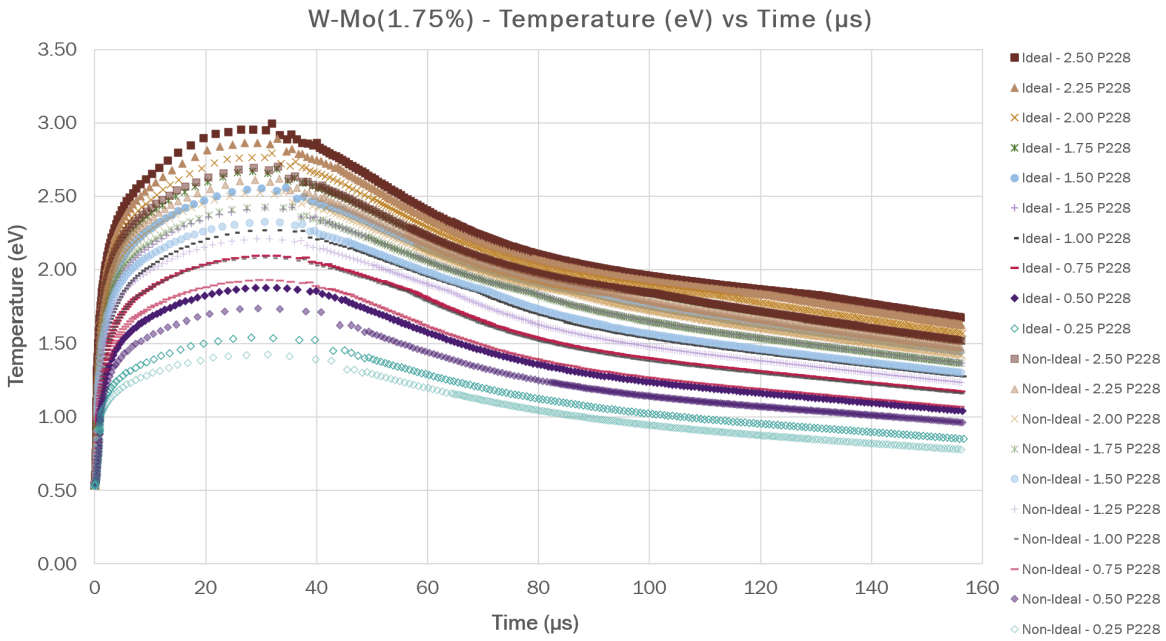

Figure 3.31: W-Mo(1.75%) Temperature (eV) versus Time (μs) as generated by ETFLOW

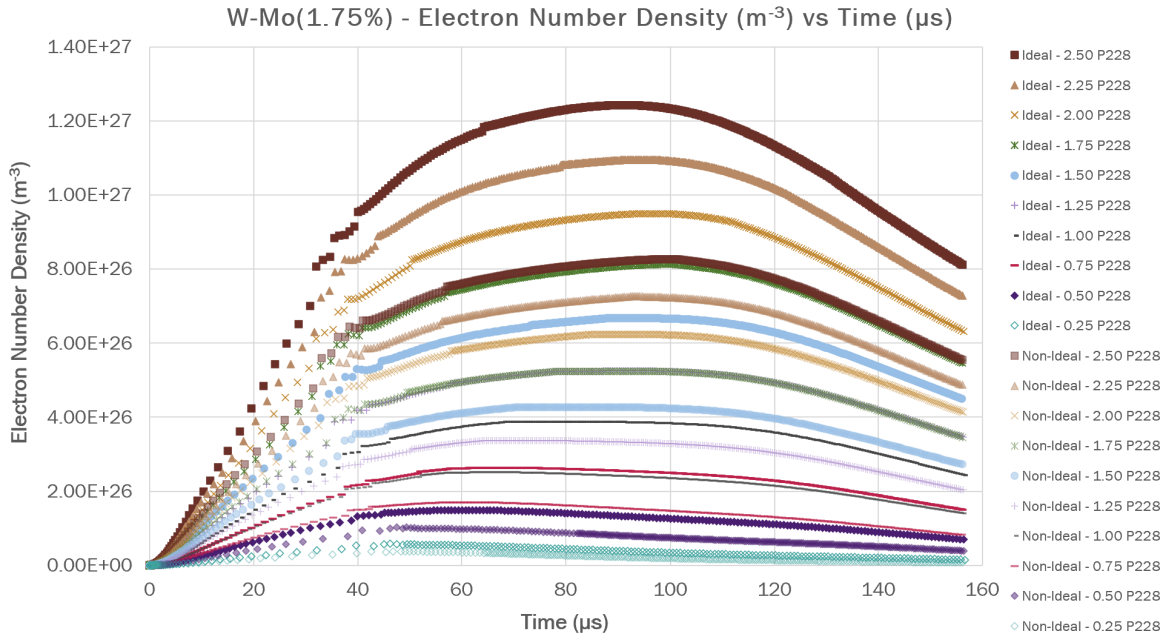

Figure 3.32: W-Mo(1.75%) Electron Number Density (m^{-3}) versus Time (μs) as generated by ETFLOW

during the 2.50 P228 case, having a recorded value of $1.2426 \times 10^{27}\ m^{-3}$. The highest electron number density to occur in Non-Ideal simulations also occurred during the 2.50 P228 case and had a value of $8.2642 \times 10^{26}\ m^{-3}$.

3.5.5 W-Mo(2.00%) Alloy

The fifth and final Tungsten-Molybdenum alloy in the set was W-Mo(2.00%). This alloy had the highest amount of Molybdenum by weight out of all the alloys in the set. As such, this alloy had lowest amount of Tungsten compared to others in the set and would, therefore, behave the least like Pure Tungsten when simulated. However, the alloy was 98.0% Tungsten, so it was not as big of a difference as say, W(3.00%)-Mo, the results of which can be found in Appendix A.1.1.

Table 3.25 contains the Ideal data from the ETFLOW simulations using this model. The values of heat flux (GW/m^2), temperature (eV), electron number density (m^{-3}), and total ablated mass (mg) observe the trend of decreasing with decreasing current. As with the previous alloys in this set, the heat flux values did not change with the increase in Molybdenum concentration – this indicates that, at least for this alloy, it is not sensitive to minor Molybdenum concentration fluctuations of up to 1.00%. The 2.50, 2.00, 1.75, 1.25, and 0.75 P228 set of heat flux values were once again smaller than their Non-Ideal equivalent, as the Non-Ideal heat flux values also did not change with the increase in Molybdenum content. Once again, there is a decrease in the peak temperature values and an increase in the electron number density and total mass ablated as more ionization is occurring thanks to the increase in Molybdenum in the alloy.

Table 3.26 is the collection of peak plasma parameter data for the Non-Ideal ETFLOW simulations of W-Mo(2.00%). As previously mentioned, the heat flux for the Non-Ideal simulations did not change (when rounded to three significant figures) with increasing Molybdenum concentration. Subsequently, this has led to there not being any noticeable variation in the heat flux calculations across all five alloys. The tendency of the temperature (eV), electron number density (m^{-3}), and total ablated mass (mg) to decrease with decreasing current was noted for these simulations, as is expected in ETFLOW simulations. With the increase in Molybdenum content, the general values for the temperature decreased compared to previous alloy simulations, i.e. the peak values for the 2.00% simulations were lower than those of the 1.75% simulations. The increase in Molybdenum concentration also caused more ionization to occur, increasing the electron number density and total ablated mass when

Table 3.25: ETFLOW Simulations of W-Mo(2.00%) Alloy - Ideal Cases

Ideal Cases				
I (kA)	q" (GW/m^2)	T_{peak} (eV)	N_E (m^{-3})	M_{tot} (mg)
2.50	393.6	2.995	1.243×10^{27}	1.625
2.25	318.6	2.892	1.096×10^{27}	1.464
2.00	252.0	2.792	9.500×10^{26}	1.301
1.75	192.6	2.685	8.136×10^{26}	1.139
1.50	141.9	2.555	6.684×10^{26}	0.972
1.25	98.44	2.425	5.249×10^{26}	0.803
1.00	63.03	2.268	3.880×10^{26}	0.629
0.75	35.46	2.095	2.634×10^{26}	0.454
0.50	15.74	1.876	1.491×10^{26}	0.277
0.25	3.932	1.540	5.780×10^{25}	0.111

compared to previous simulations with lower concentrations of Molybdenum.

Table 3.26: ETFLOW Simulations of W-Mo(2.00%) Alloy - Non-Ideal Cases

Non-Ideal Cases				
I (kA)	q" (GW/m^2)	T_{peak} (eV)	N_E (m^{-3})	M_{tot} (mg)
2.50	392.7	2.703	8.265×10^{26}	1.158
2.25	318.0	2.619	7.267×10^{26}	1.042
2.00	251.8	2.529	6.237×10^{26}	0.924
1.75	192.9	2.430	5.241×10^{26}	0.804
1.50	141.8	2.325	4.276×10^{26}	0.682
1.25	98.29	2.211	3.371×10^{26}	0.560
1.00	63.03	2.081	2.515×10^{26}	0.436
0.75	35.43	1.929	1.702×10^{26}	0.311
0.50	15.74	1.737	1.021×10^{26}	0.190
0.25	3.910	1.424	3.749×10^{25}	0.072

Figure 3.33 depicts the temperature (eV) data for both the Ideal and Non-Ideal model simulations of W-Mo(2.00%) as a function of time (μs). This plot has the expected peak at around 30 μs with the secondary artifacting peak at around 35 μs. This artifacting bump is much more apparent in Figure 3.33 across all simulations than it has been in previous simulations in this set. The highest temperature was once again recorded in the Ideal 2.50 P228 simulation and had a peak documented at 2.9953 eV. The highest temperature from a Non-Ideal simulation was recorded during a 2.50 P228 simulation, peaking at 2.7025 eV.

Figure 3.34 presents the electron number density (m^{-3}) for the Ideal and Non-Ideal models

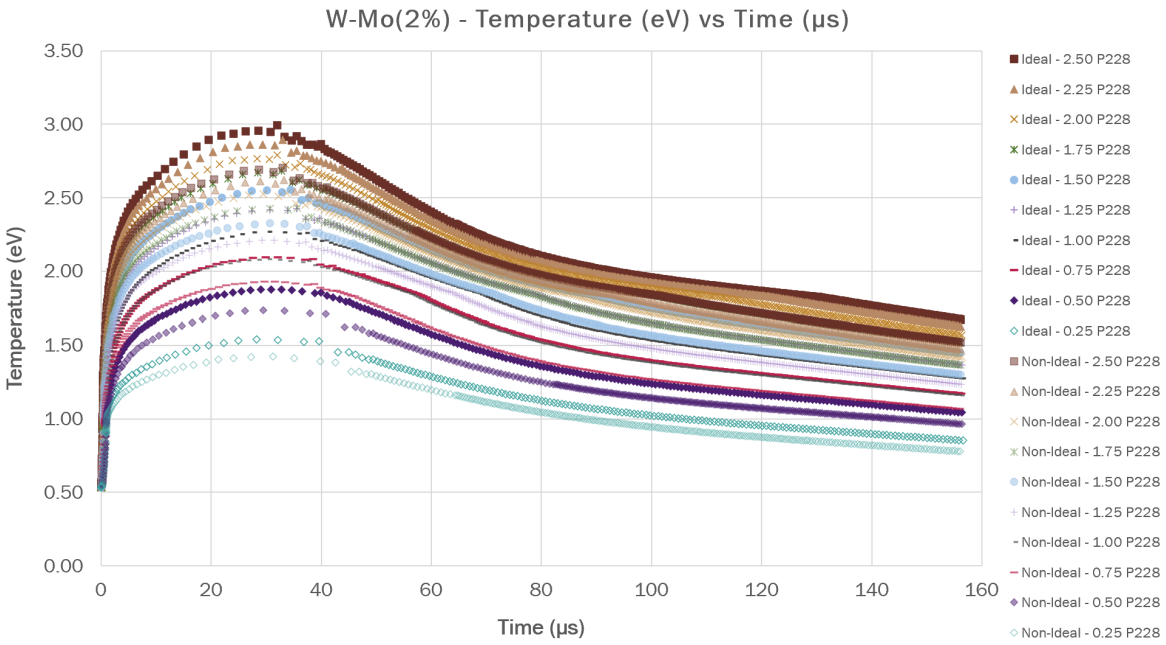

Figure 3.33: W-Mo(2.00%) Temperature (eV) versus Time (μs) as generated by ETFLOW

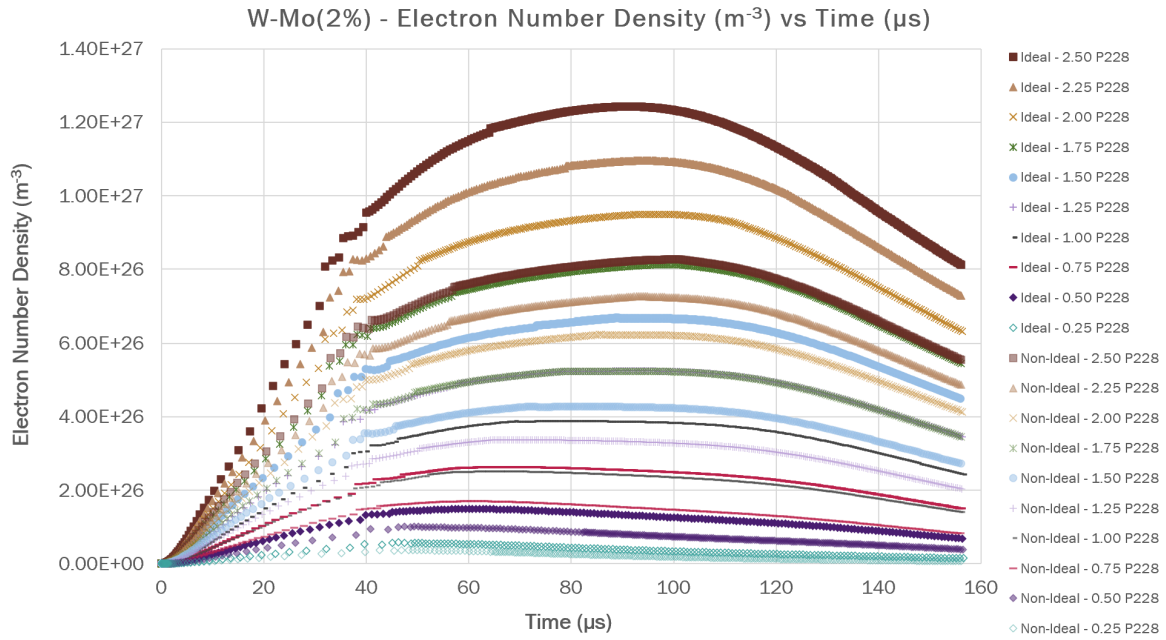

Figure 3.34: W-Mo(2.00%) Electron Number Density (m^{-3}) versus Time (μs) as generated by ETFLOW

simulated for W-Mo(2.00%) using ETFLOW. The expected computational artifacting occurs between 20 and 40 μs, corresponding to the artifacting "timestamp" that is seen in Figure 3.33. This artifacting does not interfere with the actual peak of the electron number density curves, which occurs at 90 μs. The highest peak electron number density is recorded for the Ideal 2.50 P228 simulation at $1.2427 \times 10^{27}\ m^{-3}$. The highest peak value recorded for Non-Ideal simulations occurred for the same simulation, 2.50 P228, and was $8.2655 \times 10^{26}\ m^{-3}$.

3.6 Godiva IV Material Data

This section contains the data from simulations of the Godiva IV alloy set. This set of alloys was created by perturbing the amount of Molybdenum present in the alloy, starting with the control case of U-Mo(1.50%) by 0.25% in either direction, so increasing the concentration by 0.25% and decreasing the concentration by 0.25% from the original 1.50%. This was done twice, yielding a set of five alloys to examine with concentrations of Molybdenum ranging from 1.00% to 2.00%. The goal of this perturbation was to study the effects that changing the concentrations of the constituent metals had on the sensitivity of ETFLOW calculations to mass.

An additional layer of sensitivity study was performed with the utilization of two Thermal Conductivity cases – referred to a "High" and "Low" throughout the document. The "High" and "Low" Thermal Conductivities were calculated using Equation **??**. As this equation had a temperature range of $298K < T < 773K$, or $0.0257eV < T < 0.0666eV$, and both ends of the range were well withing the bounds of the operating conditions of Godiva IV, it was deemed necessary to pick both extremes and test to see if the Thermal Conductivity had any impact on plasma parameter calculations as this equation was entirely temperature based and disregarded mass.

Given the number of factors at play, the individual alloy sections have been broken down into two sections each to make information consumption easier. Each section contains the data from the High and Low Thermal Conductivity case set, each with their own set of Ideal and Non-Ideal runs of the standard 0.25 – 2.50 P228 current profiles. Select plasma parameters and key plots have been presented in each section.

3.6.1 U-Mo(1.00%) Alloy

The first alloy of the Uranium-Molybdenum alloy set to be examined is U-Mo(1.00%). This alloy has the lowest concentration by weight Molybdenum, and therefore has the highest amount of Uranium. Unlike W-Mo(1.00%), however, which performed more like Pure Tungsten when there was very little Molybdenum in the alloy, U-Mo(1.00%) did not simulate this way, as will be seen in the following results. It can be said that it simulated closer to Molybdenum, though, it was "pulled up" slightly, having higher over all totals and peak values thanks to the presence of the Uranium. However, the fact that the values did not reach those of Pure Uranium indicate that adding Molybdenum, even in small quantities helps mitigate the ablative process, a boon for a material such as this one.

3.6.1.1 Ideal Simulation Comparison

Tables 3.27 and 3.28 contain the select plasma parameter data from the High and Low Thermal Conductivity U-Mo(1.00%) variants simulated using the Ideal model in ETFLOW. These two tables were created to easily be able to see the differences in the values generated in each case using the same ETFLOW model. Immediately apparent is the fact that values generated using the Low Thermal Conductivity U-Mo(1.00%) are larger across the board. Heat fluxes (GW/m^2), temperatures (eV), electron number densities (m^{-3}), and total ablated masses (mg) are generally all higher in the simulations that used Low Thermal Conductivity in the material properties entry. The one instance when this does not occur are for a few entries of heat flux, like with some of the Non-Ideal entries seen in other materials, for the 2.25, 1.50, 0.75, and 0.50 P228 current profiles.

Compared to the W-Mo(1.00%) analogue, for the same Ideal simulation – both cases of U-Mo(1.00%) had values over those simulated for W-Mo(1.00%) in terms of the heat flux and electron number density. However, the two cases of U-Mo(1.00%) were significantly below the predictions made in the W-Mo(1.00%) simulations for the peak temperature and electron number density. Obviously, these materials are not a direct 1:1 as the material properties are different as well as the method by which the properties were assigned to the ETFLOW library. However, as W-Mo was to serve as an analogue both in terms of a computational and physical sense, it was interesting to see where the predictions differ and how these differences are actually reflected in the physical work.

Table 3.27: ETFLOW Simulations of U-Mo(1.00%) Alloy - High Thermal Conductivity - Ideal Cases

High Thermal Conductivity Ideal Cases				
I (kA)	q" (GW/m^2)	T_{peak} (eV)	N_E (m^{-3})	M_{tot} (mg)
2.50	394.1	2.842	1.559×10^{27}	1.286
2.25	319.3	2.784	1.370×10^{27}	1.144
2.00	252.1	2.596	1.167×10^{27}	1.001
1.75	193.1	2.464	9.745×10^{26}	0.863
1.50	141.8	2.354	7.944×10^{26}	0.730
1.25	98.30	2.363	6.266×10^{26}	0.604
1.00	62.96	2.064	4.725×10^{26}	0.482
0.75	35.46	1.864	3.318×10^{26}	0.365
0.50	15.71	1.660	2.005×10^{26}	0.248
0.25	3.930	1.360	7.987×10^{25}	0.123

Table 3.28: ETFLOW Simulations of U-Mo(1.00%) Alloy - Low Thermal Conductivity - Ideal Cases

Low Thermal Conductivity Ideal Cases				
I (kA)	q" (GW/m^2)	T_{peak} (eV)	N_E (m^{-3})	M_{tot} (mg)
2.50	394.1	2.899	1.565×10^{27}	1.290
2.25	318.9	2.756	1.365×10^{27}	1.145
2.00	252.2	2.643	1.166×10^{27}	1.001
1.75	192.9	2.494	9.750×10^{26}	0.865
1.50	141.7	2.352	7.955×10^{26}	0.733
1.25	98.50	2.204	6.274×10^{26}	0.607
1.00	63.87	2.067	4.737×10^{26}	0.485
0.75	35.42	1.863	3.330×10^{26}	0.367
0.50	15.70	1.659	2.014×10^{26}	0.251
0.25	3.932	1.356	8.038×10^{25}	0.126

3.6.1.2 Non-Ideal Simulation Comparison

Tables 3.29 and 3.30 are the collection of the High and Low Thermal Conductivity U-Mo(1.00%) Non-Ideal plasma parameters.

As in the Ideal simulation cases, the Low Thermal Conductivity U-Mo(1.00%) plasma parameters were larger than those calculated for the High Thermal Conductivity U-Mo(1.00%) simulations. The Heat fluxes (GW/m^2), temperatures (eV), electron number densities (m^{-3}), and total ablated masses (mg) were generally all higher for these simulations than for their

Table 3.29: ETFLOW Simulations of U-Mo(1.00%) Alloy - High Thermal Conductivity - Non-Ideal Cases

High Thermal Conductivity Non-Ideal Cases				
I (kA)	q" (GW/m^2)	T_{peak} (eV)	N_E (m^{-3})	M_{tot} (mg)
2.50	393.8	2.546	9.784×10^{26}	0.869
2.25	319.2	2.412	8.543×10^{26}	0.775
2.00	252.1	2.308	7.314×10^{26}	0.685
1.75	192.7	2.224	6.140×10^{26}	0.596
1.50	141.9	2.116	5.074×10^{26}	0.511
1.25	98.52	1.985	4.042×10^{26}	0.427
1.00	62.98	1.840	3.089×10^{26}	0.346
0.75	35.45	1.693	2.176×10^{26}	0.264
0.50	15.75	1.504	1.284×10^{26}	0.178
0.25	3.932	1.253	5.163×10^{25}	0.086

High Thermal Conductivity Counterparts. The exceptions this being the 2.25 and 0.50 P228 current profile heat fluxes being lower in the Low Thermal Conductivity cases. In the instance of 1.00 P228, the heat flux values were the same in both cases. Values of peak temperature, electron number density, and total ablated mass were higher in the Low Thermal Conductivity set. Both instances had values lower than their Ideal counterparts for the same current profile – both compared to their own Ideal case and that of the other Thermal Conductivity Case.

Table 3.30: ETFLOW Simulations of U-Mo(1.00%) Alloy - Low Thermal Conductivity - Non-Ideal Cases

Low Thermal Conductivity Non-Ideal Cases				
I (kA)	q" (GW/m^2)	T_{peak} (eV)	N_E (m^{-3})	M_{tot} (mg)
2.50	394.0	2.496	9.787×10^{26}	0.870
2.25	319.1	2.413	8.552×10^{26}	0.778
2.00	252.2	2.308	7.325×10^{26}	0.687
1.75	192.7	2.224	6.150×10^{26}	0.599
1.50	141.9	2.114	5.084×10^{26}	0.514
1.25	98.53	1.983	4.053×10^{26}	0.430
1.00	62.98	1.838	3.101×10^{26}	0.349
0.75	35.45	1.691	2.184×10^{26}	0.267
0.50	15.73	1.501	1.291×10^{26}	0.181
0.25	3.936	1.248	5.181×10^{25}	0.090

3.6.1.3 Select Graphical Comparison

The plots in Figure 3.35 and 3.36 are the temperature curves (μs) for the Ideal and Non-Ideal data generated for the High and Low Thermal Conductivity variants of U-Mo(1.00%) as a function of time (μs). Both sets of curves experienced peaking between 20 and 35 μs and had computational artifacting on either said of the center of the curve. In some instances, there were two peaks of artifacting on either side of the peak, as in the Ideal 2.50 P228 High Thermal Conductivity simulation. Comparing the peak values of temperature between the two Thermal Conductivity cases, the peak value for the High Thermal Conductivity case was recorded in the Ideal 2.50 P228 simulation as 2.8422 eV. For the Low Thermal Conductivity case, the same simulation yielded a peak value of 2.8993 eV. The Non-Ideal simulations for each case had peak temperatures of 2.5464 eV and 2.4955 eV, respectively. It should be noted that in this instance – the Low Thermal Conductivity case had a lower peak temperature than the High Thermal Conductivity case in the Non-Ideal simulations for 2.50 P228. This was the only instance where this occurred.

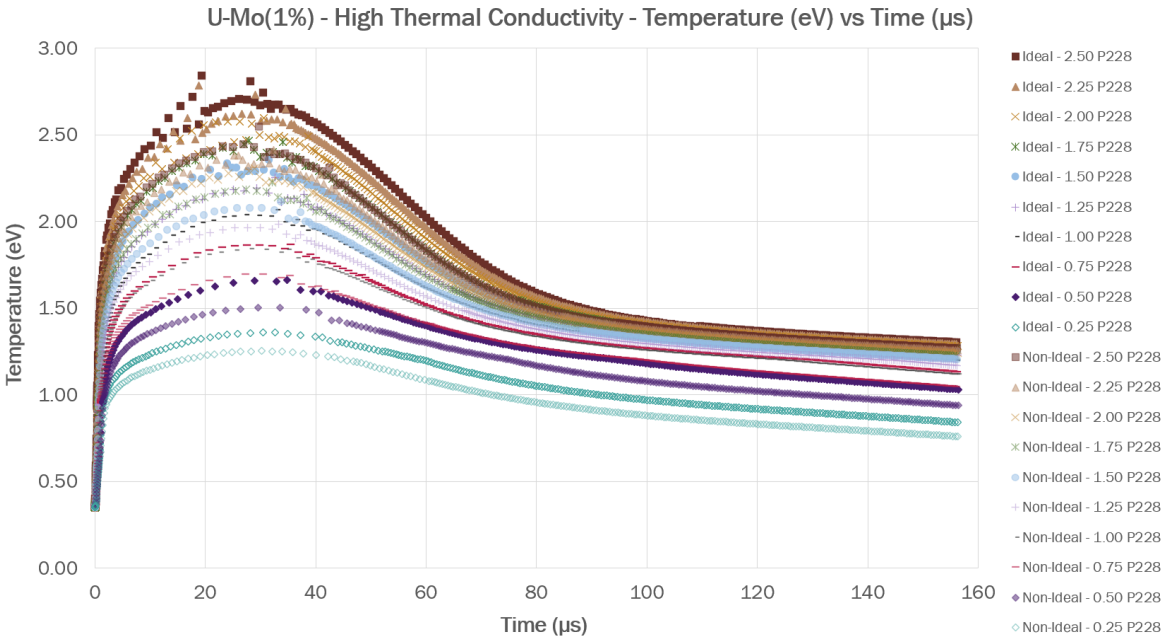

Figure 3.35: U-Mo(1.00%) Temperature (eV) versus Time (μs) as generated by ETFLOW using a high thermal conductivity case

Figures 3.37 and 3.38 depict the electron number density data (m^{-3}) for both the Ideal and Non-Ideal models in ETFLOW for the High and Low Thermal Conductivity cases of U-Mo(1.00%). The centers of both plots peak at around 80μs, much earlier than in other

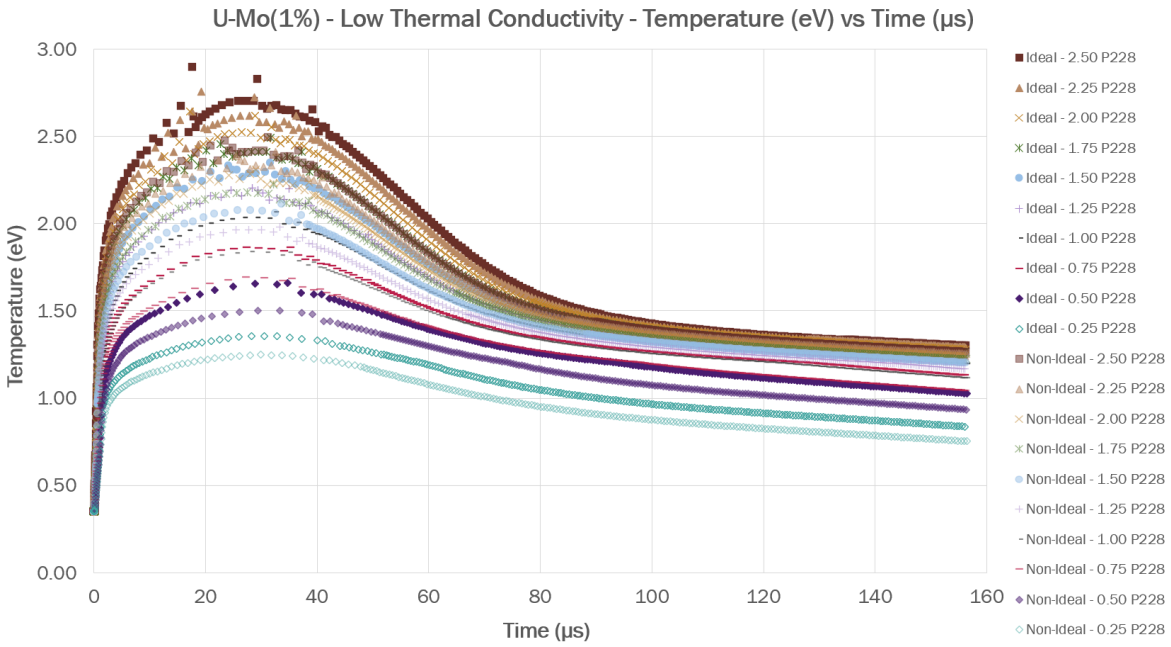

Figure 3.36: U-Mo(1.00%) Temperature (eV) versus Time (μs) as generated by ETFLOW using a low thermal conductivity case

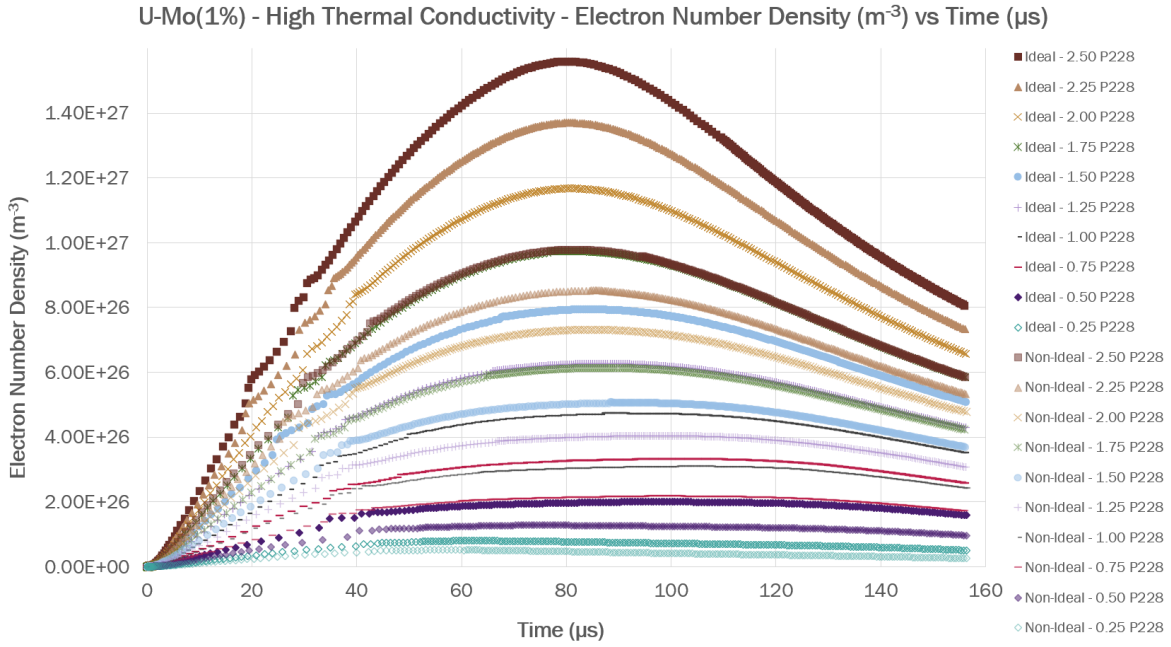

Figure 3.37: U-Mo(1.00%) Electron Number Density (m^{-3}) versus Time (μs) as generated by ETFLOW using a high thermal conductivity case

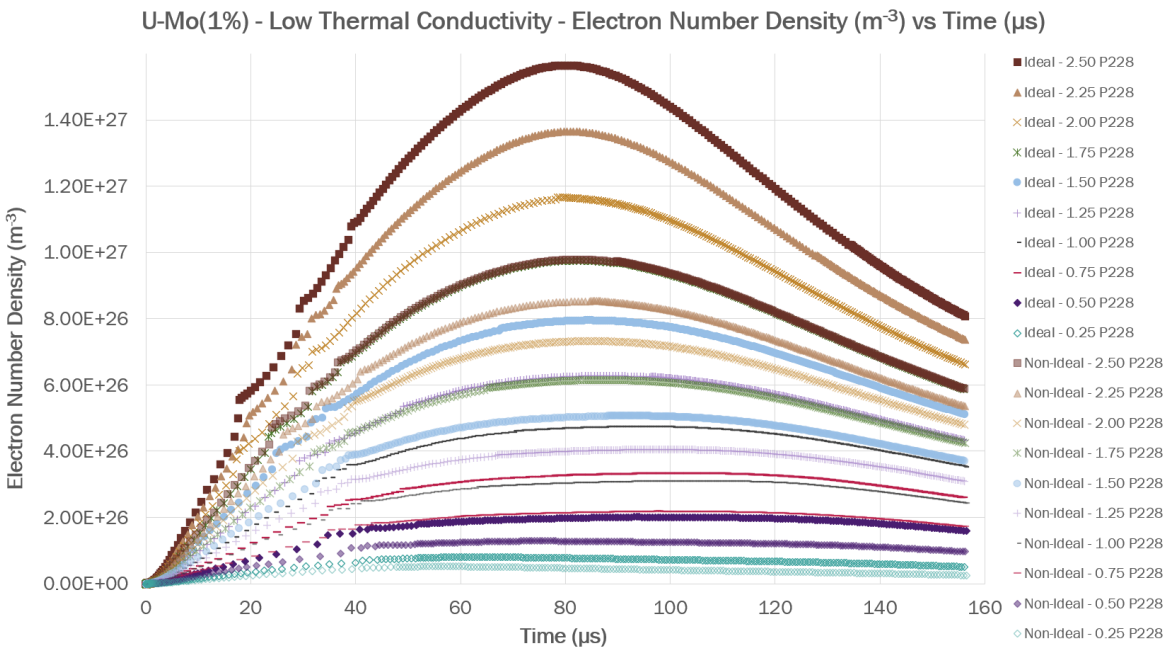

Figure 3.38: U-Mo(1.00%) Electron Number Density (m^{-3}) versus Time (μs) as generated by ETFLOW using a low thermal conductivity case

material simulations. Computational artifacting occurred in both U-Mo(1.00%) variants between 20 and 40 μs, with the Low Thermal Conductivity case experiencing more up to 45 μs. The highest overall electron number densities recorded occurred in the Ideal 2.50 P228 cases of both the High and Low Thermal Conductivity variants, having peak values of $1.5589 \times 10^{27}\ m^{-3}$ and $1.5647 \times 10^{27}\ m^{-3}$, respectively. The Non-Ideal 2.50 P228 simulations had peak values of $9.7836 \times 10^{26}\ m^{-3}$ and $9.7867 \times 10^{26}\ m^{-3}$ for the High and Low Thermal Conductivity cases. In both cases (Ideal versus Non-Ideal), the Low Thermal Conductivity variant of U-Mo(1.00%) had higher peak values than the High Thermal Conductivity variant.

3.6.2 U-Mo(1.25%) Alloy

The second Uranium-Molybdenum alloy investigated in the set was U-Mo(1.25%). This material had a slight increase in the concentration of Molybdenum when compared to the first U-Mo alloy, however, it does not contain as much as the Godiva IV alloy itself. As with all alloys in this set, four studies were performed looking into two variants of this material – a High and Low Thermal Conductivity case and the standard Ideal and Non-Ideal ETFLOW model.

3.6.2.1 Ideal Simulation Comparison

Tables 3.31 and 3.32 present the select peak plasma parameters computed using the Ideal model of ETFLOW for the High and Low Thermal Conductivity cases of U-Mo(1.25%). Immediately of note, should be that there is no change in the heat flux values (GW/m^2) between Tables 3.31 and 3.27 and only a single value that is different between Tables 3.32 and 3.28. The singular Ideal heat flux value that was different between U-Mo(1.00%) and U-Mo(1.25%) was for the Low Thermal Conductivity 2.00 P228 simulation in which the U-Mo(1.00%) simulation had a value of 252.1758 (GW/m^2) and the U-Mo(1.25%) simulation had a value of 252.1004 (GW/m^2). Based on other simulations in the set, the U-Mo(1.00%) is above the average value of heat flux for this P228 current multiplier value. In general, values of temperature (eV), electron number density (m^{-3}), and total ablated mass (mg) were lower for both cases. However, when compared directly to each other, i.e. High versus Low Thermal Conductivity, the values computed in the Low Thermal Conductivity simulations were still higher than their High Thermal Conductivity simulation equivalents.

Table 3.31: ETFLOW Simulations of U-Mo(1.25%) Alloy - High Thermal Conductivity - Ideal Cases

High Thermal Conductivity Ideal Cases				
I (kA)	q" (GW/m^2)	T_{peak} (eV)	N_E (m^{-3})	M_{tot} (mg)
2.50	394.1	2.844	1.558×10^{27}	1.284
2.25	319.3	2.780	1.369×10^{27}	1.142
2.00	252.1	2.596	1.166×10^{27}	1.000
1.75	193.1	2.472	9.737×10^{26}	0.862
1.50	141.8	2.354	7.938×10^{26}	0.729
1.25	98.30	2.251	6.262×10^{26}	0.603
1.00	62.96	2.064	4.721×10^{26}	0.481
0.75	35.46	1.865	3.316×10^{26}	0.364
0.50	15.71	1.661	2.004×10^{26}	0.248
0.25	3.930	1.360	7.977×10^{25}	0.123

Table 3.32: ETFLOW Simulations of U-Mo(1.25%) Alloy - Low Thermal Conductivity - Ideal Cases

Low Thermal Conductivity Ideal Cases				
I (kA)	q" (GW/m^2)	T_{peak} (eV)	N_E (m^{-3})	M_{tot} (mg)
2.50	394.1	2.899	1.563×10^{27}	1.288
2.25	318.9	2.755	1.364×10^{27}	1.143
2.00	252.1	2.649	1.170×10^{27}	1.003
1.75	192.9	2.494	9.742×10^{26}	0.864
1.50	141.7	2.352	7.948×10^{26}	0.732
1.25	98.50	2.203	6.270×10^{26}	0.606
1.00	63.87	2.067	4.735×10^{26}	0.485
0.75	35.42	1.863	3.329×10^{26}	0.367
0.50	15.70	1.659	2.013×10^{26}	0.251
0.25	3.932	1.356	7.998×10^{25}	0.126

3.6.2.2 Non-Ideal Simulation Comparison

Tables 3.33 and 3.34 contain the Non-Ideal simulated peak plasma parameters for the High and Low Thermal Conductivity cases of U-Mo(1.25%). As with the Ideal cases, there were many similarities between heat flux values (GW/m^2) in the Tables, however it was swapped in which set had the singular value that was different. For the Non-Ideal simulations, Tables 3.33 and 3.29 had a value that was different, again in the 2.00 P228 simulation and Tables 3.34 and 3.30 were the same. The values at 2.00 P228 were 252.1401 (GW/m^2) and 251.9528 (GW/m^2) for U-Mo(1.00%) and U-Mo(1.25%), respectively. Once again, the Low Thermal Conductivity case simulation have values larger than their High Thermal Conductivity equivalents. Compared to the results of the previous U-Mo alloy, there was a decrease in the values of temperature, electron number density, and total ablated mass in both Thermal Conductivity cases.

Table 3.33: ETFLOW Simulations of U-Mo(1.25%) Alloy - High Thermal Conductivity - Non-Ideal Cases

High Thermal Conductivity Non-Ideal Cases				
I (kA)	q" (GW/m^2)	T_{peak} (eV)	N_E (m^{-3})	M_{tot} (mg)
2.50	393.8	2.541	9.772×10^{26}	0.867
2.25	319.2	2.412	8.536×10^{26}	0.774
2.00	252.0	2.327	7.297×10^{26}	0.683
1.75	192.7	2.224	6.136×10^{26}	0.595
1.50	141.9	2.116	5.071×10^{26}	0.510
1.25	98.52	1.985	4.040×10^{26}	0.427
1.00	62.98	1.840	3.088×10^{26}	0.346
0.75	35.45	1.693	2.174×10^{26}	0.263
0.50	15.75	1.504	1.283×10^{26}	0.178
0.25	3.936	1.253	5.120×10^{25}	0.086

Table 3.34: ETFLOW Simulations of U-Mo(1.25%) Alloy - Low Thermal Conductivity - Non-Ideal Cases

Low Thermal Conductivity Non-Ideal Cases				
I (kA)	q" (GW/m^2)	T_{peak} (eV)	N_E (m^{-3})	M_{tot} (mg)
2.50	394.0	2.496	9.778×10^{26}	0.869
2.25	319.1	2.413	8.545×10^{26}	0.777
2.00	252.2	2.310	7.319×10^{26}	0.687
1.75	192.7	2.223	6.146×10^{26}	0.598
1.50	141.9	2.114	5.081×10^{26}	0.513
1.25	98.53	1.983	4.051×10^{26}	0.430
1.00	62.98	1.838	3.100×10^{26}	0.348
0.75	35.45	1.691	2.183×10^{26}	0.266
0.50	15.73	1.502	1.291×10^{26}	0.181
0.25	3.936	1.249	5.202×10^{25}	0.090

3.6.2.3 Select Graphical Comparison

The graphs in Figures 3.39 and 3.40 are the temperature (eV) curves for the Ideal and Non-Ideal model simulations in ETFLOW for the High and Low Thermal Conductivity versions of U-Mo(1.25%). As seen in the temperature plots for U-Mo(1.00%), the peaks of all temperature curves occur around the 30 μs mark and both have rather pronounced artifacting on either side of this maximum. In the High Thermal Conductivity curves, this artifacting is quite extreme in the higher current Ideal simulations, though distortion can be seen in numerous curves across both sets of curves.

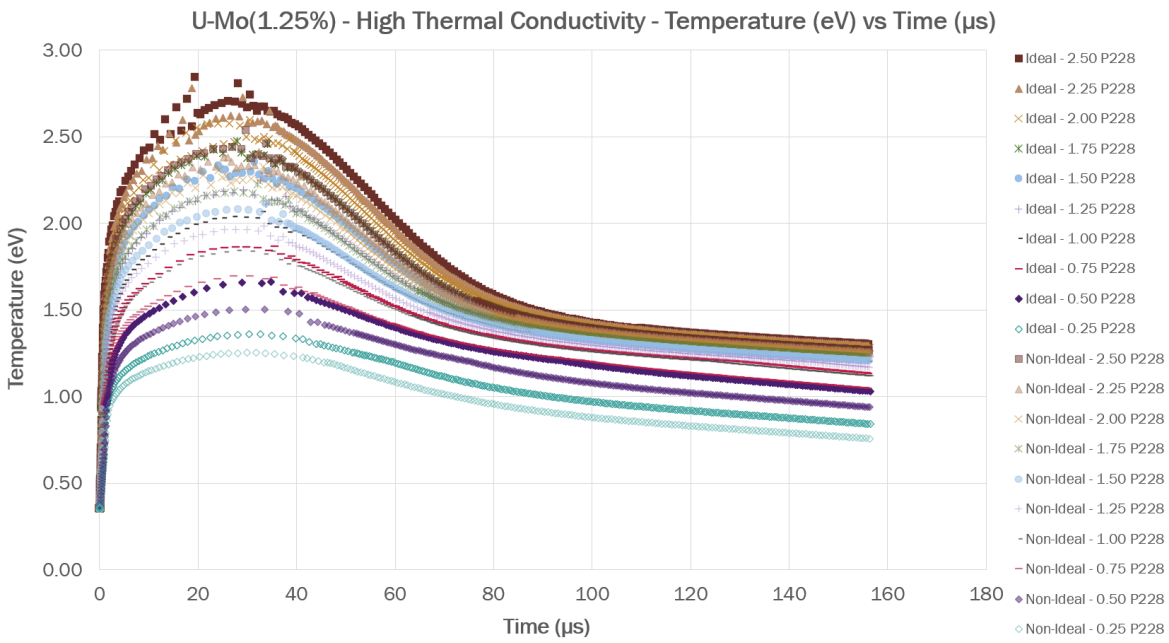

Figure 3.39: U-Mo(1.25%) Temperature (eV) versus Time (μs) as generated by ETFLOW using a high thermal conductivity case

The highest recorded temperature value was in the Low Thermal Conductivity Ideal 2.50 P228 simulation, reaching a value of 2.8986 eV, followed closely by the High Thermal Conductivity Ideal 2.50 P228 simulation. This simulation reached a peak value of 2.8436 eV. The Non-Ideal model simulations lagged further behind, though it was in the High Thermal Conductivity Non-Ideal 2.50 P228 simulation that the highest value was recorded, reaching a value of 2.5407 eV - this value is the result of one of the artifacting peaks seen around the curve maximum. The Low Thermal Conductivity peak value was also recorded during the Non-Ideal 2.50 P228 simulation, producing a more reasonable value of 2.4959 eV. It should be stated that, while the artifacting is most likely computational, these spikes can occur in real life experiments, during which time the plasma behaves in a way that was previously unaccounted for.

Figures 3.41 and 3.42 present the electron number density (m^{-3}) per unit time (μs) plots for the High and Low Thermal Conductivity versions of U-Mo(1.25%) that were simulated using the Ideal and Non-Ideal models in ETFLOW. The electron number density curves from both the High and Low Thermal Conductivity cases feature a peak at 80 μs and artifacting between 20 and 40 μs - this pattern was seen in the preceding plots for U-Mo(1.00%). Much like the plots seen in the U-Mo(1.00%) case study, the distortion caused by the artifacting does not affect the overall peak values for the electron number density curves for any of the

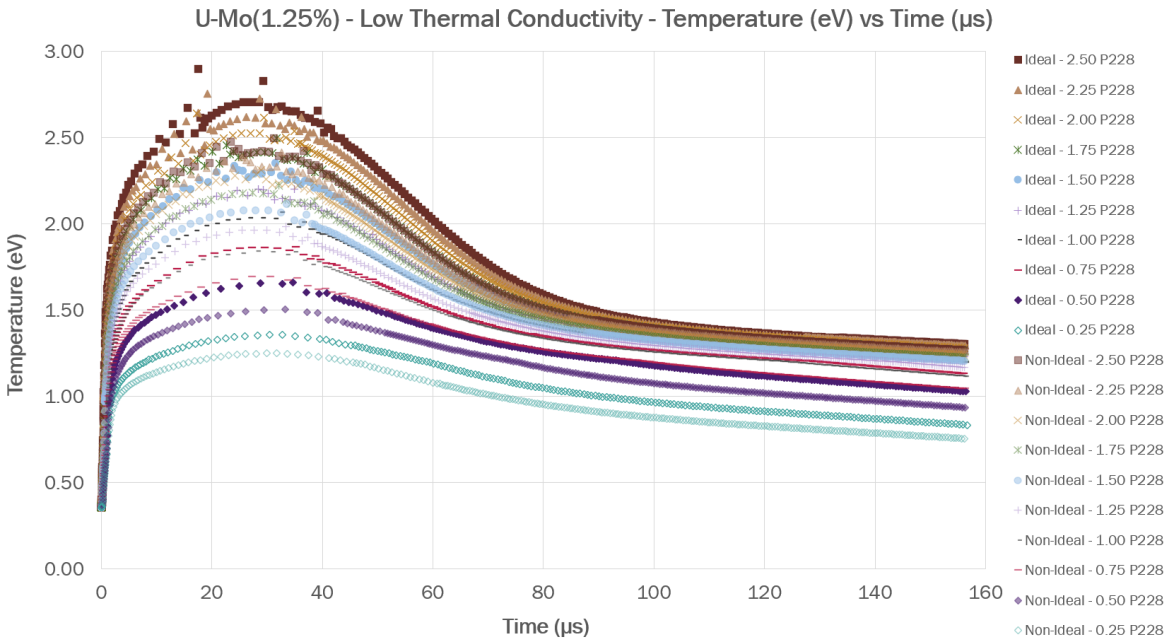

Figure 3.40: U-Mo(1.25%) Temperature (eV) versus Time (μs) as generated by ETFLOW using a low thermal conductivity case

simulations. The highest overall electron number densities recorded occurred in the Ideal 2.50 P228 cases of both the High and Low Thermal Conductivity variants, having peak values of $1.5575 \times 10^{27}\ m^{-3}$ and $1.5633 \times 10^{27}\ m^{-3}$, respectively. The Non-Ideal 2.50 P228 simulations had peak values of $9.7725 \times 10^{26}\ m^{-3}$ and $9.7782 \times 10^{26}\ m^{-3}$ for the High and Low Thermal Conductivity cases. While the Low Thermal Conductivity values were higher than their High Thermal Conductivity counterparts, in general, all values of electron number density decreased with the addition of Molybdenum, implying less ionization occurring and less freeing of electrons.

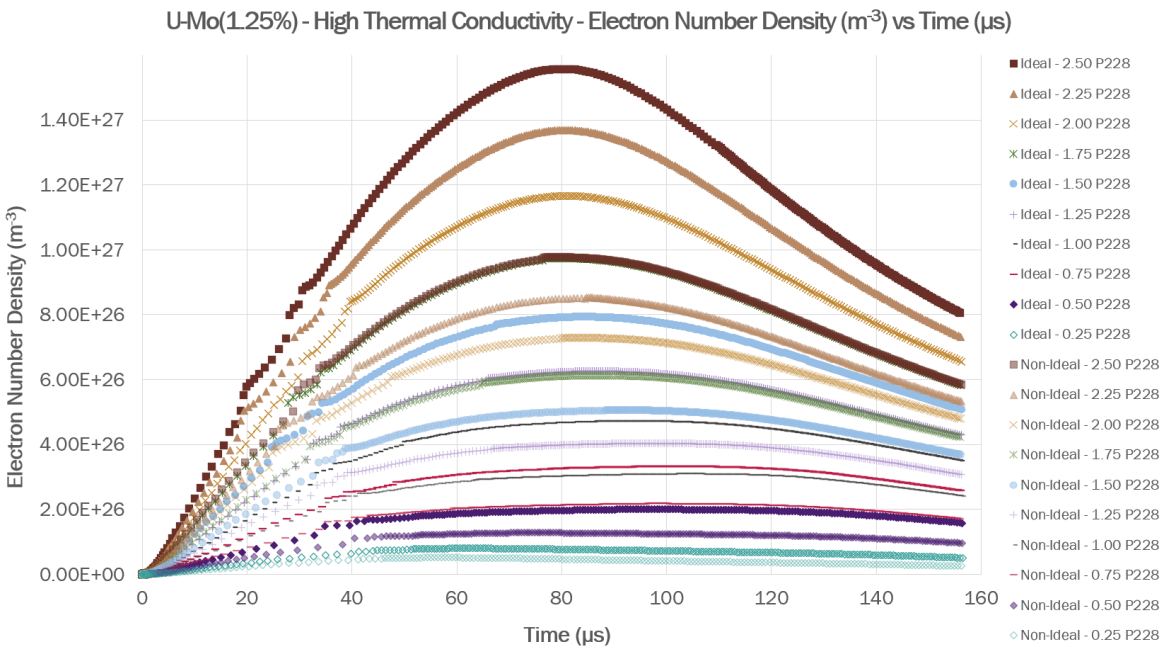

Figure 3.41: U-Mo(1.25%) Electron Number Density (m^{-3}) versus Time (μs) as generated by ETFLOW using a high thermal conductivity case

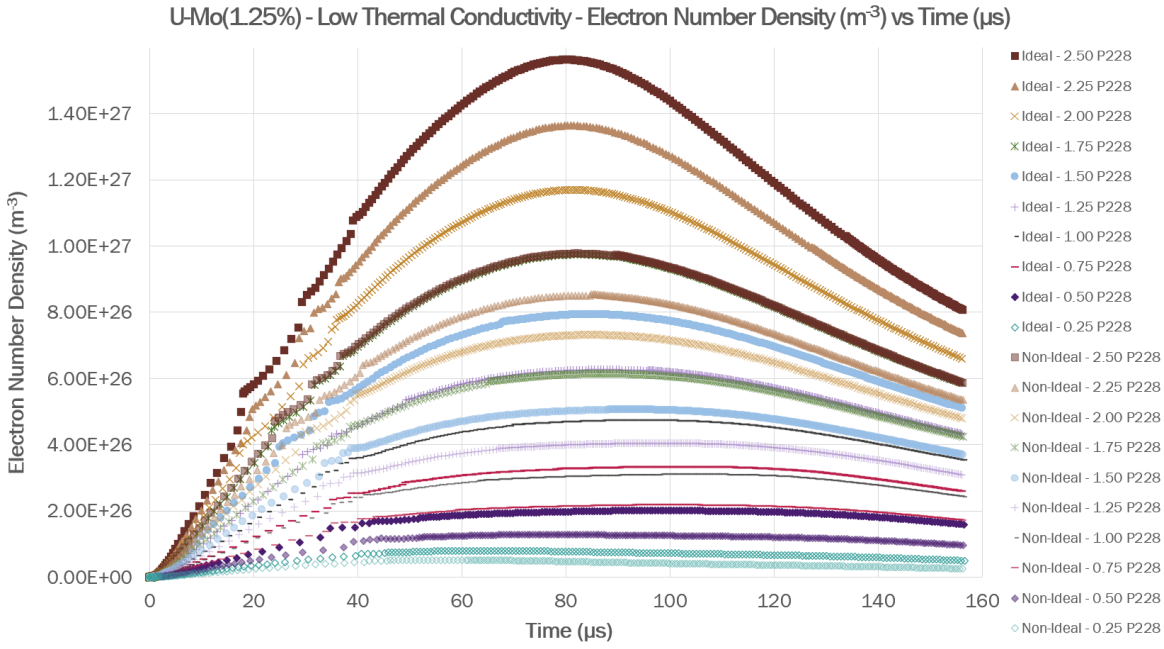

Figure 3.42: U-Mo(1.25%) Electron Number Density (m^{-3}) versus Time (μs) as generated by ETFLOW using a low thermal conductivity case

3.6.3 U-Mo(1.50%) Alloy

The third alloy that was simulated in the Uranium-Molybdenum alloy set was the Godiva IV alloy itself, U-Mo(1.50%). This alloy was the main point of interest in this set as this alloy exists in the real world and can be tested more easily than the others in this set. Additionally, results from these simulations can be used in direct comparison to experimental findings that launched the initial inquiry.

3.6.3.1 Ideal Simulation Comparison

Tables 3.35 and 3.36 present the plasma parameter data for the High and Low Thermal Conductivity U-Mo(1.50%) variants that were computed using the Ideal ETFLOW model. In general, peak values of temperature (eV), electron number density (m^{-3}), and total ablated mass (mg) decreased with the addition of Molybdenum between simulation sets, however, the Low Thermal Conductivity cases still had values that were higher than those generated using the High Thermal Conductivity cases. For instance, the Low 2.50 P228 case had a total ablated mass of 1.2865 mg, where as the High 2.50 P228 case had a total ablated mass of 1.2821 mg. In context, this would mean that the Low Thermal Conductivity material performed worse as more material was lost per pulse as this would shorten the overall life span of the Godiva IV device. Heat flux values (GW/m^2) were the same as those in the previous material simulations, with the exception of High 0.50 P228, Low 1.75 P228, and Low 0.75 P228.

Table 3.35: ETFLOW Simulations of U-Mo(1.50%) Alloy - High Thermal Conductivity - Ideal Cases

High Thermal Conductivity Ideal Cases				
I (kA)	q" (GW/m^2)	T_{peak} (eV)	N_E (m^{-3})	M_{tot} (mg)
2.50	394.2	2.853	1.556×10^{27}	1.282
2.25	319.3	2.776	1.368×10^{27}	1.141
2.00	252.1	2.596	1.167×10^{27}	0.999
1.75	193.1	2.481	9.778×10^{26}	0.863
1.50	141.8	2.354	7.932×10^{26}	0.728
1.25	98.30	2.251	6.258×10^{26}	0.603
1.00	62.96	2.064	4.719×10^{26}	0.481
0.75	35.46	1.865	3.315×10^{26}	0.364
0.50	15.70	1.662	2.003×10^{26}	0.248
0.25	3.930	1.360	7.975×10^{25}	0.123

Table 3.36: ETFLOW Simulations of U-Mo(1.50%) Alloy - Low Thermal Conductivity - Ideal Cases

Low Thermal Conductivity Ideal Cases				
I (kA)	q" (GW/m^2)	T_{peak} (eV)	N_E (m^{-3})	M_{tot} (mg)
2.50	394.1	2.898	1.562×10^{27}	1.287
2.25	319.3	2.765	1.369×10^{27}	1.143
2.00	252.1	2.635	1.169×10^{27}	1.001
1.75	193.0	2.476	9.753×10^{26}	0.864
1.50	141.8	2.354	7.943×10^{26}	0.731
1.25	98.50	2.202	6.266×10^{26}	0.605
1.00	62.87	2.067	4.733×10^{26}	0.484
0.75	35.45	1.872	3.331×10^{26}	0.367
0.50	15.70	1.659	2.012×10^{26}	0.251
0.25	3.932	1.357	7.993×10^{25}	0.126

3.6.3.2 Non-Ideal Simulation Comparison

Tables 3.37 and 3.38 contain the select plasma parameter data from the Non-Ideal ETFLOW model simulations of the High and Low Thermal Conductivity U-Mo(1.50%) alloy.

Table 3.37: ETFLOW Simulations of U-Mo(1.50%) Alloy - High Thermal Conductivity - Non-Ideal Cases

High Thermal Conductivity Non-Ideal Cases				
I (kA)	q" (GW/m^2)	T_{peak} (eV)	N_E (m^{-3})	M_{tot} (mg)
2.50	393.8	2.535	9.813×10^{26}	0.868
2.25	319.1	2.415	8.529×10^{26}	0.773
2.00	252.0	2.327	7.292×10^{26}	0.682
1.75	192.7	2.224	6.132×10^{26}	0.594
1.50	141.9	2.116	5.067×10^{26}	0.510
1.25	98.52	1.985	4.038×10^{26}	0.427
1.00	62.98	1.840	3.087×10^{26}	0.345
0.75	35.45	1.694	2.173×10^{26}	0.263
0.50	15.73	1.505	1.284×10^{26}	0.178
0.25	3.936	1.254	5.117×10^{25}	0.086

Generally, peak values of temperature (eV), electron number density (m^{-3}), and total ablated mass (mg) for the Low cases are higher than those for the High cases, with the exception of the 2.50 P228 peak temperature. The High 2.50 P228 peak temperature recorded was 2.5353 eV, significantly higher than the Low 2.50 P228 value of 2.4959 eV. Minor changes

were noted in the heat flux (GW/m^2) values with the increase of Molybdenum, but generally, the values remained the same between simulation sets. Overall, the increase in Molybdenum content lowered the peak plasma parameters.

Table 3.38: ETFLOW Simulations of U-Mo(1.50%) Alloy - Low Thermal Conductivity - Non-Ideal Cases

Low Thermal Conductivity Non-Ideal Cases				
I (kA)	q" (GW/m^2)	T_{peak} (eV)	N_E (m^{-3})	M_{tot} (mg)
2.50	394.0	2.496	9.770×10^{26}	0.868
2.25	319.1	2.413	8.539×10^{26}	0.776
2.00	251.9	2.326	7.300×10^{26}	0.685
1.75	192.7	2.223	6.142×10^{26}	0.597
1.50	141.9	2.115	5.077×10^{26}	0.512
1.25	98.53	1.983	4.050×10^{26}	0.429
1.00	62.82	1.838	3.096×10^{26}	0.348
0.75	35.45	1.691	2.182×10^{26}	0.266
0.50	15.73	1.502	1.292×10^{26}	0.181
0.25	3.936	1.249	5.165×10^{25}	0.089

3.6.3.3 Select Graphical Comparison

Figures 3.43 and 3.44 present the temperature (eV) data as a function of time (μs) generated using the Ideal and Non-Ideal ETFLOW models for the High and Low Thermal Conductivity U-Mo(1.50%) alloy. Both sets of plots have their maximum centered at around 25 μs with artifacting occurring on either side of this maximum. Compared to the previous plots, this center is shifted slightly to the left. The Ideal 2.50 P228 High Thermal Conductivity simulation has the most artifacting out of the set – with a double tail to the left of the curve maximum. The highest documented temperature of this set was recorded for the Ideal 2.50 P228 Low Thermal Conductivity simulation and had a value of 2.8979 eV. The next highest value recorded was for the Ideal 2.50 P228 High Thermal Conductivity simulation at 2.8534 eV. For the Non-Ideal simulations, the highest peak temperature was again reported in the 2.50 P228 High Thermal Conductivity simulation, with a value of 2.5353 eV. The peak temperature value for the Low Thermal Conductivity simulation was logged as 2.4959 eV.

The plots in Figures 3.45 and 3.46 are of the electron number densities (m^{-3}) calculated using the Ideal and Non-Ideal ETFLOW models for the High and Low Thermal Conductivity variants of U-Mo(1.50%) as a function of time (μs). The maximum of both sets of plots centers around the 80 μs time mark with artifacting occurring much earlier, between 20 and

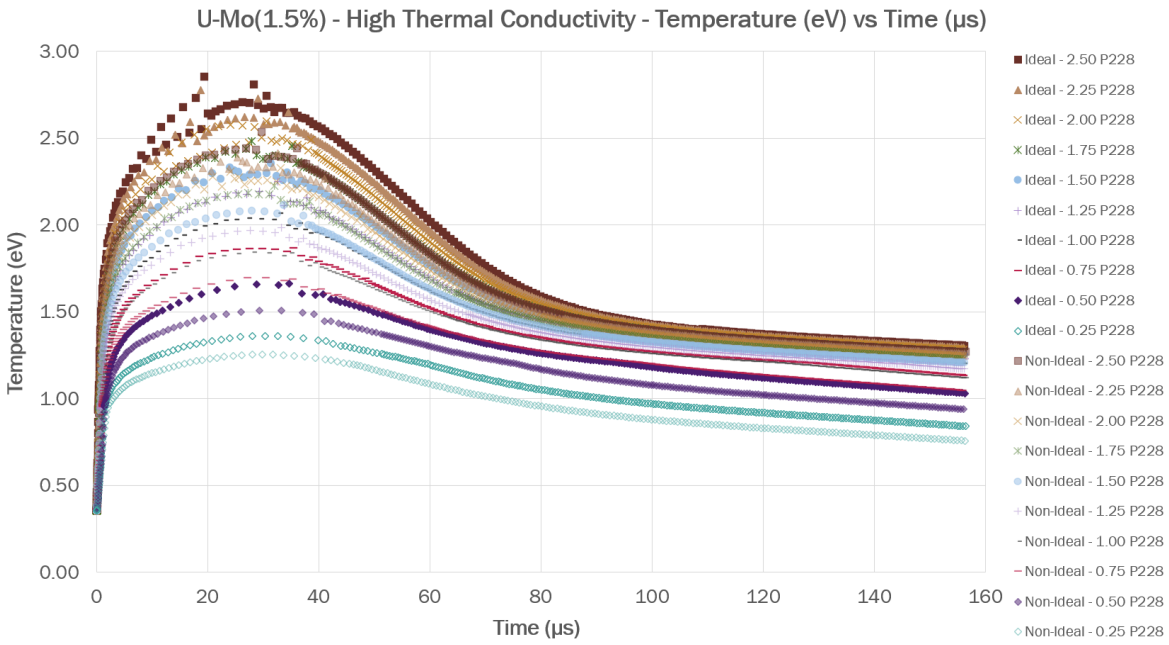

Figure 3.43: U-Mo(1.50%) Temperature (eV) versus Time (μs) as generated by ETFLOW using a high thermal conductivity case

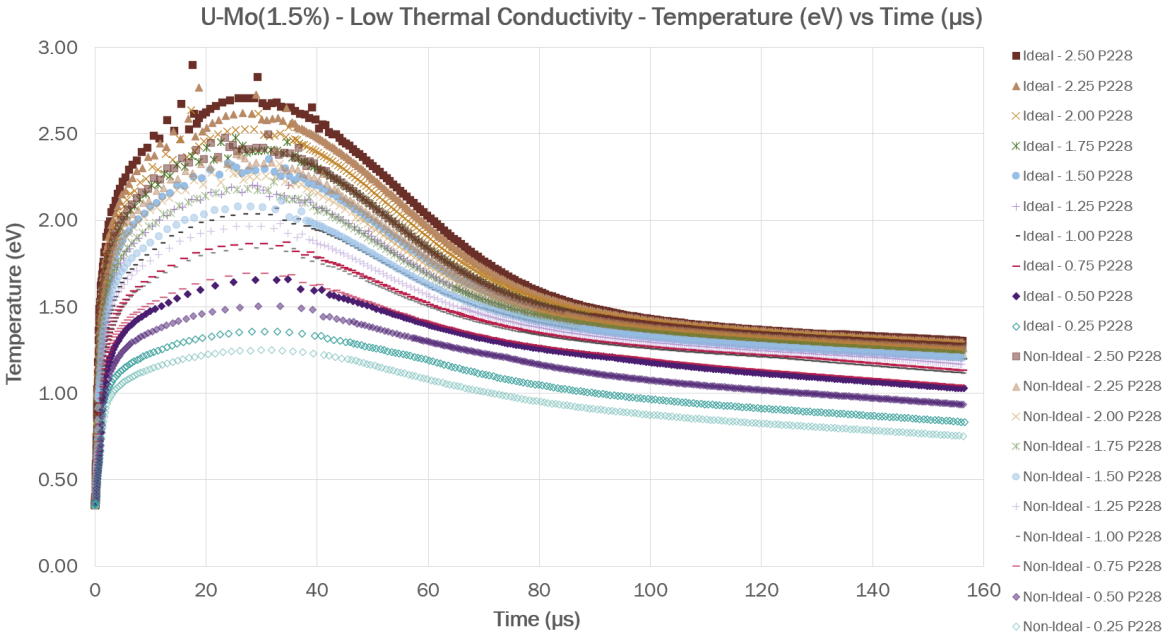

Figure 3.44: U-Mo(1.50%) Temperature (eV) versus Time (μs) as generated by ETFLOW using a low thermal conductivity case

40 μs. As with prior alloys in this set, this artifacting does not affect the maximum value of the center peak. In both graphs, the highest electron number densities were recorded for the Ideal model simulations, with the highest overall values belonging to the 2.50 P228 simulations. The largest value was $1.5619 \times 10^{27}\ m^{-3}$, from the Low cases, followed by $1.5557 \times 10^{27}\ m^{-3}$ of the High. From the Non-Ideal model, the Low 2.50 P228 simulation had the largest electron number density of $9.7698 \times 10^{26}\ m^{-3}$, followed by the High case value of $9.8132 \times 10^{26}\ m^{-3}$.

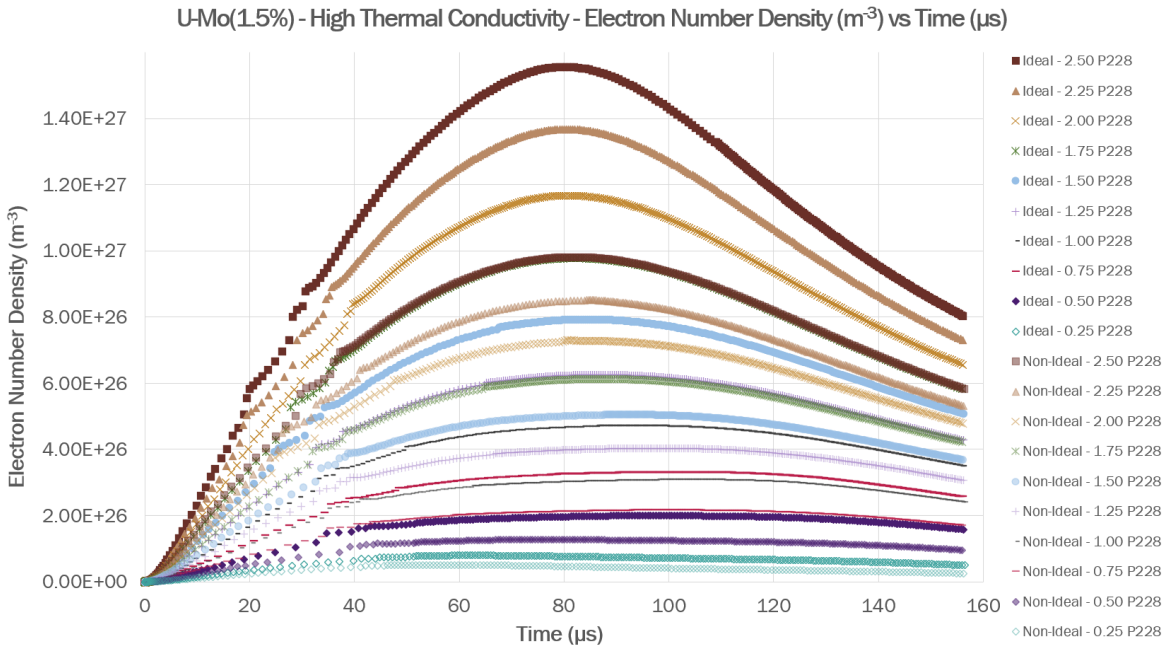

Figure 3.45: U-Mo(1.50%) Electron Number Density (m^{-3}) versus Time (μs) as generated by ETFLOW using a high thermal conductivity case

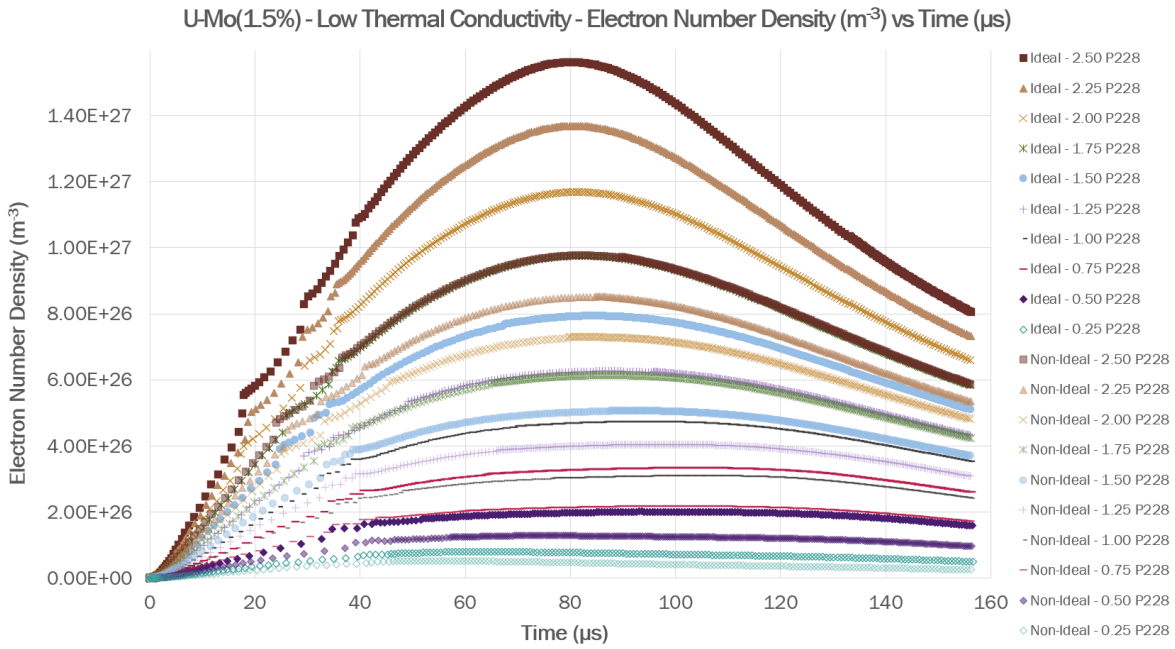

Figure 3.46: U-Mo(1.50%) Electron Number Density (m^{-3}) versus Time (μs) as generated by ETFLOW using a low thermal conductivity case

3.6.4 U-Mo(1.75%) Alloy

The fourth Uranium-Molybdenum alloy investigated was U-Mo(1.75%) – this was the first alloy to have a Molybdenum content above the control. It was expected and demonstrated in the results that the continued increase in Molybdenum content would generate lower the plasma parameters for all variants and ETFLOW models. Additionally, certain parameters, such as the heat flux (GW/m^2) were effectively the same across all four simulation sets when compared to other alloys in the set of the same type, i.e. High Thermal Conductivity case using the Ideal model for U-Mo(1.75%) versus U-Mo(1.50%).

3.6.4.1 Ideal Simulation Comparison

Tables 3.39 and 3.40 contain the select peak plasma parameter data generated using ETFLOW's Ideal model for the High and Low Thermal Conductivity variants of U-Mo(1.75%). Values for the peak temperature (eV), electron number density (m^{-3}), and total ablated mass (mg) decreased as expected with the addition of more Molybdenum to the alloy. The Low Thermal Conductivity cases had higher values for the aforementioned plasma parameters, with the most notable being the total ablated mass for the 2.50 P228 simulation being 1.2845

mg. This version of the U-Mo(1.75%) alloy ablated significantly more mass as the High Thermal Conductivity version only lost 1.2801 mg to ablation. Interestingly, there were a few High Thermal Conductivity peak temperature that were higher than their Low Thermal Conductivity equivalents – this is likely due to computational artifacting which becomes more apparent in Figures 3.47 and 3.48.

Table 3.39: ETFLOW Simulations of U-Mo(1.75%) Alloy - High Thermal Conductivity - Ideal Cases

High Thermal Conductivity Ideal Cases				
I (kA)	q" (GW/m^2)	T_{peak} (eV)	N_E (m^{-3})	M_{tot} (mg)
2.50	394.2	2.853	1.554×10^{27}	1.280
2.25	319.35	2.772	1.367×10^{27}	1.139
2.00	252.2	2.679	1.166×10^{27}	0.997
1.75	193.1	2.488	9.769×10^{26}	0.861
1.50	141.8	2.355	7.926×10^{26}	0.728
1.25	98.30	2.250	6.254×10^{26}	0.602
1.00	62.96	2.065	4.715×10^{26}	0.480
0.75	35.43	1.872	3.317×10^{26}	0.364
0.50	15.70	1.662	2.002×10^{26}	0.247
0.25	3.930	1.361	7.966×10^{25}	0.123

Table 3.40: ETFLOW Simulations of U-Mo(1.75%) Alloy - Low Thermal Conductivity - Ideal Cases

Low Thermal Conductivity Ideal Cases				
I (kA)	q" (GW/m^2)	T_{peak} (eV)	N_E (m^{-3})	M_{tot} (mg)
2.50	394.1	2.897	1.561×10^{27}	1.284
2.25	319.3	2.761	1.368×10^{27}	1.142
2.00	252.1	2.631	1.168×10^{27}	1.000
1.75	193.0	2.474	9.745×10^{26}	0.863
1.50	141.8	2.355	7.938×10^{26}	0.730
1.25	98.50	2.202	6.261×10^{26}	0.604
1.00	63.87	2.067	4.730×10^{26}	0.484
0.75	35.48	1.863	3.325×10^{26}	0.366
0.50	15.70	1.660	2.011×10^{26}	0.250
0.25	3.932	1.357	7.988×10^{25}	0.126

3.6.4.2 Non-Ideal Simulation Comparison

Contained in Tables 3.41 and 3.42 are the Non-Ideal ETFFLOW generated peak plasma parameters for the High and Low Thermal Conductivity versions of U-Mo(1.75%). Following the general trend seen thus far, the peak temperature (eV), electron number density (m^{-3}), and total ablated mass (mg) decreased with the addition of Molybdenum and the Non-Ideal values were lower than those of the Ideal simulations. The peak temperature value of High 2.50 P228, instead of being lower than the Low Thermal Conductivity values, as is the standard in the Ideal simulations, is higher than its Non-Ideal counterpart, having a value of 2.5302 eV compared to 2.4960 eV. This value, along with the value reported at Non-Ideal Low 2.25 P228 (2.4130 eV), are both higher than the previous peak for U-Mo(1.50%), which was 2.4959 and 2.4128 eV, respectively.

Table 3.41: ETFLOW Simulations of U-Mo(1.75%) Alloy - High Thermal Conductivity - Non-Ideal Cases

High Thermal Conductivity Non-Ideal Cases				
I (kA)	q" (GW/m^2)	T_{peak} (eV)	N_E (m^{-3})	M_{tot} (mg)
2.50	393.8	2.530	9.805×10^{26}	0.867
2.25	319.1	2.415	8.523×10^{26}	0.772
2.00	252.0	2.327	7.284×10^{26}	0.681
1.75	192.7	2.223	6.128×10^{26}	0.594
1.50	141.9	2.117	5.065×10^{26}	0.509
1.25	98.52	1.985	4.037×10^{26}	0.426
1.00	62.96	1.850	3.097×10^{26}	0.345
0.75	35.45	1.694	2.173×10^{26}	0.263
0.50	15.73	1.506	1.283×10^{26}	0.178
0.25	3.936	1.254	5.113×10^{25}	0.086

Table 3.42: ETFLOW Simulations of U-Mo(1.75%) Alloy - Low Thermal Conductivity - Non-Ideal Cases

Low Thermal Conductivity Non-Ideal Cases				
I (kA)	q" (GW/m^2)	T_{peak} (eV)	N_E (m^{-3})	M_{tot} (mg)
2.50	394.0	2.496	9.761×10^{26}	0.867
2.25	319.1	2.413	8.534×10^{26}	0.775
2.00	251.9	2.326	7.295×10^{26}	0.684
1.75	192.7	2.223	6.139×10^{26}	0.597
1.50	141.7	2.106	5.066×10^{26}	0.511
1.25	98.52	1.984	4.048×10^{26}	0.429
1.00	62.06	1.843	3.100×10^{26}	0.348
0.75	35.45	1.692	2.184×10^{26}	0.266
0.50	15.73	1.503	1.290×10^{26}	0.181
0.25	3.936	1.249	5.171×10^{25}	0.089

Additionally, the total ablated mass values for both instances of 2.50 P228 were the same at 0.8670 mg lost to ablation. Another anomaly found in this grouping is that the High 2.50 P228 electron number density is higher than the value calculated for Low 2.50 P228 – the values are 9.8046×10^{26} m^{-3} and 9.7614×10^{26} m^{-3}, respectively. Aside from these select values, the rest of the plasma parameters from the High Thermal Conductivity case are lower than the Low Thermal Conductivity case.

3.6.4.3 Select Graphical Comparison

Figures 3.47 and 3.48 describe the temperature (eV) data generated for the High and Low Thermal Conductivity U-Mo(1.75%) alloy using the Ideal and Non-Ideal ETFLOW models as a function of time (μs). The two sets of plots both have their maximum centered at around 25 μs with artifacting occurring on either side of this maximum – the more pronounced artifacting occurring in the High Thermal Conductivity plot. The higher current Ideal simulations have the most artifacting, with the High Thermal Conductivity simulation experiencing the most out of the set. The highest recorded temperature of this set was generated during the Ideal 2.50 P228 Low Thermal Conductivity simulation and had a value of 2.8972 eV. The next highest value recorded was generated during the Ideal 2.50 P228 High Thermal Conductivity simulation - 2.8525 eV.

For the Non-Ideal model simulations, the highest peak temperature was, once again, generated in the 2.50 P228 High Thermal Conductivity simulation, with a value of 2.5302 eV. The peak

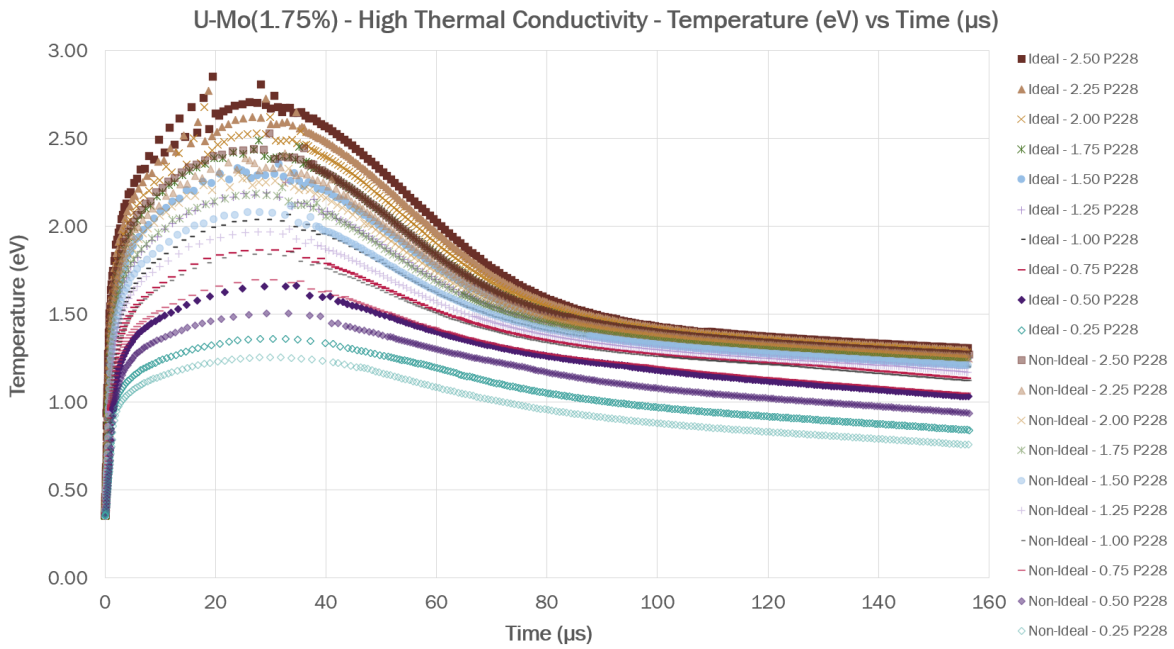

Figure 3.47: U-Mo(1.75%) Temperature (eV) versus Time (μs) as generated by ETFLOW using a high thermal conductivity case

temperature value for the Low Thermal Conductivity simulation was recorded to be 2.4960 eV. This value, along with the value reported at 2.25 P228 (2.4130 eV), are both higher than the previous peak for U-Mo(1.50%), which was 2.4959 and 2.4128 eV, respectively.

Figures 3.49 and 3.50 illustrate electron number densities (m^{-3}) for the High and Low Thermal Conductivity variants of U-Mo(1.75%) generated using the Ideal and Non-Ideal ETFLOW models as a function of time (μs). Both graphs have their maximums centered around 80 μs with their artifacting occurring between 15 and 40 μs. This artifacting does not have any affect on the peak value at the maximum's center. For both the High and Low Thermal Conductivity, the highest electron number densities recorded were from the three highest current Ideal simulations, with the highest overall being from the 2.50 P228 simulations. The largest peak value was $1.5605 \times 10^{27}\ m^{-3}$ for the Ideal 2.50 P228 Low Thermal Conductivity simulation, with the second highest being $1.5544 \times 10^{27}\ m^{-3}$ from the Ideal 2.50 P228 High Thermal Conductivity simulation. The peak values from the Non-Ideal 2.50 P228 simulations were $9.8046 \times 10^{26}\ m^{-3}$ and $9.7614 \times 10^{26}\ m^{-3}$ for the High and Low Thermal Conductivity cases.

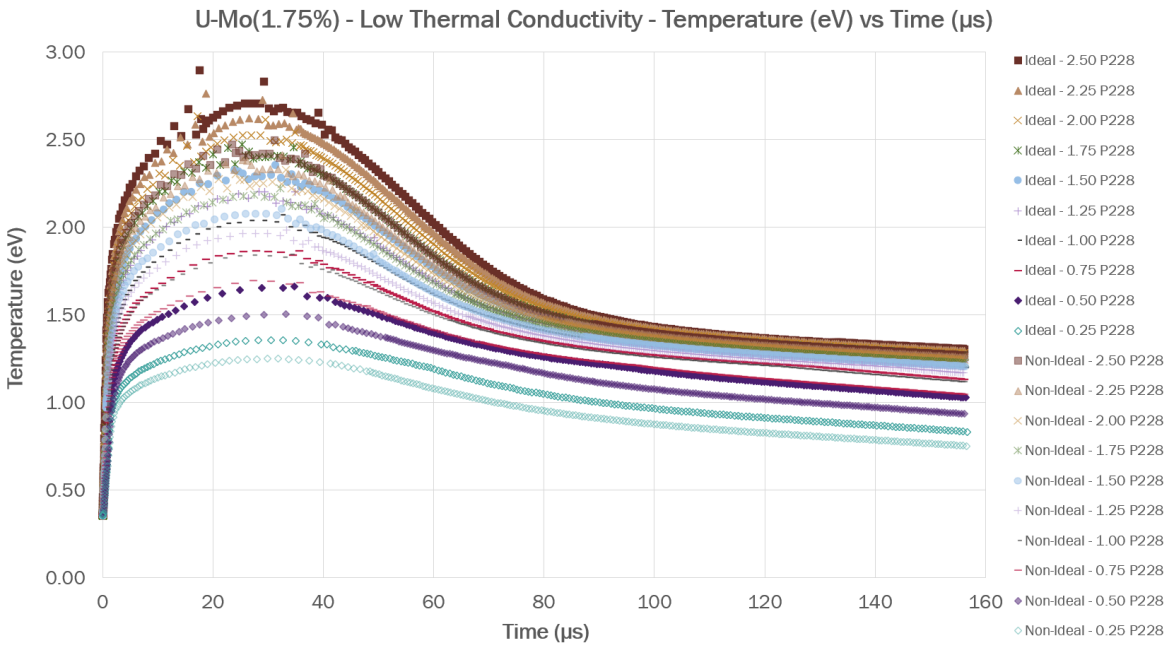

Figure 3.48: U-Mo(1.75%) Temperature (eV) versus Time (μs) as generated by ETFLOW using a low thermal conductivity case

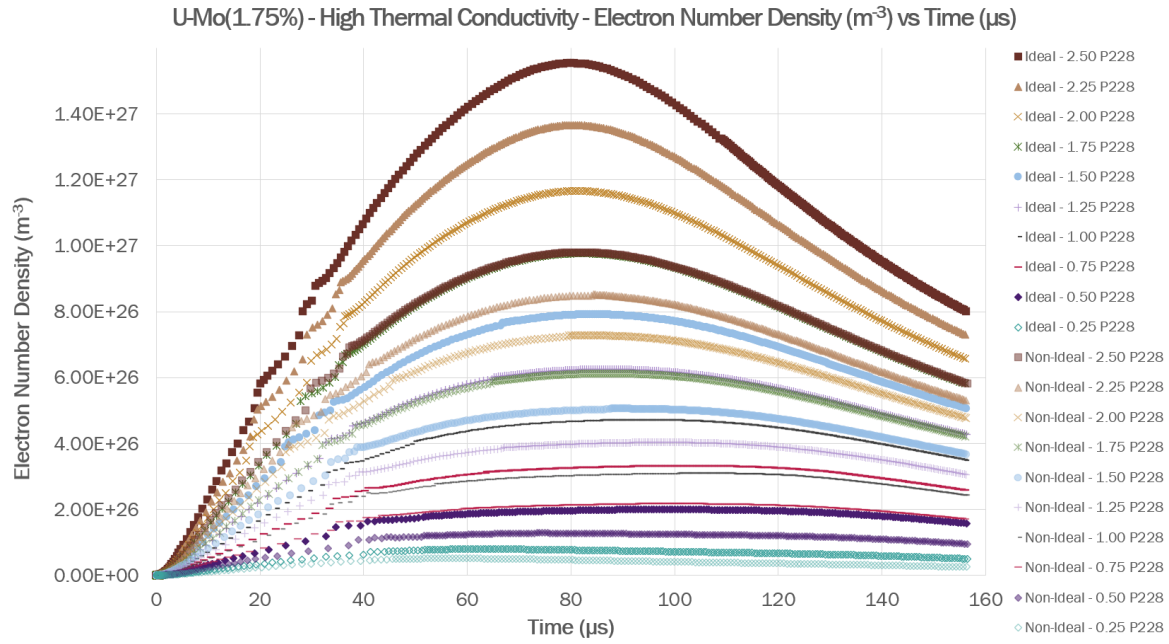

Figure 3.49: U-Mo(1.75%) Electron Number Density (m^{-3}) versus Time (μs) as generated by ETFLOW using a high thermal conductivity case

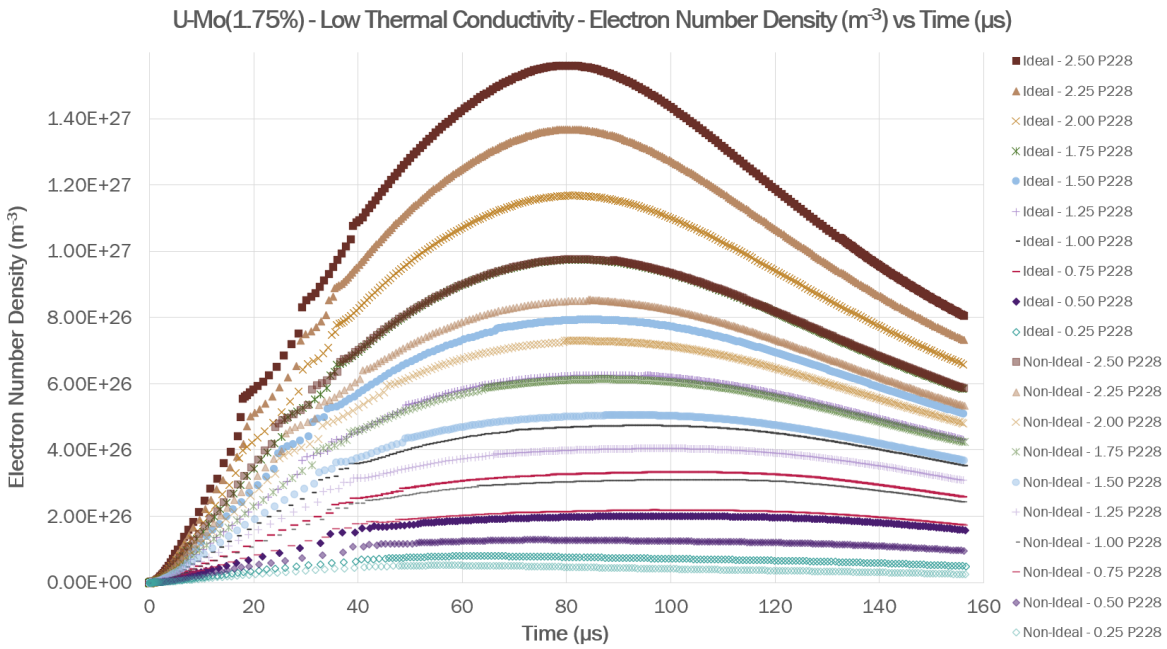

Figure 3.50: U-Mo(1.75%) Electron Number Density (m^{-3}) versus Time (μs) as generated by ETFLOW using a low thermal conductivity case

3.6.5 U-Mo(2.00%) Alloy

The last alloy tested in the Uranium-Molybdenum series was U-Mo(2.00%). This alloy had the highest concentration of Molybdenum by weight out of the entire series. Like the previous alloys simulated before it, this alloy did not experience much change, if any, in terms of the heat flux (GW/m^2) with the additional Molybdenum. The data generated for the two variations of the U-Mo(2.00%) alloy using the two ETFLOW models were all lower in value that which was computed for other materials in this set.

3.6.5.1 Ideal Simulation Comparison

Tables 3.43 and 3.44 present the plasma parameters that were generated for the High and Low Thermal Conductivity versions of U-Mo(2.00%) using the Ideal model featured in ETFLOW. The peak values of temperature (eV), electron number density (m^{-3}), and total ablated mass (mg) decreased with the addition of Molybdenum and the Low Thermal Conductivity cases, once again, had higher values than their High Thermal Conductivity case counterparts. Unlike the previously alloy simulated, there were no plasma parameters that were larger than those for an alloy with less Molybdenum.

Table 3.43: ETFLOW Simulations of U-Mo(2.00%) Alloy - High Thermal Conductivity - Ideal Cases

High Thermal Conductivity Ideal Cases				
I (kA)	q" (GW/m^2)	T_{peak} (eV)	N_E (m^{-3})	M_{tot} (mg)
2.50	394.2	2.852	1.553×10^{27}	1.278
2.25	319.3	2.768	1.365×10^{27}	1.137
2.00	252.2	2.676	1.165×10^{27}	0.996
1.75	193.0	2.475	9.725×10^{26}	0.859
1.50	141.8	2.355	7.920×10^{26}	0.727
1.25	98.30	2.250	6.250×10^{26}	0.601
1.00	62.96	2.065	4.713×10^{26}	0.480
0.75	35.43	1.872	3.315×10^{26}	0.364
0.50	15.70	1.663	2.002×10^{26}	0.247
0.25	3.930	1.361	7.960×10^{25}	0.123

Table 3.44: ETFLOW Simulations of U-Mo(2.00%) Alloy - Low Thermal Conductivity - Ideal Cases

Low Thermal Conductivity Ideal Cases				
I (kA)	q" (GW/m^2)	T_{peak} (eV)	N_E (m^{-3})	M_{tot} (mg)
2.50	394.1	2.897	1.559×10^{27}	1.283
2.25	319.3	2.758	1.367×10^{27}	1.140
2.00	252.1	2.627	1.166×10^{27}	0.999
1.75	193.0	2.534	9.725×10^{26}	0.862
1.50	141.8	2.347	7.956×10^{26}	0.731
1.25	98.50	2.202	6.257×10^{26}	0.604
1.00	63.87	2.067	4.728×10^{26}	0.483
0.75	35.48	1.863	3.324×10^{26}	0.366
0.50	15.70	1.660	2.012×10^{26}	0.250
0.25	3.932	1.357	7.982×10^{25}	0.126

3.6.5.2 Non-Ideal Simulation Comparison

Tables 3.45 and 3.46 contain the peak plasma parameters that were computed using the Non-Ideal model in ETFLOW for the High and Low Thermal Conductivity versions of U-Mo(2.00%). Like the Ideal simulations, the peak temperature (eV), electron number density (m^{-3}), and total ablated mass (mg) decreased with the addition of Molybdenum. The Low Thermal Conductivity cases, once again, had higher values than their High Thermal Conductivity case counterparts with the exception of the High Thermal Conductivity 2.50 P228 case. All values for this simulation are larger than their Low Thermal Conductivity

Table 3.45: ETFLOW Simulations of U-Mo(2.00%) Alloy - High Thermal Conductivity - Non-Ideal Cases

High Thermal Conductivity Non-Ideal Cases				
I (kA)	q" (GW/m^2)	T_{peak} (eV)	N_E (m^{-3})	M_{tot} (mg)
2.50	393.8	2.526	9.796×10^{26}	0.866
2.25	319.1	2.415	8.516×10^{26}	0.771
2.00	252.0	2.339	7.296×10^{26}	0.682
1.75	193.1	2.247	6.129×10^{26}	0.593
1.50	141.9	2.117	5.060×10^{26}	0.509
1.25	98.52	1.986	4.035×10^{26}	0.426
1.00	62.96	1.850	3.095×10^{26}	0.345
0.75	35.45	1.695	2.174×10^{26}	0.263
0.50	15.73	1.507	1.282×10^{26}	0.178
0.25	3.936	1.254	5.110×10^{25}	0.086

equivalent.

Table 3.46: ETFLOW Simulations of U-Mo(2.00%) Alloy - Low Thermal Conductivity - Non-Ideal Cases

Low Thermal Conductivity Non-Ideal Cases				
I (kA)	q" (GW/m^2)	T_{peak} (eV)	N_E (m^{-3})	M_{tot} (mg)
2.50	394.0	2.496	9.753×10^{26}	0.866
2.25	319.1	2.413	8.527×10^{26}	0.774
2.00	251.9	2.326	7.287×10^{26}	0.683
1.75	193.1	2.244	6.142×10^{26}	0.596
1.50	141.7	2.106	5.063×10^{26}	0.511
1.25	98.52	1.984	4.046×10^{26}	0.428
1.00	63.06	1.844	3.099×10^{26}	0.347
0.75	35.45	1.692	2.183×10^{26}	0.266
0.50	15.73	1.503	1.289×10^{26}	0.181
0.25	3.936	1.250	5.168×10^{25}	0.089

3.6.5.3 Select Graphical Comparison

Figures 3.51 and 3.52 detail the High and Low Thermal Conductivity U-Mo(2.00%) alloy temperature (eV) data as a function of time (μs) for the Ideal and Non-Ideal models of ETFLOW. The two sets of graphs have their centers around 25 μs with pronounced artifacting to the left and right of this maximum. The High Thermal Conductivity curves have the most pronounced artifacting, with the Ideal 2.50 P228 curve being split near the top of the

peak; other high current Ideal simulations also experienced a significant level of artifacting, with the bulk being seen in the High Thermal Conductivity cases. The highest documented temperature of this set was generated during the Ideal 2.50 P228 Low Thermal Conductivity simulation and had a value of 2.8965 eV. The second highest value recorded was generated during the Ideal 2.50 P228 High Thermal Conductivity simulation - 2.8516 eV. The highest peak temperatures recorded for Non-Ideal simulations were, again, generated in the 2.50 P228 simulations. The highest between the High and Low Thermal Conductivity cases was noted to be from the High 2.50 P228 simulation, having a recorded value of 2.5255 eV. The value from the Low 2.50 P228 was 2.4962 eV. It should be noted this the peak temperature of the Low Thermal Conductivity case was higher than the previous U-Mo alloy, U-Mo(1.75%).

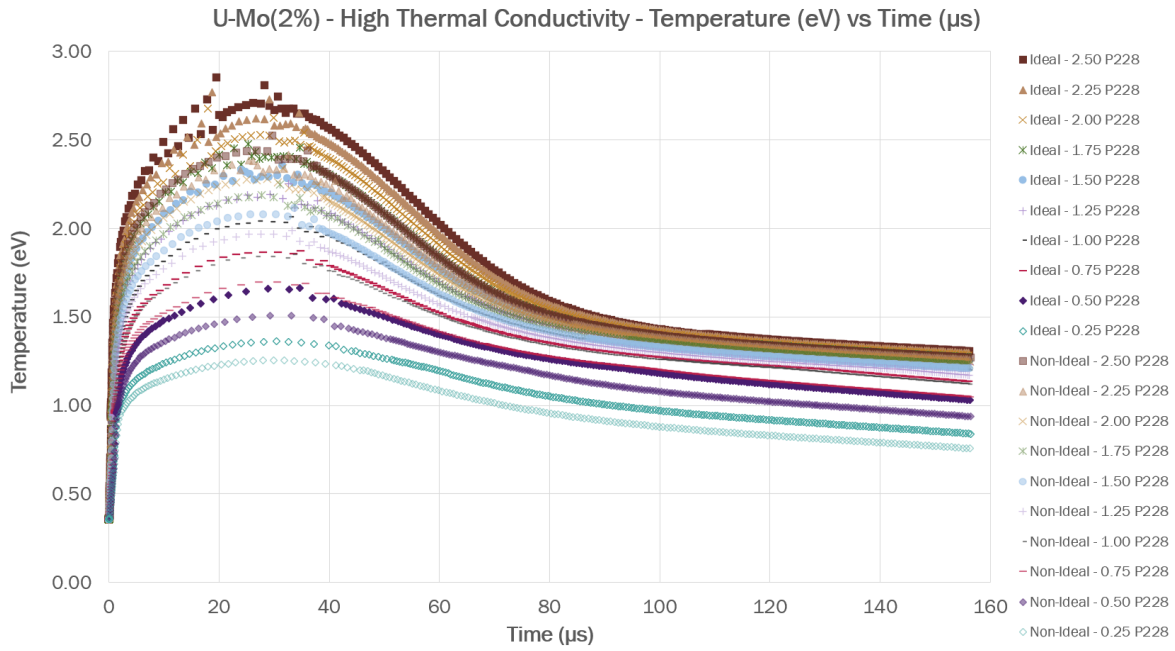

Figure 3.51: U-Mo(2.00%) Temperature (eV) versus Time (μs) as generated by ETFLOW using a high thermal conductivity case

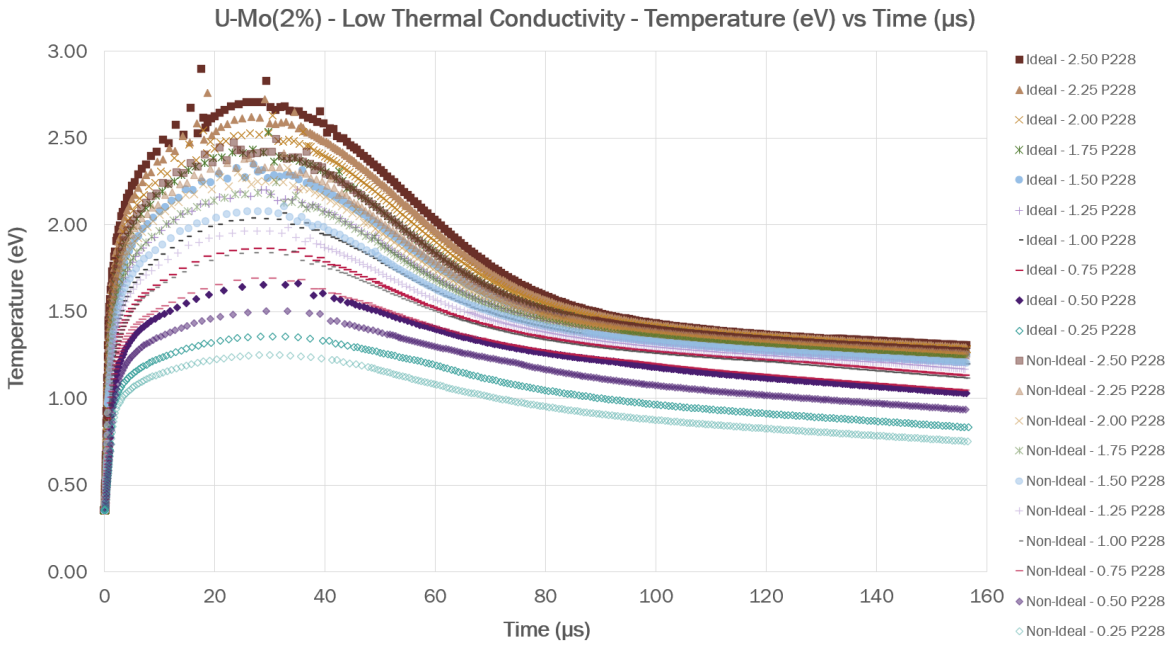

Figure 3.52: U-Mo(2.00%) Temperature (eV) versus Time (μs) as generated by ETFLOW using a low thermal conductivity case

Figure 3.53 and 3.54 detail the electron number densities (m^{-3}) for Ideal and Non-Ideal High and Low Thermal Conductivity U-Mo(2.00%) variant data generated using ETFLOW as a function of time (μs). Both sets of plots have their maximums centered around 80 μs with artifacting occurring between 20 and 40 μs; this artifacting has no affect on the peak value of the curves. In terms of highest electron number density values, the top performers were the higher current Ideal simulations for both the High and Low Thermal Conductivity cases. The largest electron number density occurred during an Ideal 2.50 P228 simulation of the Low Thermal Conductivity U-Mo(2.00%) variant, having a peak value of $1.5591 \times 10^{27}\ m^{-3}$. The same current profile simulation in High Thermal Conductivity U-Mo(2.00%) resulted in a peak value of $1.5530 \times 10^{27}\ m^{-3}$. The peak values from the Non-Ideal 2.50 P228 simulations were $9.7961 \times 10^{26}\ m^{-3}$ and $9.7530 \times 10^{26}\ m^{-3}$ for the High and Low Thermal Conductivity cases.

3.7 General Conclusions

Based on the results compiled in this section, it can be concluded that ETCOMBFLOW can accurately simulate an electrothermal plasma on a heavy metal's surface. More specifically

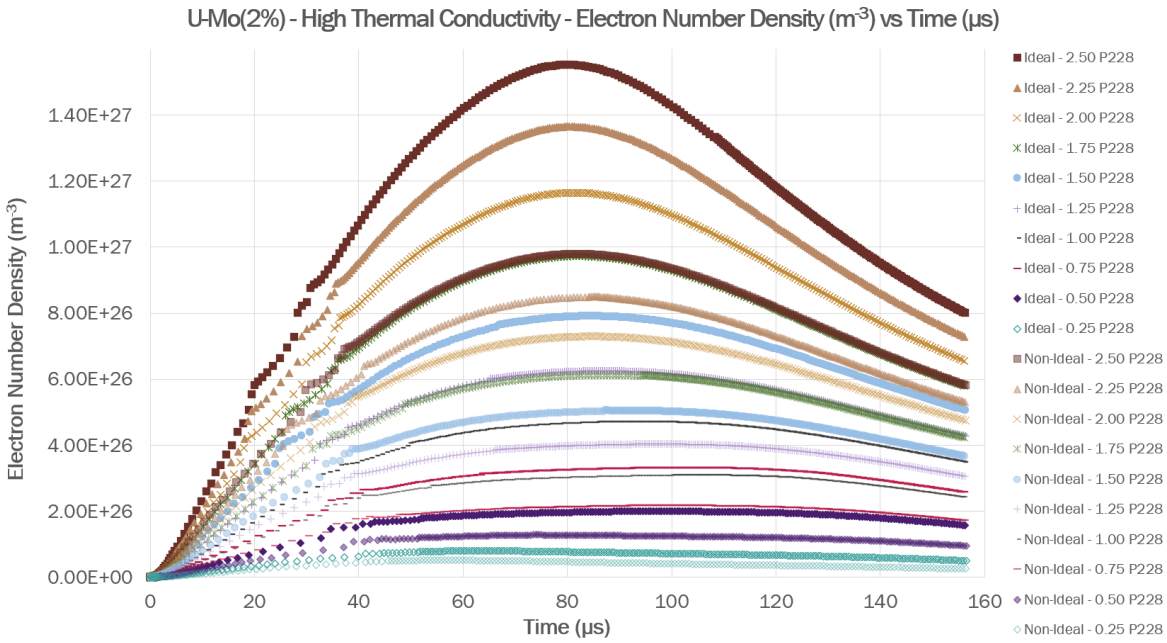

Figure 3.53: U-Mo(2.00%) Electron Number Density (m^{-3}) versus Time (μs) as generated by ETFLOW using a high thermal conductivity case

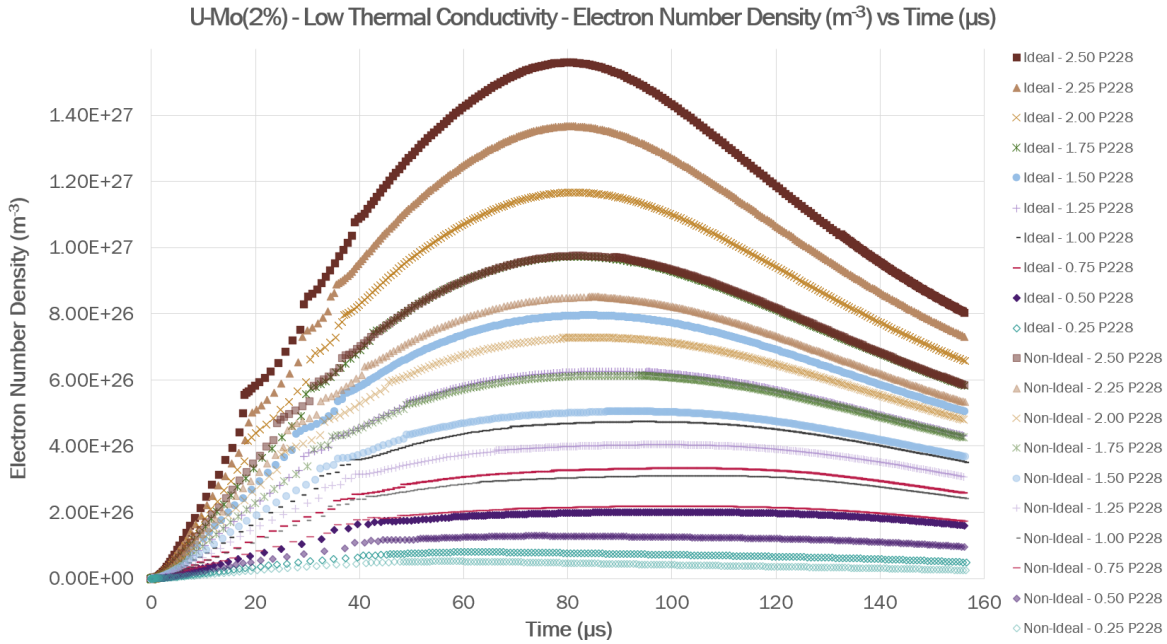

Figure 3.54: U-Mo(2.00%) Electron Number Density (m^{-3}) versus Time (μs) as generated by ETFLOW using a low thermal conductivity case

to Godiva IV, an ET plasma was successfully simulated in a capillary configuration, implying that the configuration discussed in Section 2.1 could be conducive to ablation.

Chapter 4

Proof of Concept: Spectroscopy Experiments and Heat Flux Study

After completing a rather extensive materials simulation study using ETFLOW, it was determined that further simulation and physical experimentation were needed to confirm the results of the ETFLOW ET plasma simulations. The need for leveraging other programs to simulate some of the ET plasma formation arises from ETFLOW's inability to compute the subsurface layer information during a shot. As the heat transfer to these layers is key to understanding how these plasmas work in the real world, ANSYS was selected to perform the heat flux study. ANSYS is an Engineering Simulation Software that allows the user to create a multiphysics computer-aided engineering simulation of an item or object of interest.

Two versions of the heat flux study were performed – one in which data from ETFLOW, simulating HELIOS, was used and another in which the data from laser spectroscopy experiments were simulated. The results from both studies were compared to each other to help validate the method used.

4.1 ANSYS Simulation Setup

4.1.1 Model Creation

To begin the validation process, a simple model was first created to represent a block of material that has a plasma impinging on the surface. The initial block was $2\ mm \times 2\ mm \times 1\ mm$. At the center of the block a bore hole was made and then filled with a cylindrical "plug"

of material that was 11 μm in diameter and 30 μm long. The purpose of this "plug" was to serve as an impact/impingement location for the plasma and to allow for easier meshing. An unmeshed version of the block can be found in Figure 4.1.

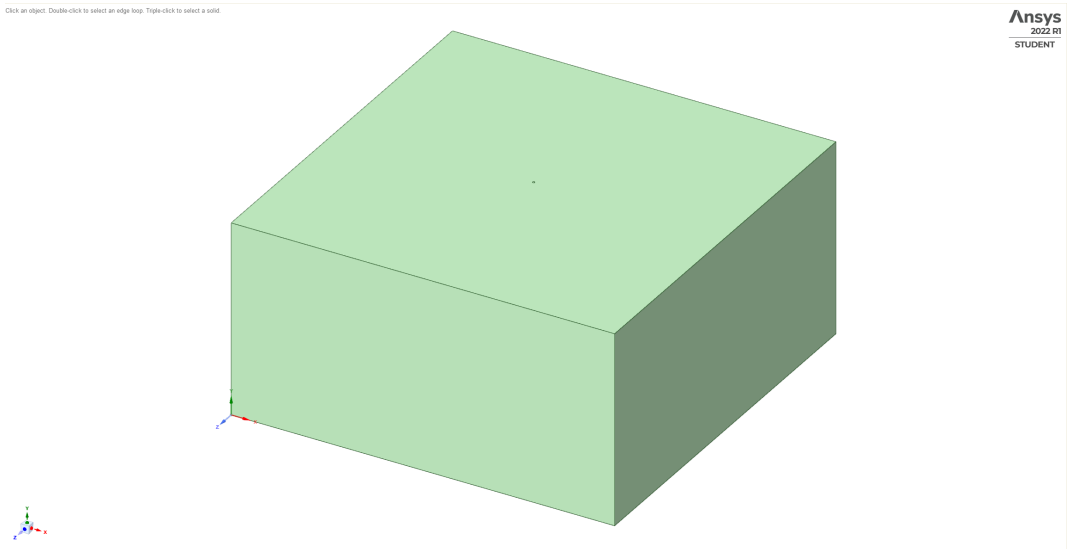

Figure 4.1: ANSYS rendering of a material block with a 11 μm diameter, 30 μm deep impact hole used for heat flux studies.

This design was later changed after it was determined that it was not necessary to have such a large block of material for the simulation to work. As such, the block's dimensions were reduced to 1 $mm \times 1\ mm \times 0.5\ mm$. An addition was made to the bore hole at the center of the block to include a disk that serves as the averaged width and depth of the impact crater. The crater dimensions, along with the bore hole dimensions were then changed (in multiple models) according to the recorded dimensions from four laser ablation samples. An example of the final model can be found in Figure 4.2 and the various dimensions used to make each of the models can be found in Tables 4.1 and 4.2.

Table 4.1: Laser Impact Crater Dimensions

General Impact Crater Dimensions		
Power (W)	Crater Depth (μm)	Bore Hole Depth (μm)
0.60	2.293	32.599
1.20	3.517	37.414
1.80	4.409	38.780
2.40	4.422	46.372
3.00	5.222	48.478

Table 4.2: Crater Specific Dimensions

Sample Specific Crater Dimensions		
Sample	Crater Width (μm)	Bore Hole Width (μm)
5-1 ETD 094	64.075	13.160
5-2 ETD 102	62.555	10.450
5-4 ETD 116 & 118	46.540	17.870
5-5 ETD 122 & 124	36.590	14.840

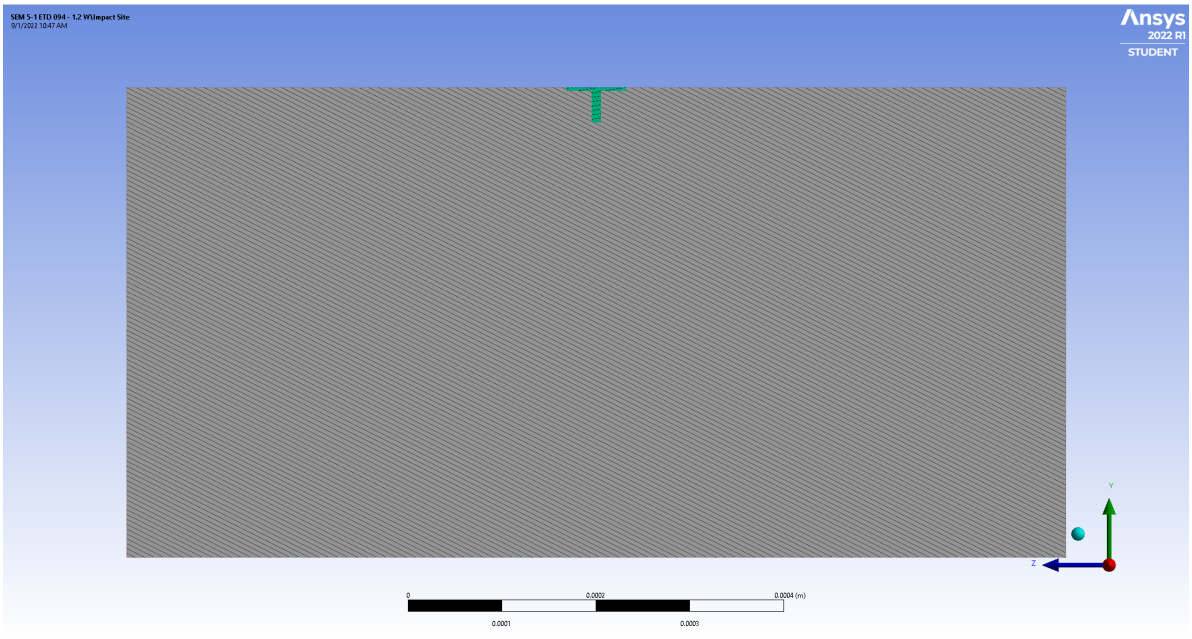

Figure 4.2: ANSYS rendering of a material block cross-section with updated bore hole, including the impact site crater caused by melting due to the laser.

The updated impact site model is shown in Figure 4.3. The Isometric view of the Impact Site is depicted in Figure 4.3(a) and the Right view of the Impact Site, as seen in Figure 4.2, is depicted in Figure 4.3(b). Exact dimensions are not given on these figures as there are five versions that were used for the various simulations performed. The dimensions of the plug, in addition to when they used, i.e. which laser power they are associated with, can be found in Tables 4.1 and 4.2.

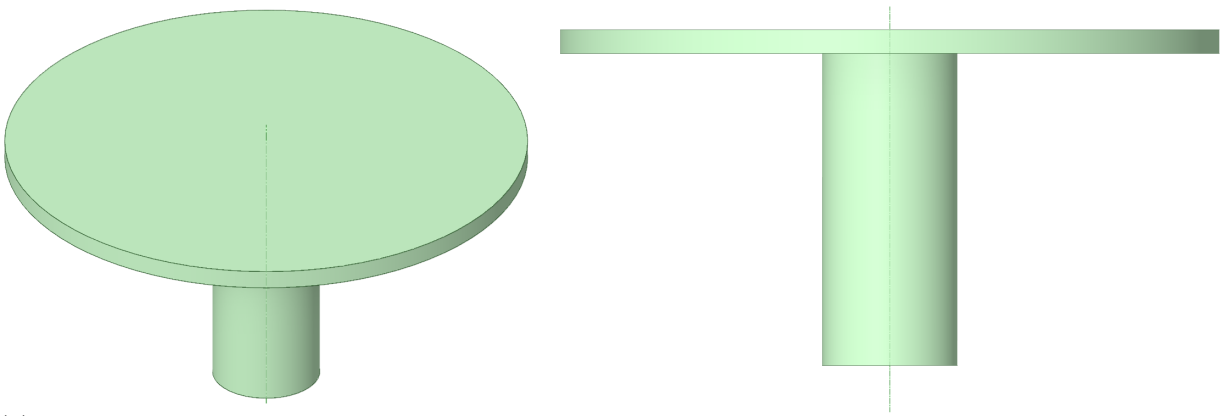

(a) Isometric view of the Impact Site "Plug" from the updated ANSYS model.

(b) Right view of the Impact Site "Plug" from the updated ANSYS model.

Figure 4.3: Laser Impact Site Model Example

The material used, for comparison purposes for the second round of analysis, was Tungsten. To ensure that the material data was consistent across all simulations, the Engineering Data entry was built for Tungsten using the values for Density, Melting Temperature, Isotropic Thermal Conductivity, and Specific Heat Constant Pressure that were using in the ETFLOW material library. All other Material Field Variables values were set to have their Lower and Upper Limits be Programmed Controlled. These values, minus the Material Field Variables, can be found in Table 4.3.

Table 4.3: Material Properties for the Engineering Data entry for Tungsten in ANSYS based on the ETFLOW Materials Library.

Tungsten Material Engineering Data		
Property	Value	Unit
Material Field Variables	Table	
Density	19400	$kg \cdot m^{-3}$
Melting Temperature	3410	C
Isotropic Thermal Conductivity	174	$W \cdot m^{-1}C^{-1}$
Specific Heat Constant Pressure	134	$J \cdot kg^{-1}C^{-1}$

When meshing the material block, the Physics Preference was set to CFD or Computational Fluid Dynamics. This branch of Fluid Mechanics uses numerical analysis and data structures to solve problems involving fluid flows and later analyze them; using this setting allowed for Fluent to be used as the Solver. Fluent is an extremely accurate fluid simulation software that is part of the ANSYS suite of programs. As the initial problem (plasma impinging on

a surface) can be treated as an exceptionally hot gas (a fluid) interacting with the surface of a material, it was decided that this approach would yield the most accurate results. The rendering of the CFD mesh can be seen in Figure 4.4.

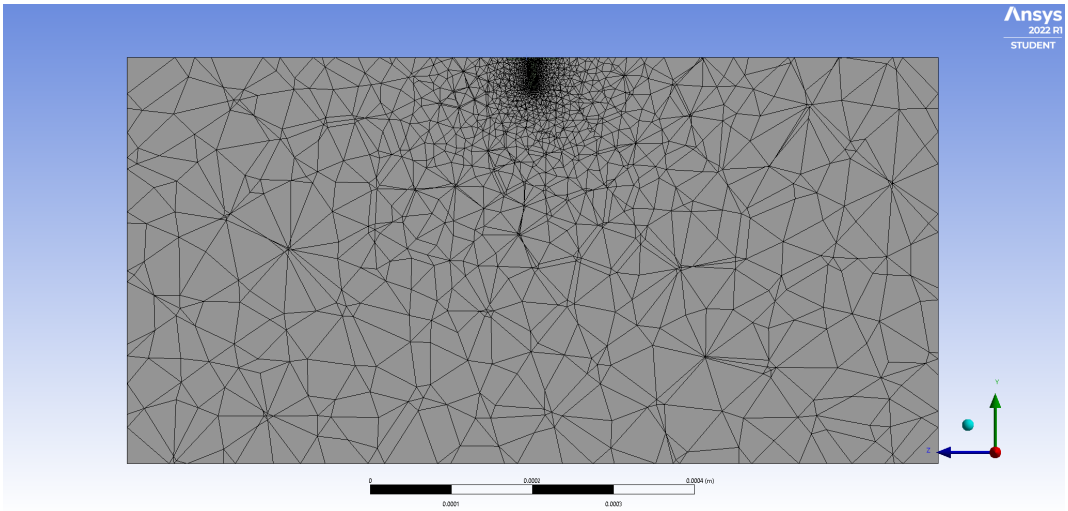

Figure 4.4: ANSYS rendering of a material block cross-section with the CFD mesh displayed.

The specific settings for the solver were as follows:

- Element Order: Linear
- Element Size: Default ($7.5E-005\ m$)
- Bounding Box Diagonal: $1.5E-003\ m$
- Average Surface Area: $2.6747E-007\ m^2$
- Minimum Edge Length: $4.1343E-005\ m$
- Smoothing: Medium

The number of Nodes and Elements varies based on the size of the Impact Site. This was impacted based on which sample was being simulated, i.e. 5-1 or 5-2 for crater width, and which laser Power was being used (for crater depth). The exact number of Nodes for each model are presented in Table 4.4. The number of Elements for each model are presented in Table 4.5.

Table 4.4: The number of Nodes generated for each model's CFD Mesh based on the crater and bore hole dimensions

Number of Nodes in CFD Mesh					
Sample	0.6 W	1.2 W	1.8 W	2.4 W	3.0 W
5-1 ETD 094	8926	9321	9321	10529	10850
5-2 ETD 102	10278	11037	11101	12448	12677
5-4 ETD 116 & 118	7595	8058	8140	8854	8998
5-5 ETD 122 & 124	8107	8775	8835	9655	9809

Table 4.5: The number of Elements generated for each model's CFD Mesh based on the crater and bore hole dimensions

Number of Elements in CFD Mesh					
Sample	0.6 W	1.2 W	1.8 W	2.4 W	3.0 W
5-1 ETD 094	10850	47997	47997	54542	56362
5-2 ETD 102	52965	57094	57600	64525	66227
5-4 ETD 116 & 118	38834	41424	41613	45797	46600
5-5 ETD 122 & 124	41580	45368	45720	50208	50990

4.1.2 Transient Thermal Analysis

As ANSYS is not capable of fully simulating a plasma, creativity was necessary in how the available data was used to facilitate a realistic solution. It was determined that the best approach was to use the Transient Thermal as in both sets of simulations, the heat flux is not constant throughout the course of the simulation. In both cases, the Initial Temperature of the material block and the ambient surroundings was set to a Uniform Temperature of 22 $\circ C$ as both HELIOS and the laser ablation experiments were performed in a room temperature environment.

Where the two sets begin to differ is in the Analysis Settings, namely in the way the stepping was controlled for each analysis. For the HELIOS based simulations, the Number Of Steps were set to the number of data points from that were from the ETFLOW simulation and each Step End Time was set to the Time Value converted from μs to s for the appropriate step. As such, Auto Time Stepping was left to read in the tabular data that provided by the user and the Solver was Program Controlled. In contrast, the Laser Ablation based simulations were set to have only 10 steps, with their Step End Time each being 1 s. Auto Time Stepping was turned OFF and was defined by the number of Substeps, which was set to 100. The decision for the switch came after conversation with a fellow researcher on the project whose

samples were the basis for the Laser Ablated ANSYS models.

Application of Convective boundaries and Heat Flux were accomplished in three parts: applying a Convective boundary the material block, a Convective boundary for the Impact Site, and the impinging Heat Flux. The material block's Convective boundary was applied to five faces – the four cardinal faces and the top (which included laser site) as these were all exposed to air in test environments, the bottom of the material block did not receive a boundary as it was implied that it would be attached to a mount or table and not exposed. For the second Convective boundary, the Impact Site, one of two scenarios was used – in the case of the HELIOS simulations, a tabular Film Coefficient was used in which there was a different value for each Step, for the Laser Ablation simulations, a constant Film Coefficient was used that was different for each case that was investigated. It should be noted that the location of where the second Convective boundary was placed had two locations, yielding two sets of simulations – in one set, the Top Face of the Impact Site was selected and in the other, entire Body of the Impact Site was chosen. Heat Flux, on the other hand, was applied to only the Top Face of the Impact Site and, in both cases, used tabular data provided by the user. In the case of the HELIOS simulations, this data was ETFLOW generated for each time step; for the Laser Ablated simulations, the Heat Flux was assumed to be deposited all at once at the first Step or Time 1 s and had a magnitude of 4×10^{10} W/m^2.

4.2 HELIOS Spectroscopy Simulations

4.2.1 HELIOS ANSYS Setup

The HELIOS simulation set was performed using the original iteration of the Heat Flux model as shown in Figure 4.1. In addition to a model featuring a 30 μm bore hole, two more were simulated with a 10 and 23 μ bore hole. This set of material blocks were designed to mimic a plasma beam impinging on a material's surface, much like the plasma jet that leaves the HELIOS system. As these simulations were based on ETFLOW data and not physical, no melt craters were included in these simulations like in the laser ablation spectroscopy simulations. The 10, 23, and 30 μm bore hole depths were selected based on feedback from experiments, providing an average depth to work with as well as diameter for the bore hole itself, 11 μm.

As a major driving factor of the ETFLOW portion of simulation was that Ideal and Non-Ideal Conductivity model calculations did, in fact, produce different values for Total Ablated Mass

as well as Temperature and Heat Flux, it was only appropriate it simulate an Ideal and Non-Ideal case for each ANSYS model, as well. To do this, a single material was selected for testing, in this case, Pure Tungsten at 2.50 × P228 as this current profile produced the highest temperatures and heat fluxes for both Ideal and Non-Ideal ETFLOW simulations. Pure Tungsten was selected for the HELIOS simulations as the four laser ablation samples discussed in Section 4.3 were Tungsten slabs.

As briefly mentioned in Section 4.1.2, the Number Of Steps that were used for each simulation were pulled directly from each ETFLOW simulation as these were the number of data points that each simulation generated. For the Ideal simulation, the Number Of Steps was 422, and for the Non-Ideal simulation, the Number Of Steps 398. Auto Time Stepping was turned Off and it was Defined By the Substeps, which was set to 1. This was to ensure that, when the time (which had been converted from μs to s) was added to each component (Convection or Heat Flux) that it did not alter the timing between steps. It should be noted that Time, Temperature, and Heat Flux (which was the Radiative Heat Flux) were taken directly from the ETFLOW generated data and were only altered in that units needed to be changed. The Convection Coefficient, however, did need to be calculated. This was done by simply dividing the Radiative Heat Flux values by the Temperature values after they had been converted from Kelvin to Celsius. With the necessary data and Convective boundaries applied, simulations could begin.

4.2.2 HELIOS ANSYS Simulation Results

In total, 12 ANSYS simulations were performed for the HELIOS/ETFLOW styled model. These simulations included Face and Body convective boundary simulations of all three models (10, 23, and 30 μm bore holes) and each were run twice using Ideal and Non-Ideal ETFLOW data for Pure Tungsten at 2.50 × P228. The values from these runs along with the number of CFD mesh Nodes and Elements can be found in Table 4.6.

Immediately apparent is the difference in Maximum Heat Flux values based on the application of the Convective boundary in the simulation. If the boundary is placed on the Top Face, listed as Face in the table, the Maximum Heat Flux value was, on average, 0.77 times higher than when the boundary was placed on the Body of the Impact Site. This applies to both the Ideal and Non-Ideal cases, even with the values for Non-Ideal simulations generally being lower than the Ideal simulations. Of the six simulations that utilized the Top Face of the Impact Plug, the 23 μm deep bore hole models had the highest Maximum Heat Flux for

Table 4.6: The maximum amount of heat flux generated when the Convective boundary for the laser is set to impinge on the Top Face of the Impact Site.

HELIOS ANSYS Simulation Information				
	CFD Mesh Information		Maximum Heat Flux (W/m^2)	
HELIOS Simulation	Nodes	Elements	Face	Body
Ideal - 10 μm	7037	34389	2.079×10^{10}	1.528×10^{10}
Ideal - 23 μm	9261	44205	2.080×10^{10}	1.632×10^{10}
Ideal - 30 μm	10340	48570	2.075×10^{10}	1.660×10^{10}
Non-Ideal - 10 μm	7037	34389	1.390×10^{10}	1.016×10^{10}
Non-Ideal - 23 μm	9261	44205	1.391×10^{10}	1.089×10^{10}
Non-Ideal - 30 μm	10340	48570	1.387×10^{10}	1.105×10^{10}

both Ideal and Non-Ideal cases, with values of 2.080×10^{10} W/m^2 and 1.391×10^{10} W/m^2, respectively. This was also true for the Non-Ideal, Body Convective Boundary 23 μm case, which had a value of 1.086×10^{10} W/m^2. For the Ideal, Body Convective Boundary cases, the 30 μm case had the highest Maximum Heat Flux value at 1.664×10^{10} W/m^2.

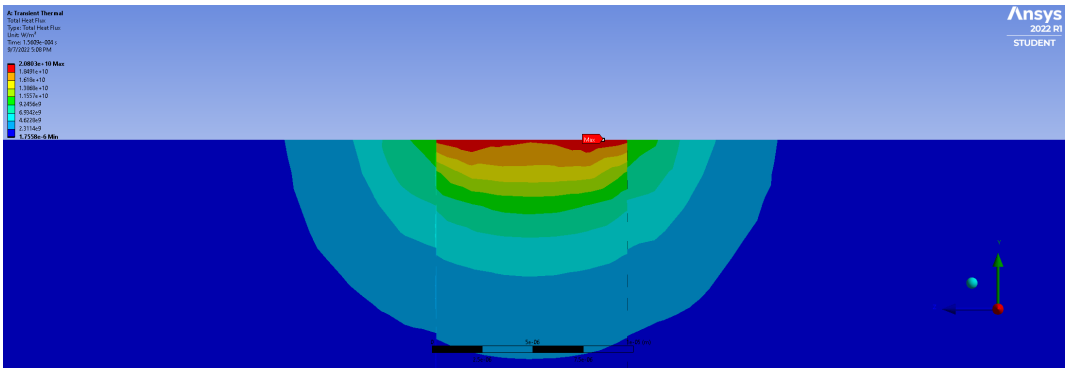

Figure 4.5: ANSYS Total Heat Flux results based Ideal ETFLOW data with the Convective boundary set to the Top Face of the Impact Site.

Select examples of the ANSYS outputs for the Ideal runs can been found in Figures 4.5 and 4.7. In Figure 4.5, the Heat Flux is dissipated through the material from the top surface of the Impact Site. The heat radiates outward from the center of the top of the Impact Site in a hemisphere configuration, with the highest amount of flux being deposited in the center of the top of the Impact Site. The size of the heat flux zone is roughly 25 μm in diameter and 11.25 μm deep – this is twice the diameter of the bore hole and only half its depth. Figure 4.6 is the Non-Ideal case in which the Top Face was selected for the Convective boundary. Like in Figure 4.5, the Maximum Heat Flux was at the top of the Impact Site plug, however,

it was ringed around the edge of the plug and not distributed across the top as it was in the Ideal case.

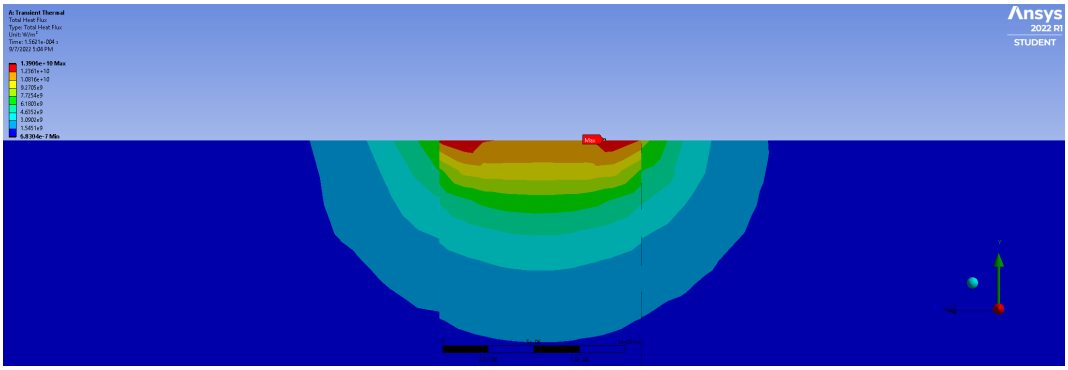

Figure 4.6: ANSYS Total Heat Flux results based Non-Ideal ETFLOW data with the Convective boundary set to the Top Face of the Impact Site.

Figure 4.7 shows how the heat dissipates through the material when the Convective boundary is set to the Body of the Impact Site in the 23 μm model. As mentioned before, the Maximum Heat Flux values for these simulations were lower than for the ones using the Top Face as the boundary. In both the Ideal and Non-Ideal cases, the highest Heat Flux values were near the top of the Impact Site plug, around the edge. The heat radiates out from the entire body of the plug, as seen in green, all the way around the plug in a roughly 60 μm diameter by 40 μm area. Seen in both cases, there is dark blue area at the bottom of the plug indicating that the heat dissipated through the sides of the plug, top to bottom. Notably, this area in Figure 4.8 is much larger than the one in Figure 4.7.

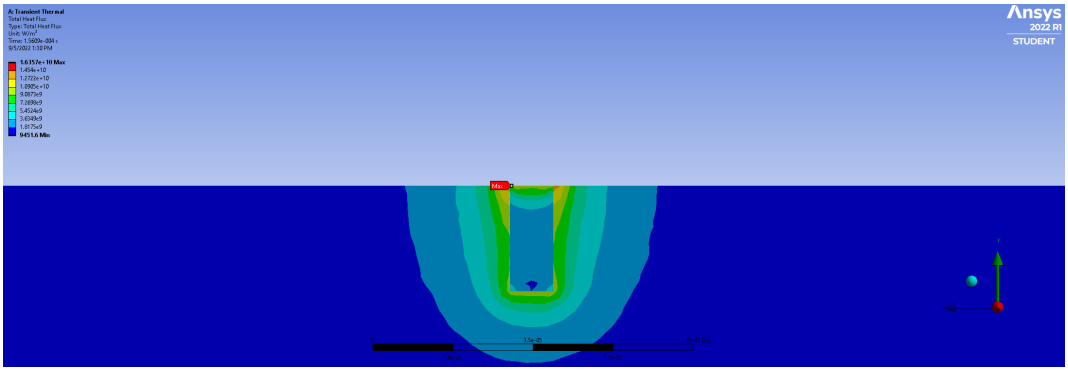

Figure 4.7: ANSYS Total Heat Flux results based Ideal ETFLOW data with the Convective boundary set to the Body of the Impact Site.

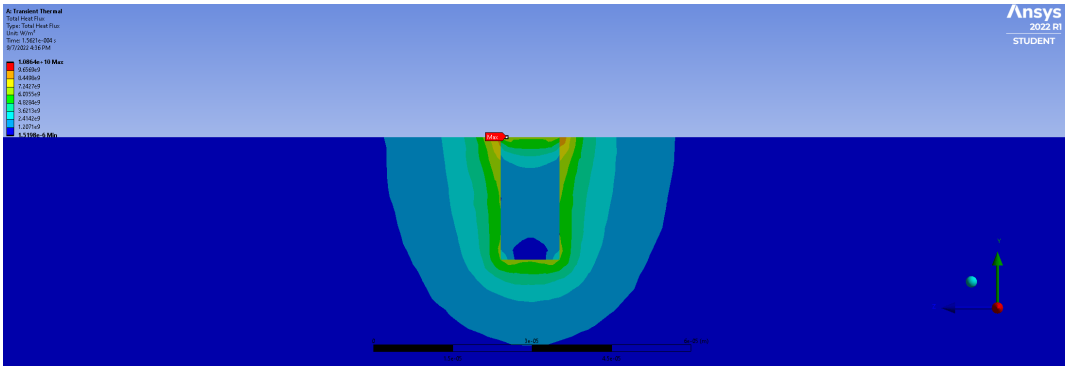

Figure 4.8: ANSYS Total Heat Flux results based Non-Ideal ETFLOW data with the Convective boundary set to the Body of the Impact Site.

While not presented in the table, it should be noted that average temperature of the material blocks themselves did not exceed melting (3410 $°C$), which also implies that the boiling or vaporization temperature was not exceeded (5930 $°C$). However, based on the temperature curve data, these temperatures were reached, though only briefly. This would indicate is that a small amount of surface matter is being vaporized and melted while the bulk of the surface is remaining intact. This partially vaporized, as well as ionized, material would turn into a cloud of plasma with particulate suspended in it. This plasma could be classified as a dusty plasma, the same one theorized to form in the capillary type space in Godiva IV.

4.3 Laser Spectroscopy – Experiments and Simulations

4.3.1 Laser Assembly Setup

The laser system used to deposit energy on the samples is a Ti:Sapphire femtosecond laser system operating at a wavelength of 800 nm and a pulse frequency of 1000 Hz. Figure 4.9 is a photograph of the experimental setup. During the experiment, tungsten samples were placed at the focal point of of the optics, perpendicular to the laser beam. The laser beam power was set at 3.0, 2.4, 1.8, 1.2, and 0.6 W, which was measured by a thermal power meter. The equivalent pulse energy is 3.0, 2.4, 1.8, 1.2, and 0.6 mJ per pulse experiment provided by 1, 10, 50, 450, and 1100 pulses.

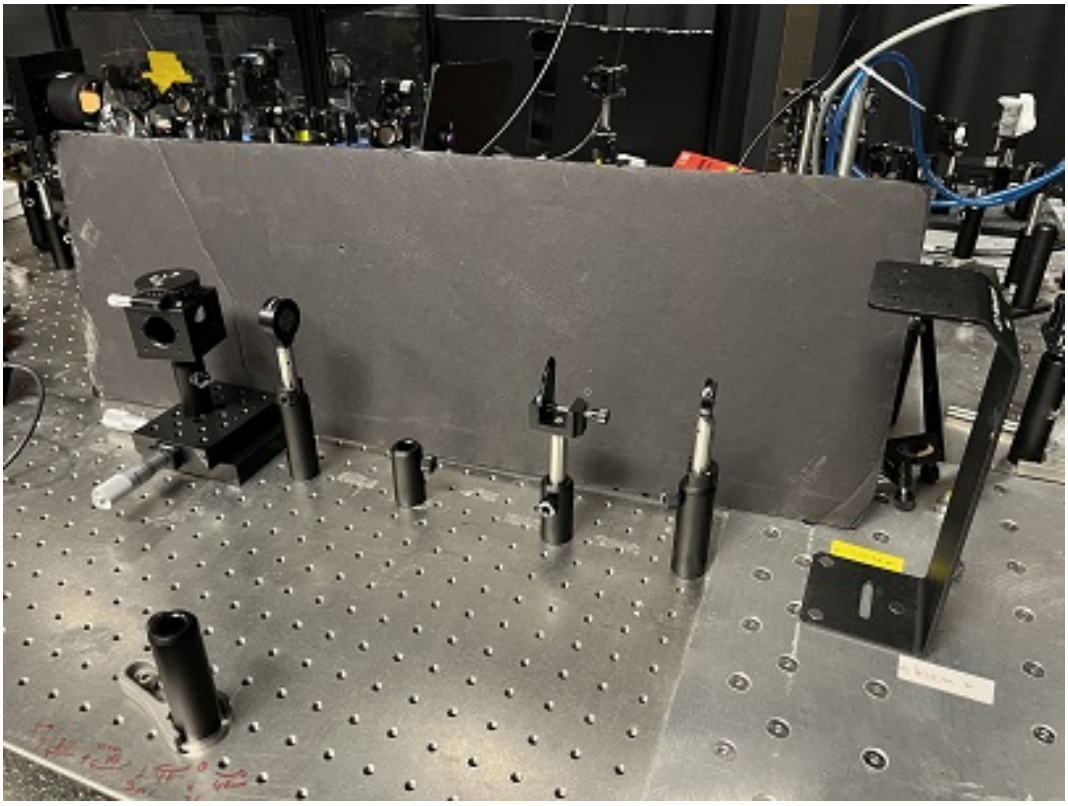

Figure 4.9: Photo of Laser System in the Laboratory Setting [6].

4.3.2 Laser Ablation ANSYS Setup

As stated previously, setup of the ANSYS model relied heavily on the physical attributes of laser ablation samples – the specific samples used in creating the models were 5-1 ETD 094, 5-2 ETD 102, 5-4 ETD 116 & 118, and 5-5 ETD 124 & 126. The SEM images in Figures 4.10 - 4.13 show what has been referred to as the "impact crater" or, as in the models, the "Impact Site." These craters are the result of the material melting around the laser impact site over the course of however many pulses that specific shot was for, in the case of the 5-# series, it was 50 laser pulses, each 100 fs in length. Shown in blue on the images are the dimensions of each crater – the width and height, as well as the bore hole diameter. To get a crater diameter, the width and height of each crater was averaged to get an approximate value, these values along with the bore hole widths were reported in Table 4.2. The crater and bore hole depths were taken from a Surface Roughness table provided by the researcher who performed the measurements. These values, originally reported as Sa, Sq, and Sz, refer to the arithmetical mean height, root mean square height, and the maximum height, respectively. Sa expresses the difference in height of each point compared to the arithmetical mean of the

surface [26]. Sq is the equivalent to the standard deviation of the heights [27]. Sz is the sum of the largest peak height value and the largest pit depth value within the defined area [28]. As such, the Sa and Sq values were averaged together to get a depth of the crater and the Sz value was taken to be the depth of the bore hole, these values were reported in Table 4.1.

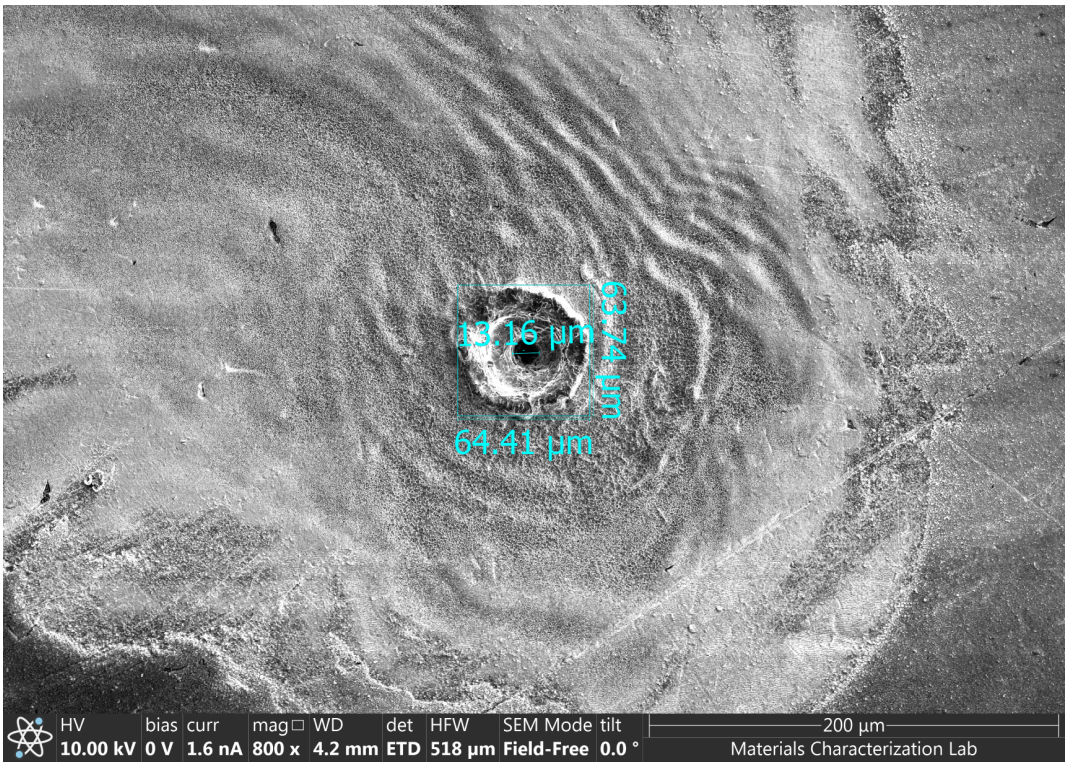

Figure 4.10: SEM Image of the laser impact site on Tungsten sample 5-1 [6].

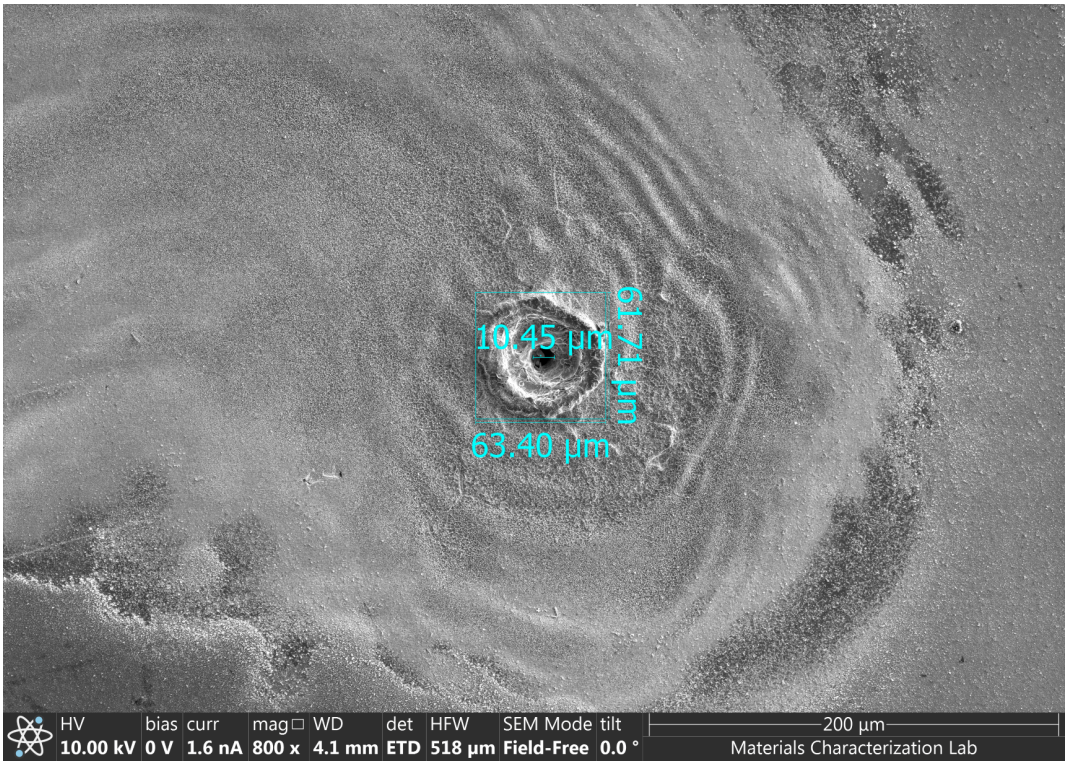

Figure 4.11: SEM Image of the laser impact site on Tungsten sample 5-2 [6].

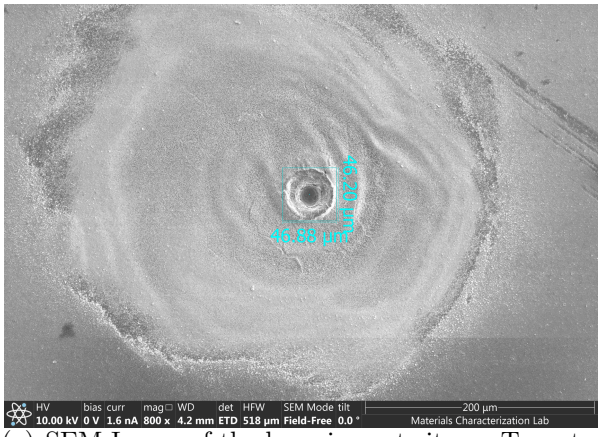

(a) SEM Image of the laser impact site on Tungsten sample 5-4 with the crater's width and length.

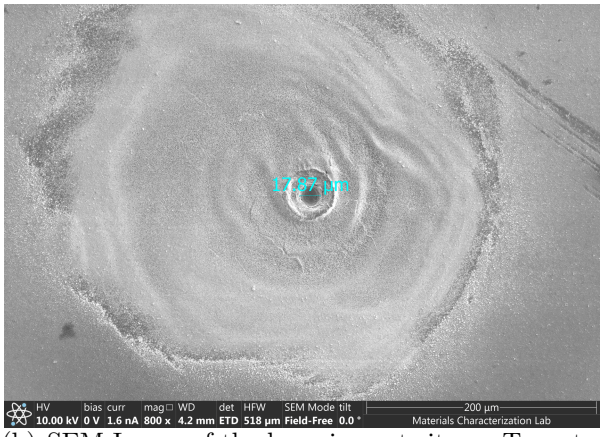

(b) SEM Image of the laser impact site on Tungsten sample 5-4 with the crater's diameter.

Figure 4.12: Tungsten Sample 5-4 SEM Images [6].

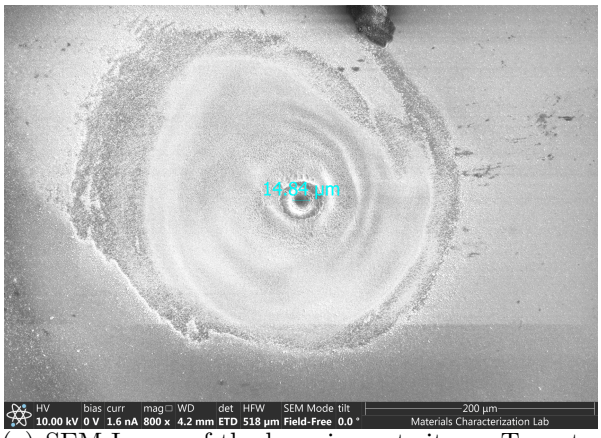

(a) SEM Image of the laser impact site on Tungsten sample 5-5 with the crater's diameter.

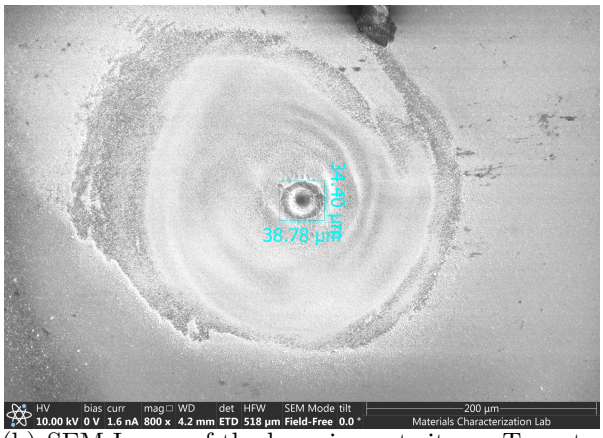

(b) SEM Image of the laser impact site on Tungsten sample 5-5 with the crater's width and length.

Figure 4.13: Tungsten Sample 5-5 SEM Images [6].

Other parameters required for the ANSYS model, however, like the Convection Coefficient ($W/m^2 \cdot C$) in Tables 4.7 and 4.8, had to be calculated for each sample, using Equation 4.1. It should be noted that as two types of boundary conditions were used, Convection via the Top Face and the Body of the Impact Site, two sets of Convection Coefficients were computed and used in their respective simulations.

$$h = \frac{P_{\text{Pulse}}}{A \cdot \Delta T}. \tag{4.1}$$

In Equation 4.1, h represents the Convection Coefficient in $W/m^2 \cdot C$, P_{Pulse} is the power of each pulse in Watts (W), and A is the area of interest in μm. ΔT is the change in temperature, $°C$, as a result of the heat that is transferred from the fluid (the plasma) to the material surface. To successfully calculate the Convection Coefficient for each sample, the primary researcher provided information on the laser powers and temperatures associated with the laser. The laser pulse strengths, as previously reported were 0.6, 1.2, 1.8, 2.4, and 3.0 W, however, there was another power that was associated with the laser, 3×10^{10} W that was also used in calculations. Two temperature values were provided for the pulse power levels of 0.7 and 2.1 W - 5200 and 5600 K, respectively. To get the temperature values for the five laser powers that were used in the experiment, the equation of a line was calculated using the power level and temperature as point pairs. Using this equation, the five temperatures for the five laser powers that were used in experiments were calculated and used as the incoming heat in the ΔT portion of Equation 4.1. For the calculations in Table 4.7, the area used

was the area of the circle of the Top of the Impact Site; calculations for the Coefficients in Table 4.8 used was the total surface area of both the crater and the bore hole, based on the ANSYS model. Where a significant change was made was in which power was used in the actual calculation; after much deliberation with primary researcher, it was determined that the much higher 3×10^{10} W power should be used in place of the lower ones. Their reasoning for this was due to a lack of a Heat Affected Zone (HAZ) and no evidence of remelting in or around the laser site.

Table 4.7: Convection Coefficients for the Laser samples examined with SEM - Face Boundary Conditions

Convection Coefficients (W/m^2C)				
Power W	5-1 ETD 094	5-2 ETD 102	5-4 ETD 116 & 118	5-5 ETD 122 & 124
0.6	2.020×10^{15}	2.120×10^{15}	3.830×10^{15}	6.195×10^{15}
1.2	1.948×10^{15}	2.044×10^{15}	3.692×10^{15}	5.973×10^{15}
1.8	1.880×10^{15}	1.973×10^{15}	3.564×10^{15}	5.766×10^{15}
2.4	1.817×10^{15}	1.907×10^{15}	3.445×10^{15}	5.573×10^{15}
3.0	1.758×10^{15}	1.845×10^{15}	3.333×10^{15}	5.392×10^{15}

Table 4.8: Convection Coefficients for the Laser samples examined with SEM - Body Boundary Conditions

Convection Coefficients (W/m^2C)				
Power W	5-1 ETD 094	5-2 ETD 102	5-4 ETD 116 & 118	5-5 ETD 122 & 124
0.6	788.8	849.6	1170	1676
1.2	721.6	778.7	1044	1477
1.8	678.2	731.7	974.2	1372
2.4	633.1	686.4	880.9	1228
3.0	596.6	647.0	823.3	1142

With the values that were mentioned previously as well as the ones calculated specifically for this section, each sample was simulated in the manner described in Section 4.1.2 – once with the Convective boundary set to the Top Face of the Impact Site and once with the boundary set to the Body. Additionally, each sample had five run types, one for each laser power, as the depth of the crater and bore hole changed with increasing laser power. This resulted in each sample model being run a total of 10 times for a grand total of 40 simulations. The results from the simulations are in Section 4.3.3.

4.3.3 Laser Ablation ANSYS Simulation Results

Completing the simulations yielded Total Heat Flux maps that were quite interesting in the fact that, depending on how the Convective boundary was allocated to the Impact Site, the Heat Flux map would be look one of two ways. If the Convective boundary was applied to the Top Face of the Impact Site, the area of increased Heat Flux penetration would be small, a roughly 120 μm by 120 μm by 50 μm volume of space would be affected to an appreciable amount. An example of the Total Heat Flux dissipating through one of the sample models in this manner is shown in Figure 4.14. For simplification purposes, the maximum values of the Total Heat Flux for each simulation performed using the Top Face as the Convective boundary have been presented in Table 4.9.

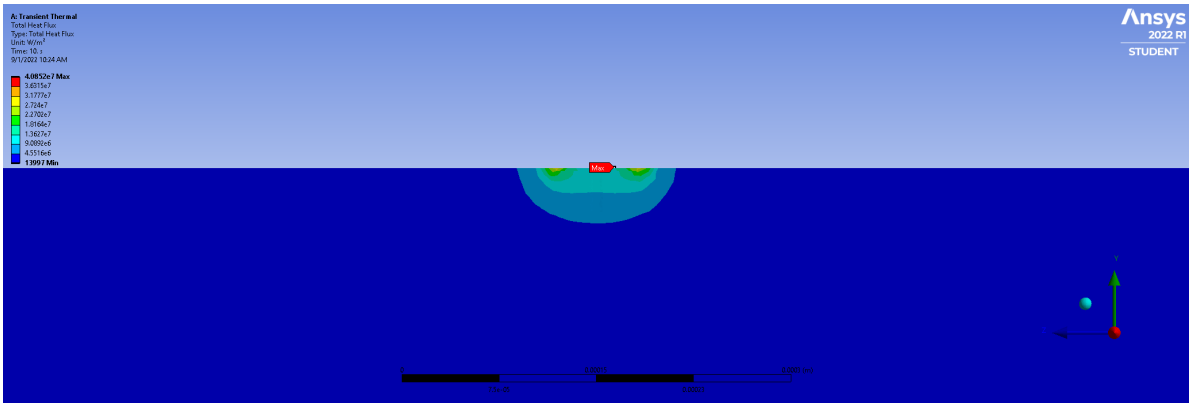

Figure 4.14: ANSYS Total Heat Flux results based on the laser Convective boundary being placed on the Top Face of the Impact Site.

Table 4.9: The maximum amount of heat flux generated when the Convective boundary for the laser is set to impinge on the Top Face of the Impact Site.

	Maximum Heat Flux (W/m^2)			
	5-1 ETD 094	5-2 ETD 102	5-4 ETD 116 & 118	5-5 ETD 122 & 124
0.6 W	4.085×10^7	3.939×10^7	7.847×10^7	1.188×10^8
1.2 W	4.066×10^7	4.122×10^7	7.141×10^7	1.047×10^8
1.8 W	4.014×10^7	3.991×10^7	6.951×10^7	8.653×10^7
2.4 W	4.039×10^7	4.037×10^7	7.095×10^7	9.351×10^7
3.0 W	3.796×10^7	3.916×10^7	5.623×10^7	1.045×10^8

The values in Table 4.9 show how both the configuration of the model, i.e., crater/bore hole dimensions, as well as the temperature of the laser effect the resulting Heat Flux that is deposited to the area. A general trend is that increasing the Power, which increases the

Temperature, ultimately results in a decrease in the overall Maximum Heat Flux value for the simulation. This is to be expected as the Convection Coefficients that were calculated for each case decreased with increasing temperature (see Equation 4.1). All values are in the range of 10^7 W/m^2, which is high enough to ablate and melt the material that the laser is interacting with at the surface.

The same phenomenon is seen in Table 4.10 in which the Maximum Heat flux values for 0.6 W are the highest and those for 3.0 W are the lowest. Values for the Heat Flux were in the expected range of 10^7 - 10^8 W/m^2 for all samples. An example of the heat dissipation through the material with in which the Body of the Impact Site is selected can be seen in Figure 4.15. In this example, the outline of the Impact Site is clearly visible with "hot spots" along the edges of the crater (top disk) and at the bottom of the bore hole. The highest reported Heat Fluxes were located at the bottom of the bore hole, which is to be expected as this is where the laser would deposit the most energy and heat in the physical experiment.

Table 4.10: The maximum amount of heat flux generated when the Convective boundary for the laser is set to impinge on the Body of the Impact Site.

	Maximum Heat Flux (W/m^2)			
	5-1 ETD 094	5-2 ETD 102	5-4 ETD 116 & 118	5-5 ETD 122 & 124
0.6 W	7.280×10^7	7.714×10^7	4.875×10^7	3.971×10^7
1.2 W	6.435×10^7	6.721×10^7	4.360×10^7	3.413×10^7
1.8 W	6.131×10^7	6.401×10^7	4.010×10^7	3.085×10^7
2.4 W	5.480×10^7	5.748×10^7	3.674×10^7	2.781×10^7
3.0 W	5.193×10^7	5.408×10^7	3.320×10^7	2.652×10^7

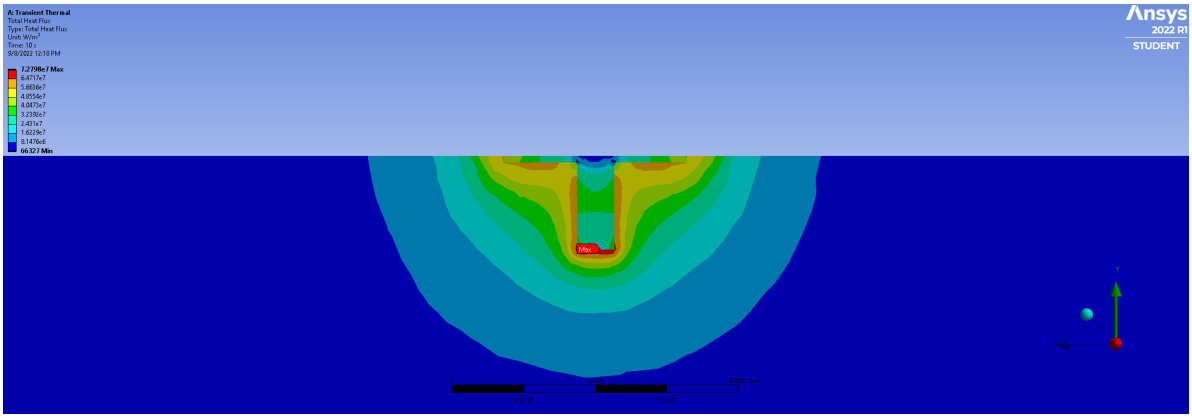

Figure 4.15: ANSYS Total Heat Flux results based on the laser Convective boundary being placed on the Body of the Impact Site for Sample 5-1 ETD 094 - 0.6 W.

Generally, temperatures that were observed in the Laser Ablation simulations indicated melting and vaporization of material occurred. This is to be expected as there was melting observed in the crater area of the SEM images and an obvious lack of material as a result the laser ablating the material. While the temperatures were much higher than those calculated in the HELIOS models, leading to the assertion that the material was completely vaporized and not turned into partially ionized cloud, it still stands that this method would produce a cloud of fully ionized material at the surface of the material, leading to more ablation. Thus, this model type, though specific to the type of aberrations seen in the measurements taken by the primary researcher, could be used to model other experiment types in the future.

Chapter 5
Summary & Conclusions

5.1 Summary of Work

The study of plasmas has been a burgeoning field for the past few decades, with advancements being made in the areas of fusion occurring at a staggering speed. To aid in this effort, research focusing on materials for use in tokamaks has been an area of interest as these materials are the main stopping point in the advancement of tokamak technology. However, ELM interactions with first wall materials are not the only type of plasma surface interaction that occurs in the world of fusion. Dusty plasmas, as previously discussed, are a class of plasmas that contain partially ionized and suspended material (that are on the scale of nanometers in size) in a plasma cloud. These plasmas have a high likelihood of recombination and are short lived in laboratory settings. It was a plasma of this kind that was theorized to form during the normal burst operations of Fast Burst Device Godiva IV, however, accounts of plasma formation were only ever through observation of mass loss in the device and not through investigation itself.

As such, this study was conducted to simulate the formation of a dusty plasma in the area between the Safety Block and Intermediate Inner Subassembly Plates. The study was broken into two parts, the first of which leveraged ETFLOW, a 1-D, time-dependent eletrothermal plasma code, to simulate the plasma parameters for the dusty plasma based on the materials that make up the ablating surface. The resulting simulation set contained a number of materials, including a set of Tungsten-Molybdenum alloys that served as an analogue for future spectroscopy experiments, a set of Uranium-Molybdenum alloys which included the U-Mo alloy that Godiva IV is composed of, TZM Alloy, and various individual elements that

were constituent parts of the other alloys or areas that needed to be filled in with simulation data. The resulting data set included a suite of 27 different materials, each with two sets cases with 10 simulations in each set. ETFLOW has two Conductivity models that the user can choose from – Ideal and Non-Ideal, it was determined that each material should be simulated using each model for the full set of 10 P228 Discharge Current variants. Upon the successful ETFLOW simulation completion and plasma parameter evaluation, phase two and three of the study could begin – the Heat Flux Study.

The Heat Flux Study was, itself, a two-part study that involved simulation and physical experiment. Simulations involved leveraging the CFD capabilities of ANSYS to simulate the ETFLOW generated data as well as the results of the laser ablation spectroscopy experiments. As just mentioned, the physical experiments included laser ablation spectroscopy which used a [LASER INFORMATION] to perform a series of ablations on Tungsten samples. The number of pulses and the laser power were varied, including 1, 5, 10, 50, 450, 600, and 1100 pulse ablation samples. Based on conversation with the researcher who performed the experiments, it was decided to simulate a select number of the 50-pulse ablation set. These results, along with those from the ANSYS simulations using the ETFLOW data, were compiled and compared – their maximum heat flux values being consolidated into the Tables in Sections 4.2.2 and 4.3.3.

5.2 Mass Loss Mitigation Model

Aside from determining the type of plasma that is forming during ablation, the task of creating a Mass Loss Mitigation Model was also a goal that we wanted to achieve or at least begin working on by the end of the project. A proposed method of determining how much mass is lost during an event such as an ELM or plasma-surface interaction would be to first run an ETFLOW simulation for the material that is being affected. This may involve creating a custom material, such as was done for the Uranium-Molybdenum alloys, in which case an appropriate literature review must be conducted to see which method is best for combining material properties together. A list of the material properties that are needed for an ETFLOW material library entry to run properly can be found in Section 3.2.3. Once the material has been created, a Discharge Current Profile – either from the library of previously performed HELIOS shots or by using and manipulating the P228 shot data, as was done here.

After the desired number of ETFLOW simulations have been performed, including Ideal and Non-Ideal simulations to create the necessary banding for physical experiment parameters, an ANSYS model can be used to model the Heat Flux as it is dissipated through the material surface. An existing model, like the 10, 23, and 30 μm set can be used or a custom set like the Laser Ablation ones can be made based on physical experiments. Generally, a sketch is needed of the energy will be deposited in the area as this will inform the design. This information can be obtained based on information about the conditions under which the material is being treated – is it a plasma facing component inside of a tokamak or the wing of an aircraft being exposed to cosmic radiation? The energy range of particles that would be impinging on the material surface in these conditions can be calculated, as well as their temperatures, the material's temperature, and other information required to make the model and subsequent calculations work. Using this information, a simulation can then be performed that would allow the user to simulate how far into the material heat and, therefore, heat damage travels. Combined with the information such as the Total Ablated Mass values that ETFLOW generates, users to make decisions about component thickness to increase the longevity of said component such that it will not succumb to failure too quickly.

5.2.1 Godiva IV Specific Model

A step that should be added to the mass loss model that is specific to Godiva IV is the addition of running the ICSBEP benchmark MCNP models prior to beginning the process of simulating the plasmas in ETFLOW and ANSYS. The reason for doing so is that the MCNP data that is calculated, such as the particle information - both energies and number density information, can be used to further inform the simulations that proceed it. The MCNP model, which is taken to be an accurate representation of the real-life Godiva IV system, has been tested and verified as part of the ICSBEP process, increasing the confidence in the output values. As mentioned, particle data can be taken from the MCNP output and entered into ANSYS along with an accurate 3D simulation of the device, rather than a simple slab of material as has been done to simulate a surface or wall. In terms of coupling the MCNP data with ETFLOW, the capillary space can be further refined to match the device specs as well as tweaking the shot times and currents to be similar to the times and energy outputs expected in the MCNP simulations. An additional step can be taken in which experimental data can be referenced from the previous Godiva IV pulses to further refine any ETFLOW/ANSYS models to fill in the gaps where simulations may not be able to provide the information, such as taking recorded temperature data from a transient and inputting that data into an ANSYS

simulation. In general, while it is easier to take a pre-made MCNP model and apply that data collection to Godiva IV, MCNP models can be made for any surface or assembly that is of interest as long as the physical parameters are known for the object. This information could then be leveraged to perform the same process as discussed for Godiva IV [29].

5.2.1.1 Godiva IV Mass Loss Calculations

Using the Surface Area for the capillary zone in Godiva IV, which was calculated using the dimensions for the Simplified Model of Godiva IV (i.e. Homogenized Fuel Ring) that were provided in Table 32 of the ICSBEP HEU-MET-FAST-086 document [1], and using the Total Moss Lost to Ablation and Engery curve data from ETFLOW, the Moss Loss per Surface Area (g/cm^2) and Mass Loss per Energy Deposited (g/MeV) values were calculated for each U-Mo Alloy. Presented in this Section are the values for U-Mo(1.5%), the alloy that Godiva IV is comprised of. The other four alloy tables can be found in Appendix B for the sake of space, but conclusions will be drawn from them here.

Table 5.1 presents the Mass Loss per Surface Area (SA) as calculated for each of the Ideal and Non-Ideal set of the High and Low Conductivity variants of the ETFLOW material based on the surface area of the Godiva IV capillary zone. These results can be directly compared to the Mass Loss per Surface Area presented in Table 5.2 that were calculated using the surface area of the capillary in ETFLOW. Immediately apparent is the increased values of Mass Loss per SA in the ETFLOW calculations compared to the Godiva IV calculations - this occurs across all Current Mulitplier values and simulation types for both Conductivity model variants of the U-Mo(1.50%) alloy. This was also the case when looking at the values in the tables for the other U-Mo alloys in Appendix B. One of the proposed reasons for this difference is the increased surface area that was used in the Godiva IV calculations compared to the ETFLOW capillary surface area - 108.07 cm^2 vs. 10.30 cm^2. When the Godiva IV surface area is normalized to Surface Area of the ETFLOW capillary, we see similar values to what the ETFLOW simulations produced, as seen in Table 5.3.

Table 5.1: The mass loss per surface area for U-Mo(1.50%) computed using the Godiva IV capillary zone surface area.

U-Mo(1.50%) - Mass Loss per Surface Area (g/cm^2)				
	Ideal		Non-Ideal	
Current (kA)	High	Low	High	Low
2.50	1.186×10^{-5}	1.190×10^{-5}	8.034×10^{-6}	8.032×10^{-6}
2.25	1.055×10^{-5}	1.058×10^{-5}	7.153×10^{-6}	7.178×10^{-6}
2.00	9.242×10^{-6}	9.264×10^{-6}	6.310×10^{-6}	6.335×10^{-6}
1.75	7.982×10^{-6}	7.993×10^{-6}	5.500×10^{-6}	5.527×10^{-6}
1.50	6.741×10^{-6}	6.764×10^{-6}	4.718×10^{-6}	4.742×10^{-6}
1.25	5.576×10^{-6}	5.600×10^{-6}	3.947×10^{-6}	3.971×10^{-6}
1.00	4.450×10^{-6}	4.480×10^{-6}	3.195×10^{-6}	3.217×10^{-6}
0.75	3.370×10^{-6}	3.399×10^{-6}	2.435×10^{-6}	2.462×10^{-6}
0.50	2.292×10^{-6}	2.320×10^{-6}	1.647×10^{-6}	1.675×10^{-6}
0.25	1.138×10^{-6}	1.165×10^{-6}	7.971×10^{-7}	8.267×10^{-7}

Table 5.2: The mass loss per surface area for U-Mo(1.50%) computed using the ETFLOW capillary surface area.

U-Mo(1.50%) - Mass Loss per Surface Area (g/cm^2)				
	Ideal		Non-Ideal	
Current (kA)	High	Low	High	Low
2.50	1.244×10^{-4}	1.249×10^{-4}	8.425×10^{-5}	8.424×10^{-5}
2.25	1.107×10^{-4}	1.109×10^{-4}	7.502×10^{-5}	7.528×10^{-5}
2.00	9.692×10^{-5}	9.715×10^{-5}	6.617×10^{-5}	6.644×10^{-5}
1.75	8.370×10^{-5}	8.383×10^{-5}	5.768×10^{-5}	5.796×10^{-5}
1.50	7.070×10^{-5}	7.094×10^{-5}	4.948×10^{-5}	4.974×10^{-5}
1.25	5.848×10^{-5}	5.873×10^{-5}	4.139×10^{-5}	4.165×10^{-5}
1.00	4.667×10^{-5}	4.698×10^{-5}	3.350×10^{-5}	3.373×10^{-5}
0.75	3.534×10^{-5}	3.564×10^{-5}	2.554×10^{-5}	2.582×10^{-5}
0.50	2.404×10^{-5}	2.433×10^{-5}	1.727×10^{-5}	1.757×10^{-5}
0.25	1.194×10^{-5}	1.222×10^{-5}	8.360×10^{-6}	8.669×10^{-6}

Table 5.3 contains the values of the Mass Loss per Surface Area (Godiva IV) normalized to the ETFLOW capillary surface area. As stated previously, normalizing the Godiva IV surface area to that of the ETFLOW capillary surface area produced values that were on par with those produced from the pure ETFLOW capillary surface area. The same can be found to occur for the other U-Mo alloys in Appendix B. This proves that the ETFLOW model is scaleable to the size of the capillary zone physically present in Godiva IV and that it can be

used to simulate electrothermal plasma formations, successfully.

Table 5.3: Godiva IV mass loss per surface area for U-Mo(1.50%) normalized to the ETFLOW capillary surface area.

U-Mo(1.50%) - Mass Loss per Surface Area (g/cm^2)				
	Ideal		Non-Ideal	
Current (kA)	High	Low	High	Low
2.50	1.223×10^{-4}	1.227×10^{-4}	8.279×10^{-5}	8.277×10^{-5}
2.25	1.088×10^{-4}	1.090×10^{-4}	7.371×10^{-5}	7.396×10^{-5}
2.00	9.523×10^{-5}	9.546×10^{-5}	6.502×10^{-5}	6.528×10^{-5}
1.75	8.224×10^{-5}	8.236×10^{-5}	5.667×10^{-5}	5.695×10^{-5}
1.50	6.946×10^{-5}	6.970×10^{-5}	4.861×10^{-5}	4.887×10^{-5}
1.25	5.746×10^{-5}	5.771×10^{-5}	4.067×10^{-5}	4.092×10^{-5}
1.00	4.586×10^{-5}	4.616×10^{-5}	3.292×10^{-5}	3.315×10^{-5}
0.75	3.472×10^{-5}	3.502×10^{-5}	2.509×10^{-5}	2.537×10^{-5}
0.50	2.362×10^{-5}	2.390×10^{-5}	1.697×10^{-5}	1.726×10^{-5}
0.25	1.173×10^{-5}	1.201×10^{-5}	8.214×10^{-6}	8.518×10^{-6}

As Godiva IV has been in service for around 60 years, it is reasonable to assume that a number of burst operations have occurred during its service career. During a 2019 trip to the DAF for a routine burst experiment set, it was recorded that the device had, including those bursts, burst around 2163 times. While, the exact number of each burst type, i.e. amount of reactivity insertion, and frequency were not noted at that time, the fact that an appreciable amount of mass (i.e. around 1.5 g) had been lost from the device over its operational history. As mentioned in Chapter 1 and Chapter 3, operators observed the missing mass while cleaning massing the device during a move from LANL to the DAF, where it currently resides. The main theory was ablation in a capillary like void between the Intermediate Inner Subassembly Plate (IISP) and the Safety Block.

Table 5.4 presents the raw, un-normalized Mass Loss per Godiva IV capillary Surface Area data over 2163 bursts. Like with the singleton "bursts," the Mass Loss per Godiva IV capillary Surface Area was significantly less than the Mass Loss per ETFLOW capillary Surface Area, as seen in Table 5.5. This was resolved, however, once the Godiva IV Surface Area was normalized, producing values much closer to those seen in the pure ETFLOW calculations (Table 5.6). While these values are lower than the expected value of around 1.5 g that was cited, it is important to note that other factors may have attributed to some of the mass loss in addition to the abblative process, such as the oxidization of the U-Mo alloy that comprises the fuel. It should be noted that Uranium-Oxide "dust" has been found on components of

the device due to exposure to the air in the room that device inhabits. In an attempt to mitigate some of the oxidization, the fuel was aluminum-ion plated, reducing contamination and loss of fuel [30]. While the plating has helped, it did not completely stop all fuel loss, as is evident in observations, measurement, and simulations.

Table 5.4: The mass loss per surface area for U-Mo(1.50%) computed using the Godiva IV capillary zone surface area for 2163 bursts.

U-Mo(1.50%) - Mass Loss per Surface Area (g/cm^2)				
	Ideal		Non-Ideal	
Current (kA)	High	Low	High	Low
2.50	0.026	0.026	0.017	0.017
2.25	0.023	0.023	0.015	0.016
2.00	0.020	0.020	0.014	0.014
1.75	0.017	0.017	0.012	0.012
1.50	0.015	0.015	0.010	0.010
1.25	0.012	0.012	0.009	0.009
1.00	0.010	0.010	0.007	0.007
0.75	0.007	0.007	0.005	0.005
0.50	0.005	0.005	0.004	0.004
0.25	0.002	0.003	0.002	0.002

Table 5.5: The mass loss per surface area for U-Mo(1.50%) computed using the ETFLOW capillary surface area for 2163 bursts.

U-Mo(1.50%) - Mass Loss per Surface Area (g/cm^2)				
	Ideal		Non-Ideal	
Current (kA)	High	Low	High	Low
2.50	0.269	0.270	0.182	0.182
2.25	0.239	0.240	0.162	0.163
2.00	0.210	0.210	0.143	0.144
1.75	0.181	0.181	0.125	0.125
1.50	0.153	0.153	0.107	0.108
1.25	0.126	0.127	0.090	0.090
1.00	0.101	0.102	0.072	0.073
0.75	0.076	0.077	0.055	0.056
0.50	0.052	0.053	0.037	0.038
0.25	0.026	0.026	0.018	0.019

Table 5.6: The mass loss per surface area for U-Mo(1.50%) computed using the normalized surface area for 2163 bursts.

U-Mo(1.50%) - Mass Loss per Surface Area (g/cm^2)				
	Ideal		Non-Ideal	
Current (kA)	High	Low	High	Low
2.50	0.264	0.265	0.179	0.179
2.25	0.235	0.236	0.159	0.160
2.00	0.206	0.206	0.141	0.141
1.75	0.178	0.178	0.123	0.123
1.50	0.150	0.151	0.105	0.106
1.25	0.124	0.125	0.088	0.089
1.00	0.099	0.100	0.071	0.072
0.75	0.075	0.076	0.054	0.055
0.50	0.051	0.052	0.037	0.037
0.25	0.025	0.026	0.018	0.018

A question was raised as to how much mass was lost as a result of the energy deposited in the area, as calculated by ETFLOW, the results of which can be found in Table 5.7. It should be noted that the unit of the Deposited Energy is MeV, as such, the amount of mass lost due to energy deposition is quite high per MeV. With increased current, for all U-Mo alloys, there was higher energy deposition, which lead to generally higher mass loss values, regardless of the Conductivity model used in ETFLOW or the Conductivity variant of the alloy.

Table 5.7: The mass loss per energy deposited for U-Mo(1.50%).

U-Mo(1.50%) - Mass Loss per Energy Deposited (g/MeV)				
	Ideal		Non-Ideal	
Current (kA)	High	Low	High	Low
2.50	5.184×10^{13}	5.374×10^{13}	4.358×10^{13}	3.083×10^{13}
2.25	5.374×10^{13}	5.365×10^{13}	3.114×10^{13}	3.109×10^{13}
2.00	3.583×10^{13}	4.530×10^{13}	2.643×10^{13}	2.646×10^{13}
1.75	4.340×10^{13}	2.983×10^{13}	2.616×10^{13}	2.621×10^{13}
1.50	2.922×10^{13}	2.924×10^{13}	2.536×10^{13}	2.532×10^{13}
1.25	3.190×10^{13}	2.676×10^{13}	1.942×10^{13}	1.946×10^{13}
1.00	2.335×10^{13}	2.341×10^{13}	1.699×10^{13}	1.701×10^{13}
0.75	1.535×10^{13}	1.849×10^{13}	1.345×10^{13}	1.348×10^{13}
0.50	1.472×10^{13}	1.475×10^{13}	8.180×10^{12}	8.182×10^{12}
0.25	2.885×10^{12}	2.881×10^{12}	1.432×10^{12}	1.430×10^{12}

Figure 5.1 is a plot of the Mass Loss per Normalized Surface Area versus the Peak Energy Deposited for each variant of the U-Mo(1.50%) alloy. It can be easily seen that, at lower energies, there is very tight banding between each of the variants, with the Ideal and Non-Ideal Conductivity cases overlapping their respectively High-Low counterparts. After roughly $3.224 \times 10^{15}\ MeV$, the tight banding seen in the Ideal Conductivity cases is lost and values become more spread out. It should also be noted that the Non-Ideal Conductivity case values, while remaining tightly bound together, all occur prior to $3.359 \times 10^{15}\ MeV$ and only have a maximum mass loss per normalized surface area value (for the Low Thermal Conductivity U-Mo(1.50%) Variant) of $8.277 \times 10^{-5}\ g/cm^2$, which occurs at $3.331 \times 10^{15}\ MeV$. This contrasts the Ideal Conductivity cases which have a maximum value of $1.277 \times 10^{-4}\ g/cm^2$, which occurs at $5.807 \times 10^{15}\ MeV$, also for the Low Thermal Conductivity U-Mo(1.50%) Variant. Similar results can be found in the plots for the other U-Mo alloys in Appendix B.

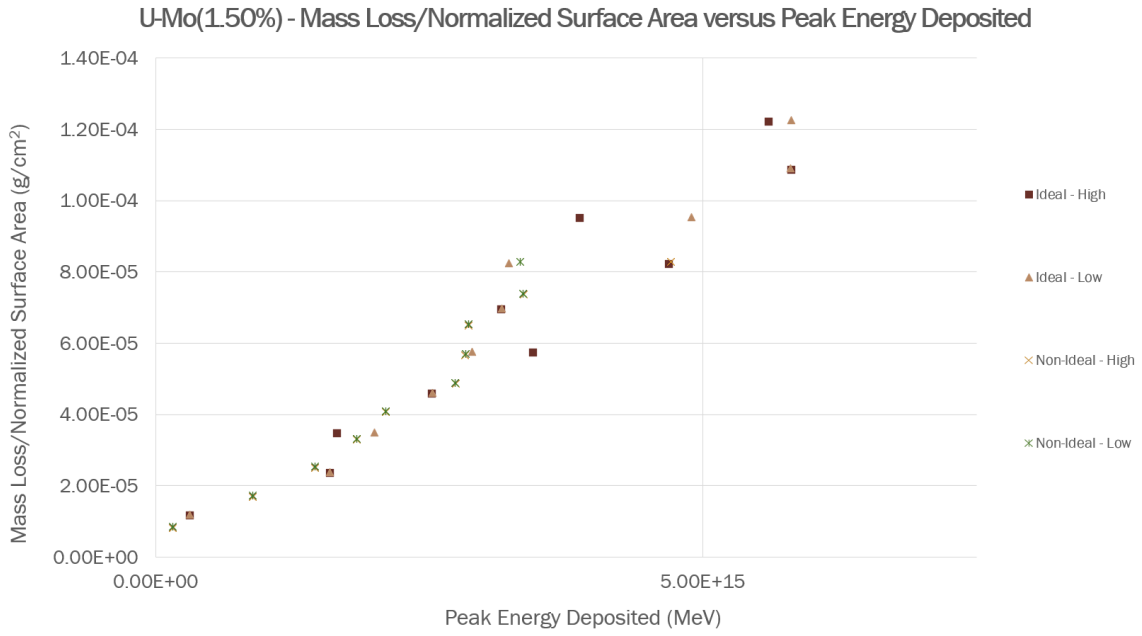

Figure 5.1: The Mass Loss/Normalized Surface Area (g/cm^2) plotted against the Deposited Energy (MeV) for U-Mo(1.50%)

5.3 Final Conclusions

The ultimate goal of this study was to quantify and qualify the ablative process that is occurring during normal burst operations in Godiva IV and based on the information gathered

from simulations and the original observations themselves, it can be concluded that a loosely formed, partially ionized plasma does form during the pulse. This conclusion was based on the ETFLOW data as well as the fact that the ANSYS model did not show temperatures that would indicate melting or vaporization of all of the material in the path of the heat that was being impinged. This means that, while the bulk of the material does in fact heat up (and it is through rapid thermal expansion that burst operations self-terminate), only some surface material may experience heat up significant enough to vaporize it into a plasma, creating cloud just about the surface of the material, in this case the Safety Block. As the pulse is terminated so quickly, and the heating source is therefore removed just as quickly, it is safe to say that this plasma is not maintained and dissipates quickly, likely through recombination and is redeposited on the surface as soot.

Chapter 6
Future Work

6.1 Proposed Work

Continued work in this area would include expanded ETFLOW and ANSYS simulations. While number simulations have been performed in ETFLOW, more materials can always be added to the catalogue. In the past, the primary focus has been placed on Refractory Metals as these materials produce great electrothermal plasmas for surface depositions and fuel pellet injectors – as such, there are a number of simulations involving alloys made up of these metals. In the study that was performed here, gaps were filled by adding singleton materials (i.e., Pure Tungsten and Molybdenum) that were being simulated with new Discharge Current Profiles as well as adding new alloys that never been simulated before (such as Tungsten-Molybdenum and Uranium-Molybdenum). By continuing to add to the "library," researchers will be able to further materials research for electrothermal plasma and fusion applications, alike.

In the same vein as continuing more simulation work with ETFLOW would be to continue more simulation work with ANSYS. While discussed, an ANSYS model that directly mimics the HELIOS system was not created at this time; however, the creation of such a model would allow for the direct coupling of ETFLOW data with ANSYS and allow for better simulations to occur. It would also be a desire for more of the materials that were simulated using ETFLOW to be simulated in an ANSYS model, specifically the more exotic alloys, and have these materials simulated in the HELIOS system model. Additionally, improvements to the Laser Ablation model should be made in which the number of pulses be more accurately represented during the simulation.

Lastly, if it is at all possible, gaining access to Godiva IV so that spectroscopy of the plasma

could occur in real time as well as pre- and post-burst mass measurements to confirm the amount of mass lost per burst time would be a wonderful way to fully close out the project.

6.2 Impact

Previously, not much computational work had been performed on electrothermal plasma formation regarding heavy metals where the goal was to specifically look for a dusty plasma like formation. As Godiva IV is such a unique device, being able to predict the ablation behavior of the bursts it performs is useful in helping prolong its lifespan as we will be able to predict the amount of damage each burst will do. As demonstrated in Section 5.2.1.1, ETFLOW is a useful tool in accomplishing this goal and, coupled with MCNP and ANSYS, can provide a wealth of information for both this device, and others. Through this process, the limits of ETFLOW have continued to be pushed and the limits of what this program can successfully do tested - in doing so, we continue to discover new, exciting areas of research that this code is capable of exploring, opening new doors that had previously been closed due to limitations in previously existing software.

Appendix A
ETFLOW Simulation Results

As stated throughout the document, numerous materials were simulated using ETFLOW - however, not all could be included in the main body of the research document. Provided in this appendix are the tables and plots for the materials that were simulated in addition to those discussed in the results section of this document.

A.1 Tungsten-Molybdenum Alloys

Combined Ideal and Non-Ideal ETFLOW simulation results for the second set of Tungsten-Molybdenum alloys that were simulated. Referred to as W(%)-Mo alloys, these alloys were ones in which the concentration of Tungsten was the main focus of alteration, rather than the Molybdenum. The W-Mo alloys that were chosen were done so in a way that they mimicked Uranium enrichments in various nuclear fuel types: two Light Water Reactor fuel enrichments, one at the highest end of the Low Enriched Uranium spectrum, and two Highly Enriched Uranium variants.

A.1.1 W(3.00%)-Mo Results

Table A.1: ETFLOW Simulations of W(3.00%)-Mo - Ideal Cases

Ideal Cases				
I (kA)	q" (GW/m^2)	T_{peak} (eV)	N_E (m^{-3})	M_{tot} (mg)
2.50	393.4	2.850	1.305×10^{27}	1.691
2.25	319.0	2.762	1.154×10^{27}	1.528
2.00	252.3	2.666	1.005×10^{27}	1.364
1.75	192.6	2.560	8.630×10^{26}	1.194
1.50	141.8	2.458	7.225×10^{26}	1.028
1.25	98.42	2.330	5.755×10^{26}	0.852
1.00	63.05	2.187	4.347×10^{26}	0.673
0.75	35.37	2.023	2.947×10^{26}	0.487
0.50	15.73	1.813	1.694×10^{26}	0.300
0.25	3.937	1.486	6.610×10^{25}	0.124

Table A.2: ETFLOW Simulations of W(3.00%)-Mo - Non-Ideal Cases

Non-Ideal Cases				
I (kA)	q" (GW/m^2)	T_{peak} (eV)	N_E (m^{-3})	M_{tot} (mg)
2.50	393.8	2.575	8.723×10^{26}	1.437
2.25	319.0	2.508	7.782×10^{26}	1.270
2.00	252.1	2.428	6.736×10^{26}	0.974
1.75	192.8	2.337	5.738×10^{26}	0.851
1.50	141.4	2.238	4.742×10^{26}	0.725
1.25	98.53	2.130	3.744×10^{26}	0.596
1.00	62.87	2.007	2.793×10^{26}	0.466
0.75	35.44	1.862	1.908×10^{26}	0.334
0.50	15.62	1.677	1.173×10^{26}	0.207
0.25	3.939	1.371	4.434×10^{25}	0.083

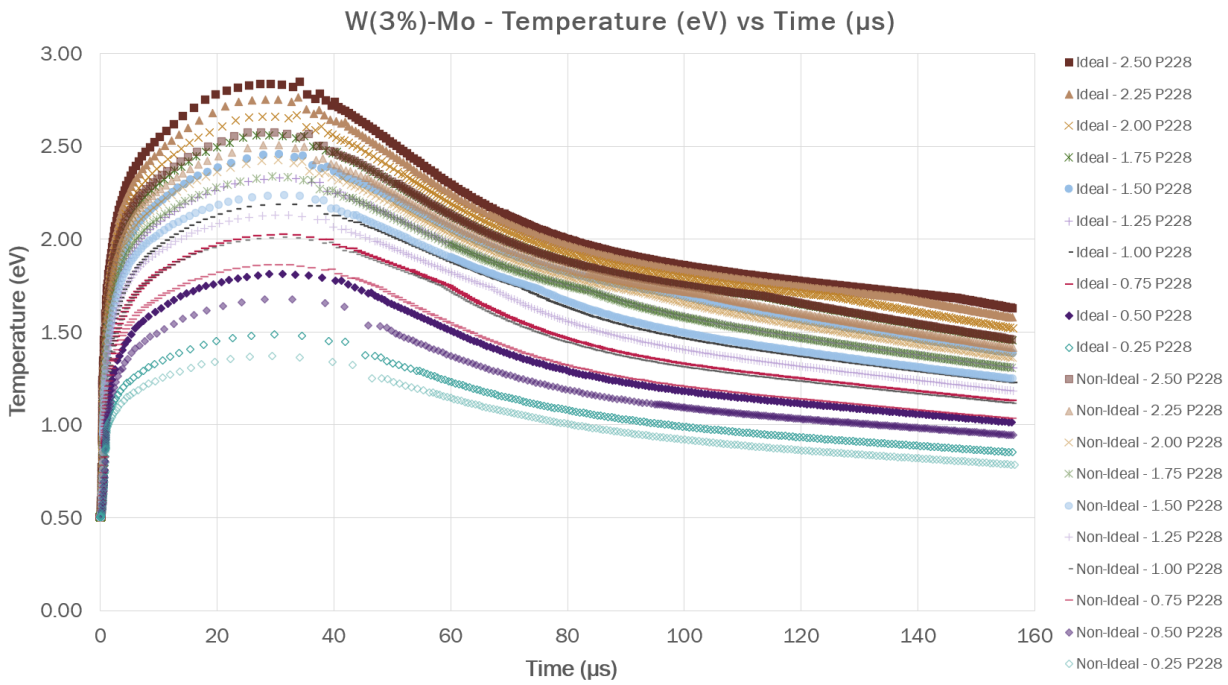

Figure A.1: W(3.00%)-Mo Temperature (eV) versus Time (μs) as generated by ETFLOW

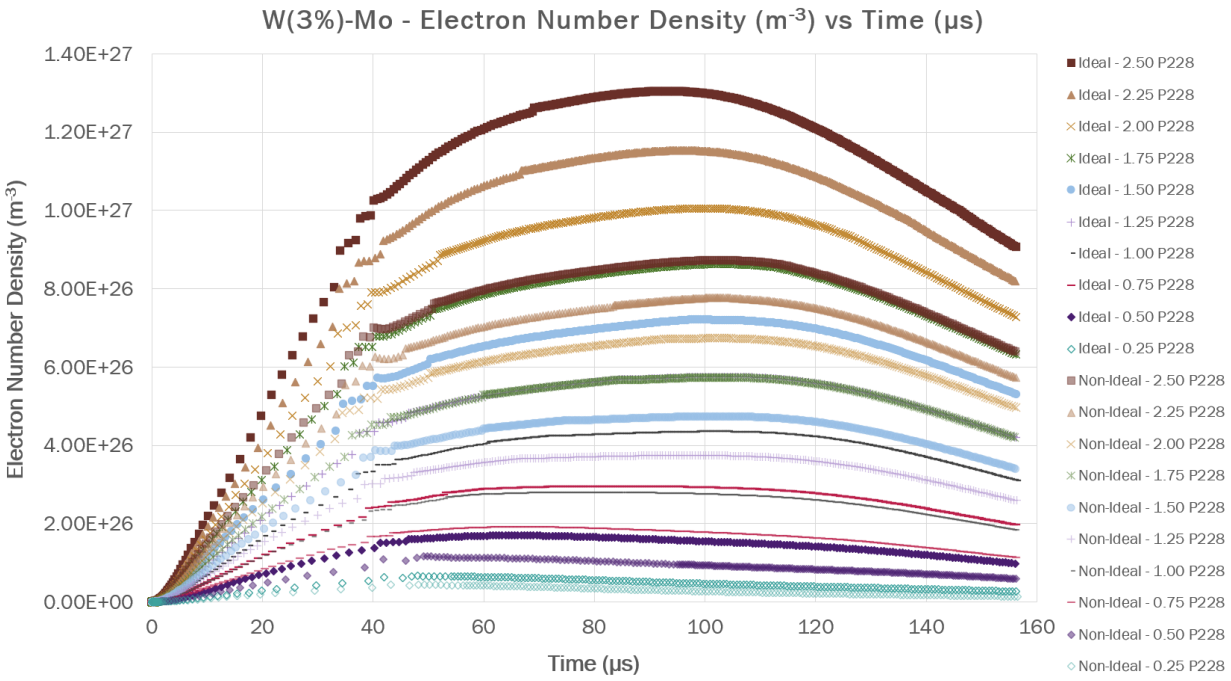

Figure A.2: W(3.00%)-Mo Electron Number Density (m^{-3}) versus Time (μs) as generated by ETFLOW

A.1.2 W(5.00%)-Mo Results

Table A.3: ETFLOW Simulations of W(5.00%)-Mo - Ideal Cases

Ideal Cases				
I (kA)	q" (GW/m^2)	T_{peak} (eV)	N_E (m^{-3})	M_{tot} (mg)
2.50	393.3	2.853	1.304×10^{27}	1.690
2.25	319.0	2.765	1.152×10^{27}	1.527
2.00	252.3	2.669	1.004×10^{27}	1.362
1.75	192.6	2.562	8.618×10^{26}	1.196
1.50	141.8	2.460	7.211×10^{26}	1.027
1.25	98.42	2.333	5.743×10^{26}	0.851
1.00	63.05	2.189	4.335×10^{26}	0.672
0.75	35.47	2.025	2.938×10^{26}	0.486
0.50	15.73	1.814	1.689×10^{26}	0.300
0.25	3.937	1.487	6.590×10^{25}	0.124

Table A.4: ETFLOW Simulations of W(5.00%)-Mo - Non-Ideal Cases

Non-Ideal Cases				
I (kA)	q" (GW/m^2)	T_{peak} (eV)	N_E (m^{-3})	M_{tot} (mg)
2.50	394.1	2.578	8.718×10^{26}	1.211
2.25	318.8	2.513	7.775×10^{26}	1.094
2.00	252.1	2.430	6.724×10^{26}	0.973
1.75	192.8	2.339	5.727×10^{26}	0.850
1.50	141.4	2.240	4.731×10^{26}	0.724
1.25	98.50	2.132	3.734×10^{26}	0.596
1.00	62.87	2.009	2.786×10^{26}	0.465
0.75	35.46	1.864	1.903×10^{26}	0.334
0.50	15.62	1.679	1.170×10^{26}	0.206
0.25	3.939	1.372	4.420×10^{25}	0.083

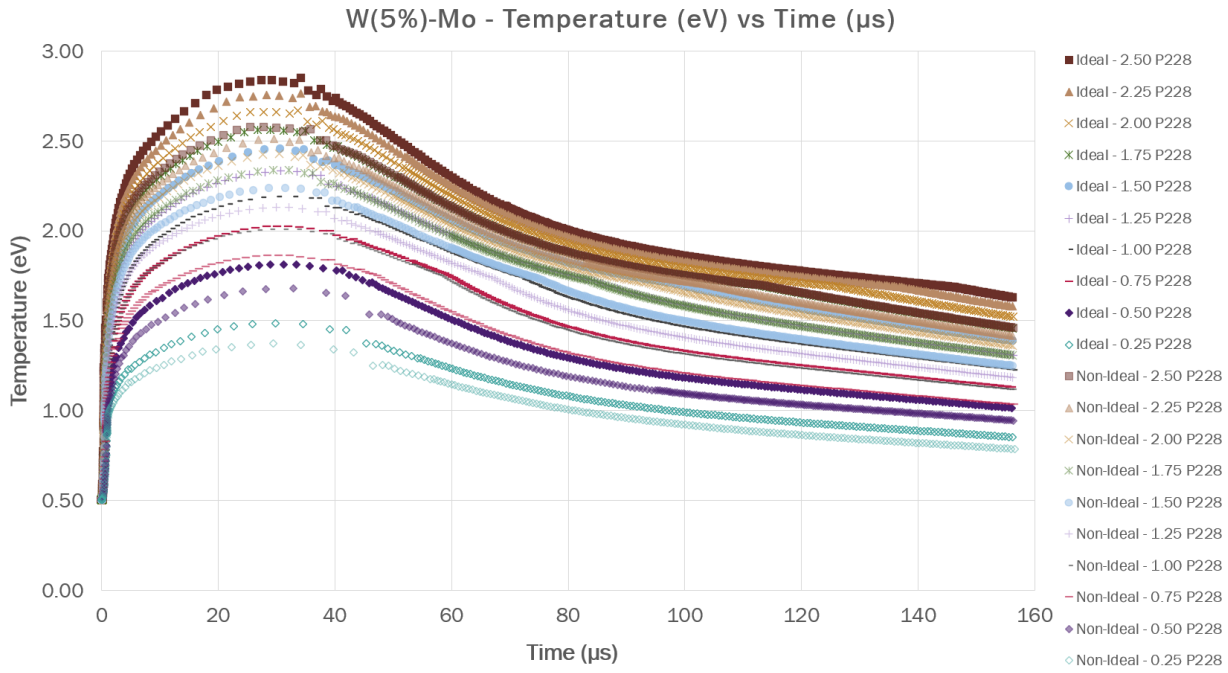

Figure A.3: W(5.00%)-Mo Temperature (eV) versus Time (μs) as generated by ETFLOW

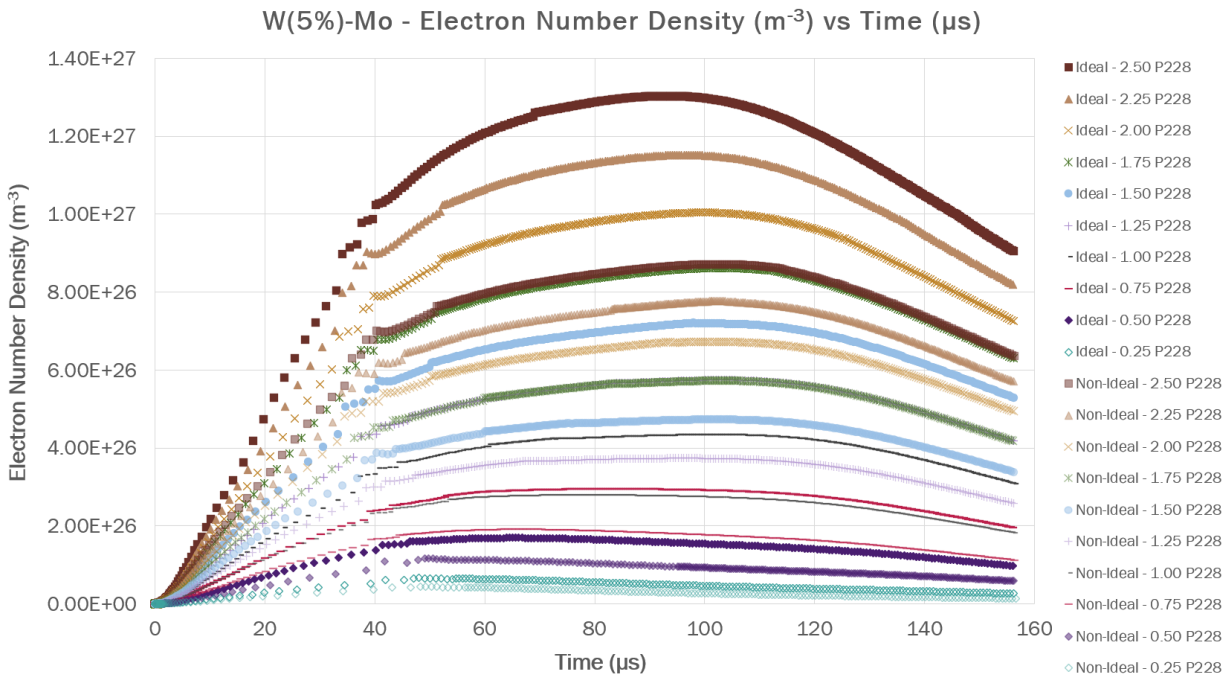

Figure A.4: W(5.00%)-Mo Electron Number Density (m^{-3}) versus Time (μs) as generated by ETFLOW

A.1.3 W(19.5%)-Mo Results

Table A.5: ETFLOW Simulations of W(19.5%)-Mo - Ideal Cases

Ideal Cases				
I (kA)	q" (GW/m^2)	T_{peak} (eV)	N_E (m^{-3})	M_{tot} (mg)
2.50	393.0	2.887	1.296×10^{27}	1.681
2.25	318.8	2.795	1.143×10^{27}	1.517
2.00	251.9	2.684	9.958×10^{26}	1.352
1.75	193.0	2.582	8.536×10^{26}	1.186
1.50	141.8	2.476	7.124×10^{26}	1.017
1.25	98.42	2.347	5.670×10^{26}	0.843
1.00	63.05	2.203	4.254×10^{26}	0.664
0.75	35.40	2.037	2.882×10^{26}	0.480
0.50	15.76	1.824	1.665×10^{26}	0.296
0.25	3.937	1.496	6.447×10^{25}	0.121

Table A.6: ETFLOW Simulations of W(19.5%)-Mo - Non-Ideal Cases

Non-Ideal Cases				
I (kA)	q" (GW/m^2)	T_{peak} (eV)	N_E (m^{-3})	M_{tot} (mg)
2.50	394.1	2.595	8.644×10^{26}	1.201
2.25	318.8	2.529	7.693×10^{26}	1.085
2.00	252.1	2.446	6.643×10^{26}	0.965
1.75	192.9	2.351	5.642×10^{26}	0.841
1.50	141.3	2.254	4.643×10^{26}	0.716
1.25	98.50	2.145	3.664×10^{26}	0.589
1.00	62.91	2.021	2.736×10^{26}	0.460
0.75	35.46	1.874	1.867×10^{26}	0.330
0.50	15.62	1.678	1.149×10^{26}	0.204
0.25	3.939	1.381	4.318×10^{25}	0.081

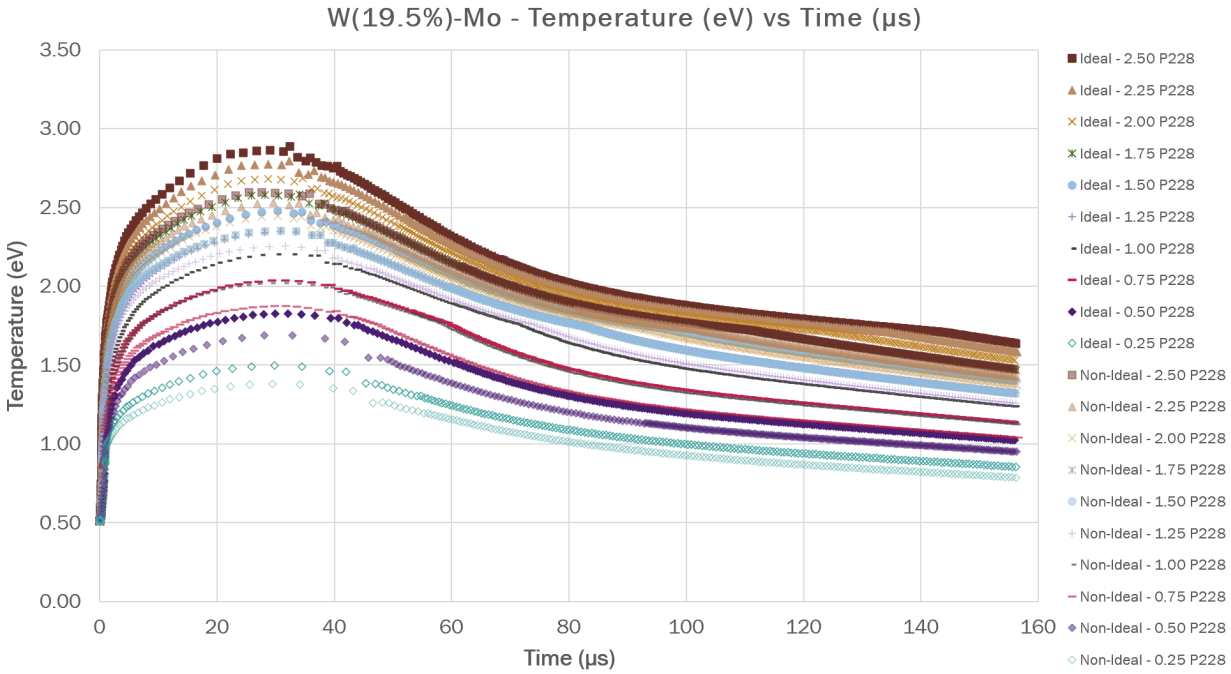

Figure A.5: W(19.5%)-Mo Temperature (eV) versus Time (μs) as generated by ETFLOW

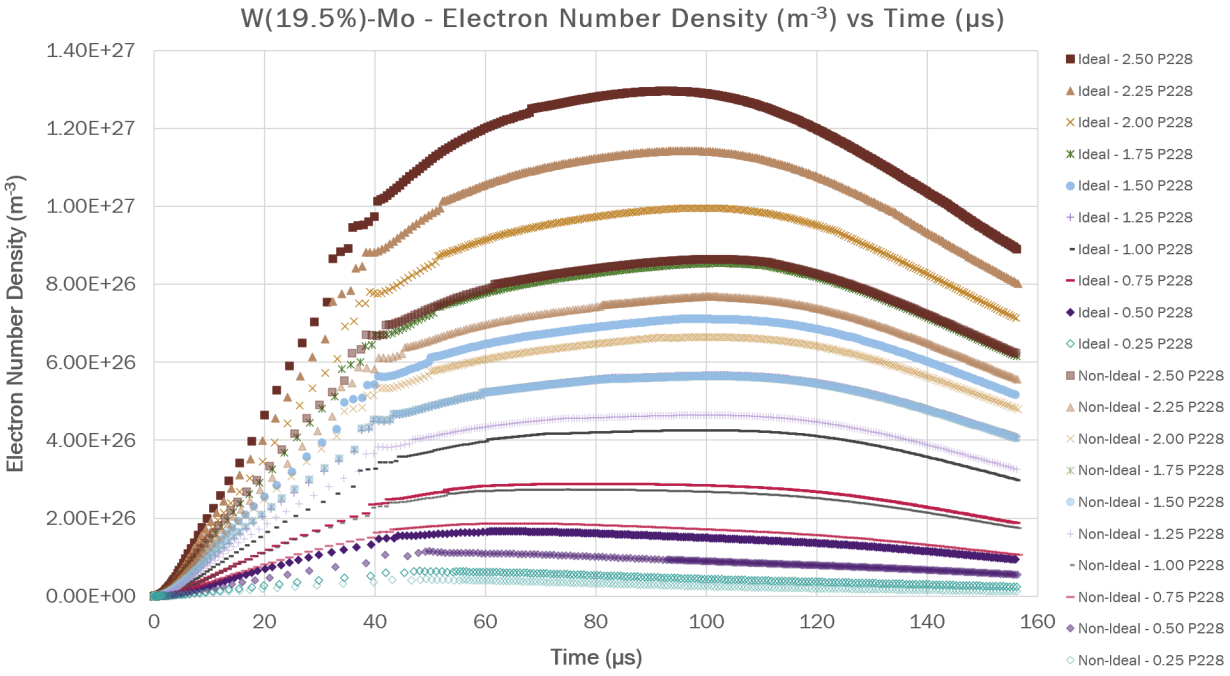

Figure A.6: W(19.5%)-Mo Electron Number Density (m^{-3}) versus Time (μs) as generated by ETFLOW

A.1.4 W(90.0%)-Mo Results

Table A.7: ETFLOW Simulations of W(90.0%)-Mo - Ideal Cases

Ideal Cases				
I (kA)	q" (GW/m^2)	T_{peak} (eV)	N_E (m^{-3})	M_{tot} (mg)
2.50	393.6	2.985	1.248×10^{27}	1.631
2.25	318.6	2.883	1.101×10^{27}	1.470
2.00	251.6	2.779	9.543×10^{26}	1.306
1.75	192.6	2.677	8.180×10^{26}	1.144
1.50	141.9	2.547	6.728×10^{26}	0.977
1.25	98.51	2.422	5.290×10^{26}	0.807
1.00	63.02	2.263	3.917×10^{26}	0.633
0.75	35.42	2.090	2.656×10^{26}	0.456
0.50	15.76	1.872	1.506×10^{26}	0.278
0.25	3.941	1.534	5.844×10^{25}	0.112

Table A.8: ETFLOW Simulations of W(90.0%)-Mo - Non-Ideal Cases

Non-Ideal Cases				
I (kA)	q" (GW/m^2)	T_{peak} (eV)	N_E (m^{-3})	M_{tot} (mg)
2.50	394.0	2.703	8.308×10^{26}	1.162
2.25	318.2	2.613	7.314×10^{26}	1.046
2.00	251.4	2.513	6.277×10^{26}	0.927
1.75	193.1	2.430	5.283×10^{26}	0.808
1.50	141.8	2.319	4.318×10^{26}	0.686
1.25	98.38	2.204	3.395×10^{26}	0.562
1.00	62.99	2.075	2.535×10^{26}	0.438
0.75	35.46	1.923	1.717×10^{26}	0.312
0.50	15.74	1.733	1.030×10^{26}	0.191
0.25	3.916	1.419	3.911×10^{25}	0.073

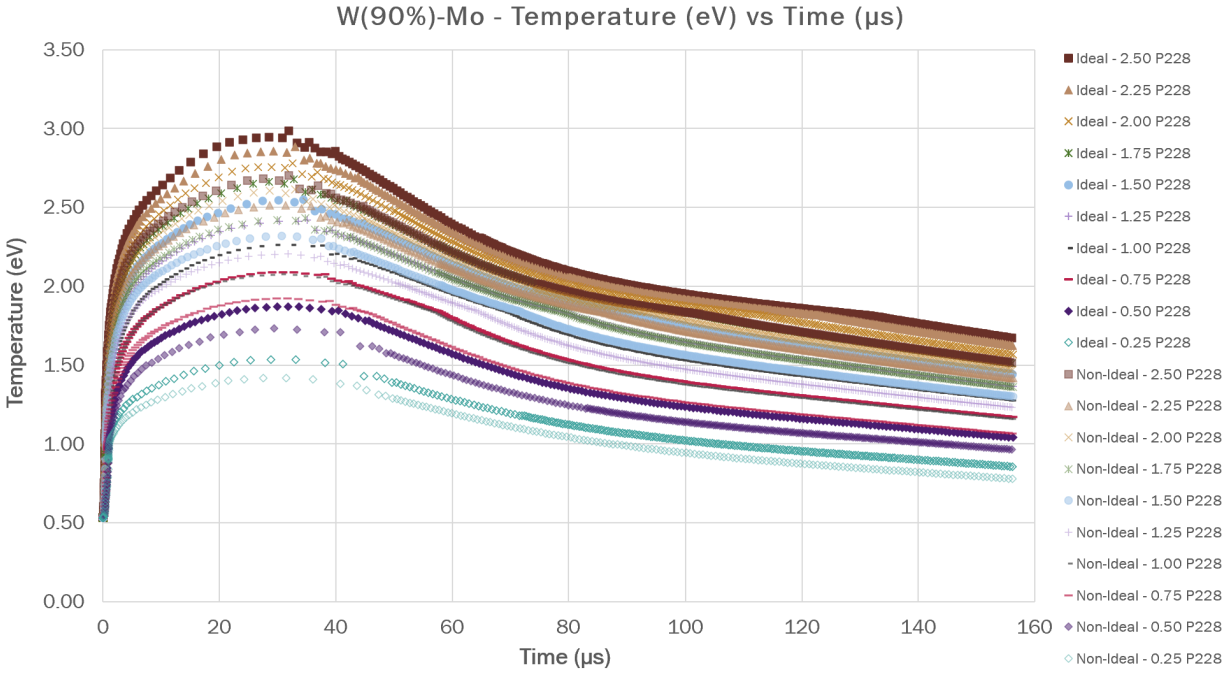

Figure A.7: W(90.0%)-Mo Temperature (eV) versus Time (μs) as generated by ETFLOW

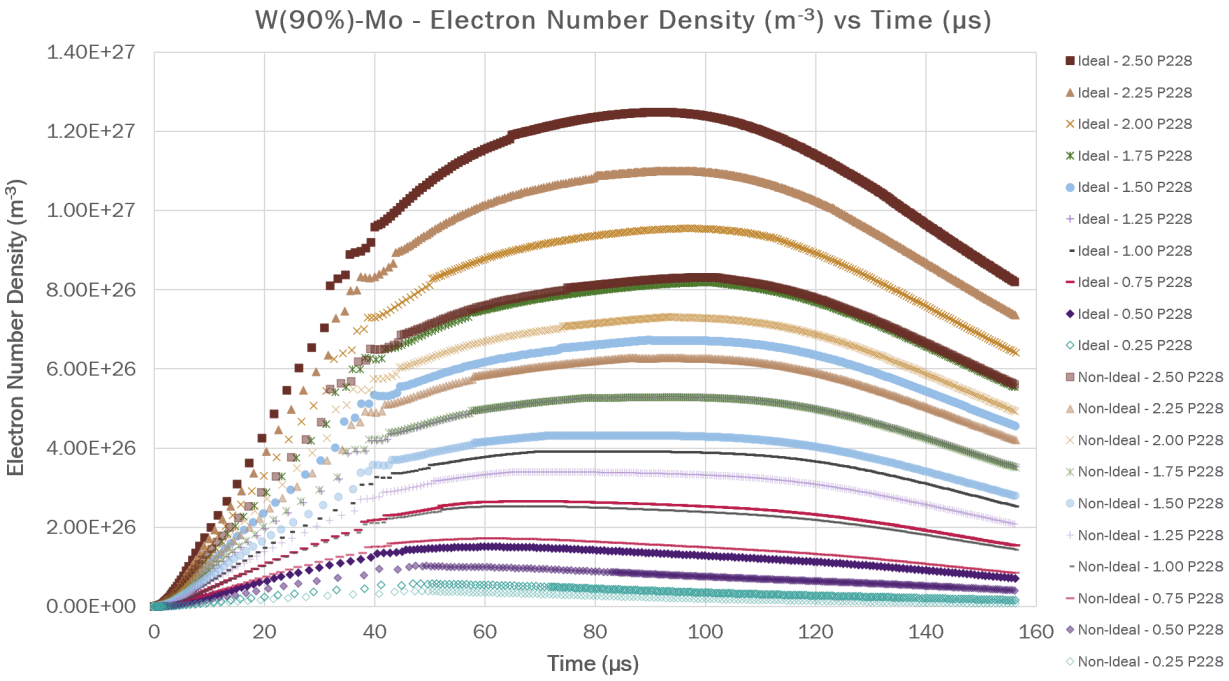

Figure A.8: W(90.0%)-Mo Electron Number Density (m^{-3}) versus Time (μs) as generated by ETFLOW

A.1.5 W(98.5%)-Mo Results

Table A.9: ETFLOW Simulations of W(98.5%)-Mo - Ideal Cases

Ideal Cases				
I (kA)	q" (GW/m^2)	T_{peak} (eV)	N_E (m^{-3})	M_{tot} (mg)
2.50	393.6	2.996	1.242×10^{27}	1.625
2.25	318.6	2.893	1.095×10^{27}	1.464
2.00	252.0	2.793	9.497×10^{26}	1.301
1.75	192.6	2.685	8.133×10^{26}	1.139
1.50	141.9	2.555	6.681×10^{26}	0.972
1.25	98.44	2.423	5.246×10^{26}	0.803
1.00	63.03	2.268	3.878×10^{26}	0.629
0.75	35.42	2.096	2.633×10^{26}	0.453
0.50	15.76	1.876	1.490×10^{26}	0.277
0.25	3.932	1.540	5.776×10^{25}	0.111

Table A.10: ETFLOW Simulations of W(98.5%)-Mo - Non-Ideal Cases

Non-Ideal Cases				
I (kA)	q" (GW/m^2)	T_{peak} (eV)	N_E (m^{-3})	M_{tot} (mg)
2.50	392.7	2.703	8.263×10^{26}	1.158
2.25	318.0	2.620	7.264×10^{26}	1.041
2.00	252.0	2.527	6.239×10^{26}	0.923
1.75	192.9	2.430	5.239×10^{26}	0.804
1.50	141.8	2.326	4.274×10^{26}	0.682
1.25	98.46	2.210	3.368×10^{26}	0.656
1.00	63.03	2.081	2.514×10^{26}	0.436
0.75	35.43	1.929	1.701×10^{26}	0.310
0.50	15.68	1.735	9.950×10^{25}	0.190
0.25	3.910	1.424	3.747×10^{25}	0.072

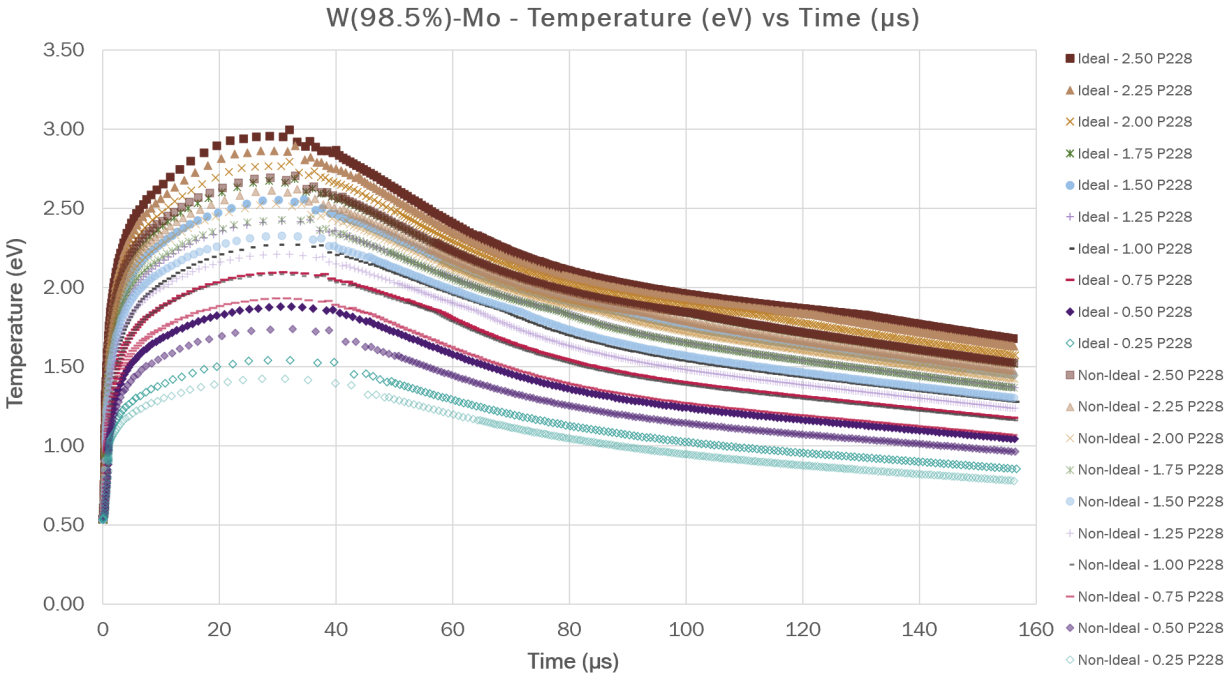

Figure A.9: W(98.5%)-Mo Temperature (eV) versus Time (μs) as generated by ETFLOW

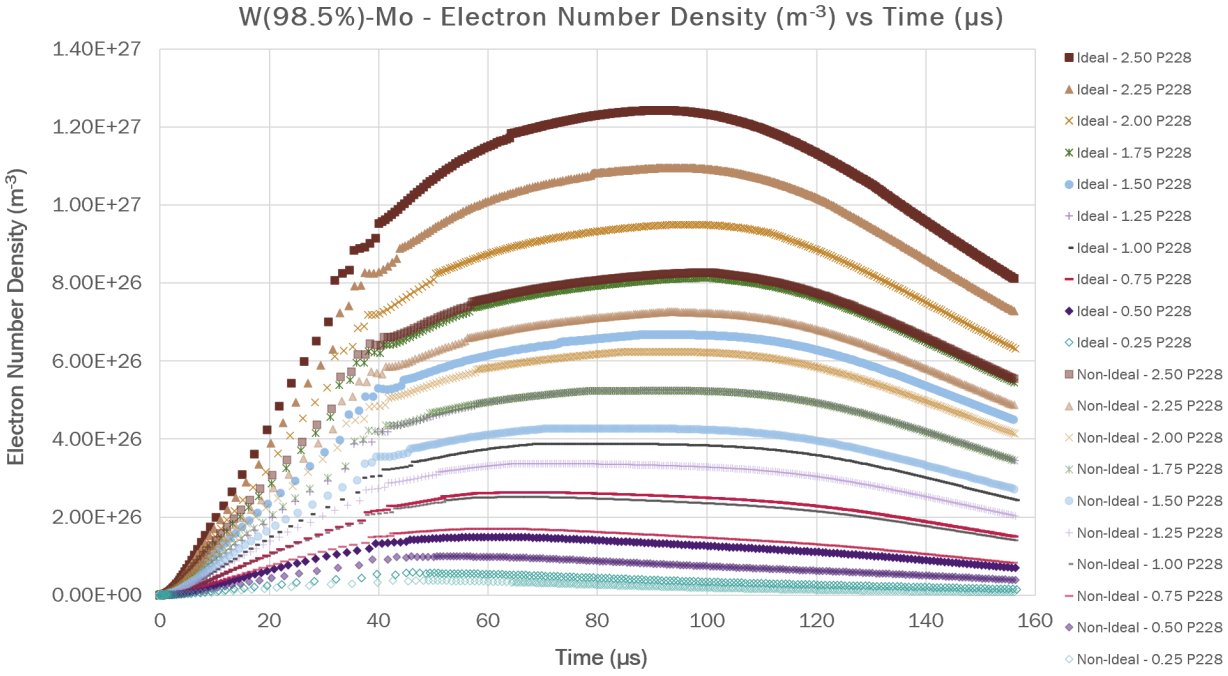

Figure A.10: W(98.5%)-Mo Electron Number Density (m^{-3}) versus Time (μs) as generated by ETFLOW

Appendix B
Mass Loss Calculations

B.1 Uranium Alloy Mass Loss Calculations

As stated in Section 5.2.1, mass loss calculations were performed for each of the five U-Mo alloys in the Godiva Alloy set. While not presented in that section due to space, the results for U-Mo(1.00%, 1.25%, 1.75%, 2.00%) are presented in SectionB.1. Results include the Mass Loss per Unit Surface Area (g/cm^2) based on the capillary surface areas of Godiva IV and ETFLOW, the Mass Loss per Unit Surface Area for each capillary case based on 2200 operational bursts, and the Mass Loss per Energy Deposited (g/MeV).

B.1.1 U-Mo(1.00%) Mass Loss Calculations

Table B.1: The mass loss per surface area for U-Mo(1.00%) computed using the Godiva IV capillary zone surface area.

U-Mo(1.00%) - Mass Loss per Surface Area (g/cm^2)				
	Ideal		Non-Ideal	
Current (kA)	High	Low	High	Low
2.50	1.190×10^{-5}	1.194×10^{-5}	8.042×10^{-6}	8.054×10^{-6}
2.25	1.059×10^{-5}	1.059×10^{-5}	7.173×10^{-6}	7.196×10^{-6}
2.00	9.266×10^{-6}	9.268×10^{-6}	6.340×10^{-6}	6.361×10^{-6}
1.75	7.987×10^{-6}	8.005×10^{-6}	5.512×10^{-6}	5.539×10^{-6}
1.50	6.758×10^{-6}	6.780×10^{-6}	4.727×10^{-6}	4.752×10^{-6}
1.25	5.589×10^{-6}	5.613×10^{-6}	3.954×10^{-6}	3.978×10^{-6}
1.00	4.459×10^{-6}	4.489×10^{-6}	3.200×10^{-6}	3.225×10^{-6}
0.75	3.375×10^{-6}	3.400×10^{-6}	2.440×10^{-6}	2.466×10^{-6}
0.50	2.297×10^{-6}	2.324×10^{-6}	1.650×10^{-6}	1.678×10^{-6}
0.25	1.141×10^{-6}	1.169×10^{-6}	8.003×10^{-7}	8.300×10^{-7}

Table B.2: The mass loss per surface area for U-Mo(1.00%) computed using the ETFLOW capillary surface area.

U-Mo(1.00%) - Mass Loss per Surface Area (g/cm^2)				
	Ideal		Non-Ideal	
Current (kA)	High	Low	High	Low
2.50	1.248×10^{-4}	1.252×10^{-4}	8.433×10^{-5}	8.446×10^{-5}
2.25	1.110×10^{-4}	1.111×10^{-4}	7.523×10^{-5}	7.547×10^{-5}
2.00	9.717×10^{-5}	9.719×10^{-5}	6.649×10^{-5}	6.671×10^{-5}
1.75	8.376×10^{-5}	8.395×10^{-5}	5.781×10^{-5}	5.809×10^{-5}
1.50	7.087×10^{-5}	7.111×10^{-5}	4.958×10^{-5}	4.984×10^{-5}
1.25	5.861×10^{-5}	5.886×10^{-5}	4.147×10^{-5}	4.172×10^{-5}
1.00	4.677×10^{-5}	4.707×10^{-5}	3.356×10^{-5}	3.382×10^{-5}
0.75	3.540×10^{-5}	3.566×10^{-5}	2.559×10^{-5}	2.587×10^{-5}
0.50	2.409×10^{-5}	2.437×10^{-5}	1.731×10^{-5}	1.760×10^{-5}
0.25	1.197×10^{-5}	1.226×10^{-5}	8.393×10^{-6}	8.704×10^{-6}

Table B.3: Godiva IV mass loss per surface area for U-Mo(1.00%) normalized to the ETFLOW capillary surface area.

U-Mo(1.00%) - Mass Loss per Surface Area (g/cm^2)				
	Ideal		Non-Ideal	
Current (kA)	High	Low	High	Low
2.50	1.227×10^{-4}	1.231×10^{-4}	8.286×10^{-5}	8.299×10^{-5}
2.25	1.091×10^{-4}	1.092×10^{-4}	7.392×10^{-5}	7.415×10^{-5}
2.00	9.548×10^{-5}	9.550×10^{-5}	6.533×10^{-5}	6.555×10^{-5}
1.75	8.230×10^{-5}	8.249×10^{-5}	5.680×10^{-5}	5.708×10^{-5}
1.50	6.964×10^{-5}	6.987×10^{-5}	4.871×10^{-5}	4.897×10^{-5}
1.25	5.759×10^{-5}	5.784×10^{-5}	4.075×10^{-5}	4.099×10^{-5}
1.00	4.595×10^{-5}	4.625×10^{-5}	3.297×10^{-5}	3.323×10^{-5}
0.75	3.478×10^{-5}	3.504×10^{-5}	2.514×10^{-5}	2.542×10^{-5}
0.50	2.367×10^{-5}	2.395×10^{-5}	1.701×10^{-5}	1.729×10^{-5}
0.25	1.176×10^{-5}	1.205×10^{-5}	8.247×10^{-6}	8.552×10^{-6}

Table B.4: The mass loss per surface area for U-Mo(1.00%) computed using the Godiva IV capillary zone surface area for 2163 bursts.

U-Mo(1.00%) - Mass Loss per Surface Area (g/cm^2)				
	Ideal		Non-Ideal	
Current (kA)	High	Low	High	Low
2.50	0.026	0.026	0.017	0.017
2.25	0.023	0.023	0.016	0.016
2.00	0.020	0.020	0.014	0.014
1.75	0.017	0.017	0.012	0.012
1.50	0.015	0.015	0.010	0.010
1.25	0.012	0.012	0.009	0.009
1.00	0.010	0.010	0.007	0.007
0.75	0.007	0.007	0.005	0.005
0.50	0.005	0.005	0.004	0.004
0.25	0.002	0.003	0.002	0.002

Table B.5: The mass loss per surface area for U-Mo(1.00%) computed using the ETFLOW capillary surface area for 2163 bursts.

U-Mo(1.00%) - Mass Loss per Surface Area (g/cm^2)				
	Ideal		Non-Ideal	
Current (kA)	High	Low	High	Low
2.50	0.270	0.271	0.182	0.183
2.25	0.240	0.240	0.163	0.163
2.00	0.210	0.210	0.144	0.144
1.75	0.181	0.182	0.125	0.126
1.50	0.153	0.154	0.107	0.108
1.25	0.127	0.127	0.090	0.090
1.00	0.101	0.102	0.073	0.073
0.75	0.077	0.077	0.055	0.056
0.50	0.052	0.053	0.037	0.038
0.25	0.026	0.027	0.018	0.019

Table B.6: The mass loss per surface area for U-Mo(1.00%) computed using the normalized surface area for 2163 bursts.

U-Mo(1.00%) - Mass Loss per Surface Area (g/cm^2)				
	Ideal		Non-Ideal	
Current (kA)	High	Low	High	Low
2.50	0.265	0.266	0.179	0.180
2.25	0.236	0.236	0.160	0.160
2.00	0.207	0.207	0.141	0.142
1.75	0.178	0.178	0.123	0.123
1.50	0.151	0.151	0.105	0.106
1.25	0.125	0.125	0.088	0.089
1.00	0.099	0.100	0.071	0.072
0.75	0.075	0.076	0.054	0.055
0.50	0.051	0.052	0.037	0.037
0.25	0.025	0.026	0.018	0.018

Table B.7: The mass loss per energy deposited for U-Mo(1.00%).

U-Mo(1.00%) - Mass Loss per Energy Deposited (g/MeV)				
	Ideal		Non-Ideal	
Current (kA)	High	Low	High	Low
2.50	5.182×10^{13}	5.383×10^{13}	4.357×10^{13}	3.082×10^{13}
2.25	5.373×10^{13}	5.367×10^{13}	3.112×10^{13}	3.108×10^{13}
2.00	3.582×10^{13}	4.530×10^{13}	3.170×10^{13}	3.176×10^{13}
1.75	4.338×10^{13}	3.093×10^{13}	2.616×10^{13}	2.621×10^{13}
1.50	2.921×10^{13}	2.924×10^{13}	2.536×10^{13}	2.531×10^{13}
1.25	3.189×10^{13}	2.676×10^{13}	1.942×10^{13}	1.946×10^{13}
1.00	2.335×10^{13}	2.341×10^{13}	1.699×10^{13}	1.699×10^{13}
0.75	1.535×10^{13}	1.533×10^{13}	1.345×10^{13}	1.348×10^{13}
0.50	1.471×10^{13}	1.475×10^{13}	8.525×10^{12}	8.187×10^{12}
0.25	2.888×10^{12}	2.884×10^{12}	1.430×10^{12}	1.431×10^{12}

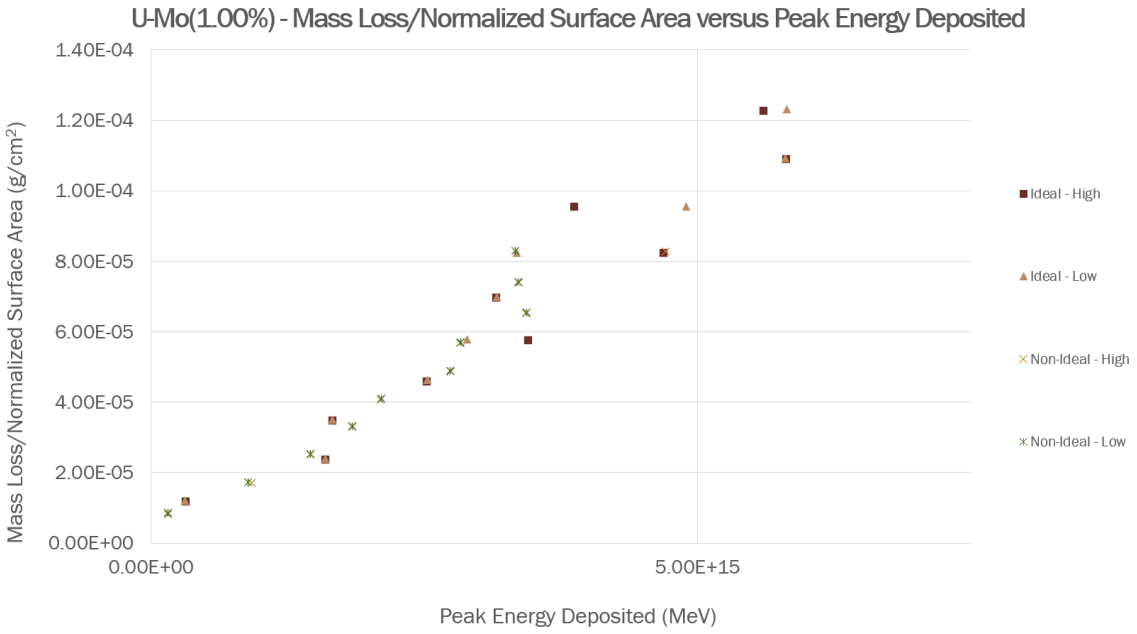

Figure B.1: The Mass Loss/Normalized Surface Area (g/cm^2) plotted against the Deposited Energy (MeV) for U-Mo(1.00%)

B.1.2 U-Mo(1.25%) Mass Loss Calculations

Table B.8: The mass loss per surface area for U-Mo(1.25%) computed using the Godiva IV capillary zone surface area.

U-Mo(1.25%) - Mass Loss per Surface Area (g/cm^2)				
	Ideal		Non-Ideal	
Current (kA)	High	Low	High	Low
2.50	1.189×10^{-5}	1.192×10^{-5}	8.027×10^{-6}	8.043×10^{-6}
2.25	1.057×10^{-5}	1.058×10^{-5}	7.164×10^{-6}	7.187×10^{-6}
2.00	9.253×10^{-6}	9.277×10^{-6}	6.317×10^{-6}	6.353×10^{-6}
1.75	7.976×10^{-6}	7.995×10^{-6}	5.506×10^{-6}	5.533×10^{-6}
1.50	6.750×10^{-6}	6.772×10^{-6}	4.723×10^{-6}	4.747×10^{-6}
1.25	5.583×10^{-6}	5.606×10^{-6}	3.951×10^{-6}	3.975×10^{-6}
1.00	4.455×10^{-6}	4.484×10^{-6}	3.197×10^{-6}	3.223×10^{-6}
0.75	3.373×10^{-6}	3.397×10^{-6}	2.437×10^{-6}	2.464×10^{-6}
0.50	2.295×10^{-6}	2.322×10^{-6}	1.649×10^{-6}	1.676×10^{-6}
0.25	1.140×10^{-6}	1.167×10^{-6}	7.984×10^{-7}	8.285×10^{-7}

Table B.9: The mass loss per surface area for U-Mo(1.25%) computed using the ETFLOW capillary surface area.

U-Mo(1.25%) - Mass Loss per Surface Area (g/cm^2)				
	Ideal		Non-Ideal	
Current (kA)	High	Low	High	Low
2.50	1.246×10^{-4}	1.250×10^{-4}	8.418×10^{-5}	8.435×10^{-5}
2.25	1.109×10^{-4}	1.109×10^{-4}	7.513×10^{-5}	7.537×10^{-5}
2.00	9.704×10^{-5}	9.729×10^{-5}	6.625×10^{-5}	6.663×10^{-5}
1.75	8.365×10^{-5}	8.384×10^{-5}	5.774×10^{-5}	5.802×10^{-5}
1.50	7.079×10^{-5}	7.102×10^{-5}	4.953×10^{-5}	4.979×10^{-5}
1.25	5.855×10^{-5}	5.880×10^{-5}	4.143×10^{-5}	4.168×10^{-5}
1.00	4.672×10^{-5}	4.703×10^{-5}	3.353×10^{-5}	3.380×10^{-5}
0.75	3.537×10^{-5}	3.563×10^{-5}	2.556×10^{-5}	2.584×10^{-5}
0.50	2.407×10^{-5}	2.435×10^{-5}	1.729×10^{-5}	1.758×10^{-5}
0.25	1.195×10^{-5}	1.224×10^{-5}	8.373×10^{-6}	8.689×10^{-6}

Table B.10: Godiva IV mass loss per surface area for U-Mo(1.25%) normalized to the ETFLOW capillary surface area.

U-Mo(1.25%) - Mass Loss per Surface Area (g/cm^2)				
	Ideal		Non-Ideal	
Current (kA)	High	Low	High	Low
2.50	1.225×10^{-4}	1.229×10^{-4}	8.271×10^{-5}	8.288×10^{-5}
2.25	1.089×10^{-4}	1.090×10^{-4}	7.382×10^{-5}	7.406×10^{-5}
2.00	9.534×10^{-5}	9.560×10^{-5}	6.510×10^{-5}	6.547×10^{-5}
1.75	8.219×10^{-5}	8.238×10^{-5}	5.673×10^{-5}	5.701×10^{-5}
1.50	6.955×10^{-5}	6.978×10^{-5}	4.866×10^{-5}	4.892×10^{-5}
1.25	5.753×10^{-5}	5.777×10^{-5}	4.071×10^{-5}	4.096×10^{-5}
1.00	4.591×10^{-5}	4.621×10^{-5}	3.295×10^{-5}	3.321×10^{-5}
0.75	3.475×10^{-5}	3.501×10^{-5}	2.511×10^{-5}	2.539×10^{-5}
0.50	2.365×10^{-5}	2.392×10^{-5}	1.699×10^{-5}	1.727×10^{-5}
0.25	1.175×10^{-5}	1.202×10^{-5}	8.227×10^{-6}	8.537×10^{-6}

Table B.11: The mass loss per surface area for U-Mo(1.25%) computed using the Godiva IV capillary zone surface area for 2163 bursts.

U-Mo(1.25%) - Mass Loss per Surface Area (g/cm^2)				
	Ideal		Non-Ideal	
Current (kA)	High	Low	High	Low
2.50	0.026	0.026	0.017	0.017
2.25	0.023	0.023	0.015	0.016
2.00	0.020	0.020	0.014	0.014
1.75	0.017	0.017	0.012	0.012
1.50	0.015	0.015	0.010	0.010
1.25	0.012	0.012	0.009	0.009
1.00	0.010	0.010	0.007	0.007
0.75	0.007	0.007	0.005	0.005
0.50	0.005	0.005	0.004	0.004
0.25	0.002	0.003	0.002	0.002

Table B.12: The mass loss per surface area for U-Mo(1.25%) computed using the ETFLOW capillary surface area for 2163 bursts.

U-Mo(1.25%) - Mass Loss per Surface Area (g/cm^2)				
	Ideal		Non-Ideal	
Current (kA)	High	Low	High	Low
2.50	0.270	0.270	0.182	0.182
2.25	0.240	0.240	0.163	0.163
2.00	0.210	0.210	0.143	0.144
1.75	0.181	0.181	0.125	0.126
1.50	0.153	0.154	0.107	0.108
1.25	0.127	0.127	0.090	0.090
1.00	0.101	0.102	0.073	0.073
0.75	0.077	0.077	0.055	0.056
0.50	0.052	0.053	0.037	0.038
0.25	0.026	0.026	0.018	0.019

Table B.13: The mass loss per surface area for U-Mo(1.25%) computed using the normalized surface area for 2163 bursts.

U-Mo(1.25%) - Mass Loss per Surface Area (g/cm^2)				
	Ideal		Non-Ideal	
Current (kA)	High	Low	High	Low
2.50	0.265	0.266	0.179	0.179
2.25	0.236	0.236	0.160	0.160
2.00	0.206	0.207	0.141	0.142
1.75	0.178	0.178	0.123	0.123
1.50	0.150	0.151	0.105	0.106
1.25	0.124	0.125	0.088	0.089
1.00	0.099	0.100	0.071	0.072
0.75	0.075	0.076	0.054	0.055
0.50	0.051	0.052	0.037	0.037
0.25	0.025	0.026	0.018	0.018

Table B.14: The mass loss per energy deposited for U-Mo(1.25%).

U-Mo(1.25%) - Mass Loss per Energy Deposited (g/MeV)				
	Ideal		Non-Ideal	
Current (kA)	High	Low	High	Low
2.50	5.182×10^{13}	5.383×10^{13}	4.358×10^{13}	3.082×10^{13}
2.25	5.373×10^{13}	5.367×10^{13}	3.113×10^{13}	3.108×10^{13}
2.00	3.583×10^{13}	4.529×10^{13}	2.642×10^{13}	3.176×10^{13}
1.75	4.339×10^{13}	3.094×10^{13}	2.616×10^{13}	2.621×10^{13}
1.50	2.921×10^{13}	2.924×10^{13}	2.536×10^{13}	2.532×10^{13}
1.25	3.190×10^{13}	2.676×10^{13}	1.942×10^{13}	1.946×10^{13}
1.00	2.335×10^{13}	2.341×10^{13}	1.699×10^{13}	1.699×10^{13}
0.75	1.535×10^{13}	1.533×10^{13}	1.345×10^{13}	1.348×10^{13}
0.50	1.471×10^{13}	1.475×10^{13}	8.522×10^{12}	8.185×10^{12}
0.25	2.886×10^{12}	2.882×10^{12}	1.433×10^{12}	1.431×10^{12}

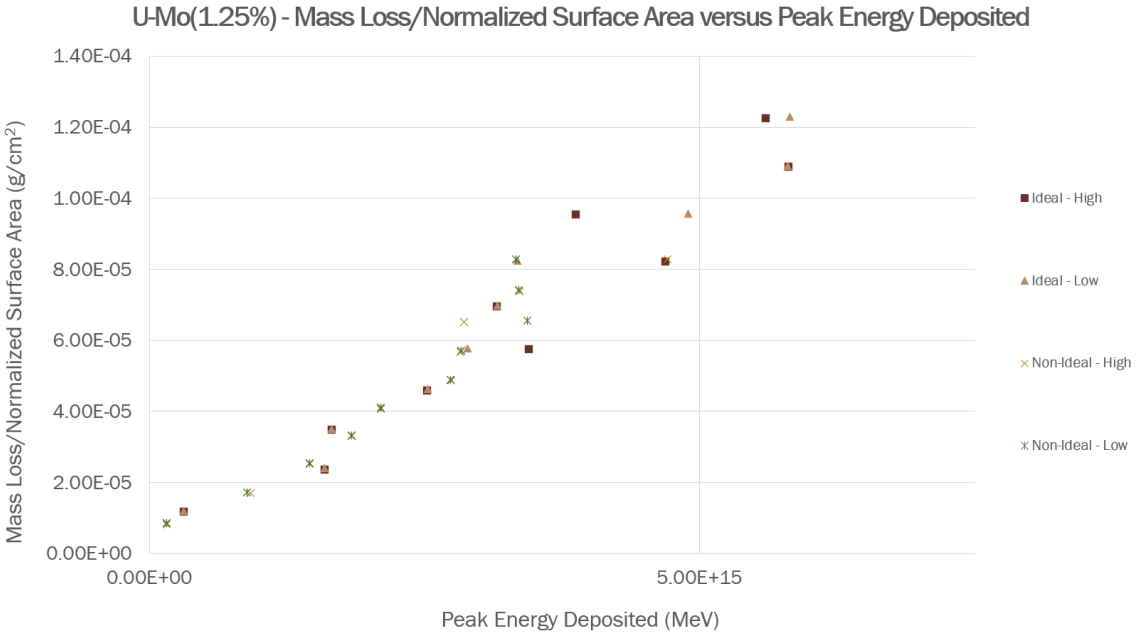

Figure B.2: The Mass Loss/Normalized Surface Area (g/cm^2) plotted against the Deposited Energy (MeV) for U-Mo(1.25%)

B.1.3 U-Mo(1.75%) Mass Loss Calculations

Table B.15: The mass loss per surface area for U-Mo(1.75%) computed using the Godiva IV capillary zone surface area.

U-Mo(1.75%) - Mass Loss per Surface Area (g/cm^2)				
	Ideal		Non-Ideal	
Current (kA)	High	Low	High	Low
2.50	1.185×10^{-5}	1.189×10^{-5}	8.023×10^{-6}	8.022×10^{-6}
2.25	1.054×10^{-5}	1.056×10^{-5}	7.144×10^{-6}	7.169×10^{-6}
2.00	9.226×10^{-6}	9.251×10^{-6}	6.305×10^{-6}	6.327×10^{-6}
1.75	7.971×10^{-6}	7.982×10^{-6}	5.494×10^{-6}	5.521×10^{-6}
1.50	6.733×10^{-6}	6.756×10^{-6}	4.713×10^{-6}	4.732×10^{-6}
1.25	5.570×10^{-6}	5.594×10^{-6}	3.943×10^{-6}	3.967×10^{-6}
1.00	4.446×10^{-6}	4.475×10^{-6}	3.194×10^{-6}	3.216×10^{-6}
0.75	3.368×10^{-6}	3.391×10^{-6}	2.433×10^{-6}	2.462×10^{-6}
0.50	2.290×10^{-6}	2.318×10^{-6}	1.647×10^{-6}	1.673×10^{-6}
0.25	1.137×10^{-6}	1.164×10^{-6}	7.959×10^{-7}	8.261×10^{-7}

Table B.16: The mass loss per surface area for U-Mo(1.75%) computed using the ETFLOW capillary surface area.

U-Mo(1.75%) - Mass Loss per Surface Area (g/cm^2)				
	Ideal		Non-Ideal	
Current (kA)	High	Low	High	Low
2.50	1.242×10^{-4}	1.247×10^{-4}	8.414×10^{-5}	8.412×10^{-5}
2.25	1.105×10^{-4}	1.108×10^{-4}	7.492×10^{-5}	7.518×10^{-5}
2.00	9.675×10^{-5}	9.701×10^{-5}	6.612×10^{-5}	6.635×10^{-5}
1.75	8.359×10^{-5}	8.371×10^{-5}	5.761×10^{-5}	5.790×10^{-5}
1.50	7.061×10^{-5}	7.085×10^{-5}	4.943×10^{-5}	4.963×10^{-5}
1.25	5.841×10^{-5}	5.866×10^{-5}	4.136×10^{-5}	4.161×10^{-5}
1.00	4.663×10^{-5}	4.693×10^{-5}	3.350×10^{-5}	3.373×10^{-5}
0.75	3.532×10^{-5}	3.556×10^{-5}	2.551×10^{-5}	2.582×10^{-5}
0.50	2.402×10^{-5}	2.430×10^{-5}	1.727×10^{-5}	1.754×10^{-5}
0.25	1.192×10^{-5}	1.220×10^{-5}	8.346×10^{-6}	8.663×10^{-6}

Table B.17: Godiva IV mass loss per surface area for U-Mo(1.75%) normalized to the ETFLOW capillary surface area.

U-Mo(1.75%) - Mass Loss per Surface Area (g/cm^2)				
	Ideal		Non-Ideal	
Current (kA)	High	Low	High	Low
2.50	1.221×10^{-4}	1.225×10^{-4}	8.267×10^{-5}	8.266×10^{-5}
2.25	1.086×10^{-4}	1.089×10^{-4}	7.362×10^{-5}	7.387×10^{-5}
2.00	9.507×10^{-5}	9.532×10^{-5}	6.497×10^{-5}	6.520×10^{-5}
1.75	8.213×10^{-5}	8.225×10^{-5}	5.661×10^{-5}	5.689×10^{-5}
1.50	6.938×10^{-5}	6.962×10^{-5}	4.856×10^{-5}	4.876×10^{-5}
1.25	5.740×10^{-5}	5.764×10^{-5}	4.064×10^{-5}	4.088×10^{-5}
1.00	4.581×10^{-5}	4.612×10^{-5}	3.291×10^{-5}	3.314×10^{-5}
0.75	3.471×10^{-5}	3.494×10^{-5}	2.507×10^{-5}	2.537×10^{-5}
0.50	2.360×10^{-5}	2.388×10^{-5}	1.697×10^{-5}	1.724×10^{-5}
0.25	1.171×10^{-5}	1.199×10^{-5}	8.201×10^{-6}	8.512×10^{-6}

Table B.18: The mass loss per surface area for U-Mo(1.75%) computed using the Godiva IV capillary zone surface area for 2163 bursts.

U-Mo(1.75%) - Mass Loss per Surface Area (g/cm^2)				
	Ideal		Non-Ideal	
Current (kA)	High	Low	High	Low
2.50	0.026	0.026	0.017	0.017
2.25	0.023	0.023	0.015	0.016
2.00	0.020	0.020	0.014	0.014
1.75	0.017	0.017	0.012	0.012
1.50	0.015	0.015	0.010	0.010
1.25	0.012	0.012	0.009	0.009
1.00	0.010	0.010	0.007	0.007
0.75	0.007	0.007	0.005	0.005
0.50	0.005	0.005	0.004	0.004
0.25	0.002	0.003	0.002	0.002

Table B.19: The mass loss per surface area for U-Mo(1.75%) computed using the ETFLOW capillary surface area for 2163 bursts.

U-Mo(1.75%) - Mass Loss per Surface Area (g/cm^2)				
	Ideal		Non-Ideal	
Current (kA)	High	Low	High	Low
2.50	0.269	0.270	0.182	0.182
2.25	0.239	0.240	0.162	0.163
2.00	0.209	0.210	0.143	0.144
1.75	0.181	0.181	0.125	0.125
1.50	0.153	0.153	0.107	0.107
1.25	0.126	0.127	0.089	0.090
1.00	0.101	0.102	0.072	0.073
0.75	0.076	0.077	0.055	0.056
0.50	0.052	0.053	0.037	0.038
0.25	0.026	0.026	0.018	0.019

Table B.20: The mass loss per surface area for U-Mo(1.75%) computed using the normalized surface area for 2163 bursts.

U-Mo(1.75%) - Mass Loss per Surface Area (g/cm^2)				
	Ideal		Non-Ideal	
Current (kA)	High	Low	High	Low
2.50	0.264	0.265	0.179	0.179
2.25	0.235	0.235	0.159	0.160
2.00	0.206	0.206	0.141	0.141
1.75	0.178	0.178	0.122	0.123
1.50	0.150	0.151	0.105	0.105
1.25	0.124	0.125	0.088	0.088
1.00	0.099	0.100	0.071	0.072
0.75	0.075	0.076	0.054	0.055
0.50	0.051	0.052	0.037	0.037
0.25	0.025	0.026	0.018	0.018

Table B.21: The mass loss per energy deposited for U-Mo(1.75%).

U-Mo(1.75%) - Mass Loss per Energy Deposited (g/MeV)				
	Ideal		Non-Ideal	
Current (kA)	High	Low	High	Low
2.50	5.184×10^{13}	5.384×10^{13}	4.359×10^{13}	3.083×10^{13}
2.25	5.375×10^{13}	5.366×10^{13}	3.114×10^{13}	3.109×10^{13}
2.00	4.529×10^{13}	4.530×10^{13}	2.643×10^{13}	2.647×10^{13}
1.75	4.341×10^{13}	2.984×10^{13}	2.617×10^{13}	2.621×10^{13}
1.50	2.922×10^{13}	2.925×10^{13}	2.536×10^{13}	2.097×10^{13}
1.25	3.190×10^{13}	2.676×10^{13}	1.942×10^{13}	1.946×10^{13}
1.00	2.335×10^{13}	2.341×10^{13}	1.693×10^{13}	1.693×10^{13}
0.75	1.851×10^{13}	1.533×10^{13}	1.345×10^{13}	1.347×10^{13}
0.50	1.472×10^{13}	1.474×10^{13}	8.193×10^{12}	8.196×10^{12}
0.25	2.883×10^{12}	2.879×10^{12}	1.432×10^{12}	1.430×10^{12}

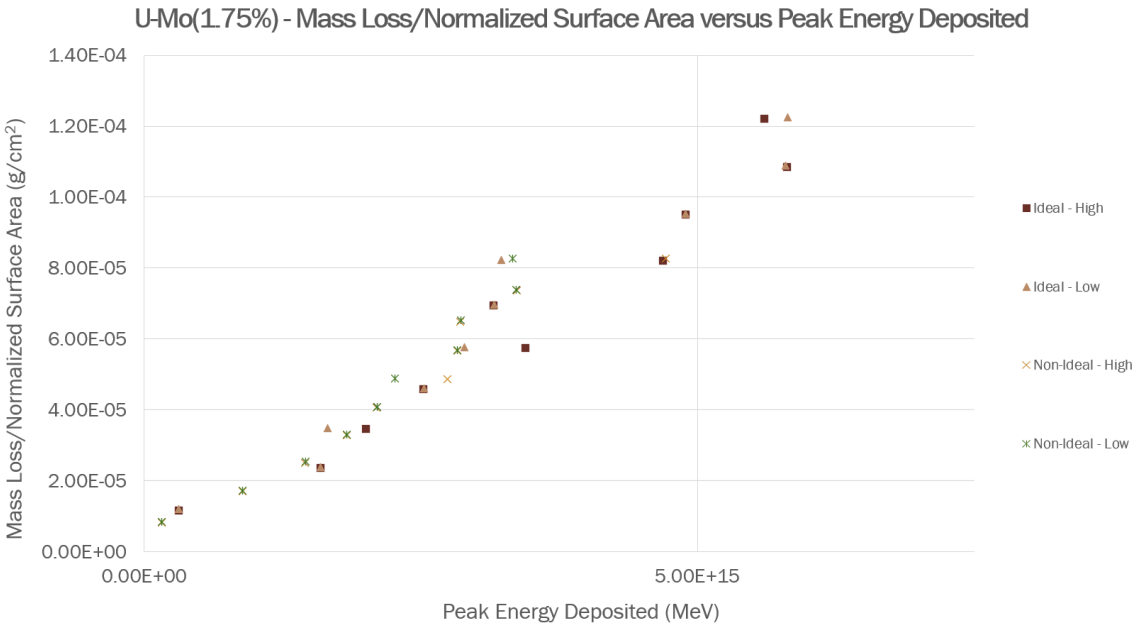

Figure B.3: The Mass Loss/Normalized Surface Area (g/cm^2) plotted against the Deposited Energy (MeV) for U-Mo(1.75%)

B.1.4 U-Mo(2.00%) Mass Loss Calculations

Table B.22: The mass loss per surface area for U-Mo(2.00%) computed using the Godiva IV capillary zone surface area.

U-Mo(2.00%) - Mass Loss per Surface Area (g/cm^2)				
	Ideal		Non-Ideal	
Current (kA)	High	Low	High	Low
2.50	1.183×10^{-5}	1.187×10^{-5}	8.012×10^{-6}	8.011×10^{-6}
2.25	1.052×10^{-5}	1.055×10^{-5}	7.135×10^{-6}	7.160×10^{-6}
2.00	9.213×10^{-6}	9.241×10^{-6}	6.313×10^{-6}	6.320×10^{-6}
1.75	7.948×10^{-6}	7.976×10^{-6}	5.492×10^{-6}	5.516×10^{-6}
1.50	6.724×10^{-6}	6.763×10^{-6}	4.708×10^{-6}	4.727×10^{-6}
1.25	5.564×10^{-6}	5.587×10^{-6}	3.940×10^{-6}	3.964×10^{-6}
1.00	4.442×10^{-6}	4.471×10^{-6}	3.190×10^{-6}	3.216×10^{-6}
0.75	3.365×10^{-6}	3.388×10^{-6}	2.434×10^{-6}	2.460×10^{-6}
0.50	2.288×10^{-6}	2.316×10^{-6}	1.645×10^{-6}	1.671×10^{-6}
0.25	1.135×10^{-6}	1.162×10^{-6}	7.946×10^{-7}	8.248×10^{-7}

Table B.23: The mass loss per surface area for U-Mo(2.00%) computed using the ETFLOW capillary surface area.

U-Mo(2.00%) - Mass Loss per Surface Area (g/cm^2)				
	Ideal		Non-Ideal	
Current (kA)	High	Low	High	Low
2.50	1.240×10^{-4}	1.245×10^{-4}	8.403×10^{-5}	8.401×10^{-5}
2.25	1.104×10^{-4}	1.106×10^{-4}	7.483×10^{-5}	7.508×10^{-5}
2.00	9.662×10^{-5}	9.691×10^{-5}	6.620×10^{-5}	6.627×10^{-5}
1.75	8.335×10^{-5}	8.365×10^{-5}	5.759×10^{-5}	5.784×10^{-5}
1.50	7.052×10^{-5}	7.092×10^{-5}	4.938×10^{-5}	4.958×10^{-5}
1.25	5.835×10^{-5}	5.860×10^{-5}	4.132×10^{-5}	4.157×10^{-5}
1.00	4.658×10^{-5}	4.689×10^{-5}	3.345×10^{-5}	3.372×10^{-5}
0.75	3.529×10^{-5}	3.553×10^{-5}	2.553×10^{-5}	2.580×10^{-5}
0.50	2.400×10^{-5}	2.429×10^{-5}	1.725×10^{-5}	1.752×10^{-5}
0.25	1.190×10^{-5}	1.219×10^{-5}	8.333×10^{-6}	8.650×10^{-6}

Table B.24: Godiva IV mass loss per surface area for U-Mo(2.00%) normalized to the ETFLOW capillary surface area.

U-Mo(2.00%) - Mass Loss per Surface Area (g/cm^2)				
	Ideal		Non-Ideal	
Current (kA)	High	Low	High	Low
2.50	1.219×10^{-4}	1.223×10^{-4}	8.256×10^{-5}	8.255×10^{-5}
2.25	1.084×10^{-4}	1.087×10^{-4}	7.352×10^{-5}	7.378×10^{-5}
2.00	9.493×10^{-5}	9.522×10^{-5}	6.505×10^{-5}	6.512×10^{-5}
1.75	8.190×10^{-5}	8.219×10^{-5}	5.659×10^{-5}	5.684×10^{-5}
1.50	6.929×10^{-5}	6.969×10^{-5}	4.852×10^{-5}	4.871×10^{-5}
1.25	5.733×10^{-5}	5.757×10^{-5}	4.060×10^{-5}	4.084×10^{-5}
1.00	4.577×10^{-5}	4.607×10^{-5}	3.287×10^{-5}	3.313×10^{-5}
0.75	3.468×10^{-5}	3.491×10^{-5}	2.509×10^{-5}	2.535×10^{-5}
0.50	2.358×10^{-5}	2.387×10^{-5}	1.695×10^{-5}	1.722×10^{-5}
0.25	1.170×10^{-5}	1.197×10^{-5}	8.188×10^{-6}	8.499×10^{-6}

Table B.25: The mass loss per surface area for U-Mo(2.00%) computed using the Godiva IV capillary zone surface area for 2163 bursts.

U-Mo(2.00%) - Mass Loss per Surface Area (g/cm^2)				
	Ideal		Non-Ideal	
Current (kA)	High	Low	High	Low
2.50	0.026	0.026	0.017	0.017
2.25	0.023	0.023	0.015	0.015
2.00	0.020	0.020	0.014	0.014
1.75	0.017	0.017	0.012	0.012
1.50	0.015	0.015	0.010	0.010
1.25	0.012	0.012	0.009	0.009
1.00	0.010	0.010	0.007	0.007
0.75	0.007	0.007	0.005	0.005
0.50	0.005	0.005	0.004	0.004
0.25	0.002	0.003	0.002	0.002

Table B.26: The mass loss per surface area for U-Mo(2.00%) computed using the ETFLOW capillary surface area for 2163 bursts.

U-Mo(2.00%) - Mass Loss per Surface Area (g/cm^2)				
	Ideal		Non-Ideal	
Current (kA)	High	Low	High	Low
2.50	0.268	0.269	0.182	0.182
2.25	0.239	0.239	0.162	0.162
2.00	0.209	0.210	0.143	0.143
1.75	0.180	0.181	0.125	0.125
1.50	0.153	0.153	0.107	0.107
1.25	0.126	0.127	0.089	0.090
1.00	0.101	0.101	0.072	0.073
0.75	0.076	0.077	0.055	0.056
0.50	0.052	0.053	0.037	0.038
0.25	0.026	0.026	0.018	0.019

Table B.27: The mass loss per surface area for U-Mo(2.00%) computed using the normalized surface area for 2163 bursts.

U-Mo(2.00%) - Mass Loss per Surface Area (g/cm^2)				
	Ideal		Non-Ideal	
Current (kA)	High	Low	High	Low
2.50	0.264	0.265	0.179	0.179
2.25	0.235	0.235	0.159	0.160
2.00	0.205	0.206	0.141	0.141
1.75	0.177	0.178	0.122	0.123
1.50	0.150	0.151	0.105	0.105
1.25	0.124	0.125	0.088	0.088
1.00	0.099	0.100	0.071	0.072
0.75	0.075	0.076	0.054	0.055
0.50	0.051	0.052	0.037	0.037
0.25	0.025	0.026	0.018	0.018

Table B.28: The mass loss per energy deposited for U-Mo(2.00%).

U-Mo(2.00%) - Mass Loss per Energy Deposited (g/MeV)				
	Ideal		Non-Ideal	
Current (kA)	High	Low	High	Low
2.50	5.185×10^{13}	5.384×10^{13}	4.360×10^{13}	3.084×10^{13}
2.25	5.375×10^{13}	5.366×10^{13}	3.115×10^{13}	3.110×10^{13}
2.00	4.530×10^{13}	4.530×10^{13}	3.168×10^{13}	2.647×10^{13}
1.75	2.984×10^{13}	4.341×10^{13}	3.147×10^{13}	3.152×10^{13}
1.50	2.923×10^{13}	2.886×10^{13}	2.536×10^{13}	2.097×10^{13}
1.25	3.190×10^{13}	2.676×10^{13}	1.942×10^{13}	1.946×10^{13}
1.00	2.335×10^{13}	2.341×10^{13}	1.693×10^{13}	1.692×10^{13}
0.75	1.851×10^{13}	1.533×10^{13}	1.344×10^{13}	1.347×10^{13}
0.50	1.471×10^{13}	1.474×10^{13}	8.191×10^{12}	8.194×10^{12}
0.25	2.882×10^{12}	2.878×10^{12}	1.431×10^{12}	1.429×10^{12}

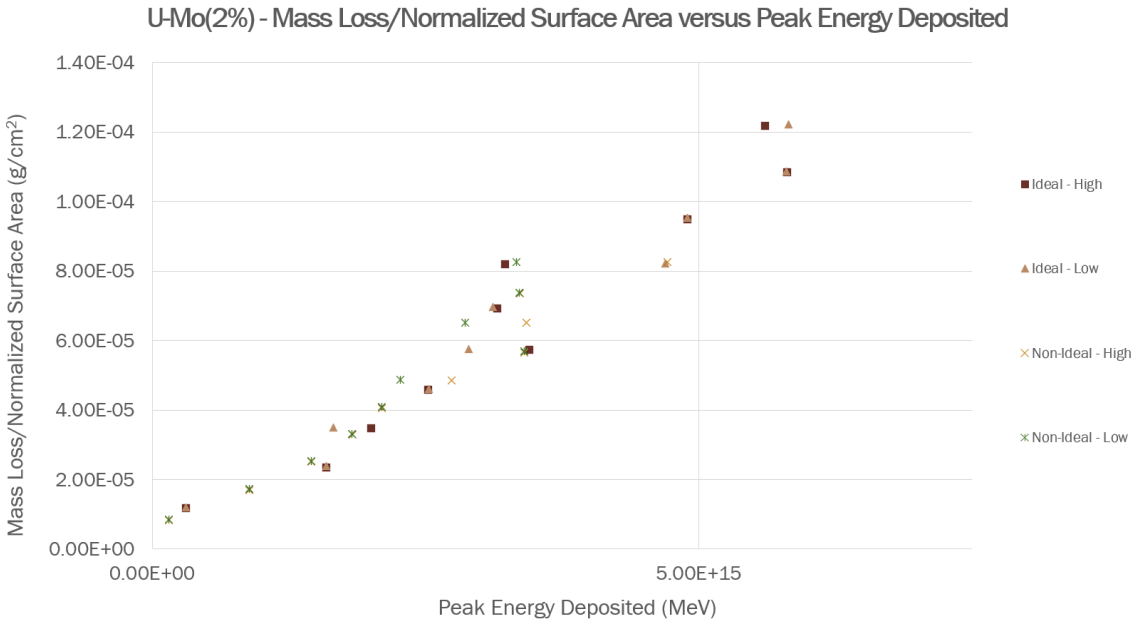

Figure B.4: The Mass Loss/Normalized Surface Area (g/cm^2) plotted against the Deposited Energy (MeV) for U-Mo(2.00%)

Bibliography

[1] R.D. Mosteller (2014) *Godiva-IV Delayed-Critical Experiments and Description of an Associated Prompted-Burst Experiment*, *International Criticality Safety Benchmark Evaluation Project (ICSBEP) Benchmark HEU-MET-FAST-086*, Nuclear Energy Agency, international Criticality Safety Benchmark Evaluation Project (ICSBEP) Handbook Entry.

[2] V.E. Hagopian (2020) "Updating the GODIVA-IV Model," BEARS Lab presentation on previous work.

[3] U. Fantz (2006) "Basics of plasma spectroscopy," *Plasma Sources Science and Technology*, **15**, pp. S137–S147.

[4] L. Winfrey (2015) "Electrothermal Plasmas," Slides on Electrothermal Plasmas.

[5] A.L. Winfrey (2010) *A Numerical Study of the Non-Ideal Behavior, Parameters, and Novel Applications of an Electrothermal Plasma Source*, Ph.D. thesis, North Carolina State University, Raleigh, NC.

[6] D. Ding (2022), "SEM Images of laser ablation impacts on Tungsten samples," .

[7] N. AlMousa and M.A. Bourham (2016) "Vapor Shield Models for Fusion Reactors Plasma-Facing Components," *Journal of Fusion Energy*, (35), pp. 786–794.

[8] University of Colorado - Boulder (2021), "Dusty Plasmas," .

[9] E. Thomas, Jr. (2016), "Introduction to the physics of complex/dusty plasmas," .

[10] J. Gilligan, M. Bourham, O. Hankins, W. Eddy, J. Hurley, and D. Black (1992) "Vapor Shield protection of plasma facing components under incident high heat flux*," *Journal of Nuclear Materials*, **196-198**, pp. 596–601.

[11] A.L. Winfrey, J.G. Gilligan, and M.A. Bourham (2013) "A Computational Study of a Capillary Discharge Pellet Accelerator Concept for Magnetic Fusion Fueling," *Journal of Fusion Energy*, **32**, pp. 227–234.

[12] A.L. Winfrey, M.A. Abd Al-Halim, J.G. Gilligan, A.V. Saveliev, and M.A. Bourham (2013) "Enhanced Performance of Electrothermal Plasma Sources as Fusion

Pellet Injection Drivers and Space Based Mini-Thrusters via Extension of a Flattop Discharge Current," *Journal of Fusion Energy*, **32**, pp. 371–377.

[13] H. Zohm (1995) "Edge localized modes (ELMs)," *Plasma Physics and Controlled Fusion*, **38**, pp. 105–128.

[14] J. Gilligan and R. Mohanti (1990) "Time-dependent numerical simulation of ablation-controlled arcs," *IEEE Transactions on Plasma Science*, **18**(2), pp. 190–197.

[15] M. Esmond and L. Winfrey (2016) "Radiation Heat Transfer and Vapor Shielding in a Two-Dimensional Model of an Electrothermal Plasma Source," *Journal of Fusion Energy*, (35), pp. 643–651.

[16] T.R. Schmidt (2017) *U.S. Fast Burst Reactors: Design and Operational History*, 1 ed., American Nuclear Society, La Grange Park, IL, USA.

[17] T.F. Wimett, R.H. White, and R.G. Wagner (1969) "Godiva IV," in *Proceedings of the National Topical Meeting on Fast Burst Reactors*, USAEC Conf-690102, U.S. Atomic Energy Commission, Albuquerque, NM, pp. 95–104.

[18] V.E. Hagopian (2020) *Updates to the Godiva-IV Model with Experimental Improvements to K-eff Values*, Master's thesis, The Pennsylvania State University, University Park, PA.

[19] J.J. Duderstadt and L.J. Hamilton (1976) *Nuclear Reactor Analysis*, John Wiley Sons, The University of Michigan, Ann Arbor, Michigan.

[20] I.P. Herman (1996) *Optical Diagnostics for Thin Film Proscessing*, chap. Chapter 6: Optical Emission Spectroscopy, Academic Press, pp. 157–213.

[21] J.R. Echols (2017) *Design and Use of a High Heat Flux Device for Exposing Tungsten to Fusion-Relevant Conditions and Evaluating Surface Effects of Exposure*, Ph.D. thesis, University of Florida, Gainesville, FL.

[22] A.L. Winfrey, M.A. Abd Al-Halim, J.G. Gilligan, A.V. Saveliev, and M.A. Bourham (2012) "A Study of Plasma Parameters in a Capillary Discharge With Calculations Using Ideal and Nonideal Plasma Models for Comparison With Experiment," *IEEE Transactions on Plasma Science*, **40**(3), pp. 843–852.

[23] J.R. Davis (1998) *Metals Handbook Desk Edition: Refractory Metals and Alloys*, *ASM International Second Edition*.

[24] INCO: The International Nickel Company, INC. (1982) *Properties of Some Metals and Alloys*, *Tech. rep.*

[25] J. Rest, Y.S. Kim, G.L. Hofman, M.K. Meyer, and S.L. Hayes (2006) *U-Mo Fuels Handbook*, *RERTR Program, Argonne National Laboratory Versions 1.0*, aNL-09/31.

[26] KEYENCE America (2022), "Sa (Arithmetical Mean Height) | Area Roughness Parameters | Introduction To Roughness," .

[27] ——— (2022), "Sq (Root Mean Square Height) | Area Roughness Parameters | Introduction To Roughness," .

[28] ——— (2022), "Sz (Maximum Height) | Area Roughness Parameters | Introduction To Roughness," .

[29] C.J. Werner (2017) *MCNP® User's Manual: Code Version 6.2*, *User Manual LA-UR-17-29981*.

[30] J. Goda, C. Bravo, T. Cutler, T. Grove, D. Hayes, J. Hutchinson, G. McKenzie, A. McSpaden, W. Myers, R. Sanchez, and J. Walker (2021) "A New Era of Nuclear Criticality Experiments: The First 10 Years of Godiva IV Operations at NCERC," *Nuclear Science and Engineering*, **195**(Supplement 1), pp. S55–S79.

Vita

Victoria E. Hagopian

Victoria E. Hagopian was born in Connecticut and spent the majority of their childhood in the Fairfield County area before moving to Chapel Hill, NC the summer of their senior year. Upon completing high school, they took a gap year during which they worked retail jobs to save money for community college which they attended the following summer. They attended Alamance Community College for three years, graduating in 2014 with their Associate of Science intent on transferring to a four-year university. While attending ACC, they were Phi Theta Kappa and Sigma Delta Mu Honors Student and worked as a Chemistry Tutor in the school's Academic Skills Lab. Upon graduation, they transferred to North Carolina State University where they pursued a Bachelor of Science degree in Nuclear Engineering, which was obtained in 2017. During their time at NCSU, they were an active member of the school's American Nuclear Society chapter and department volunteer. After graduating with their Bachelor's degree, they briefly attended the University of Florida before their advisor and lab group, the $\overline{B} \times \overline{E}$ Applied Research and Science **(BEARS)** Lab moved to the Pennsylvania State University. There, they completed a Master of Science degree in Nuclear Engineering in 2020 for their work "Updates to the Godiva-IV Model with Experimental Improvements to K-eff Values." They are an active member of the American Nuclear Society (ANS), the Institute of Electrical and Electronics Engineers (IEEE) and the American Physical Society (APS).